

이학박사 학위논문

Star Formation in Nuclear Rings of Barred Galaxies

막대은하 핵고리의 별 형성

2022년 8월

서울대학교 대학원
물리·천문학부 천문학전공
문상혁

Star Formation in Nuclear Rings of Barred Galaxies

막대은하 핵고리의 별 형성

지도교수 김 응 태

이 논문을 이학박사 학위논문으로 제출함
2022년 4월

서울대학교 대학원
물리·천문학부 천문학전공
문상혁

문상혁의 이학박사 학위논문을 인준함
2022년 6월

위 원 장 _____

부 위 원 장 _____

위 원 _____

위 원 _____

위 원 _____

Star Formation in Nuclear Rings of Barred Galaxies

by

Sanghyuk Moon
(s.moon@snu.ac.kr)

A dissertation submitted in partial fulfillment of the requirements for
the degree of

Doctor of Philosophy

in
Astronomy

in
Astronomy Program
Department of Physics and Astronomy
Seoul National University

Committee:

Professor Sung-Chul Yoon

Professor Woong-Tae Kim

Professor Taysun Kimm

Doctor Jongsoo Kim

Professor Ji-Hoon Kim

ABSTRACT

Nuclear rings are sites of compact yet intense star formation often found at centers of barred galaxies. Concentrated in a small volume, rapid formation of stars in nuclear rings has an important consequence on the buildup of dense stellar structures at galaxy centers. In addition, strong stellar feedback from nuclear rings greatly changes gas flow structure, affecting the launching of galactic winds and the fueling of nuclear activities. While observations indicate that the star formation rate of nuclear rings varies considerably with space and time, theoretical understanding of what controls star formation in nuclear rings remains elusive. In this thesis, we use three-dimensional (magneto)hydrodynamic simulations to investigate effects of mass inflow, supernova feedback, and magnetic fields on star formation in nuclear rings.

In Chapter 2, we use controlled numerical simulations to study what determines the structure and star formation rate of nuclear rings subject to constant mass inflow rates. A common numerical framework that is used throughout the thesis is introduced in this chapter. We find that, contrary to previous expectations based on one-dimensional models, the supernova feedback is not strong enough to destroy the ring or quench star formation everywhere in the ring because of their stochasticity in space and time. Under the constant mass inflow rate, the ring star formation is very steady and persistent, where the star formation rate is tightly correlated with the inflow rate and exhibits only mild temporal fluctuations. The ring gas mass at the given star formation rate is set by the force balance between the midplane pressure arising from stellar feedback and the weight of the gas under the gravitational field arising from both gas and stars.

In Chapter 3, we allow the mass inflow rate to vary in time and/or be asymmetric in space, to assess resulting effects on temporal and spatial distribution of star formation in nuclear rings. We find that a time-varying inflow rate with not too small an amplitude and timescale can cause episodic star formation in nu-

clear rings, such that the star formation rate follows the variation of the inflow rate with some time delay. Within the ring, vertical dynamical equilibrium is well maintained such that the midplane pressure balances the weight of the overlying gas, despite large time variations in the latter two quantities. The relation between the star formation rate and gas mass is consistent with the prediction from the pressure-regulated, feedback-modulated star formation theory. While asymmetry in the inflow rate does not necessarily lead to asymmetric star formation, a transient period of lopsided star formation occurs when the inflow rate from one of the two dust lanes is suddenly increased by a large factor.

In Chapter 4, we include magnetic fields in our models to study their effects on dynamical evolution of nuclear rings and star formation therein. We find that magnetic fields are efficiently amplified in the ring due presumably to rotational shear and supernova feedback. Expanding superbubbles created by clustered supernova explosions drag predominantly-toroidal fields near the midplane to produce poloidal fields away in high-altitude regions. Magnetic pressure in the ring eventually dominates the thermal and turbulent pressures and suppresses the ring star formation. Strong magnetic tension in the ring drives accretion flows from the ring radially inward and forms a circumnuclear disk in the central region, which is absent in the unmagnetized model.

Taken together, we conclude that the ring star formation rate and its long-term time variations are causally controlled by the mass inflow rate, while the supernova feedback is responsible for maintaining the vertical dynamical equilibrium and by doing so setting the depletion time, and induces small-amplitude, short-term fluctuations in the star formation rate. When magnetic fields are very strong, however, the ring star formation rate can be significantly suppressed below the mass inflow rate, complicating the relation between the inflow rate and star formation rate.

Keywords: Spiral galaxies, Galaxy evolution, Star formation, Galaxy centers, Interstellar medium, Stellar feedback, Magnetohydrodynamical simulations

Student Number: 2016-26780

Contents

Abstract	i
List of Figures	ix
List of Tables	xiii
List of Acronyms	xiv
1 Introduction	1
1.1 Observational Evidence of Bar-Driven Galaxy Evolution	2
1.1.1 Central Star Formation Enhancements	3
1.1.2 Disk-Like Bulges	5
1.2 Gas Flow in Barred Galaxies	6
1.2.1 Closed Orbits	6
1.2.2 Gaseous Response	13
1.3 Nuclear Rings	16
1.3.1 Formation Mechanisms	16
1.3.2 Physical Properties	20
1.3.3 Star Formation History	23
1.4 Scope and Outline of This Thesis	24
2 Semi-Global Numerical Simulations of Nuclear Rings Subject to Constant Mass Inflow Rates	27

2.1	Overview	27
2.2	Numerical Methods	31
2.2.1	Basic Equations	31
2.2.2	Gas Inflow Streams	37
2.2.3	Star Particles and SN Feedback	40
2.2.4	Models	41
2.3	Evolution	44
2.3.1	Overall Evolution of the Fiducial Model	44
2.3.2	Star Formation	52
2.3.3	Other Models	55
2.4	Correlations of Statistical Quantities	60
2.4.1	Ring Properties	62
2.4.2	Vertical Dynamical Equilibrium and Star Formation Feedback	65
2.5	Summary and Discussion	77
2.5.1	Summary	77
2.5.2	Discussion	81
3	Effects of Varying Mass Inflows on Star Formation in Nuclear Rings	87
3.1	Overview	87
3.2	Methods	90
3.2.1	Equations	90
3.2.2	Models	93
3.3	Results	95
3.3.1	Time Variation of the SFR	97
3.3.2	Relation between the SFR and the Inflow Rate	98
3.3.3	Self-regulation Theory	103
3.3.4	Spatial Distributions of Star Clusters	107
3.4	Summary and Discussion	111

4 Effects of Magnetic Fields on Gas Dynamics and Star Formation in Nuclear Rings	117
4.1 Overview	117
4.2 Numerical Methods	121
4.2.1 Governing Equations	122
4.2.2 Star Formation and Feedback	125
4.2.3 Magnetized Inflow Streams	126
4.2.4 Models	130
4.3 Evolution	130
4.3.1 Overall Evolution	131
4.3.2 Star Formation History	136
4.3.3 Magnetically Driven Accretion Flow	137
4.4 Magnetic Fields in the Ring	141
4.4.1 Growth of Magnetic Fields	141
4.4.2 Effects of Magnetic Fields on Star Formation	145
4.4.3 Vertical Dynamical Equilibrium	149
4.5 Summary and Discussion	150
4.5.1 Summary	150
4.5.2 Discussion	152
5 Conclusions and Future Work	157
5.1 Conclusions	157
5.2 Future Work	160
Bibliography	163
Appendix	178
A Orbit Integration of Sink Particles with the Coriolis Force	179
B Seed Magnetic Fields	185

C Magnetic Energy Conservation	187
D Mass Accretion Rates due to Maxwell and Reynolds Stresses	189
요 약	191
감사의 글	193

List of Figures

1.1	Composite image of barred spiral galaxy NGC 4535 observed with HST and ALMA	7
1.2	Closed orbits in weak bar potential	8
1.3	Closed orbits in strong bar potential	11
1.4	Gas response to weak bar potential	14
1.5	Hubble image of nuclear ring in NGC 1097	17
2.1	Rotation curve of adopted gravitational potential	33
2.2	2D histogram of mean intensity of ultraviolet radiation and gas density	35
2.3	Schematic diagram of semi-global numerical framework	38
2.4	Face-on evolution of fiducial model	45
2.5	Edge-on evolution of fiducial model	46
2.6	Phase diagram in pressure-density plane	48
2.7	Close-up view of superbubble expansion	50
2.8	Streamlines and velocity profile of galactic wind	51
2.9	Temporal histories of various physical quantities	53
2.10	Comparison of gas density snapshot of all models	56
2.11	Spatial distribution star particles	57
2.12	Temporal variations of velocity dispersion, sound speed, and scale height	59
2.13	Illustration of applying ring mask	61
2.14	Dependence of star formation rate and gas mass on inflow rate	64

2.15	Dependence of velocity dispersion and scale height on star formation rate	66
2.16	Time evolution of gas weight components	68
2.17	Gas weight versus midplane pressure	69
2.18	Dependence of gas weights on gas surface density	70
2.19	Dependence of thermal and turbulent pressures on star formation rate surface density	73
2.20	Dependence of star formation rate surface density on gas surface density, midplane pressure, and gas weight	77
3.1	Temporal histories of mass inflow rate, star formation rate, gas mass, and depletion time	96
3.2	Successive variations of mass inflow rate, gas density, star formation rate, supernova explosion rate, and gas scale height	99
3.3	Same with Figure 3.2, but for models P50, P15, off, and boost . .	102
3.4	Temporal variations of midplane pressure and gas weight	104
3.5	Comparison of measured depletion time variations with theoretical prediction	106
3.6	Spatial distribution of gas and young star clusters	108
4.1	Face-on views of the fiducial model at $t = 10, 50, 100, 220, 250$, and 285 Myr (the figure continues to the next page)	127
4.1	(continued)	128
4.2	Evolution of the radial distribution of the azimuthally-averaged gas surface density for all models	131
4.3	Superbubble breakout in the vertical direction	132
4.4	Perspective visualization of the three-dimensional magnetic field struc- ture in the fiducial model at $t = 250$ Myr	133

4.5	Temporal histories of the star formation rate (SFR), the total gas mass, the gas depletion time, and the ratio of the total magnetic to kinetic energy inside the computational domain	138
4.6	Temporal histories of the accretion rate at $R = 100\text{ pc}$	139
4.7	Radial profiles of the mass accretion rate at different epochs for the fiducial model	140
4.8	Spatial distributions of the azimuthally-averaged hydrogen number density and the regular and turbulent components of the magnetic fields at $t = 200$ and 300 Myr	142
4.9	Temporal histories of the regular, turbulent, and total magnetic field strength in the ring	143
4.10	Temporal changes of the azimuthal and radial components of the regular magnetic field	144
4.11	Temporal histories of the sound speed, the vertical velocity dispersion, and the Alfvén speed in the fiducial model	146
4.12	Gas depletion time <i>vs.</i> the total magnetic field strength in the ring .	146
4.13	Temporal histories of the total midplane pressure and gas weight, as well as the thermal, turbulent, and magnetic components of the midplane pressure	148
A.1	Illustration of Boris algorithm	181
A.2	Comparison between Boris algorithm and traditional leap-frog integrator	183
B.1	Illustration of the magnetic fields and velocity vectors in the ghost zones belonging to the nozzle at the positive y -boundary	186

List of Tables

2.1	Model parameters	42
2.2	Steady-state Properties of the Cold–Warm Gas	60
2.3	Steady-state Ring Properties	63
3.1	Summary of all models	94
3.2	Fluctuation amplitudes of $\dot{M}_{\text{SF},10}$, M_{gas} , and $t_{\text{dep},10}$	98
3.3	SFR asymmetry	110
4.1	Model parameters	121

List of Acronyms

AGN active galactic nuclei

ALMA Atacama large millimeter/submillimeter array

CMZ Central Molecular Zone

CND circumnuclear disk

COR corotation resonance

CR cosmic ray

FFT fast Fourier transform

FUV far ultraviolet

HST Hubble space telescope

IFU integral-field unit

ILR inner Lindblad resonance

ISM interstellar medium

MHD magnetohydrodynamic

MJI magneto-Jeans instability

OLR outer Lindblad resonance

PHANGS Physics at High Angular resolution in Nearby GalaxieS

PRFM pressure-regulated, feedback-modulated

SFR star formation rate

SN supernova

UHR ultraharmonic resonance

Chapter 1

Introduction

Isolated galaxies are not just passively aging. Vast amount of energy stored in the galactic gravitational potential and differential rotation can be tapped to excite a wealth of dynamical phenomena. An outstanding example is the dynamical instability of stellar disks that lead to bar formation, which in turn changes structure of a host galaxy via its non-axisymmetric gravitational force. These internal, *secular* evolution of galaxies can be as important as violent transformation involving mergers or interactions, especially toward late universe (Kormendy & Kennicutt 2004).

One important consequence of nonlinear interaction between the bar and the gas disk is the radial inflow of gas that can lead to intense star formation activities within the central kiloparsec region of galaxies. Energetic stellar feedback from such localized star formation in the forms of supernovae, radiation, and cosmic ray pressure can launch galactic scale outflows that can regulate the growth of the host galaxy and enrich the circumgalactic medium with metals (Veilleux et al. 2005; Zhang 2018). Prolonged star formation at central regions can build up dense stellar components that would manifest themselves as disk-like bulges ubiquitously found in local Universe (Kormendy & Kennicutt 2004; Fisher & Drory 2011). If sufficiently massive and compact, they might weaken or even destroy the bar (Shen & Sellwood 2004; Athanassoula et al. 2005; Kataria & Das 2018). Unraveling not

only the physical processes governing the star formation in galaxy centers but also the complex gas dynamics affected by stellar feedback is therefore extremely important in understanding the formation and evolution of disk galaxies, their morphological transformation across the Hubble type, and gas transport to the central region that can ignite nuclear starbursts or the active galactic nuclei (AGN).

This thesis explores effects of the three most important physical agents, namely the bar-driven mass inflow, supernova feedback, and magnetic fields, on the star formation in nuclear rings at the centers of barred galaxies. The main goal of this thesis is to clarify what controls the SFR and its temporal variations. The methodological approach adopted in this exploration is that of the standard scientific experimentation, where an experimenter controls all the variables except for the one whose effect is to be investigated. To do this, we develop a new numerical testbed for star-forming nuclear rings that is able to precisely control the ring size and mass inflow rate. We then perform a series of (magneto)hydrodynamic simulations by turning each ‘knobs’ of aforementioned physical agents. Each chapter of this thesis presents the results of such numerical experiments with the physical interpretations attempted whenever possible, and discuss their astronomical implications.

In the remainder of this chapter, we present observational evidence that suggests the existence of bar-driven galaxy evolution and review our current theoretical understanding of gas dynamics in barred galaxies. Then we will introduce the nuclear ring, which is the main celestial object under the present investigation. Current knowledge regarding their origin, physical properties, and star formation history will be reviewed. Lastly, we will present the scope and outline of this thesis.

1.1 Observational Evidence of Bar-Driven Galaxy Evolution

Theoretical considerations and numerical simulations have unequivocally demonstrated that dynamical effects of bars are significant enough to affect the gaseous

and stellar structure of galaxies (some aspects of it will be reviewed in Section 1.2). There is a substantial amount of observational evidence as well that points to the existence of the bar-driven evolution, even though it is very difficult to directly observe such a process because we can only see a snapshot of any given galaxy. This chapter presents observational evidence which suggests that bars lead to intense star formation activity around galactic centers, producing disk-like bulges.

1.1.1 Central Star Formation Enhancements

It had long been known that some galaxies have peculiar nuclei composed of multiple “hot spots” (Morgan 1958; Sérsic & Pastoriza 1965). Subsequent spectroscopic observations revealed that the bright emission from the hot spots is produced by a large number of young hot stars, suggesting that some galaxies are undergoing intense star formation in their nuclei (Osmer et al. 1974; Pastoriza 1975; Alloin & Kunth 1979). At the same time, a potentially interesting trend has been reported that those galaxies with central starburst activities tend to be barred (Sérsic & Pastoriza 1967; Heckman 1980; Devereux 1987; Arsenault 1989; Ho et al. 1997).

Observational evidence for the bar-driven star formation enhancement at galaxy centers has been accumulated mostly through careful comparisons between the barred and unbarred galaxies. For example, Ellison et al. (2011) constructed from a visually classified galaxy catalog of Nair & Abraham (2010) a matched sample of 294 barred and 588 unbarred galaxies that are similar in stellar mass, redshift, and the galaxy axial ratio (proxy for the inclination) and have well-determined fiber SFR. For galaxies with the stellar mass $M_* > 10^{10} M_\odot$, they found that the fiber SFRs are $\sim 60\%$ higher in barred galaxies compared to the unbarred counterparts at the given fiber stellar mass, indicating that bars tend to enhance the central star formation. However, they also found no star formation enhancement for lower mass galaxies with $M_* < 10^{10} M_\odot$, indicating that bars do not always enhance the central star formation (see also Devereux 1987; Ho et al. 1997). In a similar study but using different galaxy sample and bar identification method, Wang et al. (2012)

found that strong bars enhance the central SFR on average, but for individual galaxies they either enhance or suppress the central SFR, indicating that bars do not necessarily lead to central star formation and sometimes even suppress it.

Oh et al. (2012) visually classified 94,519 galaxies between the redshift $0.01 < z < 0.05$ to construct a late-type galaxy sample of 6658 galaxies with good image quality, in 36% among which they detected a bar and measured their length. They found that the fraction of galaxies with central star formation is overall higher in barred galaxies compared to unbarred galaxies at fixed galaxy stellar mass and color, and this effect is stronger for redder and less massive galaxies. The bar effect is found to be stronger in long-barred galaxies than short-barred galaxies. Not only the fraction of galaxies but also the emission line strengths at centers which trace the SFR are found to be higher in barred galaxies compared to unbarred galaxies with similar galaxy properties, in line with the findings of Ellison et al. (2011).

More recently, Lin et al. (2020) used integral-field unit (IFU) data to identify 121 “turnover” galaxies that exhibit a central upturn of the SFR, traced by the equivalent widths of Balmer lines and the 4000 Å break, within the bulge radius or the bar length. The bar fraction among the turnover galaxies is found to be 89%, which is much higher than that among the control galaxies, 34%, having similar stellar mass and color. It is found that the turnover galaxies are mostly massive, $M_* > 10^{10} M_\odot$, reminiscent of the findings in Ellison et al. (2011) where only those galaxies with $M_* > 10^{10} M_\odot$ exhibit central star formation enhancement.

Overall, observational evidence so far suggests that bars *on average* tend to enhance the central star formation in massive ($M_* > 10^{10} M_\odot$) galaxies that host a sufficiently strong bar. However, not all barred galaxies exhibit central star formation enhancement and vice versa, indicating that the presence of a bar is neither necessary nor sufficient condition for central star formation enhancement.

1.1.2 Disk-Like Bulges

A common conception of bulges is that they are any smooth, centrally concentrated stellar structure protruding out against a disk (Wyse et al. 1997). Although it provides convenient working definition, it also hides striking structural diversities linked to their origin. A widely used subdivision scheme is proposed by Athanassoula (2005), which distinguishes three types of bulges. First, *classical bulges* are the ones most consistent with the traditional view that a bulge is a miniature elliptical galaxy living at the centers of spirals, characterized by de Vaucouleur’s $r^{1/4}$ light profile or the Sérsic index $n = 4$. They are thought to form by hierarchical mergers or rapid gravitational collapse in the early universe. Second, *box/peanut bulges* are so called because they have boxy or peanut-like light distribution. They are generally regarded as nothing but edge-on bars which are vertically thickened via dynamical instabilities, masquerading as bulges. Last, *disk-like bulges* are flat, rotationally supported disks at galactic centers which have distinct light profile and kinematics from the main galactic disks. It is customary to call both box/peanut bulges and disk-like bulges together as *pseudobulges* as opposed to classical bulges, but it must be noted that box/peanuts and disk-like bulges can have vastly different origin. Fisher & Drory (2011) found that majority of nearby ($d < 11$ Mpc) bulges are rather flat, characterized by the Sérsic index $n < 2$, while the “classical” bulges with $n > 2$ start to dominate only above $M_* > 10^{10.5} M_\odot$.

Two competing scenario may be proposed for the origin of disk-like bulges. First, they can form by bar-driven mass inflow and ensuing central star formation (Section 1.1.1). Second, dry mergers or central star formation by external gas accretion can also form disk-like bulges. Those two scenarios, however, predict different kinematic properties of the resulting disk-like bulges. In the former scenario, gas transport process occurs in-plane with the main galactic disk, forming a central gas disk in nearly circular rotation. The resulting disk-like bulge would therefore have low velocity dispersion, with the kinematic axis well aligned with the host galaxy. In contrast, bulges produced via the second scenario can show misaligned angular

momentum with respect to the main disk and would have higher velocity dispersion, because the external gas accretion or mergers do not necessarily occur in the disk plane but rather have relatively random angular momentum vectors.

Gadotti et al. (2020) examined the stellar kinematics around the bulge region of 21 nearby ($d < 40$ Mpc), massive ($M_* > 10^{10} M_\odot$) barred spiral galaxies that have a variety of nuclear morphological features such as nuclear rings, nuclear spirals, nuclear lenses, inner bars, or nuclear disks. In all galaxies they found rotation-dominated, kinematically cold nuclear disks whose kinematic axis is very well aligned with the main galactic disk which qualify as disk-like bulges formed by bar-driven processes. Moreover, the radii of such disks are well correlated with bar lengths, supporting the bar-driven formation scenario.

1.2 Gas Flow in Barred Galaxies

Figure 1.1(a) shows the distribution of stars and molecular gas in the barred spiral galaxy NGC 4535, revealed by the Hubble space telescope (HST) and Atacama large millimeter/submillimeter array (ALMA). It presents a pair of grand-design spiral arms made up of both stars and gas emanating from the bar ends. For the gas, the spiral arms make a sharp turn near the bar ends and form a pair of “dust lanes” running almost straight along the leading edges of the bar. The dust lanes curl inward as they approach the center, where a large quantity of gas and young massive stars are found. Developing a physical theory of the gas flow associated with those structures is of utmost importance in understanding the evolution of barred galaxies, some aspect of which was reviewed in Section 1.1.

1.2.1 Closed Orbits

Even though the interstellar medium (ISM) is far from an aggregate of collisionless particles, the orbit theory provides an extremely useful conceptual tool to understand the complicated gas flow pattern in barred galaxies. In this section, we will first explain the concept of the orbital resonances and the epicyclic theory that

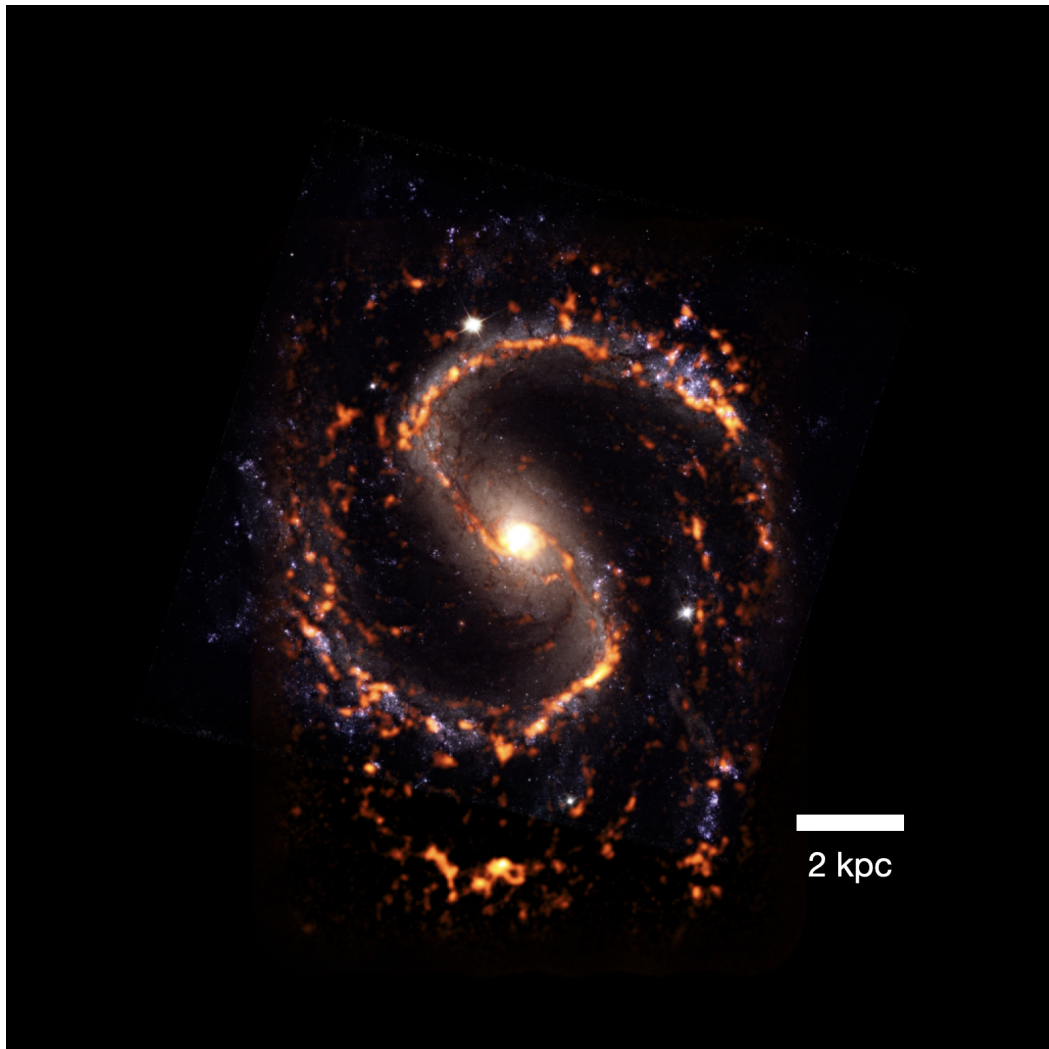


Figure 1.1. Barred Spiral Galaxy NGC 4535 observed with the HST (background three-color image) and the ALMA (foreground orange colors). Credit: ALMA (ESO/NAOJ/NRAO)/ESA/NASA/PHANGS, S. Dagnello (NRAO)

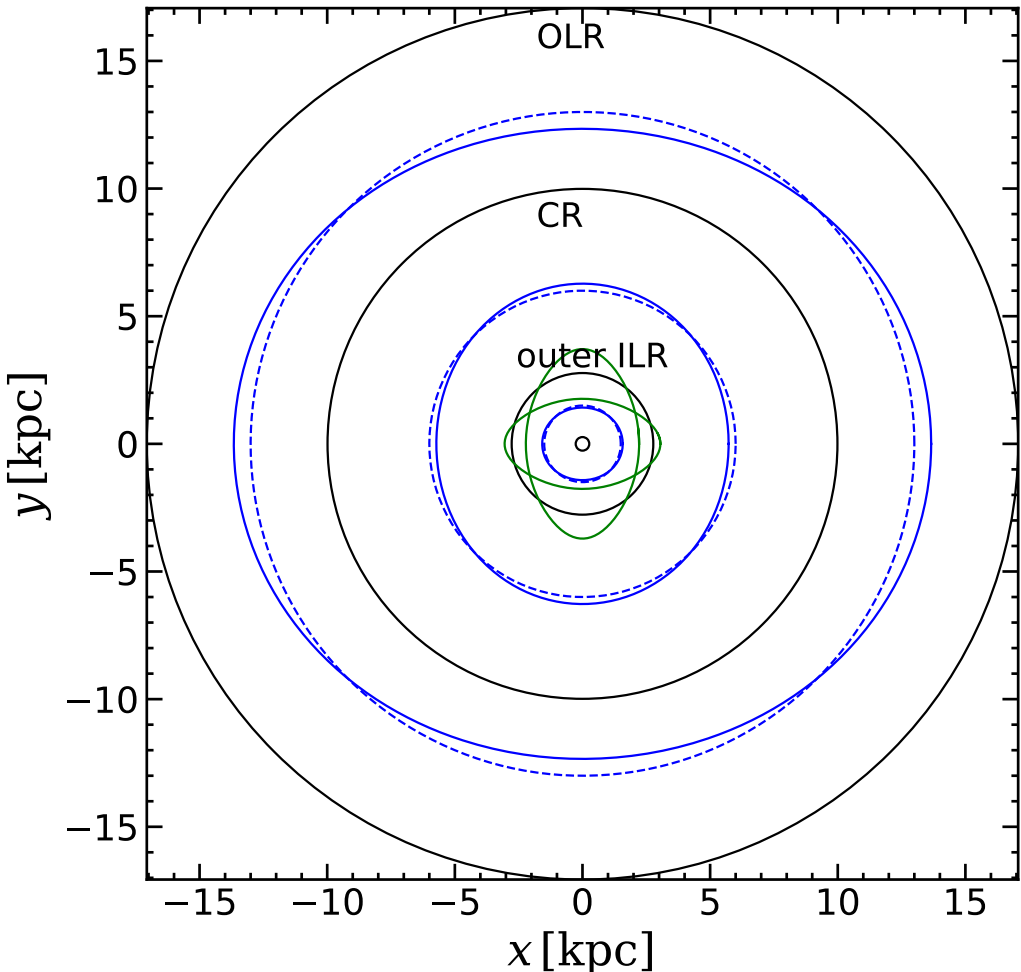


Figure 1.2. Closed orbits in a weak bar potential. The black circles mark the positions of the inner ILR, outer ILR, COR, and OLR, from inner to outer region. The blue dashed lines represent the unperturbed circular orbits, while the blue solid lines show the closed epicyclic orbit around each circular orbit, obtained from Equation (1.1). The green solid lines represent the numerically obtained closed orbits near the outer ILR, where the epicyclic approximation breaks down.

applies to the weakly barred potential, and how they are related to the general closed orbit families in weak or strong bars.

For a weakly barred potential, one can use the linear perturbation theory, or the epicyclic approximation, to obtain the analytic solution for the nearly-circular orbits which are closed in the frame corotating with the bar. For example, it can be shown that under the sinusoidal $m = 2$ perturbation of the form $\Phi_b(R) \cos[m(\varphi - \Omega_p t)]$, there exist closed orbits, corresponding to the particular solution of the driven oscillator, whose radial excursion with respect to the guiding center is given by (Binney & Tremaine 2008)

$$\delta R(t) = -\frac{1}{\kappa_0^2 - m^2(\Omega_0 - \Omega_p)^2} \left[\frac{d\Phi_b}{dR} \Big|_{R_0} + \frac{2\Omega_0\Phi_b}{R(\Omega_0 - \Omega_p)} \right] \cos[m(\Omega_0 - \Omega_p)t]. \quad (1.1)$$

Here, $\Phi_b(R)$ is the perturbation amplitude at radius R , φ is the azimuthal angle, Ω_p is the pattern speed of the perturbation, and κ_0 is the epicyclic frequency at the guiding center, respectively. The guiding center follows the circular orbit at $R = R_0$ with constant angular speed Ω_0 . It can be seen that δR diverges at the radius of the orbital resonances that occur when the forcing frequency $m(\Omega - \Omega_p)$ equals the natural frequencies, κ and 0. The common terminology for these resonances are inner Lindblad resonance (ILR), corotation resonance (COR), and outer Lindblad resonance (OLR) when $m(\Omega - \Omega_p)$ equals κ , 0, and $-\kappa$, respectively. A realistic bar has nonzero $m > 2$ perturbations which will create additional resonances, e.g., $\Omega - \Omega_p = \kappa/4$ which is often called ultraharmonic resonance (UHR).

Far from the resonances, the closed, nearly-circular orbits are well described by Equation (1.1). One can see that the sign of δR changes before and after the resonances, which means the orientation of the closed orbits changes by 90° at each resonance. This is illustrated in Figure 1.2, where we plot the unperturbed circular orbit (dashed blue lines) and the corresponding perturbed orbit (solid blue line) under the $m = 2$ sinusoidal ‘bar’ lying in the y -direction superimposed on the axisymmetric galactic potential. In the presence of the bar perturbation, the

nearly-circular closed orbits are of elliptical shape and are very well described by Equation (1.1)*. Note that the orientations of the closed orbits are perpendicular to the bar inside the ILR, parallel to the bar between the ILR and COR, again perpendicular to the bar between the COR and OLR. When there are two ILRs as in this case, the orbits are perpendicular to the bar between the inner and outer ILRs and parallel to the bar inside the inner ILR. Near the resonances, however, the forcing is too strong such that the epicyclic theory cannot predict the existence of possible closed orbits. The green solid lines show two examples of closed orbits near the outer ILR, found by numerical orbit integration. One of them is elongated along the bar, while the other is oriented perpendicular to the bar. Moreover, *those two orbits cross with one another*, which has important consequences when one considers the gas flow. These two orbits are called x_1 and x_2 orbits, which will be explained in the followings.

For a strong bar, the linear epicyclic theory breaks down even for the regions far from the resonances and it is necessary to adopt numerical integration to investigate the closed orbit families. Such inquiry had been heavily worked out by George Contopoulos, whose nomenclature of the various orbit families is now widely used (Contopoulos & Papayannopoulos 1980; Contopoulos & Grosbol 1989). Here, we focus on the two prograde stable closed orbit families which are called x_1 and x_2 following Contopoulos & Papayannopoulos (1980), because they are the orbits most relevant to the gas flow. Figure 1.3 visually illustrates the x_1 and x_2 orbits in blue and green lines, respectively, under a model galactic potential comprising a bulge and a bar with the axial ratio 2.5 whose boundary is delineated with the black solid line. The x_1 orbits consist main orbital family that exists all the way to the center and are generally elongated along the major axis of a bar, such that they are believed to be the backbone of the stellar bar (see, however, Gajda et al. 2016). The presence of the x_2 family depends on the bar parameter, such that they are absent when the bar is too strong, rotates too fast, or the central bulge component

*The numerically integrated orbits are indistinguishable with the analytically obtained orbit using Equation (1.1).

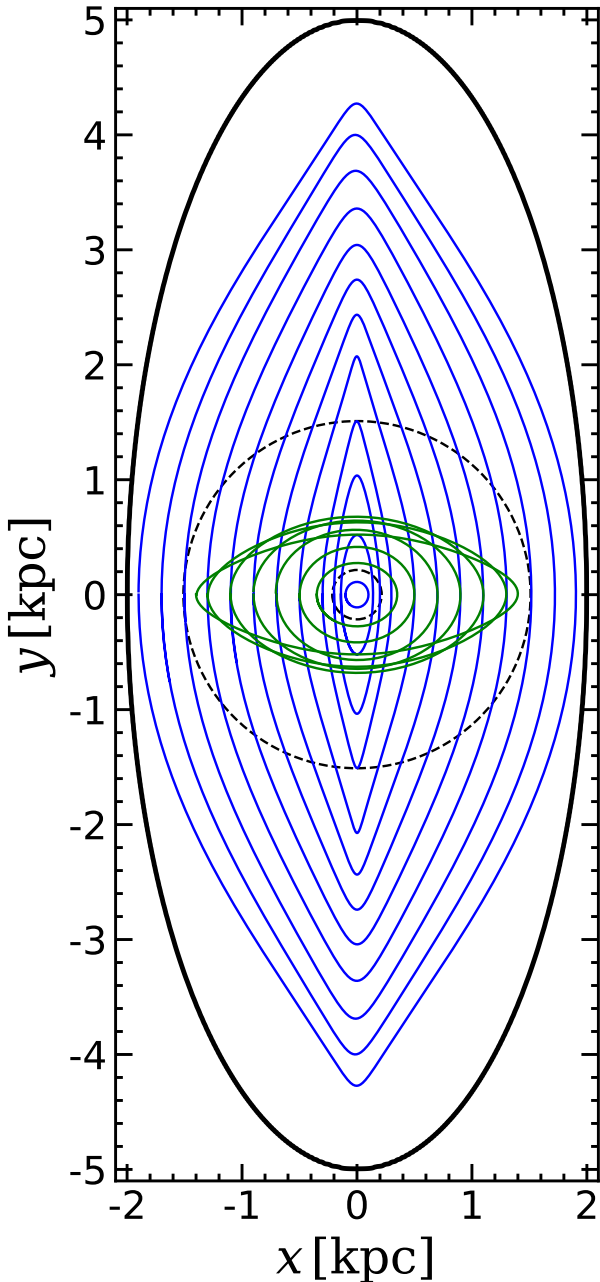


Figure 1.3. Closed orbits in a strong bar potential. The bar is outlined by the thick solid black line. The dashed circles at $R = 0.215$ kpc and $R = 1.51$ kpc mark the positions of the inner and outer ILR, respectively. The blue and green solid lines show the representative orbits belonging to x_1 and x_2 families, respectively. The x_2 orbits only exist roughly between the inner and outer ILR.

is too weak to keep the gas on track against the strong Coriolis force. The x_2 orbits are oriented perpendicular to the bar and generally less elongated compared to the x_1 orbits, except for the outermost orbits. When they exist, they are generally found in between the two ILRs. It must be noted that the converse is not true; the presence of the ILRs does not guarantee the existence of the x_2 orbits (Regan & Teuben 2003). In Figure 1.3, rough positions[†] of the inner and outer ILRs obtained from the axisymmetrized density distribution are shown as the black dashed lines.

Although the epicyclic theory does not apply to strong bars, one can make a useful conceptual connection regarding the orientation of the orbits. The epicyclic theory predicts that the orientation of the nearly-circular closed orbits are perpendicular to the bar between the two ILRs (blue solid line in Figure 1.2). The analogous general closed orbits are those of the x_2 family. The epicyclic theory also predicts that the nearly-circular orbits are parallel to the bar inside the inner ILR or between the outer ILR and COR. The analogous orbits are those of the x_1 family. The x_1 orbits are not confined only within the inner ILR or between the outer ILR and COR but in fact found for all radii roughly inside the COR; the epicyclic theory simply fails to predict the existence of them between the two ILRs, because they are too elongated in this region even for weak bars. Between the inner and outer ILRs, both x_1 and x_2 orbits coexist. It must be noted, however, that the position of the orbital resonances has only a loose connection to the locations where the orbital families bifurcate: except for the weak bar, the $\Omega - \kappa/2$ curve significantly overestimates the envelop of the critical Ω_p below which the x_2 orbits exist (Contopoulos & Papayannopoulos 1980; van Albada & Sanders 1982). In general, the radial extent of the x_2 orbits becomes increasingly smaller for stronger and/or faster bars, compared to the radial extent of the ILR(s). For arbitrary bar strength, the radii at which various orbital families bifurcate are more physically meaningful than the locations of orbital resonances which are defined in the epicyclic theory for weak bars.

[†]For strong bars, the locations of the orbital resonances are not well defined because the “rotation curve” is different along the major and minor axes of the bar.

The motion of a test particle on the x_1 or x_2 orbits is heavily affected by non-inertial forces, where the Coriolis force is generally more important than the centrifugal force inside the COR. Consider a test particle placed at the apocenter of a x_1 orbit. Due to the gravitational pull, it will start to fall toward the center, while being gradually deflected to the right (for a bar rotating counterclockwise) due to the Coriolis force. As it approaches the pericenter, the gravity resists the Coriolis deflection, bringing the trajectory back toward the bar. After passing the pericenter, the gas slows down as the gravity pulls it back, reaching the apocenter at the opposite side. Except for the region near the apocenter, this flow is somewhat reminiscent of the gradient wind in meteorology.

1.2.2 Gaseous Response

Under an axisymmetric potential, the gas will rotate in an exactly circular orbit in a steady state. Figure 1.2 suggests that when a weak bar perturbation is introduced, the gas would want to follow slightly elliptical, closed particle orbits, when the gas sound speed is much smaller than the orbital speed. However, because the orientation of such orbits change by 90° when crossing the resonances as suggested by Equation (1.1), the orientation of the gas streamlines must somehow gradually rotates before and after the resonances. Moreover, near the resonances the different family of closed orbits cross with each other (green lines in Figure 1.2), while the gas streamlines cannot cross. How would the nature mitigate these difficulties and what would be the resulting gaseous response to the rotating bar potential?

Sanders & Huntley (1976) and Sorensen et al. (1976) were the first to answer such a question using direct numerical hydrodynamic simulations. Sanders & Huntley (1976) calculated the gaseous response to the weak oval potential of the form $\Phi_b(R) \cos[2(\varphi - \Omega_p t)]$, i.e., the same potential used when drawing Figure 1.2. Figure 1.4 reproduces Figure 1(b) of Sanders & Huntley (1976), showing gas density contours when their simulation reaches a quasi-steady state. The positions of the ILR, COR, and OLR are annotated in the red solid lines by the present

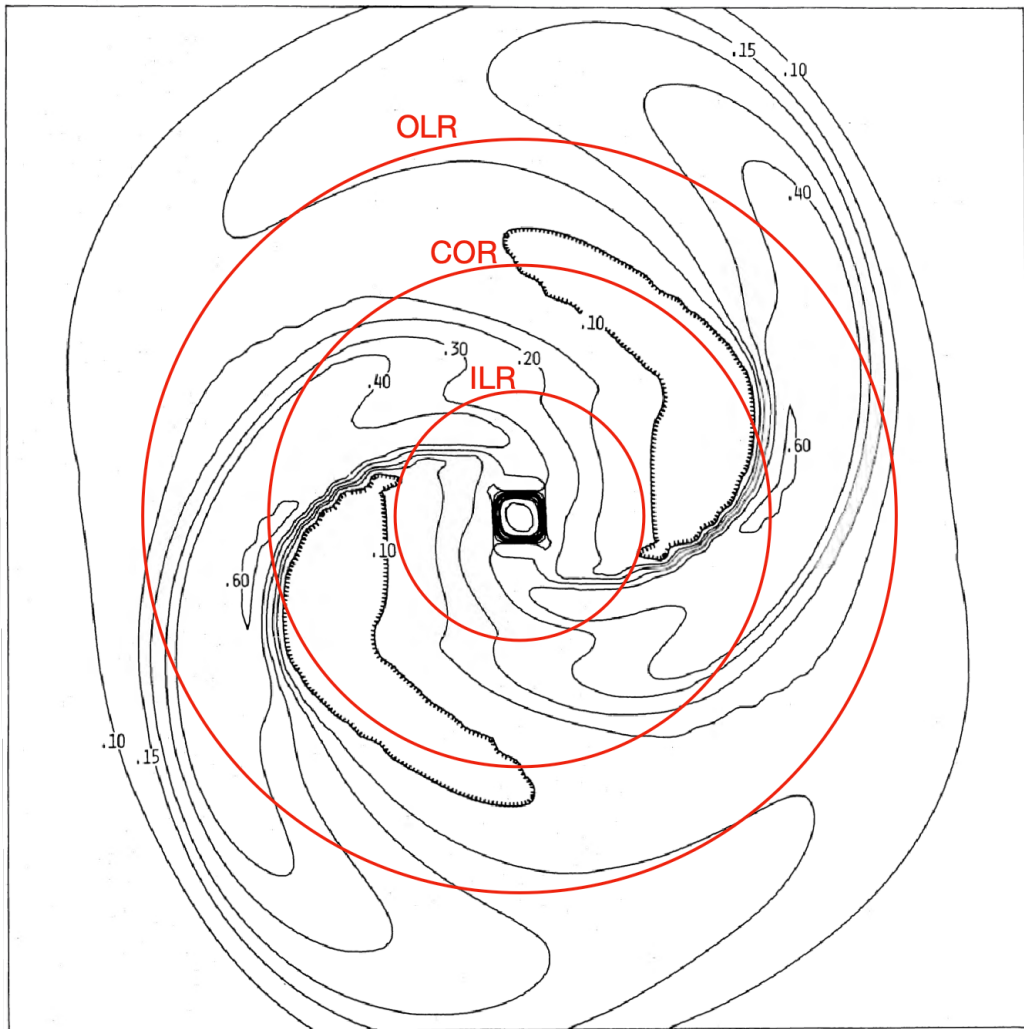


Figure 1.4. A quasi-steady state gas density distribution subject to a weak bar (oval) potential. A bar is in the horizontal direction. The three red circles mark the positions of the ILR, COR, and OLR, from inner to outer region. Note the conspicuous spiral shocks extending out from the ILR to COR. Credit: reproduced from Sanders & Huntley (1976) with the permission of the original author.

author, based on the information in Sanders & Huntley (1976). The bar is in a horizontal direction and the gas rotates clockwise about the center. Although the gravitational perturbation is only weakly non-axisymmetric, the resulting gaseous response is highly non-axisymmetric, exhibiting as large-scale two spiral arms emanating roughly from the ILR to OLR. Additional striking feature is a pair of shocks existing roughly between the ILR and COR, which is very reminiscent of dust lanes observed at the leading side of a bar (Figure 1.1). They conjectured that the spiral arms form because the orientation of the elliptical gas streamlines rotate in the opposite sense to the pattern speed when crossing the resonances from the inside, such that crowding of adjacent streamlines manifest themselves as trailing spiral arms, as in the kinematic density wave idea of Kalnajs (1973). The predicted relative locations of the arms with respect to the bar are consistent with the simulation results.

Since then, a myriad of authors have studied effects of bar strength, pattern speed, underlying galactic rotation curve, gas sound speed and resolution using diverse numerical methods, which have helped sharpening our understanding of gas flow in barred galaxies (e.g., Huntley et al. 1978; Englmaier & Gerhard 1997; Roberts et al. 1979; Sanders & Tubbs 1980; Athanassoula 1992; Piner et al. 1995; Patsis & Athanassoula 2000; Regan & Teuben 2003; Ann & Thakur 2005; Kim et al. 2012b,a; Sormani et al. 2015a,b,c). The results of these numerical studies suggest that the offset dust lanes (e.g., Figure 1.1) result from strong shocks formed at the leading side of a bar, as envisaged by Kevin Prendergast long ago (Prendergast 1962, 1967), through which gas loses angular momentum and falls toward the center approximately following one of the x_1 orbits (see Section 1.2.1 for bar orbits). The shape and curvature of dust lanes are found to be related to the bar properties such as the aspect ratio, bar pattern speed, or the central mass concentrations. Observationally, the abrupt changes in the gas velocity (Regan et al. 1999) or the magnetic field directions (Beck et al. 1999) near dust lanes corroborate their interpretation as shocks, while the observed kinematics in dust lanes suggest

significant mass inflow with the rates of order $1\text{--}10 M_{\odot} \text{ yr}^{-1}$ (Benedict et al. 1996; Regan et al. 1997, 1999; Elmegreen et al. 2009; Sormani & Barnes 2019)[‡]. In this view, dust lanes are the channels of gas inflow from the outer region toward the center which can trigger circumnuclear starburst activity at the centers of barred galaxies (Section 1.1.1). We close this section by noting that we still lack a first principle explanation why the off-axis shocks form at the leading side of a bar and what maintains them against dissipation.

1.3 Nuclear Rings

Nuclear rings are compact ring-shaped star-forming regions frequently found at the heart of barred galaxies. The earliest recognition of their existence dates back to the photographic plate era, where observers classified some galaxies having “peculiar nuclei” composed of multiple “hot spots” (Morgan 1958; Sérsic & Pastoriza 1965). Before long, it had been suggested that their bright emission is due to a large number of young hot stars (Osmer et al. 1974; Pastoriza 1975; Alloin & Kunth 1979; Telesco & Gately 1981), which have endowed them with a starburst nature. Figure 1.5 shows the latest image of one of the “hot spot galaxies” NGC 1097 taken by the HST, which clearly shows a ring of bright emission at the center of the bar where vigorous star formation takes place. It also illustrates a pair of dust lanes running along the leading edges of the bar that smoothly joins the ring and supplies fresh gas for the star formation (see Section 1.2.2).

1.3.1 Formation Mechanisms

A widespread notion is that the location where nuclear rings form is associated with the orbital resonances, such that a ring forms between the two ILRs or between the center and the ILR if a galaxy has only a single ILR (see Schmidt et al. 2019, for a recent observational test). However, there are varied interpretations in the literature

[‡]Recent numerical study of Hatchfield et al. (2021) indicate that only $\sim 1/3$ of the inflowing gas actually accrete onto a nuclear ring, while the remaining $\sim 2/3$ goes around and hits the dust lane at the other side.

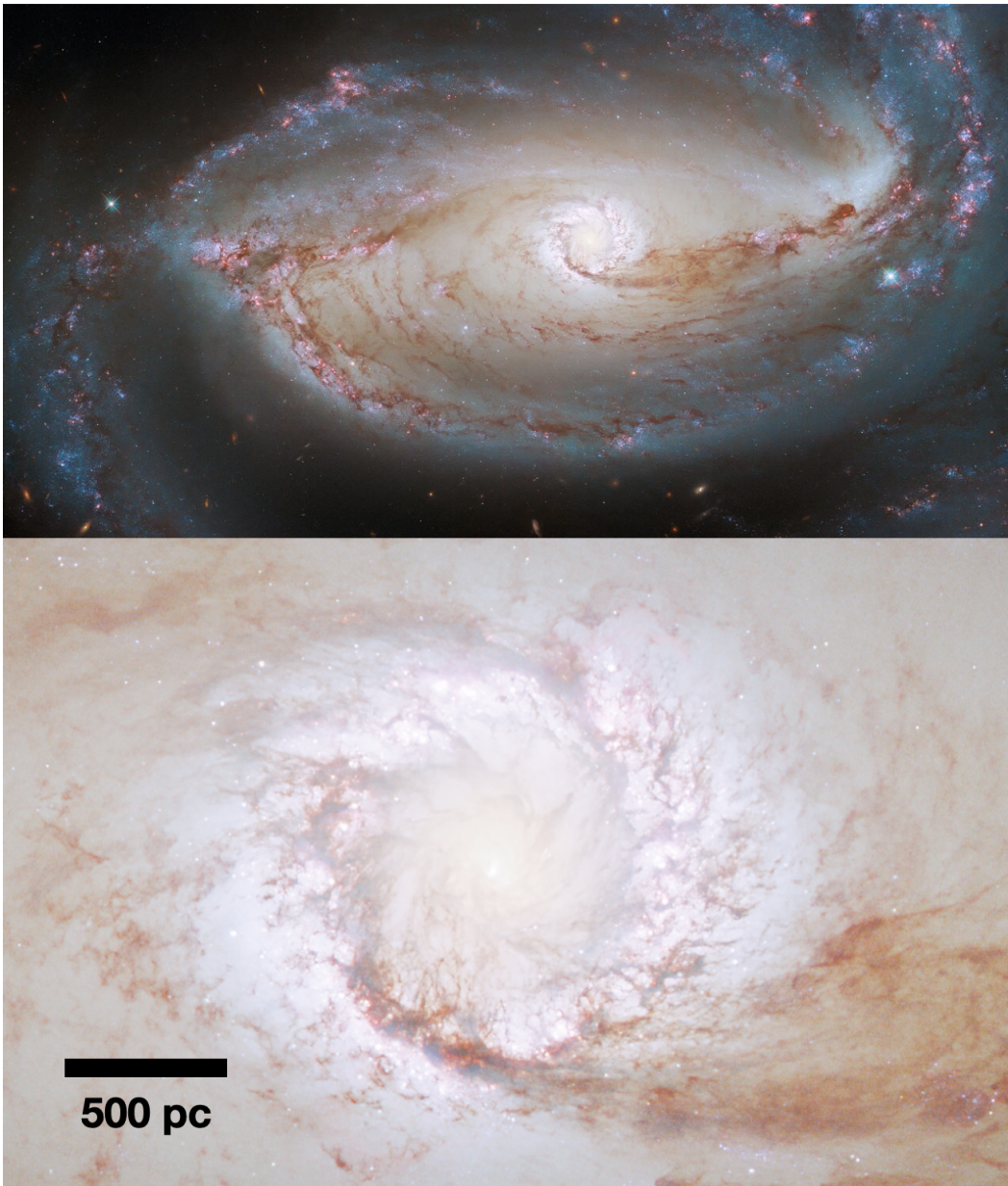


Figure 1.5. Hubble image of the prototypal barred spiral galaxy NGC 1097 (top), and the zoom-in on its central region (below). The upper image shows two large-scale dark dust lanes that run along the bar major axis, connecting the outer spiral arms to a *nuclear ring* delineated by bright, whitish ring-shaped emission. The below image reveals that the nuclear ring consists of numerous young star clusters and the interstellar medium which block their light. Credit: ESA/Hubble & NASA, D. Sand, K. Sheth.

regarding the underlying physical mechanism behind such an association, making it difficult to understand what condition is required for nuclear rings to form and what determines their precise location.

The idea that nuclear rings form at the ILR initially had been developed through the numerical studies of a gaseous response to a bar potential using the “sticky particle” scheme that models the ISM as an ensemble of colliding clouds (Schwarz 1981, 1984; Combes & Gerin 1985; Byrd et al. 1994; Rautiainen & Salo 2000). In those simulations, clouds form trailing spiral density waves between the ILR and OLR as a response to the bar forcing (see Section 1.2.2). The phase angle of the resulting spirals is such that they lead the bar between the ILR and COR but lag behind the bar between the COR and OLR. The clouds in the spiral arms therefore feel the positive or negative gravitational torque from the bar depending on which resonances they situate in between, migrating outward or inward accordingly.

For example, because the bar-driven spirals lag behind a bar between the COR and OLR (which is known only *empirically* through aforementioned simulations), the clouds in those parts of the spirals would feel positive torques from the bar and migrate outward, slowly piling up near the OLR where the spirals end, forming *outer rings*. Aforementioned simulations found that a typical timescale for this process to occur is roughly ten bar rotations or more, implying that rings form rather secularly through slow gravitational interactions (for a pattern speed $30 \text{ km s}^{-1} \text{ kpc}^{-1}$, it takes 2 Gyr for a bar to make ten rotations). They also found that unless the bar pattern speed is too high, a secondary ring forms slightly inside the COR, closer to the UHR, with which it is very tempting to associate the *inner rings*. As those simulations also exhibited gas inflow from the COR to ILR which forms a *nuclear ring*, it was natural to postulate such process is also driven by the negative gravitational torque that the bar exerts to the trailing spirals between the ILR and COR. A hypothesis thus emerged that outer, inner, and nuclear rings form at the OLR, UHR, and ILR, respectively (Buta & Combes 1996; Combes 1996). Observational surveys of the galactic rings found that the relative size of outer to

inner rings broadly peaks around two (Athanassoula et al. 1982; Buta 1986, 1995; Comerón et al. 2014), which is expected if their location is connected to resonances, supporting the above scenario.

As reviewed in Section 1.2.2, however, recent hydrodynamic simulations that model the ISM as a continuous fluid rather than an ensemble of colliding clouds have consistently found that the nonlinear interaction between the gas disk and a bar potential typically results in strong off-axis shocks attached to the leading side of the bar, even in the cases where the multiphase, cloudy nature of the ISM is taken into account (Armillotta et al. 2019; Seo et al. 2019; Tress et al. 2020). It is thus questionable whether the gravitational migration mechanism outlined above applies to nuclear rings as well, because gas can lose angular momentum purely by hydrodynamic means at the dust lane shocks. Indeed, hydrodynamic simulations indicate that the gas streamlines highly deviate from the circular rotation, such that the post-shock gas attains large infall velocities.

The ultimate radial location at which gas settles and forms a nuclear ring is of interest, where empirical evidence from simulations is that the ring forms in the region around which sufficient number of x_2 orbits exists (e.g., Regan & Teuben 2003; see Section 1.2.1 for a brief introduction of the bar orbits). The ring formation process can be roughly understood in such a way that the infalling gas gradually transitions from x_1 to x_2 orbits as it shocks multiple times at dust lanes, finally settling to the x_2 orbit of the matching angular momentum (see, e.g., Figure 2 of Athanassoula 1992 or Figure 7 of Kim et al. 2012b). The amount of angular momentum loss that would ultimately determine the ring radius depends not only on the bar potential but also on the gas sound speed, self-gravity, and magnetic fields, and is therefore difficult to predict (e.g., Kim et al. 2012a; Kim & Stone 2012; Sormani et al. 2015a). We note that Sormani et al. (2018) recently proposed an interesting mechanism for the ring formation by noticing that some of the x_2 orbits have “reversed” shear, whose associated viscous torque tend to gather the material rather than spread it.

As discussed in Section 1.2.1, x_2 orbits are found inside the ILR or between the inner and outer ILRs. For weak and slow bars, the radial extent of the outermost x_2 orbits is similar to the position of the (outer) ILR, in which case the conventional wisdom that nuclear rings form at ILR does not contradict with the idea that they form in the region dominated by x_2 orbits. However, for strong and/or fast bars, the position of ILR(s) can be quite different from the radial extent of x_2 orbits. In such a case, the radii of nuclear rings formed in numerical simulations agree much better with the latter than the former (Regan & Teuben 2003; Kim et al. 2012a), suggesting that x_2 orbits are more relevant to ring formation than ILRs.

1.3.2 Physical Properties

Frequency of occurrence

Most complete observational survey of nuclear rings to date is presented in Comerón et al. (2010). They use HST images to find nuclear rings in 20% of disk galaxies in their sample, 80% among which are barred. This ring fraction is likely a lower limit considering the limited resolution especially for distant galaxies. Indeed, Song et al. (2021) recently discovered two previously unknown nuclear rings of radii ~ 200 pc in galaxies at ~ 70 Mpc away from us using radio interferometric observations.

Lifetime

Although it is difficult to precisely age-date the rings because the old stars will gradually diffuse and mix with background stellar populations, observed absorption spectra strongly suggest the presence of ring stellar populations of at least a few hundred years old (Allard et al. 2006; Sarzi et al. 2007). More recently, Ma et al. (2018) used population synthesis models to fit observed spectral energy distributions of nuclear rings from multiband photometry and found the average ring age of 1.2 Gyr, demonstrating the longevity of nuclear rings. Finally, Bittner et al. (2020) analyzed integral field spectroscopic data obtained from Multi-Unit Spectroscopic Explorer (MUSE) and found that the ages of nuclear rings and nuclear disks are

typically a few gigayears. Combined with inputs from numerical simulations that relate the origin of nuclear rings to bars (Section 1.3.1), all these results indicate that nuclear rings are not transient but rather long-lived structures with lifetimes comparable to that of bars (a few Gyrs).

Size

Comerón et al. (2010) defined the ring radius as the peak position of the radial surface brightness profile. The radii of nuclear rings are rather continuously distributed, ranging from as small as a few tens of parsecs up to $\sim 2\text{ kpc}$, where smaller rings are more frequent than larger ones. The relative radii of almost all nuclear rings are limited below a quarter of the bar length, when they accompany a bar. While weak bars host both small and large rings, strong bars exclusively favor small rings, indicating the maximum possible ring radius is anticorrelated with the bar strength. This might be because 1)the maximum radius of $x2$ orbits decreases with the increasing bar strength, 2)the stronger bar removes more angular momentum at the dust lanes through gravitational torque, or 3)the stronger bar produces stronger dust lane shocks where gas loses more angular momentum. These three points are not mutually exclusive but interrelated in a complicated manner which is not well understood.

Mass

Ma et al. (2018) used population synthesis technique to not only measure the age of nuclear rings but also their total stellar mass. The derived total stellar mass of nuclear rings typically ranges $\sim 10^{8-10} M_{\odot}$ (two very young rings with age less than 50 Myr in their sample have lower stellar masses $\sim 2 \times 10^7 M_{\odot}$). It has been suggested that the gas mass in nuclear rings is relatively constant (e.g., Kim & Moon 2016; Ma et al. 2018). This is based on the observation that the total gas mass within a central kiloparsec of several nearby bright barred galaxies are similar at a few times $10^8 M_{\odot}$ (Sheth et al. 2005), although resolved measurements for

individual nuclear rings show somewhat larger variations. Some examples include NGC 1097 ($1.3 \times 10^9 M_\odot$; Hsieh et al. 2011), NGC 1326 ($6 \times 10^7 M_\odot$; Fazeli et al. 2020), NGC 1808 ($1.6 \times 10^9 M_\odot$; Salak et al. 2016), NGC 6951 ($3.8 \times 10^8 M_\odot$; García-Burillo et al. 2005) and NGC 7217 ($3.8 \times 10^8 M_\odot$; Combes et al. 2004), where the CO-to-H₂ conversion factor is rescaled to a common value $X_{\text{CO}} = 2.8 \times 10^{20} \text{ cm}^{-2} (\text{K km s}^{-1})^{-1}$ used in Sheth et al. (2005). A wealth of data recently published by Physics at High Angular resolution in Nearby GalaxieS (PHANGS) collaboration with unprecedented resolution will be extremely useful to measure the gas mass in other nuclear rings.

Star formation rate

The current SFR of nuclear rings are mostly traced by H α emission from massive stars. Mazzuca et al. (2008) measured the SFR for 20 nuclear rings based on H α luminosity and found a wide range of $\text{SFR} \sim 0.1\text{--}10 M_\odot \text{ yr}^{-1}$. Ma et al. (2018) combined HST H α and Spitzer 8 μm data to derive the SFR of 6 nuclear rings (3 of which are in Mazzuca et al. (2008) sample) after careful background subtraction using the method developed in Ma et al. (2017), finding somewhat smaller values: 0.04, 0.065, 0.08, 0.188, 0.294, and $2.307 M_\odot \text{ yr}^{-1}$. Despite systematic uncertainties, it seems that nuclear rings have a wide range of the SFR, compared to their gas mass. A possible reason for this behavior will be presented in Chapter 2. We note that the observed range of the ring SFR is somewhat similar to that of the mass inflow rate (see Section 1.2.2), indicating possible connection between the two.

Magnetic fields

Magnetic fields in external galaxies have been probed mostly via the radio synchrotron observations. Volume-averaged, equipartition magnetic field strengths in a few nuclear rings are $\sim 55 \mu\text{G}$ (NGC 1097; Beck et al. 2005), $\sim 63 \mu\text{G}$ (NGC 1365; Beck et al. 2005), and $\sim 84 \mu\text{G}$ (NGC 5792; Yang et al. 2022), which are stronger than typical magnetic field strengths in the main disk region of spiral galaxies

$\sim 10\text{--}30 \mu\text{G}$ (Beck 2015, and references therein). The equipartition assumption between magnetic fields and cosmic rays, however, is neither based on solid theoretical ground nor validated by observations. Especially for nuclear starburst regions, it has been suggested that the equipartition assumption would underestimate the true magnetic field strength (Beck & Krause 2005; Yoast-Hull et al. 2016). Furthermore, given the small size of nuclear rings $\lesssim 1 \text{ kpc}$ (see above) and short dynamical timescales, the spatial distribution of gas and cosmic rays might be quite different, making it difficult to associate observed magnetic fields with dense gas composing the ring. Despite all the uncertainties, the above considerations suggest that nuclear rings are likely to possess strong magnetic fields with strengths at least $\gtrsim 50 \mu\text{G}$.

1.3.3 Star Formation History

The ring SFRs given in the preceding section only trace current ($\lesssim 10 \text{ Myr}$) star formation activity. A wide range of SFRs among different nuclear rings might reflect systematic variations from galaxy to galaxy, but could also indicate large temporal variations. If the ring star formation proceeds in episodic rather than continuous fashion, there might be a significant undetected population of quiescent nuclear rings. The mass of disk-like bulges would sensitively depend on the star formation history of nuclear rings throughout their lifetime.

Allard et al. (2006) and Sarzi et al. (2007) measured spectroscopic indices of stellar absorption lines for 8 nuclear rings and compare them with theoretical stellar population models assuming various star formation histories. They found that the observed ring spectra require at least two stellar populations consisting of old ($> 3 \text{ Gyr}$) and young ($< 500 \text{ Myr}$) ages, where the former represents the underlying bulge and disk stars. Their data points additionally support the scenario that the young ($< 500 \text{ Myr}$) population is built up through multiple bursts separated by $\sim 100 \text{ Myr}$ rather than constant star formation, although it is difficult to reconstruct the exact star formation history.

The temporal variations of the ring SFR seem to involve multiple timescales.

Gadotti et al. (2019) reconstructed the star formation history of the nuclear ring in NGC 1097 by fitting the observed spectrum to a combination of single stellar population models. They found three major peaks in the ring star formation history, one at the current epoch, second at ~ 0.5 Gyr ago, and the third at ~ 2.5 Gyr ago. For the same galaxy, Prieto et al. (2019) age-dated the star clusters in the ring to obtain a recent ($\lesssim 100$ Myr) star formation history. They found a pronounced burst at ~ 4 Myr, followed by second one at ~ 30 Myr ago, and potential bursts at ~ 60 Myr and ~ 90 Myr ago. Taken together, the SFR of nuclear rings seems to considerably change over time, with various timescales ranging from a few tens of megayears up to a few gigayears.

It is likely that different physical mechanisms are responsible for various timescales in the ring star formation. Theoretical studies and numerical simulations have suggested a number of scenarios that can produce episodic star formation in nuclear rings. It might be possible to classify these scenarios into two very broad categories, those involving internal processes such as supernova feedback, turbulence, or gravitational and hydrodynamic instabilities (Loose et al. 1982; Elmegreen 1994; Krumholz & Kruijssen 2015; Krumholz et al. 2017), and those involving external processes such as time-varying bar-driven mass inflow rates or minor mergers (Mihos & Hernquist 1994; Seo & Kim 2013, 2014; Seo et al. 2019; Ramón-Fox & Aceves 2020). The relative importance of these different mechanisms in connection with the observed star formation history of nuclear rings is poorly understood.

1.4 Scope and Outline of This Thesis

So far, we have discussed the observational aspects of the bar-driven star formation in galaxy centers and, in relation to which, reviewed our current theoretical understanding of gas flow in barred galaxies. Special focus was given to the ability of bars to transport gas to the central region, often resulting in nuclear rings of intense star formation. The interplay between the mass inflow, magnetic fields, star formation and ensuing feedback occurring in nuclear rings is the central theme of

this thesis.

Although the gas dynamics in the bar region and the formation mechanism of nuclear rings are still not completely understood, they are not in the scope of this work. The N-body dynamics of stellar disks that lead to bar formation and interactions between stellar and gaseous components are not treated in this work as well. Instead, we begin the inquiry from the middle of the problem, by assuming fixed stellar background potential and parametrizing the most salient physics that are known to govern the formation of nuclear rings: the final angular momentum of the gas that enters the ring. We have developed a semi-global numerical framework where the computational domain only encompasses a nuclear ring and its immediate vicinity. A stellar bar is assumed to span a much larger region than covered by the computational domain, where all the complicated interactions take place to determine the final angular momentum of the gas entering into the computational domain. The angular momentum, and therefore the size of a nuclear ring, and magnetic field strength of the inflowing gas as well as the mass inflow rate are the main free parameters that can be controlled via boundary conditions. By taking this approach, we are allowed to not only circumvent the difficult problem of ring formation but also gain control over the main physical agents that can affect the star formation in nuclear rings.

The rest of this thesis is organized as follows. In Chapter 2, we introduce our semi-global numerical framework, and using it study the star formation in nuclear rings subject to constant mass inflow rates. We present the dependence of the SFR and gas mass on the mass inflow rates and interpret the various scaling relations in terms of the pressure-regulated, feedback-modulated star formation theory. We also discuss what determines the SFR and depletion time in nuclear rings. In Chapter 3, we focus on effects of time variations in the mass inflow rate by allowing the mass inflow rate to oscillate in time with differing timescales. We also investigate possible outcomes of the asymmetric mass inflows to understand the lopsided star formation observed in some nuclear rings. In Chapter 4, we explore the other important

dimension of the parameter space by investigating effects of magnetic fields on gas flow and star formation in nuclear rings. We conclude this thesis and discuss possible future work in Chapter 5.

Chapter 2

Semi-Global Numerical Simulations of Nuclear Rings Subject to Constant Mass Inflow Rates^{*}

2.1 Overview

Nuclear rings were first identified in photographic plates as multiple *hot spots* near galaxy centers (Morgan 1958; Sérsic & Pastoriza 1965), which have turned out to be manifestation of compact yet vigorous star-forming regions (see also Kennicutt 1994; Kormendy & Kennicutt 2004, and references therein). They are thought to form as a result of gas redistribution due to a bar potential (e.g., Combes & Gerin 1985; Buta 1986; Shlosman et al. 1990; Garcia-Barreto et al. 1991; Buta & Combes 1996). Indeed, numerical simulations have consistently shown that the non-axsiymmetric torque exerted by a stellar bar in disk galaxies causes gas to move

^{*}A version of this chapter has been published as "Star Formation in Nuclear Rings with the TIGRESS Framework", Moon, S., Kim, W.-T., Kim, C.-G., & Ostriker, E. C. 2021, *The Astrophysical Journal*, 914, 9

radially inward along dust lanes and form a ring near the centers (e.g., Athanassoula 1992; Piner et al. 1995; Englmaier & Gerhard 1997; Patsis & Athanassoula 2000; Kim et al. 2012b; Kim & Stone 2012; Li et al. 2015). It is uncertain what determines the ring locations, but theoretical proposals suggest it may be determined by radial extent of periodic orbits caused by a bar potential (Binney et al. 1991; Regan & Teuben 2003), balance between centrifugal force and external gravity (Kim et al. 2012a), or shear reversal (Sormani et al. 2018). While bars are by far the most efficient agent driving mass inflow in galactic disks, other non-axisymmetric features such as spiral arms, elongated bulges, and ovals can also drive mass inflow to fuel starburst activity (e.g., Athanassoula 1994; Combes 2001; Kim & Kim 2014; Seo & Kim 2014; Kim et al. 2018a).

Observations indicate that the star formation rate (SFR) in the rings of normal barred galaxies spans a wide range $\sim 0.1 - 10 M_{\odot} \text{ yr}^{-1}$ (Mazzuca et al. 2008; Ma et al. 2018), while the total gas mass range in the rings is more limited, $\sim (1 - 6) \times 10^8 M_{\odot}$ (Sheth et al. 2005). The central molecular zone (CMZ), which is believed to be a nuclear ring in the Milky Way, contains gas mass of $\sim (3 - 7) \times 10^7 M_{\odot}$ (Pierce-Price et al. 2000; Molinari et al. 2011; Tokuyama et al. 2019) and is forming stars at a rate $\sim 0.02 - 0.1 M_{\odot} \text{ yr}^{-1}$, measured by counting the number of young stellar objects or estimating the ionizing photon luminosity that traces recent star formation activity in a time period $\lesssim 10 \text{ Myr}$ (Yusef-Zadeh et al. 2009; Immer et al. 2012; Longmore et al. 2013; Koepferl et al. 2015). It has been noted that the observed SFR in the CMZ is a factor of ~ 10 smaller than what is expected for its gas mass or column density (Longmore et al. 2013; Kruijssen et al. 2014). Using numerical simulations, Seo & Kim (2013) and Seo et al. (2019) showed that the ring SFR is closely related to the mass inflow rate to the ring rather than the ring mass, suggesting that the low current SFR of the CMZ is due to small mass inflow rates in the near past. Since this result can in principle depend on the treatment of star formation and feedback adopted in those works, it needs to be confirmed using new simulations with more realistic treatment of relevant physics in higher

resolution. We note that there is observational evidence that the mass inflow rate to the CMZ varies considerably with time and currently has a very small value (Sormani & Barnes 2019).

As an alternative scenario, Kruijssen et al. (2014) proposed that the ring SFR undergoes quasi-periodic variations between starburst and quiescent phases, and the CMZ is currently in the quiescent phase (see also, Elmegreen 1994; Krumholz & Kruijssen 2015; Krumholz et al. 2017; Torrey et al. 2017; Armillotta et al. 2019). In this scenario, the inflowing gas gradually piles up until the ring becomes gravitationally unstable and undergoes intense star formation. Associated strong stellar feedback terminates the starburst phase rapidly, causing the ring to become quiescent until its mass grows sufficient to trigger another burst. Krumholz et al. (2017) ran numerical simulations based on vertically integrated, axisymmetric, one-dimensional (1D) models and found that the ring SFR exhibits quasi-periodic oscillations with a period ~ 20 Myr, even when the mass inflow rate is held constant.

However, it is questionable whether the quasi-periodic behavior of the ring SFR seen in the 1D models of Krumholz et al. (2017) exists in three-dimensional (3D) simulations for the CMZ (Armillotta et al. 2019; Sormani et al. 2020b; Tress et al. 2020), or realized in observed galaxies. For instance, Armillotta et al. (2019) performed a global simulation of the Milky Way using GIZMO (Hopkins 2015). They modeled a stellar bar by a rigidly rotating gravitational potential, and found that the ring SFR varies by more than an order of magnitude over a time span of ~ 500 Myr, even though the gas mass in the CMZ stays relatively constant. While the short-period (~ 50 Myr) cycle in their ring SFR is likely modulated by feedback, the long-period (~ 200 Myr) cycle that dominates the SFR might be compromised by the orbital motions of a large molecular cloud that is unresolved and somehow survives in their simulation. Similar global simulations of Sormani et al. (2020b) using AREPO (Springel 2010; Weinberger et al. 2020) found that the gas depletion time in the CMZ is quite steady and that the SFR is directly proportional to the time-varying CMZ mass (see also Tress et al. 2020). The temporal changes of the

CMZ mass and SFR in the models of Sormani et al. (2020b) might be driven by the time variation in the mass inflow rate, as suggested by Seo et al. (2019).

Diverse results from the 3D simulations mentioned above imply that there is no consensus as to what controls the ring SFR, gas mass evolution, and detailed dynamical properties. In fully global simulations, the mass inflow rate is naturally time varying since the gas density near the bar ends and along the dust lanes is highly inhomogeneous (e.g, Armillotta et al. 2019; Seo et al. 2019; Sormani et al. 2020b; Tress et al. 2020). The time-dependent mass inflow rate causes the ring size, shape, and mass to vary significantly with time, making it difficult to isolate key factors that determine the ring SFR. For a more controlled study, in this chapter we construct semi-global models that focus on a nuclear ring and nearby regions, without explicitly including a stellar bar in the simulations. Instead, our models have a stream of gas with prescribed properties entering through the domain boundaries, mimicking gas inflows along the dust lanes in global simulations (e.g., Athanassoula 1992; Kim et al. 2011b, 2012b; Sormani et al. 2015a; Shin et al. 2017). We handle star formation and associated supernova (SN) feedback by adopting the Three-phase Interstellar medium in Galaxies Resolving Evolution with Star formation and Supernova feedback (TIGRESS) algorithms developed by Kim & Ostriker (2017). While our models cannot capture the triggering by the bar potential of large-scale gas inflows, they allow us to investigate the ring region itself with high resolution, and to explore the behavior of the ring SFR when the mass inflow rate is kept constant in time (at chosen levels).

Our semi-global models are also useful for investigating the details of star formation regulation in nuclear rings. Ostriker et al. (2010) and Ostriker & Shetty (2011) developed analytical equilibrium models for the self-regulation of SFR in normal and starburst regions of galactic disks, in which the equilibrium SFR is set by the balance between the weight of the interstellar medium (ISM) and the mid-plane pressure, with the required pressure provided primarily by SN feedback and far ultraviolet (FUV) heating. This equilibrium model has been validated through

a series of local shearing-box simulations (Kim et al. 2011a, 2013; Kim & Ostriker 2015a), including spiral arms (Kim et al. 2020c), and for more extreme star-forming regions (Shetty & Ostriker 2012). In this chapter, we explore whether the self-regulation theory is also applicable to the semi-global model of the galactic centers characterized by high SFRs and short dynamical timescales.

The remainder of this chapter is organized as follows. In Section 2.2, we describe our numerical methods and our treatment of gas streams through the domain boundaries, and briefly summarize the TIGRESS framework for star formation and SN feedback. In Section 2.3, we present the temporal and morphological evolution of our models as well as the star formation histories. In Section 2.4, we present various physical quantities characterizing nuclear rings and explore their correlations, testing the self-regulation theory of star formation. Finally, we summarize and discuss our results in Section 2.5.

2.2 Numerical Methods

In this chapter, we use the TIGRESS framework to study star formation and SN feedback in a nuclear ring located near a galaxy center. Ring formation is driven by stellar bars, which cause gas to flow radially inward while still retaining enough angular momentum to circularize at some distance from the galactic nucleus. In the present chapter (and throughout the thesis) we do not model the bar explicitly, instead imposing the gas inflows via boundary conditions (see below).

2.2.1 Basic Equations

Our simulation domain is a Cartesian cube with side length L , encompassing a nuclear ring. The simulation domain rotates at an angular frequency $\boldsymbol{\Omega}_p = \Omega_p \hat{\mathbf{z}}$, where this represents the pattern speed of a bar (on larger scale than we are simulating).

The equations of hydrodynamics in the rotating frame read

$$\frac{\partial \rho}{\partial t} + \boldsymbol{\nabla} \cdot (\rho \mathbf{v}) = 0, \quad (2.1)$$

$$\frac{\partial(\rho\mathbf{v})}{\partial t} + \nabla \cdot (\rho\mathbf{v}\mathbf{v} + P\mathbb{I}) = -2\rho\boldsymbol{\Omega}_p \times \mathbf{v} - \rho\nabla\Phi_{\text{tot}}, \quad (2.2)$$

$$\begin{aligned} \frac{\partial}{\partial t} \left(\frac{1}{2}\rho v^2 + \frac{P}{\gamma-1} \right) + \nabla \cdot \left[\left(\frac{1}{2}\rho v^2 + \frac{\gamma P}{\gamma-1} \right) \mathbf{v} \right] \\ = -\rho\mathbf{v} \cdot \nabla\Phi_{\text{tot}} - \rho\mathcal{L}, \end{aligned} \quad (2.3)$$

$$\nabla^2\Phi_{\text{self}} = 4\pi G(\rho + \rho_{\text{sp}}), \quad (2.4)$$

where \mathbf{v} is the gas velocity in the rotating frame, P is the gas pressure, \mathbb{I} is the identity matrix, $\rho\mathcal{L}$ is the net cooling rate per unit volume, and $\Phi_{\text{tot}} = \Phi_{\text{cen}} + \Phi_{\text{ext}} + \Phi_{\text{self}}$ is the total gravitational potential, consisting of the centrifugal potential $\Phi_{\text{cen}} = -\frac{1}{2}\Omega_p^2(x^2 + y^2)$, the external gravitational potential Φ_{ext} giving rise to the background rotation curve, and the self-gravitational potential Φ_{self} of gas with density ρ and newly formed star particles with density ρ_{sp} .

We adopt a model for the external potential based on the archetypal barred-spiral galaxy NGC 1097, which possesses a star-forming nuclear ring with a radius of $R_{\text{ring}} \sim 700$ pc (Hsieh et al. 2011). Onishi et al. (2015) found that the observed gas kinematics near the galaxy center is consistent with the velocity field derived from the combined gravitational potential of stellar mass distribution and the supermassive black hole with mass $M_{\text{BH}} = 1.4 \times 10^8 M_{\odot}$, which we represent with a Plummer potential

$$\Phi_{\text{BH}} = -\frac{GM_{\text{BH}}}{\sqrt{r^2 + r_{\text{BH}}^2}}, \quad (2.5)$$

where $r_{\text{BH}} = 20$ pc is the softening radius. To represent stellar mass distribution, we use a modified Hubble profile with the stellar volume density

$$\rho_b = \frac{\rho_{b0}}{(1 + r^2/r_b^2)^{3/2}}, \quad (2.6)$$

and corresponding gravitational potential

$$\Phi_b = -\frac{4\pi G\rho_{b0}r_b^3}{r} \ln \left(\frac{r}{r_b} + \sqrt{1 + \frac{r^2}{r_b^2}} \right), \quad (2.7)$$

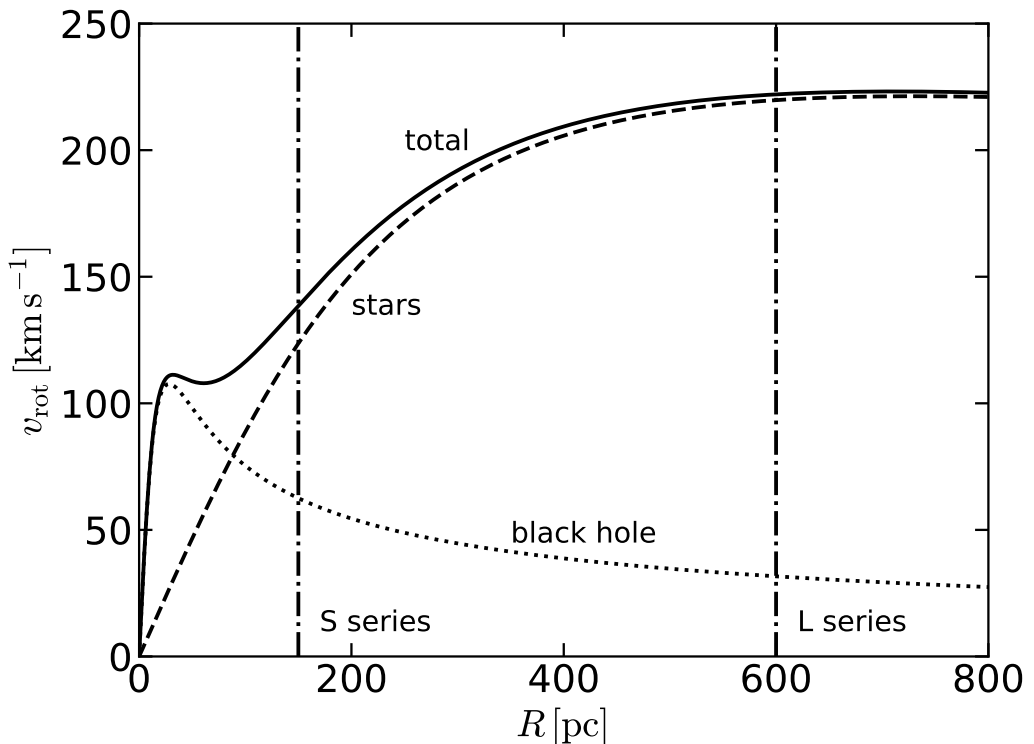


Figure 2.1. Rotation curve of our galaxy model. The solid line draws the circular velocity $v_{\text{rot}} = (Rd\Phi_b/dR + Rd\Phi_{\text{BH}}/dR)^{1/2}$, while the dashed and dotted lines show the individual contributions of Φ_b and Φ_{BH} to v_{rot} . Two vertical lines at $R_{\text{ring}} = 150$ and 600 pc mark the ring positions in our S and L series models, respectively.

with $\rho_{b0} = 50 M_\odot \text{ pc}^{-3}$ and $r_b = 250 \text{ pc}$ chosen so that the circular velocity at $r \sim 1 \text{ kpc}$ and shape at smaller scale are similar to the rotation curve for NGC 1097 from Onishi et al. (2015). Figure 2.1 shows the resulting rotation curve derived from $\Phi_{\text{ext}} = \Phi_b + \Phi_{\text{BH}}$.

The cooling rate in general depends on the chemical composition, ionization state, and temperature, while the heating rate depends on composition, electron abundance, and the radiation and cosmic ray (CR) energy densities. For the present work, in which we focus on dynamics rather than the exact thermal state, we adopt a simplified net cooling function $\rho\mathcal{L}$ in Equation (2.3) that consists of three parts:

$$\rho\mathcal{L} = n_{\text{H}}^2 \Lambda - n_{\text{H}} \Gamma_{\text{PE}} - n_{\text{H}} \Gamma_{\text{CR}}. \quad (2.8)$$

Here, $n_{\text{H}}^2 \Lambda$ is the volumetric cooling rate, where $n_{\text{H}} = \rho/(1.4271m_{\text{H}})$ is the hydrogen number density assuming the solar abundances. We shall assume that Λ depends only on the gas temperature T , and use the fitting formula of Koyama & Inutsuka (2002, see also Kim et al. 2008a) for $T < 10^{4.2} \text{ K}$, and the cooling function from Sutherland & Dopita (1993) for $T > 10^{4.2} \text{ K}$, where the latter is based on collisional ionization equilibrium at solar metallicity. The heating terms are $n_{\text{H}} \Gamma_{\text{PE}}$ representing the photoelectric heating rate by FUV radiation on dust grains, and $n_{\text{H}} \Gamma_{\text{CR}}$ representing the heating rate by CR ionization. For the equation of state $P = \rho k_{\text{B}} T / (\mu m_{\text{H}})$ with the Boltzmann constant k_{B} , we allow the mean molecular weight $\mu(T)$ to vary with T from $\mu_{\text{ato}} = 1.295$ for atomic gas to $\mu_{\text{ion}} = 0.618$ for ionized gas (see Kim & Ostriker 2017).

The main source of the FUV radiation is young massive stars, which in our simulations are a constant fraction of the mass of star cluster particles formed when gas collapses. In addition, we also allow for metagalactic FUV radiation. We therefore take the photoelectric heating rate per hydrogen Γ_{PE} as

$$\Gamma_{\text{PE}} = \Gamma_{\text{PE},0} \left(\frac{\mu(T) - \mu_{\text{ion}}}{\mu_{\text{ato}} - \mu_{\text{ion}}} \right) \left(\frac{J_{\text{FUV}}}{J_{\text{FUV},0}} + 0.0024 \right), \quad (2.9)$$

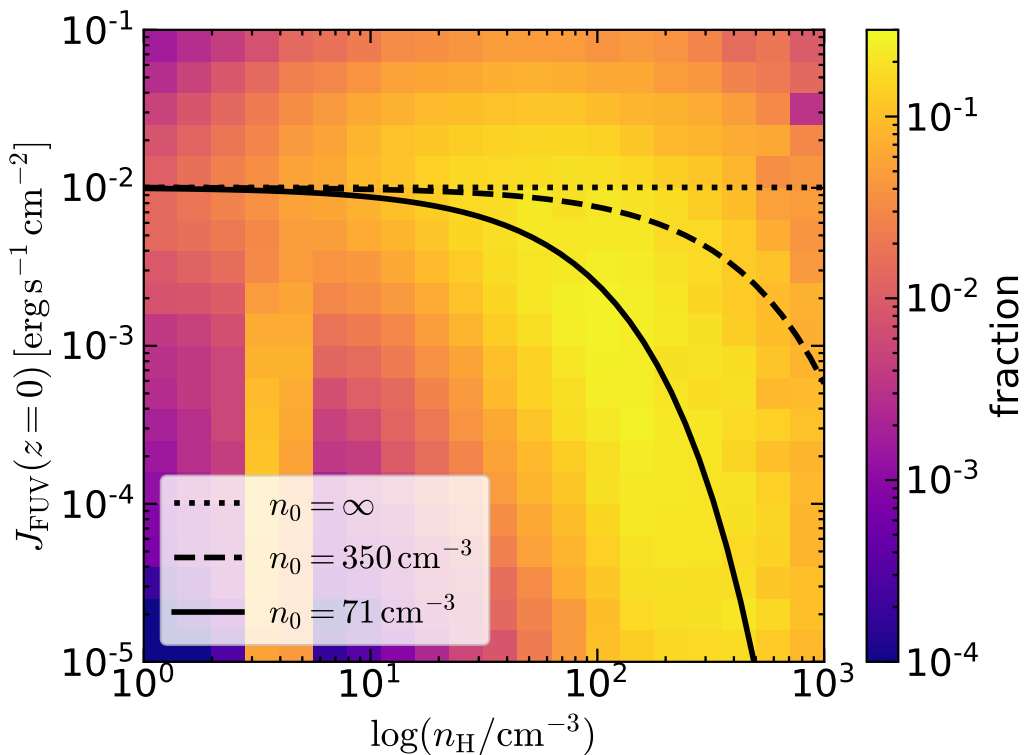


Figure 2.2. 2D histogram of J_{FUV} and n_{H} in the $z = 0$ plane, using our fiducial model. J_{FUV} is obtained by post-processing snapshots at $t = 100 - 110$ Myr, using the gas density distribution and locations and luminosities of all star particles, and employing the adaptive ray-tracing algorithm of Kim et al. (2017b). The dotted, dashed, and solid lines represent Equation (2.10) with $n_0 = \infty$, 350 cm^{-3} , and 71 cm^{-3} , respectively. Note that the vertical feature near $n_{\text{H}} = 4 \text{ cm}^{-3}$ is due to the gas along the inflowing streams.

where we take $\Gamma_{\text{PE},0} = 2 \times 10^{-26} \text{ erg s}^{-1}$ (Koyama & Inutsuka 2002) and $J_{\text{FUV},0} = 2.1 \times 10^{-4} \text{ erg s}^{-1} \text{ cm}^{-2} \text{ sr}^{-1}$ (Draine 1978) as normalizing factors based on solar neighborhood conditions. The term in the first parentheses in Equation (2.9) is to make the photoelectric heating completely shut off in the fully ionized gas. The small additional factor in the last parentheses in Equation (2.9) comes from the metagalactic radiation (Sternberg et al. 2002).

The FUV intensity would have large values in the regions near star particles and small values in deep inside clouds away from star particles due to dust attenuation. While it would be desirable to apply full radiative transfer to compute the FUV intensity $J_{\text{FUV}}(\mathbf{x}, t)$ throughout the domain, time-dependent ray tracing from every star particle would be prohibitively expensive given the large ($\gtrsim 200$) number of sources in our simulations. Instead, we adopt a simpler and less computationally expensive approach. We calculate the total FUV luminosity \mathcal{L}_{FUV} of all star particles in the simulation domain (see Section 2.2.3) and use this to set the local J_{FUV} in a cell with density n_H according to

$$J_{\text{FUV}} = \frac{\mathcal{L}_{\text{FUV}}}{4\pi L^2} \left(\frac{1 - E_2(\tau_{\perp}/2)}{\tau_{\perp}} \right) e^{-n_H/n_0}. \quad (2.10)$$

Here, $\tau_{\perp} = \kappa_d \Sigma$ with $\kappa_d = 10^3 \text{ cm}^2 \text{ g}^{-1}$ is the vertical optical depth for $\Sigma \equiv M_{\text{gas}}/L^2$ the average gas surface density, E_2 is the second exponential integral, and n_0 is a turnover density. M_{gas} is the total gas mass in the computational domain. The first two factors in Equation (2.10) correspond to the solution of the radiation transfer equation in a plane-parallel geometry (see, e.g., Ostriker et al. 2010), while the exponential term takes into account the local shielding of FUV radiation inside dense clumps with $n_H \gtrsim n_0$.

To motivate Equation (2.10) and determine an appropriate value of n_0 for each of our models, we first run simulations by taking $n_0 = \infty$ (i.e, without FUV shielding) and select 11 snapshots during $100 \text{ Myr} \leq t \leq 110 \text{ Myr}$ after a nuclear ring already formed (see Section 2.3.1). We then post-process the snapshots by applying the adaptive ray-tracing algorithm developed by Kim et al. (2017b) to directly

measure J_{FUV} produced by all star particles. Figure 2.2 plots the normalized two-dimensional (2D) histogram of J_{FUV} and n_{H} in the midplane of our fiducial model (see below) at $t = 100\text{--}110$ Myr. The dotted, dashed, and solid lines draw Equation (2.10) with $n_0 = \infty$, 350 cm^{-3} , and 71 cm^{-3} , respectively, the last of which best describes $J_{\text{FUV}}(z = 0)$ resulting from the ray-tracing method. For each model we use the same procedure to compute n_0 ; Table 2.1 lists the adopted values obtained in this way. Overall, models with higher inflow rate and smaller ring size have higher gas density and thus larger n_0 .

In addition to photoelectric heating, we include CR heating which is responsible for heating the cold and dense gas for which photoelectric heating almost shuts off due to the exponential factor in Equation (2.10). We assume the CR heating rate is proportional to the SFR surface density Σ_{SFR} , also allowing for attenuation by a factor of Σ_0/Σ above a critical gas surface density $\Sigma_0 = 10.7 M_{\odot} \text{ pc}^{-2}$ (Neufeld & Wolfire 2017). We normalize by the CR heating rate and the SFR surface density in the solar neighborhood, $\Gamma_{\text{CR},0} = 3.2 \times 10^{-27} \text{ erg s}^{-1}$ and $\Sigma_{\text{SFR},0} = 3 \times 10^{-3} M_{\odot} \text{ yr}^{-1} \text{ kpc}^{-2}$ (Gong et al. 2017; Neufeld & Wolfire 2017). We thus have

$$\Gamma_{\text{CR}} = \Gamma_{\text{CR},0} \left(\frac{\mu(T) - \mu_{\text{ion}}}{\mu_{\text{ato}} - \mu_{\text{ion}}} \right) \frac{\Sigma_{\text{SFR}}}{\Sigma_{\text{SFR},0}} \min \left\{ 1, \frac{\Sigma_0}{\Sigma} \right\}, \quad (2.11)$$

where the factor in the parentheses shuts off CR heating by ionization in fully ionized gas.[†]

2.2.2 Gas Inflow Streams

In our simulations, the hydrodynamic effect of a non-axisymmetric bar is implemented via idealized gas streams originating on the y -boundaries, as depicted in Figure 2.3. We create the inflows via a pair of square-shaped nozzles each of size L_{in}^2 , offset by impact parameter b_{in} relative to the y -axis. The direction of the inflow velocity is inclined to the y -axis by angle θ_{in} to reflect that dust lanes are usually

[†]In this thesis, we do not consider CR heating by scattering off free electrons in fully ionized gas (e.g., Draine 2011).

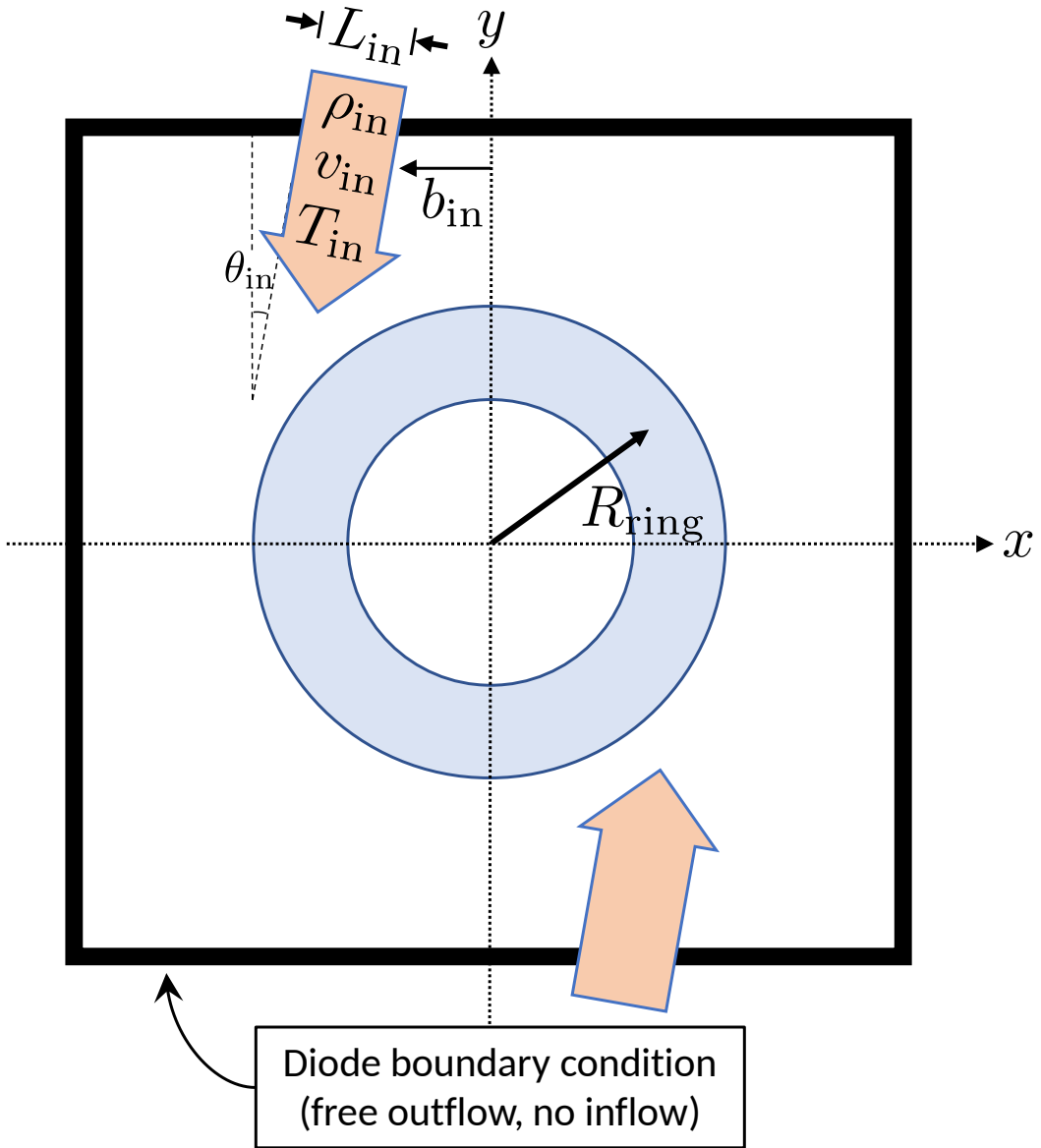


Figure 2.3. Schematic of the imposed gas inflows in our simulations, mimicking bar-driven inflows. Two gas streams flow into the computational domain through square-shaped nozzles with side L_{in} , located at the positive and negative y -boundaries (large arrows). $\theta_{in} = 10^\circ$ and b_{in} refer to the inclination angle and the impact parameter of the inflow stream relative to the y -axis. The blue shaded annulus represents the expected location for the ring formation. See text for details.

inclined relative to the bar semi-major axis (e.g., Comerón et al. 2009; Kim et al. 2012b).[‡]

We vary the density ρ_{in} and speed v_{in} of the streams in order to control both the mass inflow rate \dot{M}_{in} and the ring radius R_{ring} that forms. From the condition that the specific angular momentum of the stream *in the inertial frame* is equal to that of circular ring consistent with the background rotation at radius $R = R_{\text{ring}}$, we find

$$v_{\text{in}}(x, y) = \frac{R_{\text{ring}} v_{\text{rot}}(R_{\text{ring}}) - R^2 \Omega_p}{|x \cos \theta_{\text{in}} - y \sin \theta_{\text{in}}|}, \quad (2.12)$$

where $R = \sqrt{x^2 + y^2}$ is the galactocentric radius at the location of the nozzle. Note that v_{in} depends on x and y , indicating the inflow velocity varies across the nozzles; on the boundary $|y| = L/2$. The mass inflow rate is then given by

$$\dot{M}_{\text{in}} = 2 \int_{-L_{\text{in}}/2}^{L_{\text{in}}/2} \int_{b_{\text{in}}}^{b_{\text{in}} + L_{\text{in}}} \rho_{\text{in}} v_{\text{in}} \cos \theta_{\text{in}} dx dz. \quad (2.13)$$

For inflowing gas, we set the temperature to $T_{\text{in}} = 2 \times 10^4$ K, which is typical of the warm neutral medium in our models. The choice of T_{in} is immaterial, however, because the temperature of the inflowing gas is quickly adjusted according to the heating and cooling rates once the stream enters the computational domain.

We caution the reader that if the simulation domain is large enough that $R^2 \Omega_p > R_{\text{ring}} v_{\text{rot}}(R_{\text{ring}})$ at the nozzles, it is not possible to choose a value for the inflow velocity consistent with a circular orbit at $R = R_{\text{ring}}$. In this case, simple consideration of angular momentum conservation for ring formation is inadequate. Instead, it would be necessary to allow for a bar torque such that the inflowing gas can lose enough angular momentum to settle on a circular orbit at R_{ring} . For our idealized semi-global setup, the box size is therefore limited.

[‡]We find that gas streams escape the computational domain without forming a ring when θ_{in} is too small.

2.2.3 Star Particles and SN Feedback

A complete description of the creation and evolution of star particles and the prescription for treating supernovae (SNe) can be found in Kim & Ostriker (2017). Here, we briefly summarize the key components. A cell undergoing gravitational collapse spawns a sink/star particle if the following three conditions hold simultaneously: (1) the gas density in the cell exceeds the Larson-Penston density threshold $\rho_{LP} = 8.86c_s^2/(G\Delta x^2)$, for grid spacing Δx ; (2) the cell lies at a local potential minimum; and (3) the velocity is converging in all three directions. A portion of the mass from a volume, $(3\Delta x)^3$, is removed from the grid and assigned to the sink particle upon creation. Each particle represents a star cluster that fully samples the Kroupa (2001) initial mass function (IMF).

Gravitational collapse may continue even after the sink creation, building up the mass of a star cluster. To follow this process, the mass and momentum accretion rates through the cells surrounding each sink particle are computed based on the Riemann fluxes at every timestep. When the mass flux in the sink particle’s reference frame is negative in all three directions (i.e., converging flow), the sink is allowed to accrete mass and momentum according to the flux-based accretion rates. Accretion is turned off once the first SN explodes from the sink particle (occurring at $t \sim 4$ Myr). This method crudely mimics star formation process within giant molecular clouds in a coarse-grained manner.

For every sink particle with mass m_{sp} and mass-weighted mean age t_m , we assign the FUV luminosity that determines the heating rate through Equation (2.9) and (2.10) using **STARBURST99** (Leitherer et al. 1999), assuming a fully sampled Kroupa IMF. We also estimate the expected number of SNe, $\mathcal{N}_{SN} = m_{sp}\xi_{SN}(t_m)\Delta t$, during hydrodynamic time step Δt , where $\xi_{SN}(t_m)$ is the SN rate tabulated in **STARBURST99**. With our spatial resolution $\Delta x = 2$ or 4 pc, \mathcal{N}_{SN} is smaller than unity. We therefore turn on SN feedback only if $\mathcal{N}_{SN} > \mathcal{U}_{SN}$, where $\mathcal{U}_{SN} \in [0, 1]$ denotes a uniform random number.

Each SN returns mass $M_{ej} = 10 M_\odot$, momentum, and energy to the neighboring

cells. In the TIGRESS framework, the amount of momentum or energy injected depends on the local density and the resolution. If the ambient density is too high for the Sedov–Taylor stage to be resolved, we assume the remnant has already entered the snowplow phase and thus inject the expected final radial momentum $p_* = 2.8 \times 10^5 M_\odot \text{ km s}^{-1} (n_{\text{H}}/\text{cm}^{-3})^{-0.17}$ (Kim & Ostriker 2015b). If the density is sufficiently low such that the Sedov–Taylor stage is expected to be at least partially resolved, 72% of the total SN energy $E_{\text{SN}} = 10^{51} \text{ erg}$ is injected as thermal energy, while the remaining 28% is injected as kinetic energy associated with the radial momentum. In our simulations, 80%–90% of all SNe are resolved.

We follow the motion of sink particles by solving the equations of motion

$$\ddot{\mathbf{x}} = -\nabla\Phi_{\text{tot}} - 2\boldsymbol{\Omega}_p \times \dot{\mathbf{x}} \quad (2.14)$$

in the rotating frame. The original integrator used in Kim & Ostriker (2017) is for the equations of motion in a local shearing box and therefore inapplicable for our purpose. The usual explicit leap-frog integrator is also inappropriate, because it loses its symplectic nature in the presence of the velocity-dependent Coriolis force. Noting that the right-hand side of Equation (2.14) has the same form as the Lorentz force in electromagnetism, we integrate Equation (2.14) using the Boris algorithm (Boris 1970), which is frequently adopted in kinetic codes for advancing charged particles under electromagnetic fields. In Appendix A, we describe our implementation of the Boris algorithm and present a test result.

2.2.4 Models

We consider two series of models that differ in R_{ring} , the *target* size of the ring. The large ring models (**L** series) have $R_{\text{ring}} = 600 \text{ pc}$, nozzle impact parameter $b_{\text{in}} = 320 \text{ pc}$, and nozzle width $L_{\text{in}} = 200 \text{ pc}$ (see Figure 2.3). The **L** series models have domain size $L = 2048 \text{ pc}$ and number of cells per dimension $N = 512$, yielding grid spacing $\Delta x = L/N = 4 \text{ pc}$. We construct small ring models (**S** series) by scaling down the **L** series by a factor of four, such that $R_{\text{ring}} = 150 \text{ pc}$, $b_{\text{in}} = 80 \text{ pc}$,

Table 2.1. Model parameters

Model	R_{ring} (pc)	$\rho_b(R_{\text{ring}})$ ($M_\odot \text{ pc}^{-3}$)	$n_{\text{H,in}}$ (cm^{-3})	\dot{M}_{in} ($M_\odot \text{ yr}^{-1}$)	\bar{v}_{in} (km s^{-1})	v_{cir} (km s^{-1})	t_{orb} (Myr)	n_0 (cm^{-3})
(1)	(2)	(3)	(4)	(5)	(6)	(7)	(8)	(9)
L0	600	2.84	0.286	0.125	154	200	18.4	18
L1	600	2.84	1.15	0.5	154	200	18.4	35
L2*	600	2.84	4.58	2	154	200	18.4	71
L3	600	2.84	18.3	8	154	200	18.4	142
S0	150	31.5	5.71	0.125	123	133	6.92	71
S1	150	31.5	22.8	0.5	123	133	6.92	142
S2	150	31.5	91.3	2	123	133	6.92	283
S3	150	31.5	365	8	123	133	6.92	567

* Fiducial model.

$L_{\text{in}} = 50$ pc, and $L = 512$ pc. We take $N = 256$, corresponding to $\Delta x = 2$ pc, in order to mitigate a time step constraint arising from smaller cell size in the **S** series. For all models we adopt $\theta_{\text{in}} = 10^\circ$. For both series, we consider four different values for the inflow rate[§], $\dot{M}_{\text{in}} = 1/8, 1/2, 2$, and $8 M_\odot \text{ yr}^{-1}$. For the angular velocity of our computational domain, we take $\Omega_p = 36 \text{ km s}^{-1} \text{ kpc}^{-1}$, equal to the bar pattern speed in NGC 1097 (Piñol-Ferrer et al. 2014).

Table 2.1 lists the parameters of all models. Column (1) gives the model name. Columns (2) and (3) give R_{ring} and the bulge stellar density ρ_b at R_{ring} , respectively. Columns (4) and (5) give $n_{\text{H,in}} = \rho_{\text{in}}/(1.4271 m_{\text{H}})$, and \dot{M}_{in} , respectively. Column (6) gives the mean inflow velocity $\bar{v}_{\text{in}} \equiv \dot{M}_{\text{in}}/(2\rho_{\text{in}} L_{\text{in}}^2 \cos \theta_{\text{in}})$. Columns (7) and (8) list the circular velocity $v_{\text{cir}} = v_{\text{rot}}(R_{\text{ring}}) - R_{\text{ring}} \Omega_p$ and the orbital period $t_{\text{orb}} = 2\pi R_{\text{ring}}/v_{\text{cir}}$ of the ring in the rotating frame, respectively. The circular velocity in the inertial frame is 222 and 138 km s^{-1} for **L** and **S** series, respectively. Column (9) gives the value of n_0 we take for the dust attenuation (see Equation 2.10). We take model **L2** with $R_{\text{ring}} = 600$ pc and $\dot{M}_{\text{in}} = 2 M_\odot \text{ yr}^{-1}$ as our fiducial model.

The initial condition of our models is near vacuum, filled with rarefied gas with $n_{\text{H}} = 10^{-5} \exp[-|z|/(50 \text{ pc})] \text{ cm}^{-3}$ and $T = 2 \times 10^4 \text{ K}$, rotating at $\mathbf{v} = \sqrt{R(\partial\Phi_{\text{tot}}/\partial R)} \hat{\phi}$. The subsequent evolution is governed entirely by the mass inflow from the boundaries.

We integrate Equations (2.1)–(2.4) using a modified version of the **Athena** code (Stone et al. 2008), which solves the equations of hydrodynamics or magnetohydrodynamics using finite-volume Godunov methods. We do not include magnetic fields in this chapter, whose effects will be studied separately in Chapter 4. Our simulations use the van Leer integrator (Stone & Gardiner 2009), Roe’s Riemann solver with H-correction (Sanders et al. 1998), and second-order spatial reconstruction. When needed, we apply first-order flux correction (Lemaster & Stone 2009). We solve the Poisson equation via fast Fourier transform convolution with open bound-

[§]As long as \dot{M}_{in} is fixed, different combinations of ρ_{in} and L_{in} do not lead to any noticeable differences on the ring properties.

ary conditions (Skinner & Ostriker 2015); the density of star particles is included using a particle-mesh approach as in Kim & Ostriker (2017).

Within the nozzle region on the boundaries, we apply inflow boundary conditions as described in Section 2.2.2. For the rest of the boundaries, we take diode boundary conditions: we extrapolate the hydrodynamic variables from the last two active zones to the ghost cells, and set the normal velocity to zero if the gas is inflowing. This allows gas to freely escape from the computational domain, while ensuring no inflow occurs except through the nozzles.

2.3 Evolution

In this section, we describe the overall temporal and morphological evolution of our fiducial model, focusing on ring formation, star formation histories, and distributions of gas and star particles. Steady-state physical quantities averaged over the nuclear ring and their correlations will be presented in Section 2.4.

2.3.1 Overall Evolution of the Fiducial Model

Figures 2.4 and 2.5 provide a visual impression of the overall time evolution of model L2, in the x - y plane and x - z plane, respectively.

At early time, the gas streams injected through the nozzles closely follow the ballistic orbits shown as gray solid lines in the leftmost top panel. Orbit crowding, as manifested by convergence of the ballistic orbits near $(x, y) = (\pm 0.3, \pm 0.2)$ kpc, triggers the first star formation in the inflowing streams at $t = 5.1$ Myr.

In about a half of the (rotating frame) orbital time $t_{\text{orb}}/2 = 9.2$ Myr, the two inflowing streams start to collide with each other and produce strong shocks with a Mach number of ~ 15 . Star formation then begins at the contact points where the inflowing streams collide. The sink particles produced at very early time have highly eccentric orbits close to the ballistic orbits of the streams and thus most of them leave the computational domain. SN feedback from these particles (prior to

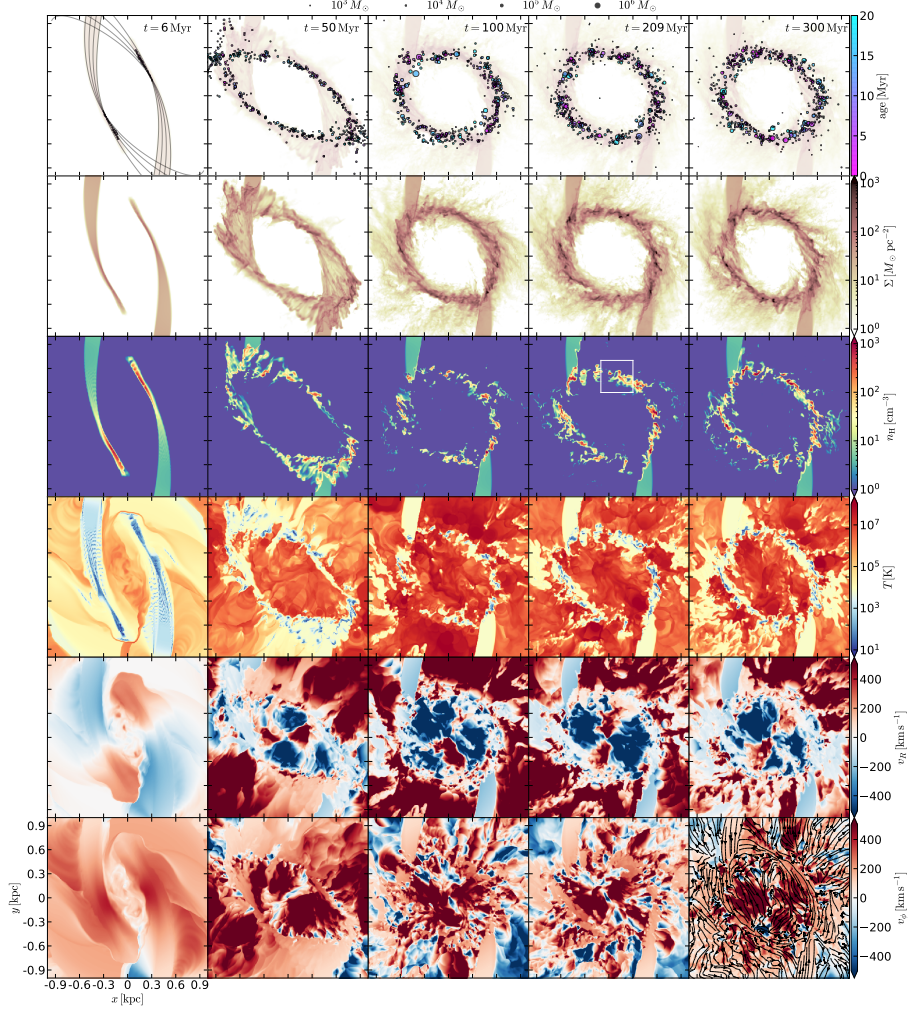


Figure 2.4. Face-on views of model L2 at $t = 6, 50, 100, 209$, and 300 Myr (columns from left to right). From top to bottom, the rows display the projected positions of sink particles, integrated gas surface density Σ , hydrogen number density n_{H} , temperature T , radial velocity v_R , and azimuthal velocity v_ϕ in the rotating frame. The last four rows show slices through $z = 0$. In the top row, Σ is also shown in the background for reference. The gray solid lines in the leftmost top panel draw the expected orbits of pressureless particles injected at the nozzles. The white square box in the fourth panel of the third row marks the zoom-in region shown in Figure 2.7. The black solid lines with arrows in the rightmost bottom panel plot the gas streamlines at the midplane. Gas streams injected from the nozzles initially follow ballistic orbits, colliding with the stream from the opposite side at $t \sim 8.5$ Myr. The collision drives strong shocks, which gradually remove the kinetic energy from the gas streams. Eventually, gas settles down to a roughly circular orbit and forms a nuclear ring with radius $R \approx 600$ pc.

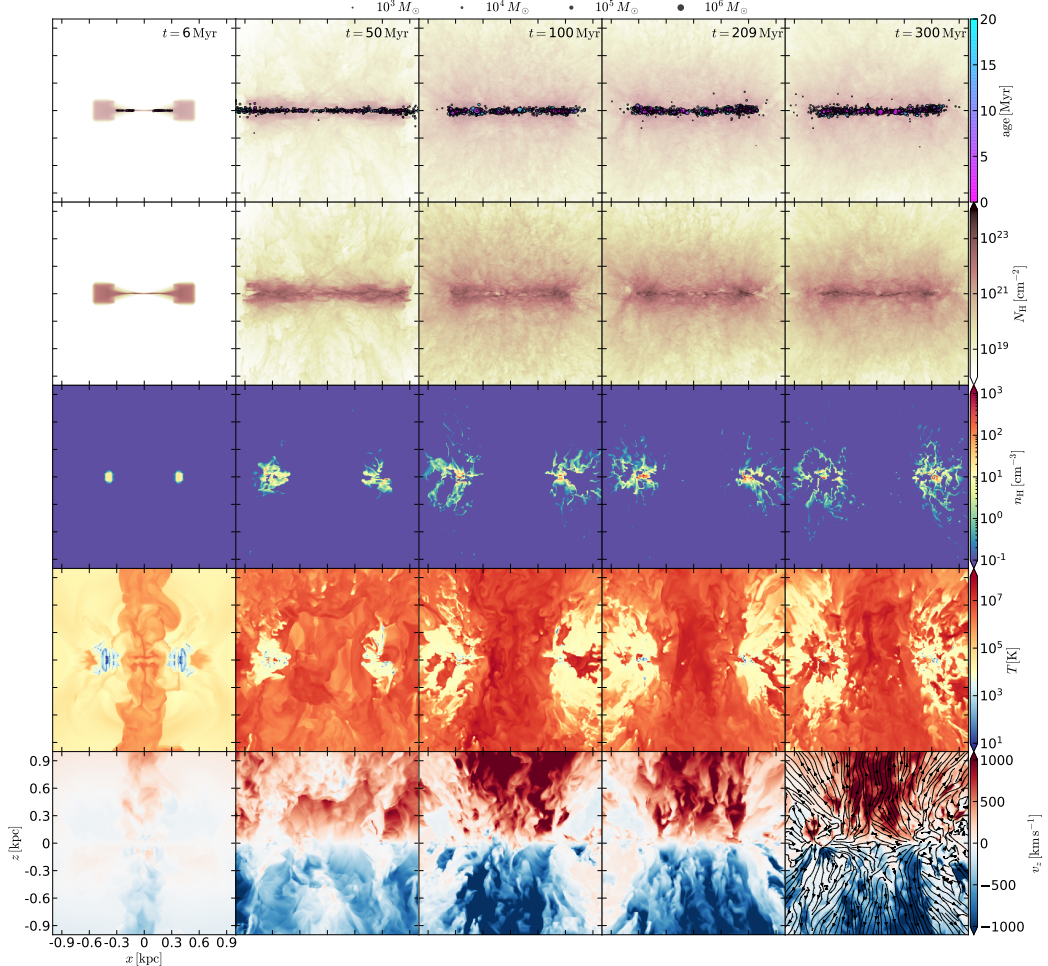


Figure 2.5. Edge-on views of model L2 at $t = 6, 50, 100, 209$, and 300 Myr (columns from left to right). From top to bottom, the rows display the projected positions of the sink particles, hydrogen column density $N_{\text{H}} = \int n_{\text{H}} dy$, hydrogen volume density n_{H} , temperature T , and vertical velocity v_z . The last three rows show slices through $y = 0$. The black solid lines with arrows in the rightmost bottom panel plot the gas streamlines. Superbubbles produced by interactions of multiple SN explosions lead to persistent winds.

their escape) produces hot gas that fills most of the volume, inside and outside the gas streams.

Unlike the early sink particles, however, gas loses a significant amount of kinetic energy at every passage of the contact points and orbits become less eccentric, eventually creating a ring-like shape. While star-forming regions are concentrated near the contact points at early time, they soon become widely distributed as strong SN feedback makes the ring highly clumpy everywhere, enabling local collapse. At $t \sim 100$ Myr, the system reaches a quasi-steady state in which the ring morphology and various statistical quantities including the ring gas mass and SFR do not change appreciably over time. The radius of the nuclear ring is $R \sim 600$ pc in model L2, consistent with the expectation from the angular momentum conservation (Equation 2.12). For the fiducial model, the in-plane width of the gas ring is ~ 200 pc. After steady state is reached, the star formation in model L2 (and other models) is not concentrated in preferred regions of the ring but occurs randomly in space and time. The star formation/feedback cycle does not have strong bursts (from either spatial or temporal correlations in gas collapse). As a result, the steady inflow rate adopted in our models gives rise to a steady SFR with small temporal fluctuations for model L2 (and other models). SN feedback never destroys the ring completely in model L2 as shown in Figure 2.4. We find that our models generally show the steady star formation and persistence of the ring.

SN feedback as well as gravitational and thermal instabilities produce cold and dense cloudlets distributed around the nuclear ring. Figure 2.6 display the volume- and mass-weighted probability distribution functions (PDFs) of n_{H} and P/k_{B} at $t = 250$ Myr. The volume fractions of the hot ($T > 2 \times 10^4$ K) and the cold-warm ($T < 2 \times 10^4$ K) phases are 84% and 16%, while their mass fractions are 2% and 98%, respectively.

The mean thermal pressure of the cold-unstable medium with $T < 5050$ K is somewhat enhanced above the equilibrium curve with the instantaneous total heating rate at that epoch, shown as the red line. This enhancement is observed

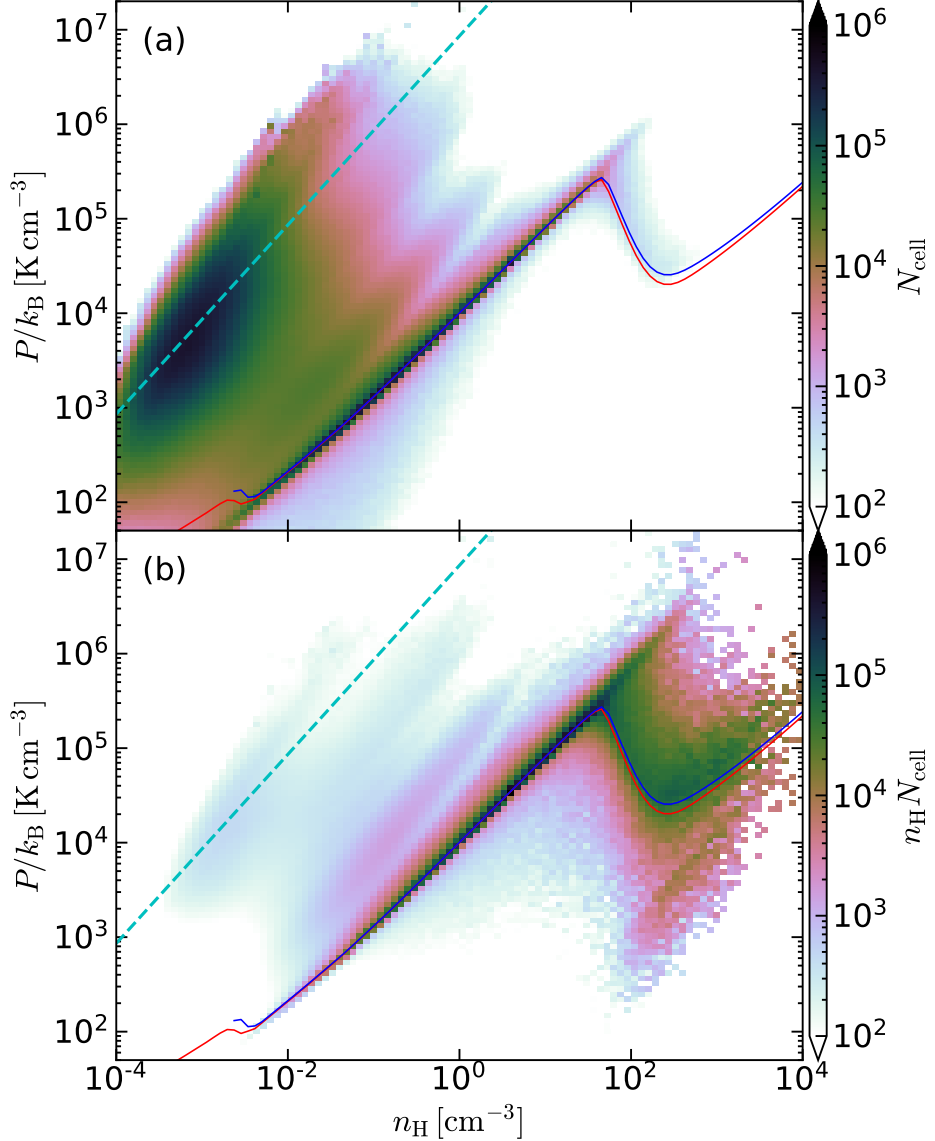


Figure 2.6. (a) Volume- and (b) density-weighted joint PDF in P/k_B and n_H of model L2 at $t = 250$ Myr. The red line is the thermal equilibrium curve under the instantaneous radiative heating rate at that epoch, while the blue line corresponds to an equilibrium curve with additional turbulent heating rate Γ_{turb} (see text), which yields slightly better agreement with the mean PDFs. Most of the warm and cold medium follows the blue line, with some scatter due to intermittent shock heating. The dashed line indicates the mean temperature $T = 3.7 \times 10^6$ K of the hot medium.

in all epochs, suggesting that it is not caused by chance due to fluctuation of heating rate. Instead, this enhanced pressure (or temperature) may be attributed to dissipation of (turbulent) kinetic energy in the ring. To get a rough estimate of the kinetic energy dissipation rate due to (marginally resolved) cloud-scale turbulence, we calculate the mass-weighted vertical velocity dispersion $\sigma_z \sim 12 \text{ km s}^{-1}$ and the scale height $H \sim 26 \text{ pc}$ of the cold-unstable medium, and estimate the turbulent heating rate (per hydrogen) as $\Gamma_{\text{turb}} = \frac{3}{2}\mu_H m_H \sigma_z^3 / H$. The blue line shows the equilibrium curve when Γ_{turb} is additionally included, showing a slightly better agreement with the PDFs for the cold-unstable medium. At $n_H = 10^3 \text{ cm}^{-3}$, the heating rates due to FUV, CR, and (assumed) turbulent dissipation are $\Gamma_{\text{PE}} = 5.8 \times 10^{-5} \Gamma_{\text{PE},0}$, $\Gamma_{\text{CR}} = 6.2 \Gamma_{\text{PE},0}$, and $\Gamma_{\text{turb}} = 3.9 \Gamma_{\text{PE},0}$, respectively. We note that actual kinetic energy dissipation rate might be even larger than Γ_{turb} considering numerical dissipation. Although our treatment of the FUV and CR heating is rather simplified, the above result suggests that the turbulent heating could be a major heating source for the dense gas where the radiation is heavily shielded (e.g., Ginsburg et al. 2016).

Figure 2.5 shows that most of the star formation takes place in the high-density gas near the midplane, while the distribution of lower-density gas extends vertically up to $|z| \sim 500 \text{ pc}$ due to SN feedback. For example, at $t = 300 \text{ Myr}$ (last column) there are three large bubbles centered at $(x, z) \sim (-700 \text{ pc}, 150 \text{ pc})$, $\sim (-500 \text{ pc}, -100 \text{ pc})$, and $\sim (-800 \text{ pc}, -150 \text{ pc})$ in the negative- x portions of the ring, that lift up the gas to high latitude. Heated by the SN shocks, gas inside the bubbles reaches $\sim 10^7 \text{ K}$. Sometimes the hot gas inside the superbubbles breaks out through the cold-warm medium, such as the bubble at $(x, z) \sim (-800 \text{ pc}, -150 \text{ pc})$. Away from the midplane the hot gas dominates.

Superbubbles created by repeated feedback from relatively young cluster particles typically have a diameter of $\sim (100\text{--}200) \text{ pc}$, comparable to the ring width of $\sim 200 \text{ pc}$, so that a fraction of the feedback energy and momentum escape from the ring through the holes like champagne flows. This is illustrated in Fig-

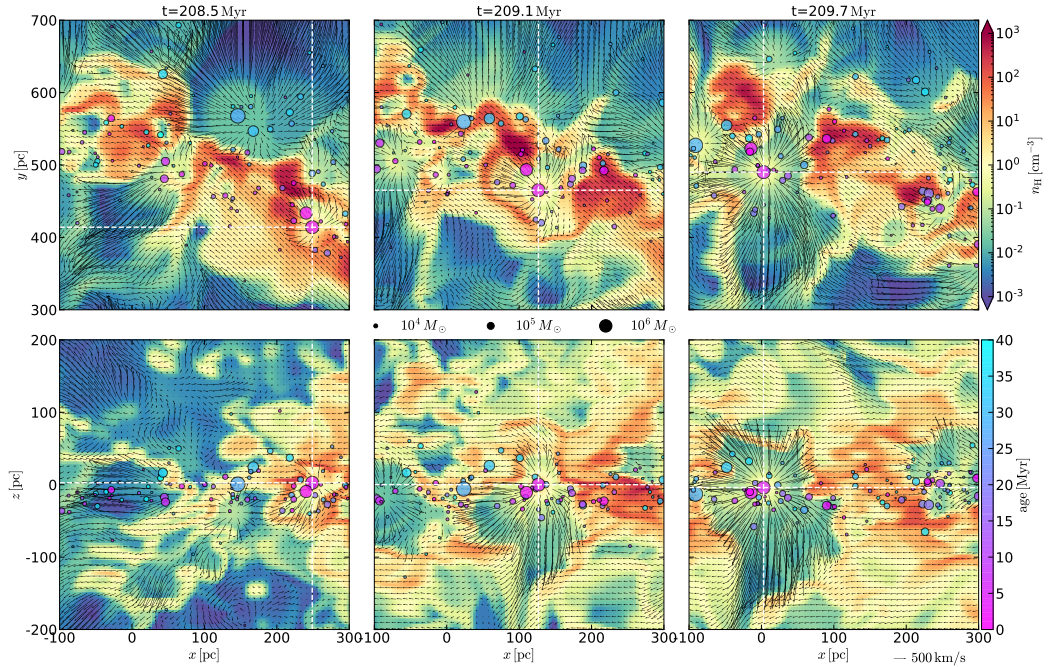


Figure 2.7. Close-up view of the ring: three consecutive snapshots of model L2 at $t = 208.5, 209.1$, and 209.7 Myr from left to right. The top panels show the density and velocities (v_x, v_y) in the $z = 0$ plane at $-0.1 \text{ kpc} \leq x \leq 0.3 \text{ kpc}$ and $0.3 \text{ kpc} \leq y \leq 0.7 \text{ kpc}$. Also shown are sink particles within $|z| \leq 0.2 \text{ kpc}$. Vertical and horizontal dashed lines trace the location of a selected sink particle, which moves over a few 100 pc within a few Myr, due to its orbital motion (including epicyclic oscillations). The bottom panels show the density and velocities (v_x, v_z) at $y = 0.41, 0.47$, and 0.49 kpc , corresponding to the y coordinates of the selected sink particle in the top panels. Other sink particles from the top panels are also shown. Arrows show the velocity field, where the arrow length is proportional to the velocity magnitude in the x - y (top panels) and x - z (bottom panels) planes.

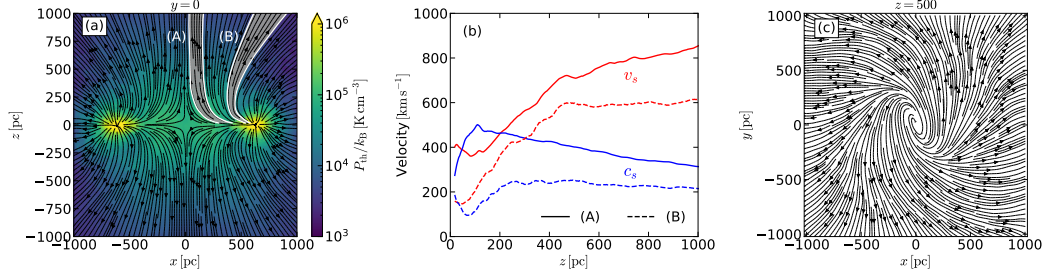


Figure 2.8. (a) Gas streamlines in model L2 overlaid over the thermal pressure in the x - z plane averaged over $t = 200$ – 300 Myr. The ring appears as bull's-eyes at $|x| \sim 600$ pc. Streamlines emerge from the ring due to the SN feedback and lead to large-scale hot superwinds. (b) Vertical profile of the poloidal velocity $\langle v_s \rangle \equiv (\langle v_R \rangle^2 + \langle v_z \rangle^2)^{1/2}$ (red) and the sound speed $\langle c_s \rangle$ (blue) along the selected streamlines (A) and (B) shown in (a). (c) Time-averaged streamlines in the x - y plane at $z = 500$ pc, showing the helical wind.

ure 2.7, which displays the density and velocity fields as well as star particles with age less than 40 Myr in a zoomed-in region within the ring for model L2 at $t = 208.5, 209.1$, and 209.6 Myr. A superbubble surrounding the star particle with $(x, y) = (250 \text{ pc}, 410 \text{ pc})$ at $t = 208.5$ Myr expands and blows out, dispersing a part of the ring and compressing the gas nearby, as the particles moves to $(x, y) = (3 \text{ pc}, 466 \text{ pc})$ at $t = 209.7$ Myr. Since orbits of star particles deviate from that of the gas, relatively old particles can explode in the regions outside the ring. For instance, the clusters near $(x, y) = (150 \text{ pc}, 570 \text{ pc})$ at $t = 208.5$ Myr are located near the outer edge of the ring. In this case, only a small fraction of the feedback energy contributes to turbulence in the ring material. Because the ring gas is spatially confined in radial direction and the gas and stellar orbits differ, much of the feedback energy is transferred to the gas outside the star-forming ring, resulting in lower feedback yield to cold–warm gas than in previous simulations with more uniform distribution of gas in the horizontal direction (see discussion in Section 2.4.2).

Hot gas created by individual SN shocks merges together to launch large, coherent outflows resembling galactic winds. These quasi-conical outflows are clearly visible in the bottom row of Figure 2.5. For the same model, Figure 2.8(a) plots in

the x - z plane gas streamlines overlaid over the thermal pressure. For these streamlines, we average over $t = 200\text{--}300$ Myr and include all of the gas in the $y = 0$ slice. The ring shows up like bull's-eyes at $|x| \sim 600$ pc in the pressure map, from which the streamlines emerge. Figure 2.8(b) plots the vertical profiles of the time-averaged poloidal velocities and the sound speed of the gas along the selected streamlines shown in Figure 2.8(a). It is apparent that the wind is accelerated beyond the sonic point, readily reaching $\approx (600\text{--}900)$ km s $^{-1}$ at $z = 1$ kpc. Figure 2.8(c) plots the time-averaged streamlines at $z = 500$ pc, showing that the winds are helical, with the rotational velocity decreasing as gas moves outward radially conserving angular momentum.

We note that the subsonic to supersonic transition of the winds was absent in the previous local simulations in which the streamlines cannot open up due to the combination of a relatively small box and SNe throughout the midplane region (e.g., Martizzi et al. 2016; Kim & Ostriker 2018). Here, the relatively small size of the star-forming ring within the domain allows streamlines to open up, leading to the characteristic biconical shape and supersonic transition often seen in both observations (Strickland et al. 2004; Yukita et al. 2012) and simulations (Wada et al. 2009; Fielding et al. 2017; Schneider et al. 2018). We note that in contrast to previous simulations of central starburst-driven winds where the locations of SN feedback were imposed by hand, here the SN location distribution arises naturally from star formation within the ring.

2.3.2 Star Formation

Figure 2.9(a) plots the temporal evolution of the total mass in the gas M_{gas} and in the sink particles M_{sp} in model L2. The total gas mass saturates to $M_{\text{gas}} \sim 8.5 \times 10^7 M_{\odot}$ within $\sim 3t_{\text{orb}}$, while M_{sp} steadily increases with time, except for the initial phase when stars formed in the inflowing streams escape from the computational box.

Figure 2.9(b) plots the mass inflow rate \dot{M}_{in} to the box, outflow rate \dot{M}_{out} from

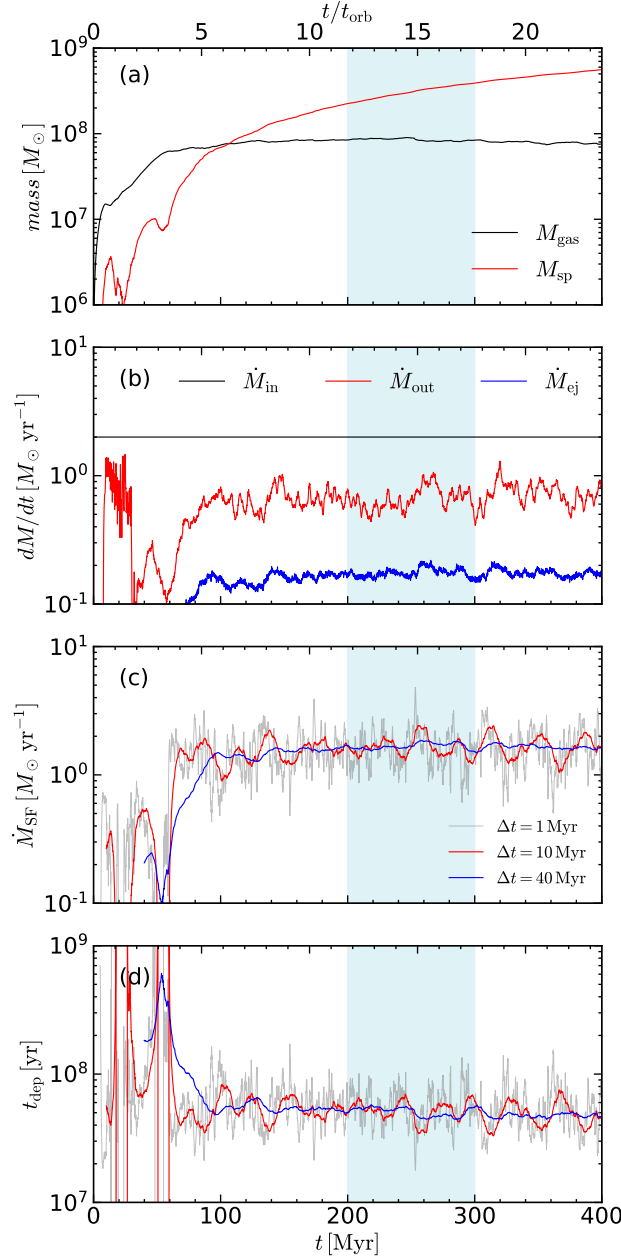


Figure 2.9. Temporal history in model L2 of (a) the total gas mass (M_{gas} ; black), the total mass of the sink particles representing star clusters (M_{sp} ; red), (b) the mass inflow rate (\dot{M}_{in} ; gray) through the nozzles, the mass outflow rate (\dot{M}_{out} ; red) through the domain boundaries, and the rate of the mass return from SN feedback (\dot{M}_{ej} ; blue), (c) the SFR averaged over $\Delta t = 1$ Myr (gray), $\Delta t = 10$ Myr (red), and 40 Myr (blue), and (d) the gas depletion time $t_{\text{dep}} = M_{\text{gas}} / \dot{M}_{\text{SF}}$ within the domain. The mean gas mass, SFR, and the depletion time in the shaded region ($200 \text{ Myr} \leq t \leq 300 \text{ Myr}$) are $8.5 \times 10^7 M_{\odot}$, $1.7 M_{\odot} \text{ yr}^{-1}$, and 51.2 Myr, respectively.

the box, and deposition rate \dot{M}_{ej} from SN ejecta in model L2. The mass inflow rate is fixed to $\dot{M}_{\text{in}} = 2 M_{\odot} \text{ yr}^{-1}$ at the nozzles, and $\dot{M}_{\text{ej}} \sim 0.2 M_{\odot} \text{ yr}^{-1}$ is roughly constant after $t = 100 \text{ Myr}$ when the SFR reaches a quasi-steady state. The mass outflow rate through the domain boundaries is quite large at early time ($t \lesssim 30 \text{ Myr}$) due to the gas leaving the domain through the y -boundaries before gas orbits are circularized (Figure 2.4). Except for these early transients, \dot{M}_{out} is dominated by SN-driven outflows and saturates to $\sim 0.67 M_{\odot} \text{ yr}^{-1}$ with some fluctuations.

We calculate the SFR at time t by

$$\dot{M}_{\text{SF}}(t, \Delta t) = \frac{M_{\text{sp}}(t) - M_{\text{sp}}(t - \Delta t)}{\Delta t}, \quad (2.15)$$

where Δt is a chosen time window for averaging. We take $\Delta t = 1, 10$, or 40 Myr to allow for different timescales pertinent to common observational tracers of the SFR (see, e.g., Kennicutt & Evans 2012): $\Delta t = 1 \text{ Myr}$ corresponds to the *instantaneous* SFR, while $\Delta t = 10$ and 40 Myr are appropriate for H α and radio free-free/recombination lines, or to FUV/IR tracers, respectively. Figure 2.9(c) and (d) plot \dot{M}_{SF} and the gas depletion time $t_{\text{dep}} \equiv M_{\text{gas}}/\dot{M}_{\text{SF}}$, respectively. At early time, the SFR is lower than the inflow rate and gas builds up in the ring, increasing M_{gas} eligible for star formation. The SFR increases with time until the system enters a quasi-steady state. In model L2, the steady-state SFR is $\dot{M}_{\text{SF}} \sim 1.66 M_{\odot} \text{ yr}^{-1}$, corresponding to 83% of \dot{M}_{in} . The average depletion time after a steady state is reached is $t_{\text{dep}} = 51.2 \text{ Myr}$.

While the mean values of the SFR are insensitive to Δt , temporal fluctuations decrease with Δt . Fluctuation amplitudes are $0.55, 0.28$, and $0.09 M_{\odot} \text{ yr}^{-1}$ for $\Delta t = 1, 10$, and 40 Myr , respectively. Our simulations do not exhibit a burst/quench cycle as seen in the model of Krumholz et al. (2017) and simulation of Torrey et al. (2017), nor the long-term variation in the depletion time seen in Armillotta et al. (2019) (who found a range $t_{\text{dep}} \sim 10^8 - 10^9 \text{ yr}$). More similar to our results were those of Sormani et al. (2020b), who ran moving-mesh simulations with star formation and feedback targeting star formation in the CMZ, and found that the

SFR and the depletion time are quite steady with time, with only modest (within a factor of 2) variations. Our results suggest that under a constant inflow rate, the SFR in nuclear rings would be quite steady. This would also imply that bursty behavior in real systems is due to variations in the feeding rate from larger scales. We shall compare the numerical results with the prediction of the self-regulation theory (Ostriker et al. 2010; Ostriker & Shetty 2011) in Section 2.4.2.

2.3.3 Other Models

Evolution of the other models is qualitatively similar to that of the fiducial model, although the ring size and shape, SFR, etc. depend significantly on the model parameters R_{ring} and \dot{M}_{in} . Figure 2.10 compares distributions in the x - y plane of gas and sink particles for all the models at $t = 250$ Myr, after a steady state is reached. The left and right columns correspond to the L and S series, respectively, with increasing \dot{M}_{in} from top to bottom. In both series, the mean surface density of the ring Σ_{ring} and its ellipticity increase with \dot{M}_{in} . The increase of Σ_{ring} with \dot{M}_{in} is because the associated higher SFR yields larger thermal and turbulent pressures via feedback that support the ring against stronger gravity (see Section 2.4.2). At higher SFR, gas turns into stars before the inflowing streams are fully circularized, yielding a more eccentric ring. Rings in the S series are overall more eccentric compared to their counterparts in the L series. This is because the ratio $t_{\text{dep}}/t_{\text{orb}}$ is smaller in the S series, implying that more gas is consumed by star formation before the orbit circularization. We note that some barred galaxies including NGC 986, NGC 1365, NGC 3351, and NGC 5383 possess an eccentric nuclear ring at their centers, similarly to our models with a high inflow rate.

Figure 2.10 shows that the masses of individual sink particles, on average, increase with \dot{M}_{in} due to the increase of Σ_{ring} . Because sink particles inherit the gas velocity from which they form, their initial orbits are eccentric, similarly to the gas ring. Unlike the gas, however, the sink particles do not suffer direct collisions at the contact points and their orbits freely precess under the total gravitational

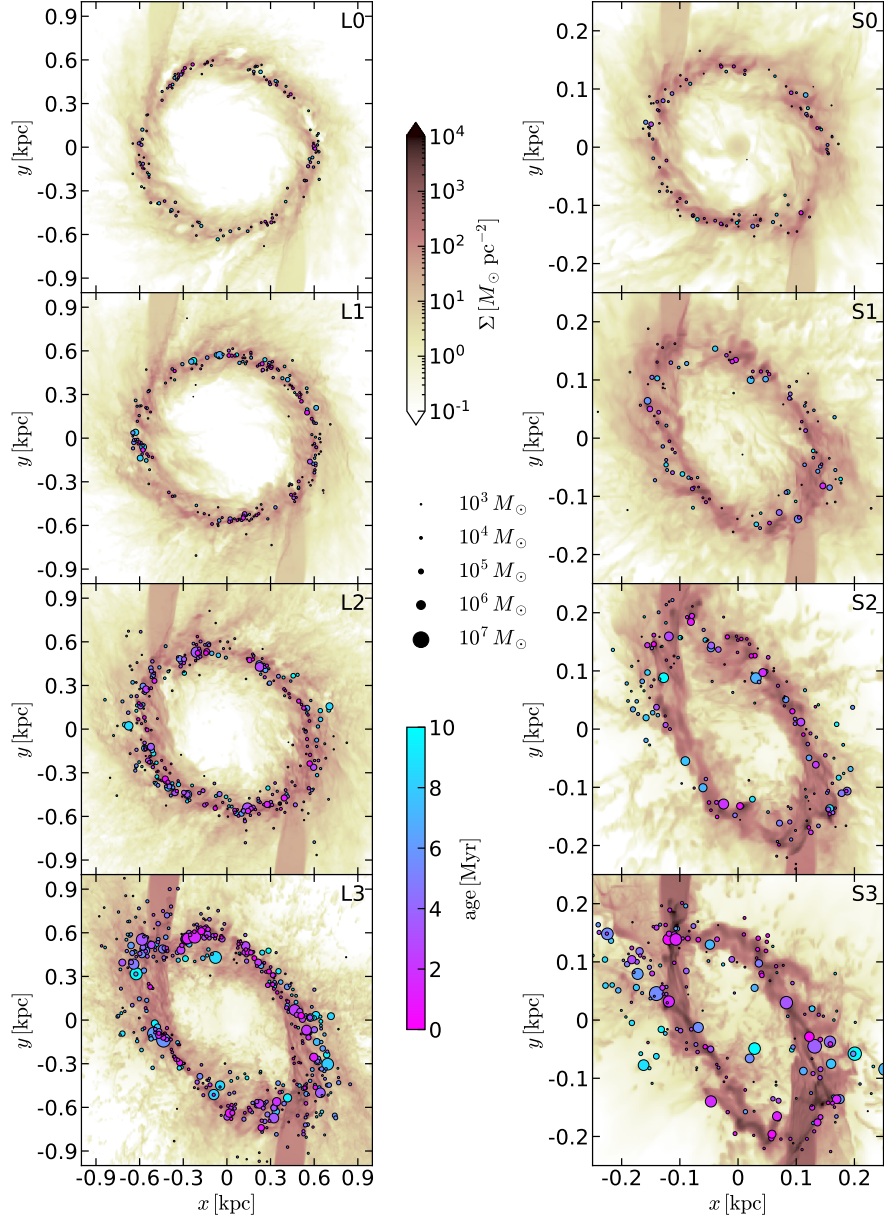


Figure 2.10. Distributions of the gas surface density Σ and sink particles with age less than 10 Myr, for all models at $t = 250$ Myr. The left and right columns are for the L and S series, respectively (note difference in box size). From top to bottom, the rows correspond to the models with $\dot{M}_{\text{in}} = 0.125, 0.5, 2$, and $8 M_{\odot} \text{ yr}^{-1}$. All panels share the same color scale for Σ and the same symbol size and color scale for star particle mass and age, given in the middle.

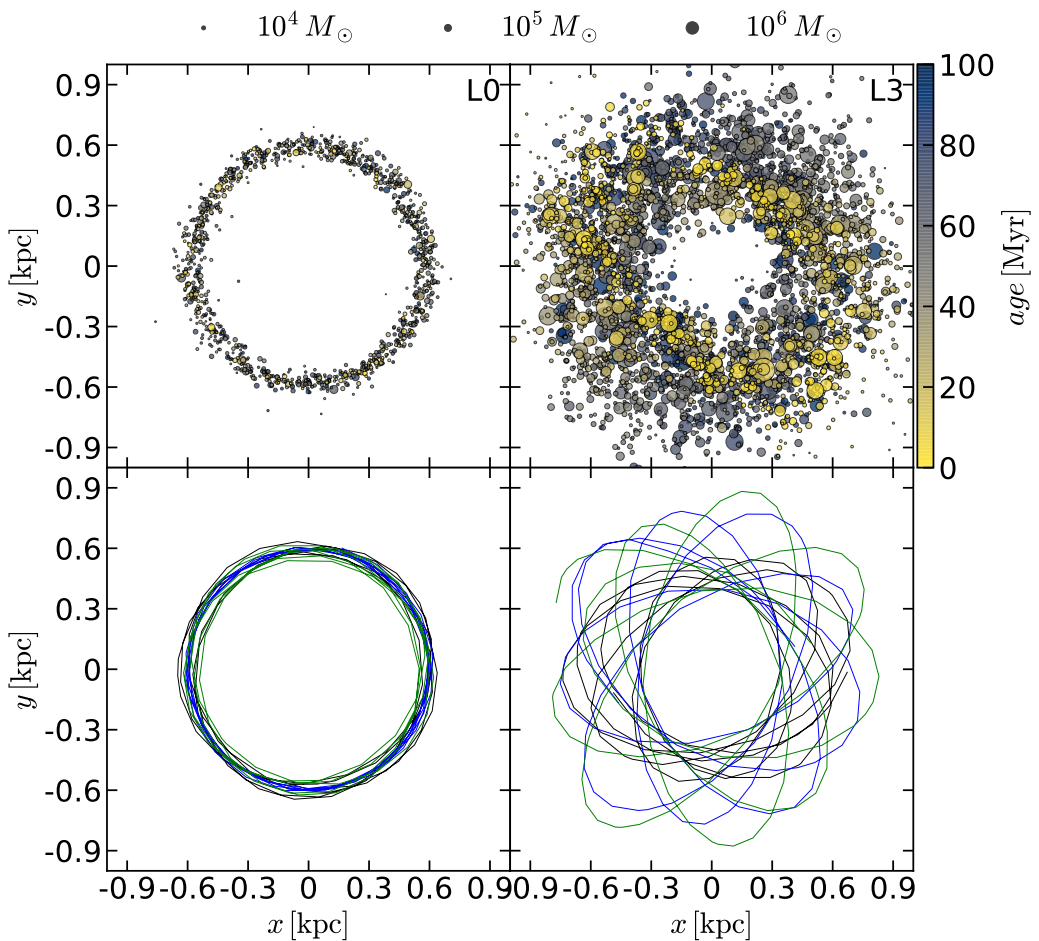


Figure 2.11. Top: spatial distributions of sink particles younger than 100 Myr at $t = 300$ Myr for models L0 (left) and L3 (right). Bottom: representative trajectories of some sink particles during $t = 200$ – 300 Myr.

potential. As a result, the spatial distribution of the sink particles deviates from that of the gas. The deviation is more prominent in models with larger \dot{M}_{in} due to more eccentric orbits of the sink particles.

Figure 2.11 compares the projected distributions of sink particles and their orbits in the x - y planes between models L0 and L3. Since the ring is almost circular in model L0, the orbits of the sink particles are also nearly circular. Consequently, both the gas and the sink particles form a narrow circular annulus near R_{ring} . In model L3, however, the orbits of the sink particles have high eccentricities and precess. As they age, they diffuse out of the gaseous ring and also precess, occupying a much wider range of radius. Young particles with $t_m \lesssim 10$ Myr are still found quite close to the eccentric gaseous ring for model L3. While our simple sink particles retain their individual identities, in reality the older massive clusters could be disrupted (de Grijs & Anders 2012; Väisänen et al. 2014) and form a psuedo-bulge (Kormendy & Kennicutt 2004).

In our simulations, the cold–warm gas with $T < 2 \times 10^4$ K comprises about 98% of the total mass. To quantify the physical properties of the cold–warm gas in our simulations, we compute the midplane values of the mass-weighted turbulent velocity dispersion σ_z and sound speed c_s , and also measure the scale height H , via

$$\sigma_z = \left(\frac{\iiint_{z=-\Delta z}^{z=\Delta z} \rho v_z^2 \Theta dx dy dz}{\iiint_{z=-\Delta z}^{z=\Delta z} \rho \Theta dx dy dz} \right)^{1/2}, \quad (2.16)$$

$$c_s = \left(\frac{\iiint_{z=-\Delta z}^{z=\Delta z} P \Theta dx dy dz}{\iiint_{z=-\Delta z}^{z=\Delta z} \rho \Theta dx dy dz} \right)^{1/2}, \quad (2.17)$$

$$H = \left(\frac{\iiint_{z=-L/2}^{z=L/2} \rho z^2 \Theta dx dy dz}{\iiint_{z=-L/2}^{z=L/2} \rho \Theta dx dy dz} \right)^{1/2}, \quad (2.18)$$

where $\Delta z = \Delta x$ is the grid spacing along the z -direction and the symbol Θ denotes the phase selector, such that $\Theta = 1$ for the cold–warm medium ($T < 2 \times 10^4$ K) and $\Theta = 0$ otherwise.

Figure 2.12 plots the temporal history of σ_z , c_s , and H for model L2, showing

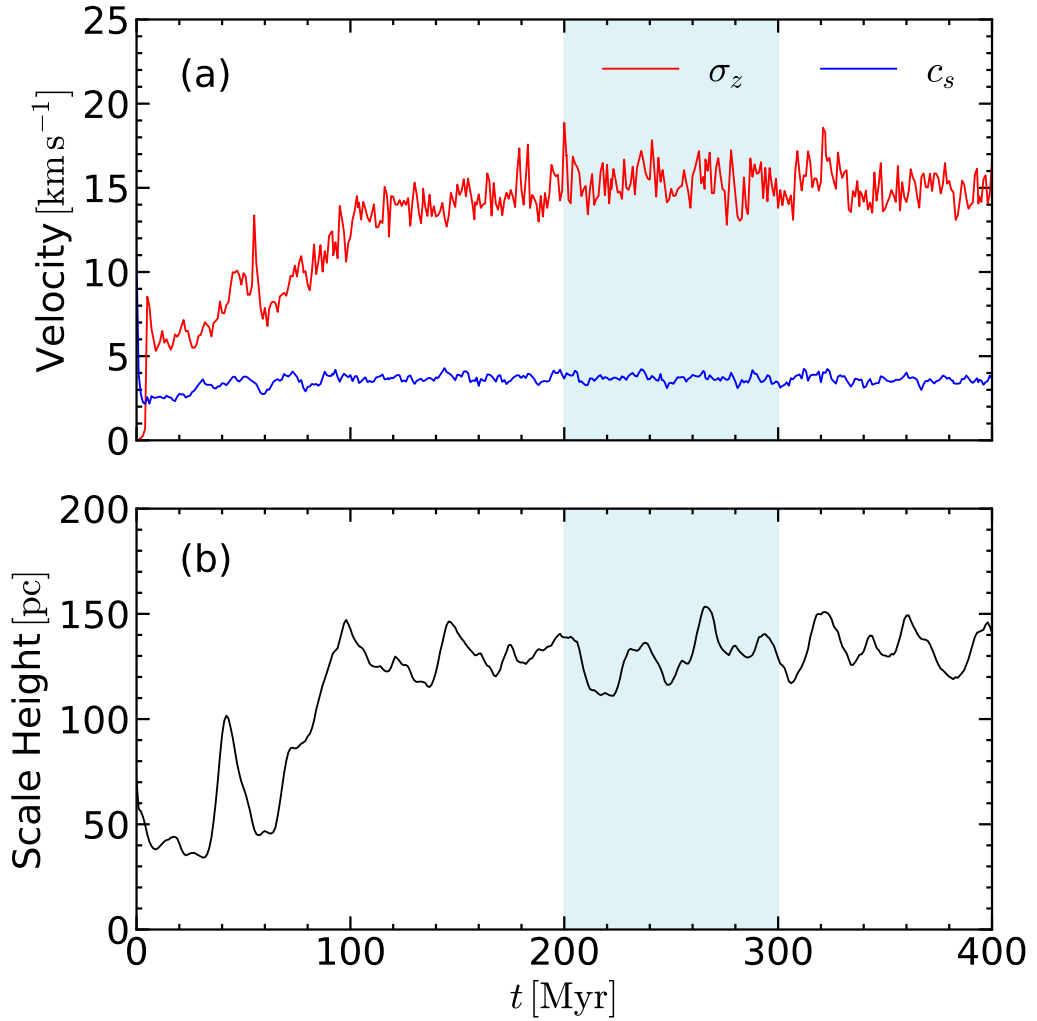


Figure 2.12. Temporal variations of (a) the vertical velocity dispersion (σ_z ; red) and the sound speed (c_s ; blue) and (b) the scale height H of the cold–warm medium in model L2. The shade indicates the time interval (200–300 Myr) over which time-averaged quantities are evaluated.

Table 2.2. Steady-state Properties of the Cold–Warm Gas

Model	σ_z	c_s	H
(1)	(2)	(3)	(4)
	(km s $^{-1}$)	(km s $^{-1}$)	(pc)
L0	8.85 ± 0.66	3.81 ± 0.20	63.88 ± 4.87
L1	12.6 ± 1.0	3.83 ± 0.20	95.0 ± 5.7
L2	15.4 ± 1.1	3.69 ± 0.22	130 ± 11
L3	17.4 ± 1.6	3.30 ± 0.24	151 ± 8
S0	11.9 ± 1.3	3.66 ± 0.31	33.8 ± 1.9
S1	13.1 ± 1.3	3.31 ± 0.32	42.8 ± 2.9
S2	14.8 ± 1.6	2.89 ± 0.28	42.5 ± 2.8
S3	23.6 ± 3.9	2.89 ± 0.35	21.5 ± 2.9

Notes. (1) Model name. (2) Vertical turbulent velocity dispersion at the midplane. (3) Isothermal sound speed at the midplane. (4) Scale height of the gas.

that these quantities remain more or less constant after $t = 100$ Myr. Note that $\sigma_z \sim 4c_s$ in model L2, indicating that the motions of the cold–warm gas are predominantly supersonic. Table 2.2 lists the mean values (with standard deviations) of σ_z , c_s , and H averaged over a time span of $\Delta t = 100$ Myr after the system reaches a quasi-steady state.¶

2.4 Correlations of Statistical Quantities

In this section, we present our measurements of various physical properties of the rings after quasi-steady state is reached, and explore correlations among these properties.

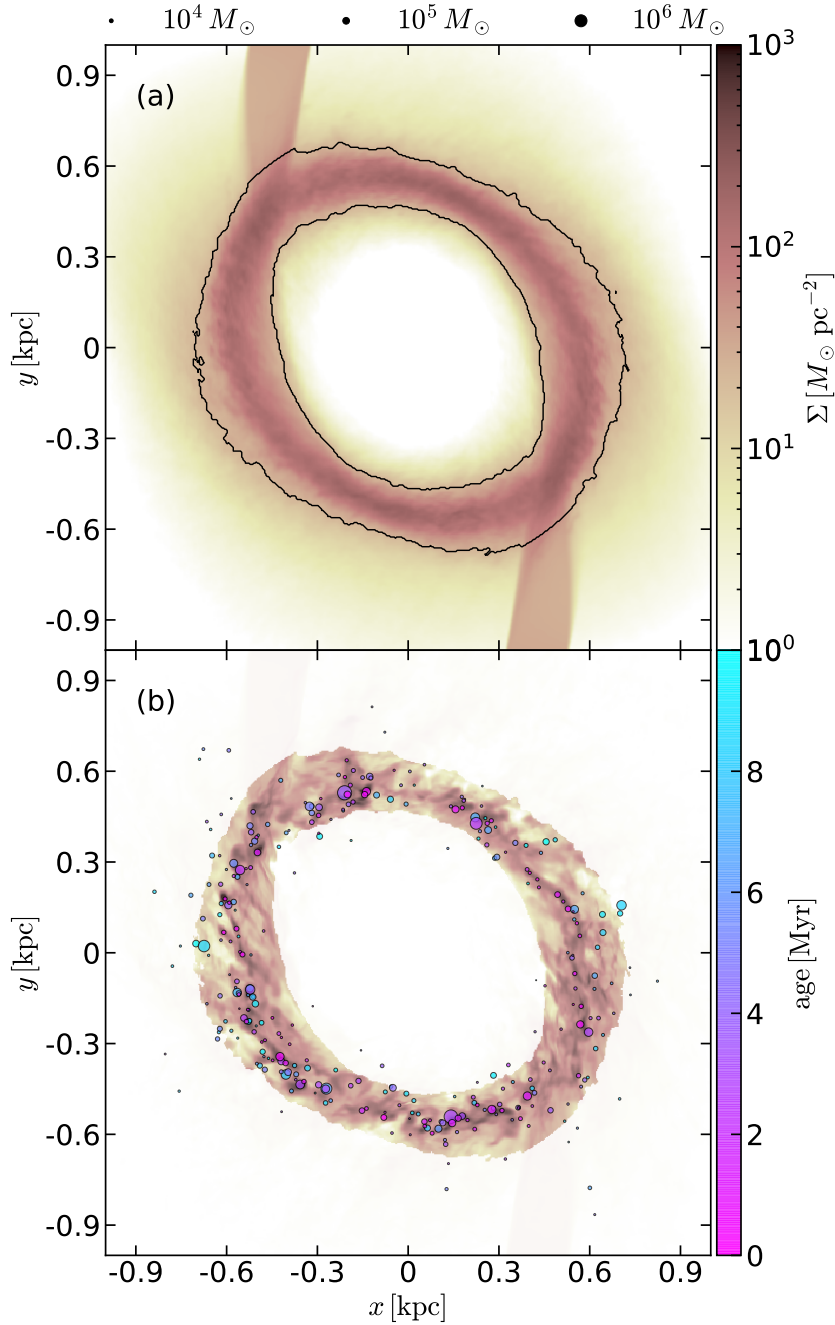


Figure 2.13. (a) Time-averaged surface density map of model L2. The solid lines delineate the boundaries of the *ring regions*. (b) Example of applying the ring mask to a snapshot of model L2 at $t = 250 \text{ Myr}$. Quantities such as Σ , Σ_{SFR} , σ , H , etc. are measured inside the ring regions.

2.4.1 Ring Properties

To properly characterize the average gas surface density Σ_{ring} of the ring, it is essential to measure the ring area A_{ring} . For this purpose, we place a circular aperture with radius R_c to exclude the gas streams, and take a temporal average $\langle \Sigma \rangle$ of the gas surface density inside the aperture over a time span of $\Delta t = 100$ Myr after the system reaches a quasi-steady state. We then identify the collection of cells with $\langle \Sigma \rangle > \Sigma_{\text{crit}}$ as the ring region (or ring mask), where Σ_{crit} is determined such that the ring region contains 90% of the total gas mass within R_c . We adjust R_c until it matches the outer semi-major axis of the ring. Figure 2.13(a) plots as black contours the ring boundaries constructed by this method, overlaid over the time-averaged surface density for model L2. We measure the ring area A_{ring} bounded by the contours, and apply the time-averaged mask to individual snapshots to calculate the ring surface density and the SFR surface density as

$$\Sigma_{\text{ring}} \equiv \frac{M_{\text{ring}}}{A_{\text{ring}}}, \quad (2.19)$$

$$\Sigma_{\text{SFR}} \equiv \frac{\dot{M}_{\text{SF}}(t, \Delta t = 10 \text{ Myr})}{A_{\text{ring}}}, \quad (2.20)$$

where M_{ring} is the gas mass contained in the ring regions. Note that in Equation (2.20), \dot{M}_{SF} counts sink particles not only inside the ring but also outside the ring since they all have formed inside the ring. The gas depletion time inside the ring is then given by $t_{\text{dep,ring}} = \Sigma_{\text{ring}}/\Sigma_{\text{SFR}}$, which is not much different from t_{dep} over the whole domain defined in Section 2.3.2 since most mass is contained in the ring. Figure 2.13(b) overlays the ring mask on top of a surface density map at $t = 250$ Myr for model L2, illustrating that most mass is enclosed within the mask. Table 2.3 lists the above steady-state physical properties of the rings for all models.

Figure 2.14 plots the dependence of \dot{M}_{SF} and M_{ring} on \dot{M}_{in} , showing strong correlations. The ring mass in the L series follows a relation $M_{\text{ring}} \approx 4 \times 10^7 M_{\odot}$ ($\dot{M}_{\text{in}}/1$

[†]We take an average over $t = 300 - 400$ Myr for models L0 and L1 and over $t = 200 - 300$ Myr for all the other models, as the former takes a longer time to reach a steady state.

Table 2.3. Steady-state Ring Properties

Model	M_{ring}	\dot{M}_{SF}	A_{ring}	Σ_{ring}	Σ_{SFR}	$t_{\text{dep,ring}}$	P_{th}	P_{turb}
(1)	(2)	(3)	(4)	(5)	(6)	(7)	(8)	(9)
	$(10^7 M_{\odot})$	$(M_{\odot} \text{yr}^{-1})$	(kpc^2)	$(M_{\odot} \text{pc}^{-2})$	$(M_{\odot} \text{yr}^{-1} \text{kpc}^{-2})$	(Myr)	$(10^6 k_{\text{B}} \text{Kcm}^{-3})$	$(10^6 k_{\text{B}} \text{Kcm}^{-3})$
L0	1.25 ± 0.05	0.0897 ± 0.0166	0.607	20.7 ± 0.8	0.148 ± 0.027	144 ± 24	0.128 ± 0.022	0.137 ± 0.022
L1	2.89 ± 0.07	0.425 ± 0.065	0.656	44.0 ± 1.0	0.648 ± 0.099	69.3 ± 9.5	0.424 ± 0.051	0.512 ± 0.079
L2	6.58 ± 0.32	1.67 ± 0.29	0.805	81.8 ± 3.9	2.07 ± 0.37	40.6 ± 7.0	0.966 ± 0.106	1.49 ± 0.19
L3	14.4 ± 0.4	6.98 ± 0.76	0.879	164 ± 5	7.94 ± 0.86	20.9 ± 2.6	1.99 ± 0.32	4.49 ± 0.78
S0	0.263 ± 0.009	0.0891 ± 0.0115	0.0475	55.3 ± 1.8	1.88 ± 0.24	30.0 ± 4.6	1.01 ± 0.30	1.44 ± 0.33
S1	0.619 ± 0.043	0.378 ± 0.056	0.0567	109 ± 8	6.67 ± 0.98	16.8 ± 3.4	2.32 ± 0.42	4.26 ± 0.82
S2	1.43 ± 0.07	1.64 ± 0.15	0.0604	236 ± 12	27.1 ± 2.5	8.81 ± 1.07	3.82 ± 0.78	12.7 ± 2.7
S3	3.66 ± 0.26	6.68 ± 0.52	0.0705	518 ± 37	94.8 ± 7.4	5.52 ± 0.67	9.51 ± 2.06	57.4 ± 19.7

Note. (1) Model name. (2) Total gas mass inside the ring. (3) Total SFR. (4) Area of the ring. (5) Mean surface density of the ring. (6) Averaged SFR surface density of the ring. (7) Gas depletion time of the ring. (8) Midplane thermal pressure. (9) Midplane turbulent pressure.

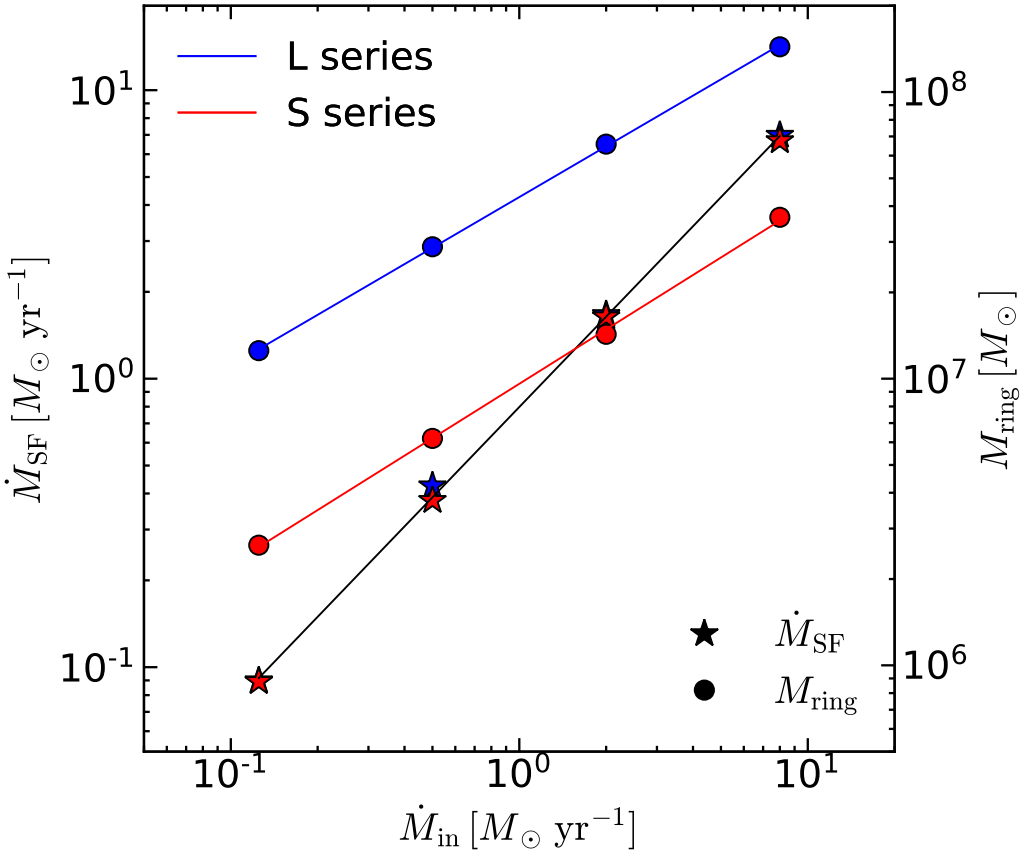


Figure 2.14. SFR \dot{M}_{SF} (star symbols, left scale) and the ring mass M_{ring} (circles, right scale) against the inflow rate \dot{M}_{in} for all models. The blue and red colors correspond to the L and S series, respectively. The solid lines show the linear fits described in the text.

$M_{\odot} \text{ yr}^{-1})^{0.6}$, scaled up by a factor of ~ 4 relative to the analogous relation for the S series, $M_{\text{ring}} \approx 1 \times 10^7 M_{\odot} (\dot{M}_{\text{in}}/1 M_{\odot} \text{ yr}^{-1})^{0.6}$. In contrast, the SFR is practically the same, $\dot{M}_{\text{SF}} \approx 0.8 \dot{M}_{\text{in}}$, for both series. This demonstrates that in our models the SFR is determined by the mass inflow rate rather than the ring mass. We note that in a given series, M_{ring} varies by a factor of ~ 10 , while \dot{M}_{in} and \dot{M}_{SF} vary by a factor of ~ 80 . This is because Σ_{SFR} is superlinearly proportional to Σ_{ring} , which we will explore in Section 2.4.2. This appears consistent with observations that ring masses do not vary much among galaxies, while SFRs vary widely (Sheth et al. 2005; Mazzuca et al. 2008).

Figure 2.15 plots the quasi-steady values of σ_z and H , measured via Equations (2.16) and (2.18), against Σ_{SFR} for all models, with error bars corresponding to the standard deviations. Note that the turbulent velocity dispersion increases weakly with Σ_{SFR} ; the same increasing trend was also seen by Shetty & Ostriker (2012, but for a much smaller range of Σ_{SFR}) and Orr et al. (2020). At low Σ_{SFR} , σ_z is comparable to the solar neighborhood TIGRESS model of Kim & Ostriker (2017). In analogous local-box TIGRESS models with higher gas and stellar density that yield $\Sigma_{\text{SFR}} \sim 0.1 - 1 M_{\odot} \text{ yr}^{-1} \text{ kpc}^{-2}$ (Kim et al. 2020a; Ostriker & Kim 2022), the values of σ_z are slightly higher, similar to the results shown here.

The scale height in the S series is smaller than in the L series because of the stronger external gravitational potential. In the L series, H increases with Σ_{SFR} due to the increase in σ_z , while it in the S series it is almost constant or decreases with Σ_{SFR} because of the increased gravity (see below).

2.4.2 Vertical Dynamical Equilibrium and Star Formation Feedback

Because the nuclear rings in our simulations are not transient but persist over many orbital times, the weight of the ISM, \mathcal{W} , must be supported by the midplane pressure P_{mid} (e.g. Boulares & Cox 1990; Elmegreen & Parravano 1994; Wolfire et al. 2003). The pressure needed for vertical dynamical equilibrium can be maintained only if there are sources of energy and momentum, primarily from young, massive stars (Ostriker et al. 2010; Ostriker & Shetty 2011): the thermal and turbulent pressures would otherwise decay due to radiative cooling and turbulent dissipation on short timescales. In our simulations, the thermal and turbulent pressures are replenished by FUV and CR heating and SN feedback, with the latter being dominant.

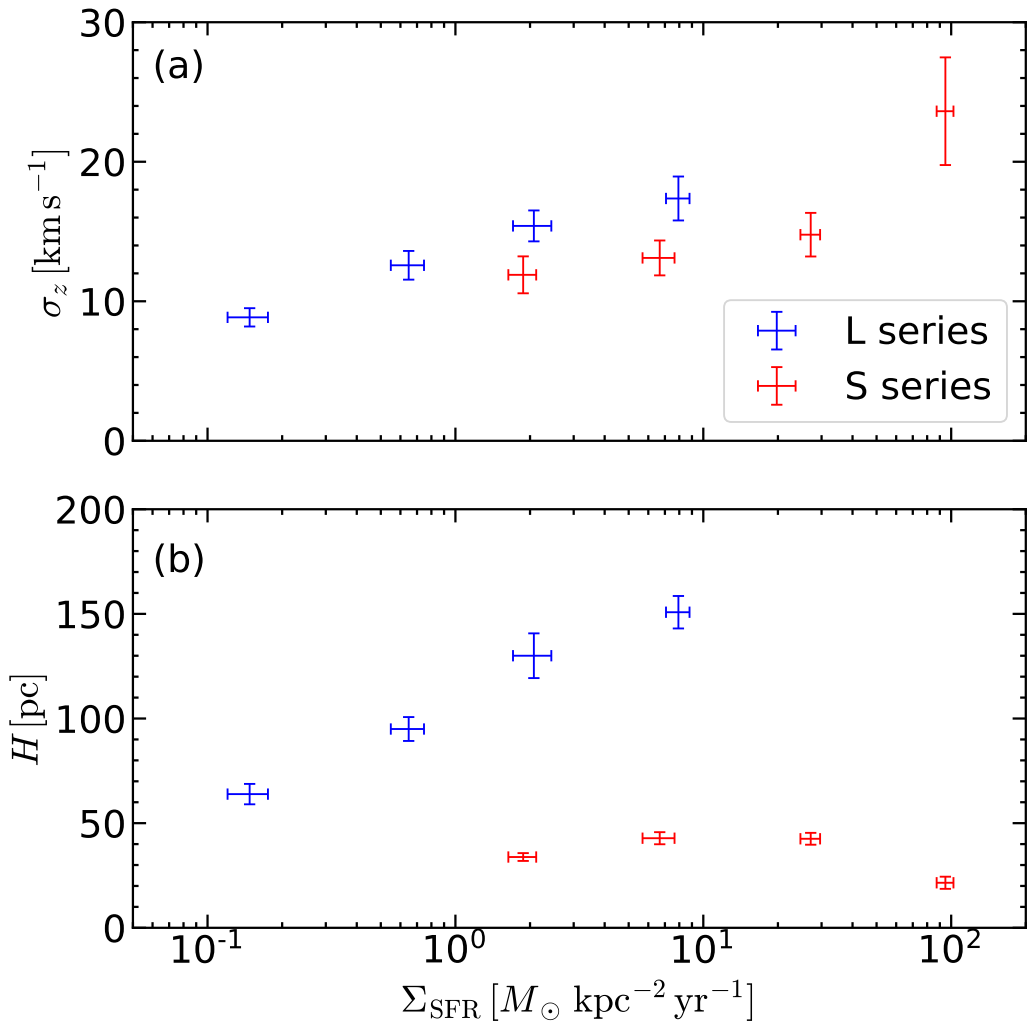


Figure 2.15. Dependence on the SFR surface density Σ_{SFR} of (a) the time-averaged vertical turbulent velocity dispersion σ_z and (b) the time-averaged vertical scale height H .

Vertical dynamical equilibrium

We measure the midplane thermal and turbulent pressures inside the ring by

$$P_{\text{th}} \equiv \frac{1}{2\Delta z A_{\text{ring}}} \int_{-\Delta z}^{\Delta z} \iint_{A_{\text{ring}}} P dx dy dz, \quad (2.21)$$

$$P_{\text{turb}} \equiv \frac{1}{2\Delta z A_{\text{ring}}} \int_{-\Delta z}^{\Delta z} \iint_{A_{\text{ring}}} \rho v_z^2 dx dy dz. \quad (2.22)$$

We separately measure the weight of the gas due to its own gravitational field, to the gravity of the sink particles, and to the external gravity from the stellar bulge as

$$\mathcal{W}_{\text{gas}} \equiv \frac{1}{A_{\text{ring}}} \iint_{A_{\text{ring}}} \left(\int_0^\infty \rho \frac{\partial \Phi_{\text{gas}}}{\partial z} dz \right) dx dy, \quad (2.23)$$

$$\mathcal{W}_{\text{sp}} \equiv \frac{1}{A_{\text{ring}}} \iint_{A_{\text{ring}}} \left(\int_0^\infty \rho \frac{\partial \Phi_{\text{sp}}}{\partial z} dz \right) dx dy, \quad (2.24)$$

$$\mathcal{W}_{\text{ext}} \equiv \frac{1}{A_{\text{ring}}} \iint_{A_{\text{ring}}} \left(\int_0^\infty \rho \frac{\partial \Phi_{\text{ext}}}{\partial z} dz \right) dx dy, \quad (2.25)$$

where Φ_{gas} and Φ_{sp} refer to the gravitational potential of the gas and sink particles, respectively, such that $\Phi_{\text{self}} = \Phi_{\text{gas}} + \Phi_{\text{sp}}$. Figure 2.16 plots the temporal evolution of \mathcal{W}_{gas} , \mathcal{W}_{sp} , and \mathcal{W}_{ext} of model L2 as red, green, and blue lines, respectively. After the system reaches a quasi-steady state ($t \gtrsim 100$ Myr), \mathcal{W}_{ext} and \mathcal{W}_{gas} do not vary much, while \mathcal{W}_{sp} keeps increasing due to the continuous creation of the sink particles. The time-averaged weights over $t = 200$ –300 Myr are $\mathcal{W}_{\text{gas}}/k_B = 1.9 \times 10^5$ K cm⁻³, $\mathcal{W}_{\text{sp}}/k_B = 6 \times 10^5$ K cm⁻³, and $\mathcal{W}_{\text{ext}}/k_B = 1.4 \times 10^6$ K cm⁻³, indicating that the gas weight in model L2 is mostly due to Φ_{sp} and Φ_{ext} rather than Φ_{gas} .

We now compare the total midplane pressure $P_{\text{mid}} = P_{\text{th}} + P_{\text{turb}}$ with the total weight $\mathcal{W}_{\text{tot}} = \mathcal{W}_{\text{gas}} + \mathcal{W}_{\text{sp}} + \mathcal{W}_{\text{ext}}$ of the ISM, checking to what extent vertical dynamical equilibrium holds. Vertical dynamical equilibrium requires

$$P_{\text{mid}} - P_{\text{top}} = \mathcal{W}_{\text{tot}}, \quad (2.26)$$

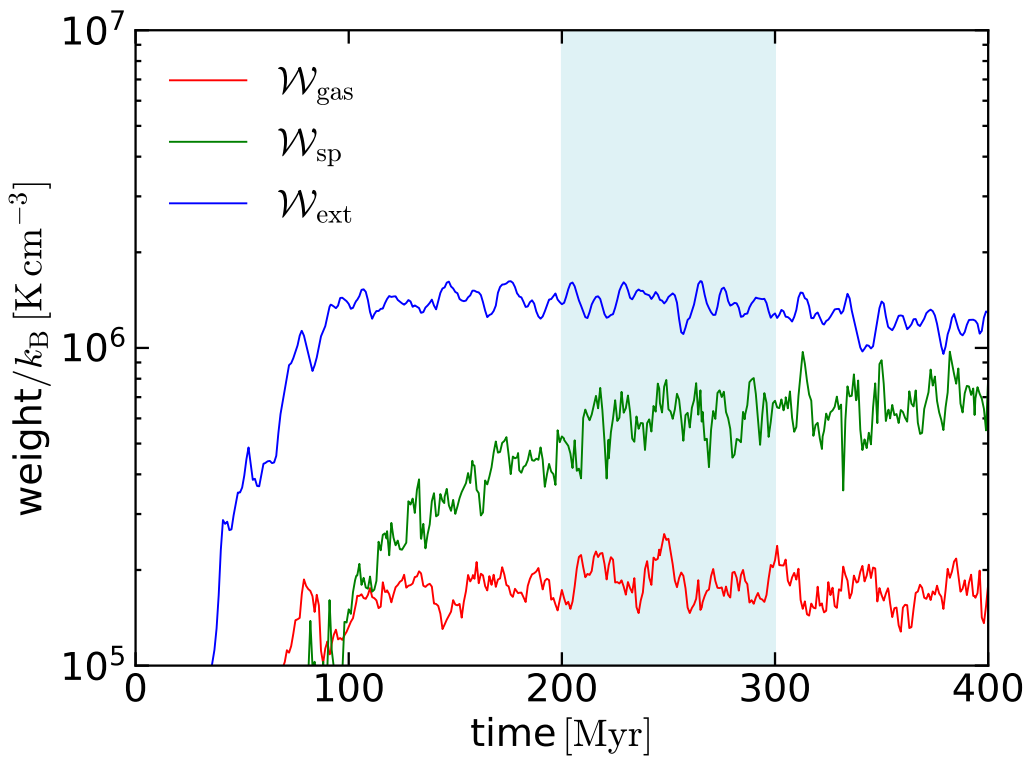


Figure 2.16. Time evolution of the gas weight contributions due to the gaseous self-gravity (\mathcal{W}_{gas}), the gravity of the sink particles (\mathcal{W}_{sp}), and the external potential (\mathcal{W}_{ext}) in model L2. The shaded region indicates that the time span over which the weights are averaged.

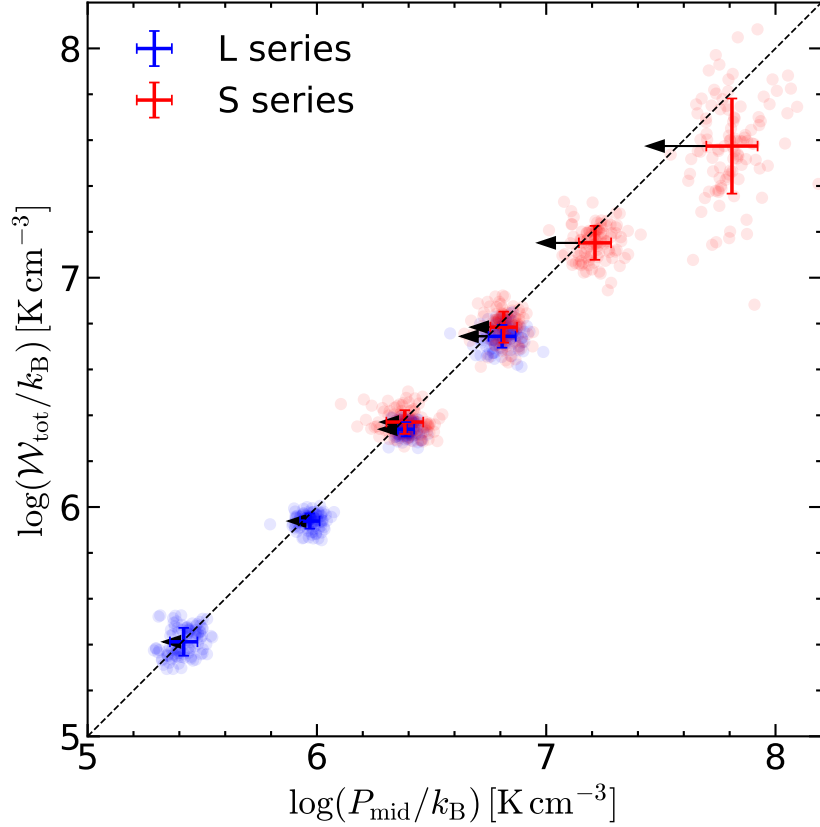


Figure 2.17. Total weight of the ISM against the total midplane pressure. Each circle corresponds to a different snapshot during $t = 200\text{--}300$ Myr. Error bars denote the temporal averages and standard deviations of each model. The dashed line corresponds to $\mathcal{W}_{\text{tot}} = P_{\text{mid}}$. Black arrows indicate the shifts of the mean values in the abscissa when P_{mid} is changed to $P_{\text{mid}} - P_{\text{top}}$.

where P_{top} is the total pressure at the top boundary ($z = L/2$) defined as

$$P_{\text{top}} \equiv \frac{1}{A_{\text{ring}}} \iint (P + \rho v_z^2)_{z=L/2} dx dy. \quad (2.27)$$

In normal situations, $P_{\text{top}} \ll P_{\text{mid}}$, leading to the usual equilibrium condition $P_{\text{mid}} \approx \mathcal{W}_{\text{tot}}$. If a system develops strong outflows with high ram pressure and the vertical extent is small, however, P_{top} may no longer be negligible compared to the midplane pressure.

Figure 2.17 plots for individual snapshots \mathcal{W}_{tot} against P_{mid} over the interval

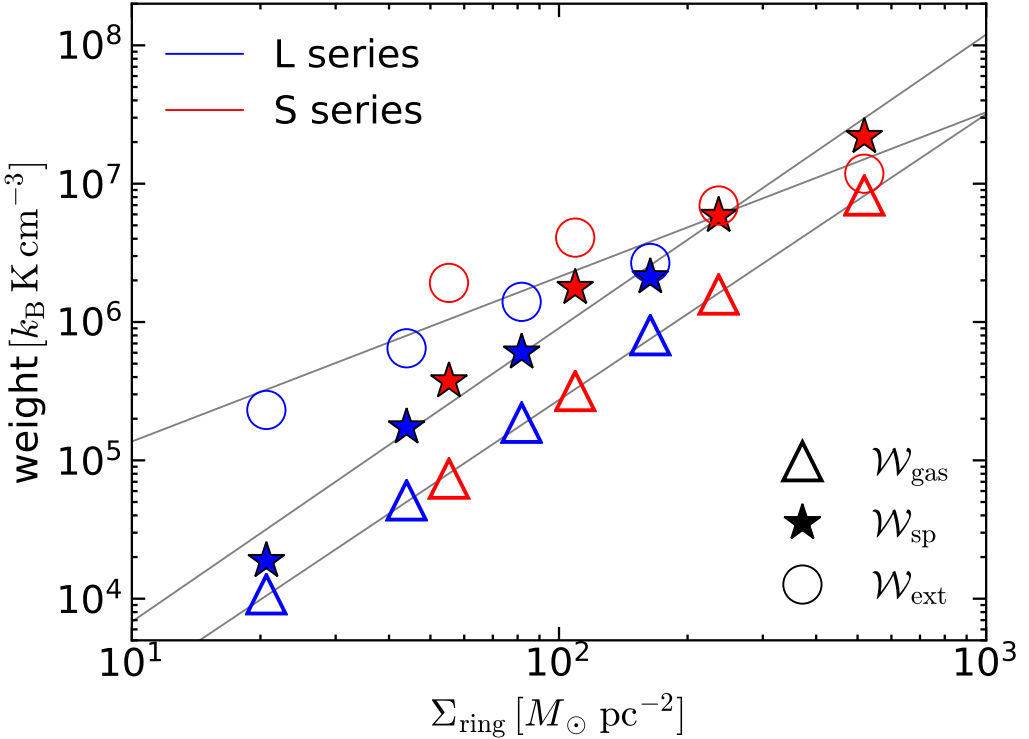


Figure 2.18. Dependence of the gas weights on the ring surface density. Blue and red symbols correspond to the L and S series, respectively. Triangles, stars, and circles represent the gas weight due to the gaseous self-gravity, the gravity of the sink particles, and the external potential, respectively. All quantities are averaged over $\Delta t = 100$ Myr. Lines are linear fits to the numerical results with slopes of 2.07, 2.12, and 1.19 for \mathcal{W}_{gas} , \mathcal{W}_{sp} , and \mathcal{W}_{ext} , respectively.

$\Delta t = 100$ Myr after steady state is reached, using blue and red for the L and S series, respectively. Additionally, points with error bars indicate means and standard deviations for each model. All models closely follow the $\mathcal{W}_{\text{tot}} = P_{\text{mid}}$ line, except for models S2 and S3 which lie slightly below the line. The black arrows denote the shifts of the mean values in the abscissa when P_{mid} is changed to $P_{\text{mid}} - P_{\text{top}}$, indicating that P_{top} is significant ($\approx 0.4P_{\text{mid}}$) in models S2 and S3. After correcting for P_{top} , all models satisfy Equation (2.26), demonstrating that vertical dynamical equilibrium is maintained in an averaged sense.

Scaling relations of the gas weights

Figure 2.18 plots the time-averaged gas weights of all models against Σ_{ring} . For a plane-parallel slab with total gas surface density Σ_{ring} , $\mathcal{W}_{\text{gas}} \approx \pi G \Sigma_{\text{ring}}^2 / 2$; while this does not apply exactly given the ring geometry, a quadratic scaling is still expected. If the scale height of the gas disk is larger than that of young stars but smaller than that of old stars, the corresponding weights for horizontally uniform disks would be $\mathcal{W}_{\text{sp}} \approx \pi G \Sigma_{\text{ring}} \Sigma_{\text{sp}}$ and $\mathcal{W}_{\text{ext}} \approx \Sigma_{\text{ring}} \sigma_z (2G\rho_b/3)^{1/2}$, where Σ_{sp} is the surface density of the sink particles, ρ_b is the volume density of old stars in the bulge at the midplane, and a Gaussian vertical profile is assumed (Ostriker & Shetty 2011); again these can only be approximate given the ring geometry, bulge stratification, etc.

Assuming that the weights are proportional to Σ_{ring}^p with a power-law index p , simple linear fits to our results yield $p = 2.07$, 2.12 , and 1.19 for \mathcal{W}_{gas} , \mathcal{W}_{sp} , and \mathcal{W}_{ext} , respectively. These are broadly consistent with the above prediction, under the condition that Σ_{sp} is roughly proportional to Σ_{ring} and that σ_z depends on Σ_{ring} only weakly (from Figure 2.15).^{||} Although the gas disks in our models neither have a plane-parallel geometry nor are well described by a Gaussian vertical profile, deviations of each weight contributions measured using Equations (2.23)–(2.25) from analytical predictions are at most a factor of ~ 3 .

The total weight of the gas is dominated by \mathcal{W}_{ext} at low Σ_{ring} , while \mathcal{W}_{sp} also becomes significant at high Σ_{ring} . For all models, self-gravity has a relatively minor contribution to the total weight, different from the models of Ostriker & Shetty (2011) and Shetty & Ostriker (2012). There, the weight in the external potential was (by design) smaller than the weight of the gas, and the weight from star particles was not considered because it was implicitly assumed that the starburst had a sufficiently short duration that significant stellar mass did not build up

^{||}Since ρ_b is larger for the S series than the L series, \mathcal{W}_{ext} is offset upward for the former, as expected from $\mathcal{W}_{\text{ext}} \propto \Sigma_{\text{ring}} \sqrt{\rho_b}$. With a constant SFR, $\Sigma_{\text{sp}} \propto \Sigma_{\text{SFR}} t$. We shall show that from self-regulation, Σ_{SFR} varies approximately linearly in \mathcal{W}_{tot} , so for weight dominated by the external potential we expect $\Sigma_{\text{sp}} \propto \Sigma_{\text{ring}} t \sigma_z \sqrt{\rho_b}$, which would then yield $\mathcal{W}_{\text{sp}} \propto \Sigma_{\text{ring}}^2 t \sigma_z \sqrt{\rho_b}$.

(the present models show that this indeed requires hundreds of Myr). In the local simulations of Ostriker & Shetty (2011) and Shetty & Ostriker (2012), M_{gas} did not build up over time but was imposed from the initial conditions, so it could be large without also having M_{sp} large (unlike the case for the present models, per Figure 2.14). In the present simulations, the value of ρ_b in the ring region is relatively large, because nuclear rings form more easily in the presence of a strong central concentration (Athanassoula 1992; Regan & Teuben 2003; Li et al. 2015). We note that if the star formation efficiency within the sink particles is not 100%, only a fraction of \mathcal{W}_{sp} would be regarded as being self-gravitational. In creating a sink particle, we assume that all of the gas in a cell is immediately converted to a star cluster. In contrast, Tress et al. (2020) assumed only 5% of the sink particle mass actually represents the mass of the star cluster, while treating the remaining 95% as gas ‘temporarily stored’ in the sink particles which is later returned to the ambient ISM via SN feedback. We have adopted the current approach for simplicity, but in future work it would be quite interesting to test whether a treatment of sink particles with mass loss would change the results for the various scaling relations studied in this chapter.

Pressure Scaling Relations and the Feedback Yields

As expected, the pressures are directly correlated with the SFR per unit area. Figure 2.19 plots P_{th} and P_{turb} against Σ_{SFR} as points with error bars, corresponding to the mean values and standard deviations, respectively. Our best fits, including both the S and L series, are

$$\frac{P_{\text{th}}}{k_B} = 5.47 \times 10^5 \text{ cm}^{-3} \text{ K} \left(\frac{\Sigma_{\text{SFR}}}{M_{\odot} \text{ kpc}^{-2} \text{ yr}^{-1}} \right)^{0.64}, \quad (2.28)$$

$$\frac{P_{\text{turb}}}{k_B} = 7.56 \times 10^5 \text{ cm}^{-3} \text{ K} \left(\frac{\Sigma_{\text{SFR}}}{M_{\odot} \text{ kpc}^{-2} \text{ yr}^{-1}} \right)^{0.89}, \quad (2.29)$$

plotted as solid lines. The thermal pressure increases with Σ_{SFR} sublinearly because of the adopted FUV shielding that is stronger for models with higher \dot{M}_{in} .

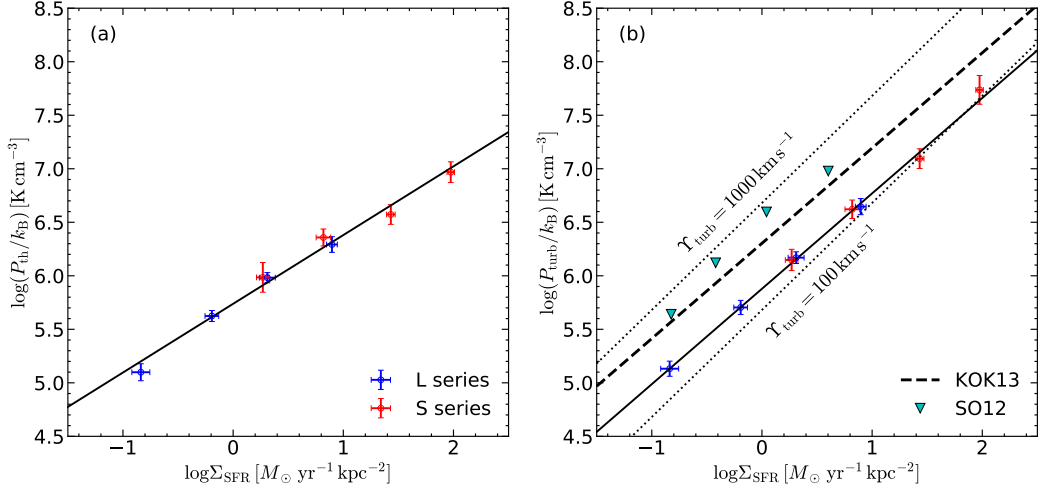


Figure 2.19. Mean (a) thermal and (b) turbulent pressure at the midplane, plotted against the mean SFR surface density within the ring, for each model (see also Table 2.3). The solid lines are the linear fits, Equations (2.28) and (2.29). In (b), cyan triangles are the results of Shetty & Ostriker (2012, Series S), while the dashed line is the extrapolation of Equation (21) from Kim et al. (2013). The two dotted lines correspond to $\Upsilon_{\text{turb}} = 100$ and 1000 km s^{-1} for reference.

The turbulent pressure driven by SN feedback is proportional almost linearly to Σ_{SFR} . As a result, the turbulent pressure dominates the thermal pressure for high Σ_{SFR} models, consistent with Ostriker & Shetty (2011). Figure 2.19 also shows, for comparison, results from simulations in Shetty & Ostriker (2012) modeling starburst regions, and the extrapolation of the relation $P_{\text{turb}}/k_B = 2.0 \times 10^6 \text{ cm}^{-3} \text{ K} (\Sigma_{\text{SFR}}/M_\odot \text{ kpc}^{-2} \text{ yr}^{-1})^{0.89}$ found by Kim et al. (2013) (see their Equation (21)) based on local simulations of normal star-forming galactic environments.

Equations (2.28) and (2.29) can be rewritten as

$$P_{\text{th}} = \Upsilon_{\text{th}} \Sigma_{\text{SFR}}, \quad (2.30)$$

$$P_{\text{turb}} = \Upsilon_{\text{turb}} \Sigma_{\text{SFR}}. \quad (2.31)$$

where Υ_{th} and Υ_{turb} are the thermal** and the turbulent feedback yields, respec-

**In our simulations, the thermal pressure mostly comes from hot bubbles created by SN feedback rather than FUV heating.

tively, given by

$$\Upsilon_{\text{th}} = 114 \text{ km s}^{-1} \left(\frac{\Sigma_{\text{SFR}}}{M_{\odot} \text{ kpc}^{-2} \text{ yr}^{-1}} \right)^{-0.36}, \quad (2.32)$$

$$\Upsilon_{\text{turb}} = 158 \text{ km s}^{-1} \left(\frac{\Sigma_{\text{SFR}}}{M_{\odot} \text{ kpc}^{-2} \text{ yr}^{-1}} \right)^{-0.11}. \quad (2.33)$$

The feedback *yield* for individual pressure terms was introduced by Kim et al. (2011a) (see their Equations (11) and (12)). There, and also in Kim et al. (2013) and Kim & Ostriker (2015a), the notation η was adopted for the ratio between P and Σ_{SFR} , adopting common astronomical units of $10^3 k_B \text{ cm}^{-3} \text{ K}$ for the former and $10^{-3} M_{\odot} \text{ kpc}^{-2} \text{ yr}^{-1}$ for the latter so that η is dimensionless. Since the ratio between P and Σ_{SFR} is naturally a velocity, we instead adopt units of kilometers per second for yields Υ . The conversion is $\Upsilon/\text{km s}^{-1} = 209\eta$. The turbulent yield in the present chapter is a factor of $\sim 2\text{--}3$ smaller than that of Shetty & Ostriker (2012) and the extrapolation of Kim et al. (2013), where the latter is $\Upsilon_{\text{turb}} = 420 \text{ km s}^{-1} (\Sigma_{\text{SFR}}/M_{\odot} \text{ kpc}^{-2} \text{ yr}^{-1})^{-0.1}$ (converting from their Equation (23) to the present units). For the set of TIGRESS simulations described in Kim et al. (2020a), Ostriker & Kim (2022) also finds $\Upsilon_{\text{turb}} \propto \Sigma_{\text{SFR}}^{-0.05}$, with a coefficient $\sim 70\%$ higher than in Equation (2.33). In Section 2.5.2, we will discuss possible causes for the lower Υ_{turb} in the present models and star-forming rings more generally.

Scaling Relations of the SFR

It is of much interest to determine what large-scale galactic properties provide the best prediction for the SFR. A simple correlation that has been extensively investigated empirically is the Kennicutt–Schmidt relation between gas and star formation surface densities (Schmidt 1959; Kennicutt 1998). Figure 2.20(a) plots

Σ_{SFR} against Σ_{ring} for all of our models. A linear fit to our models yields

$$\Sigma_{\text{SFR}} = 3.0 M_{\odot} \text{ yr}^{-1} \text{ kpc}^{-2} \left(\frac{\Sigma_{\text{ring}}}{10^2 M_{\odot} \text{ pc}^{-2}} \right)^{1.9}, \text{ for L series,} \quad (2.34\text{a})$$

$$\Sigma_{\text{SFR}} = 5.5 M_{\odot} \text{ yr}^{-1} \text{ kpc}^{-2} \left(\frac{\Sigma_{\text{ring}}}{10^2 M_{\odot} \text{ pc}^{-2}} \right)^{1.8}, \text{ for S series.} \quad (2.34\text{b})$$

While these have similar scalings with Σ_{ring} , the distinct offset between the relations for the two series makes plain that an additional parameter contributes in regulating Σ_{SFR} : surface density is not by itself sufficient.

In the theory of feedback-modulated, self-regulated star formation, the key large-scale parameter is not the gas surface density by itself, but the combination of gas and stellar parameters that go into defining the ISM weight \mathcal{W} , as described above. The individual components of pressure scale as power laws in Σ_{SFR} (the source of heat and turbulence), as shown in Figure 2.19, and the pressure balances the gas weight, as shown in Figure 2.17. Since turbulence dominates the pressure in galactic center environments and T_{turb} varies only weakly, we expect a nearly linear scaling of Σ_{SFR} with P_{mid} or \mathcal{W} , and this is indeed evident in Figures 2.20(b), and (c).

Quantitatively we find that both the L and S series follow a single relation

$$\Sigma_{\text{SFR}} = 0.71 M_{\odot} \text{ yr}^{-1} \text{ kpc}^{-2} \left(\frac{P_{\text{mid}}/k_B}{10^6 \text{ cm}^{-3} \text{ K}} \right)^{1.2}, \quad (2.35)$$

or

$$\Sigma_{\text{SFR}} = 0.75 M_{\odot} \text{ yr}^{-1} \text{ kpc}^{-2} \left(\frac{\mathcal{W}_{\text{tot}}/k_B}{10^6 \text{ cm}^{-3} \text{ K}} \right)^{1.3}, \quad (2.36)$$

which are plotted as dashed lines in Figure 2.20(b) and (c). For comparison, the extrapolation of Equation (26) from Kim et al. (2013) is $\Sigma_{\text{SFR}} = 0.48 M_{\odot} \text{ yr}^{-1} \text{ kpc}^{-2} (P_{\text{mid}}/10^6 \text{ cm}^{-3} k_B \text{ K})^{1.18}$, lower by a factor of ~ 1.5 . Similarly, the extrapolation of Equation (27) from Kim et al. (2013) is $\Sigma_{\text{SFR}} = 0.33 M_{\odot} \text{ yr}^{-1} \text{ kpc}^{-2} (\mathcal{W}_{\text{tot}}/10^6 \text{ cm}^{-3} k_B \text{ K})^{1.13}$, lower by a factor of ~ 2.3 . In local-disk TIGRESS simulations, the coefficients in the relations corresponding to Equations (2.35)–(2.36) are lower by factors

of 2.5–3 (Ostriker & Kim 2022). We discuss in Section 2.5.2 possible reasons for these offsets in $\Sigma_{\text{SFR}} - P_{\text{mid}}$ relations. The better agreement between **S** and **L** series in (b) and (c) than in (a) suggest that the $\Sigma_{\text{SFR}} - P_{\text{mid}}$ (or $\Sigma_{\text{SFR}} - \mathcal{W}_{\text{tot}}$) relation is more fundamental than the $\Sigma_{\text{SFR}} - \Sigma_{\text{ring}}$ relation for regulation of star formation in nuclear rings.

We can use the $\Sigma_{\text{SFR}} - P_{\text{mid}}$ relation together with our previous results for scalings to interpret dependences of Σ_{SFR} on Σ_{ring} . At the given Σ_{ring} , the **S** series shows enhanced Σ_{SFR} compared to the **L** series because of the stronger external gravity, which increases \mathcal{W}_{tot} . This in turn requires higher Σ_{SFR} to maintain a higher P_{mid} through feedback. However, the enhancement of Σ_{SFR} is only a factor of ~ 2 , despite a factor of 11 difference in $\rho_b(R_{\text{ring}})$. This is because stronger gravity and slightly lower σ_z makes the disk thinner in the **S** series (with $H \propto \sigma_z/\sqrt{\rho_b}$), leading to only a modest increase in the weight $\mathcal{W}_{\text{ext}} \propto \rho_b H \propto \sqrt{\rho_b} \sigma_z$ of the ISM for the given surface density. The difference in the external stellar potential is the main reason that the $\Sigma_{\text{SFR}} - \Sigma_{\text{ring}}$ relation is different between the **L** and **S** series.

As noted above, the three weight contributions are roughly given by $\mathcal{W}_{\text{gas}} \sim \pi G \Sigma_{\text{ring}}^2 / 2$, $\mathcal{W}_{\text{sp}} \sim \pi G \Sigma_{\text{ring}} \Sigma_{\text{sp}}$, and $\mathcal{W}_{\text{ext}} \sim \Sigma_{\text{ring}} \sigma_z (2G\rho_b/3)^{1/2}$. Although \mathcal{W}_{ext} is the largest among the three (except for the **S3** model), the contribution from \mathcal{W}_{sp} becomes quite significant as Σ_{ring} increases. Because of this (and since Σ_{sp} increases with Σ_{ring}), the total weight increases superlinearly with surface density (a fit gives $\mathcal{W}_{\text{tot}} \sim \Sigma_{\text{ring}}^{1.54}$). Meanwhile, Equation (2.35) indicates the total feedback yield $\Upsilon_{\text{tot}} \equiv P_{\text{mid}} / \Sigma_{\text{SFR}}$ decreases with Σ_{SFR} as $\Upsilon_{\text{tot}} = 277 \text{ km s}^{-1} (\Sigma_{\text{SFR}} / M_{\odot} \text{ yr}^{-1} \text{ kpc}^{-2})^{-0.17}$. These two effects act together to steepen the $\Sigma_{\text{SFR}} - \Sigma_{\text{ring}}$ relation via $\Sigma_{\text{SFR}} \propto \Upsilon_{\text{tot}}^{-1} \mathcal{W}_{\text{tot}} \propto \Sigma_{\text{ring}}^{1.86}$. Although the weight in our simulations is dominated by \mathcal{W}_{ext} and \mathcal{W}_{sp} rather than \mathcal{W}_{gas} , it happens that the dependence of Σ_{sp} on Σ_{ring} makes the $\Sigma_{\text{SFR}} - \Sigma_{\text{ring}}$ relation close to the self-gravity dominated case, as in Ostriker & Shetty (2011) and Shetty & Ostriker (2012).

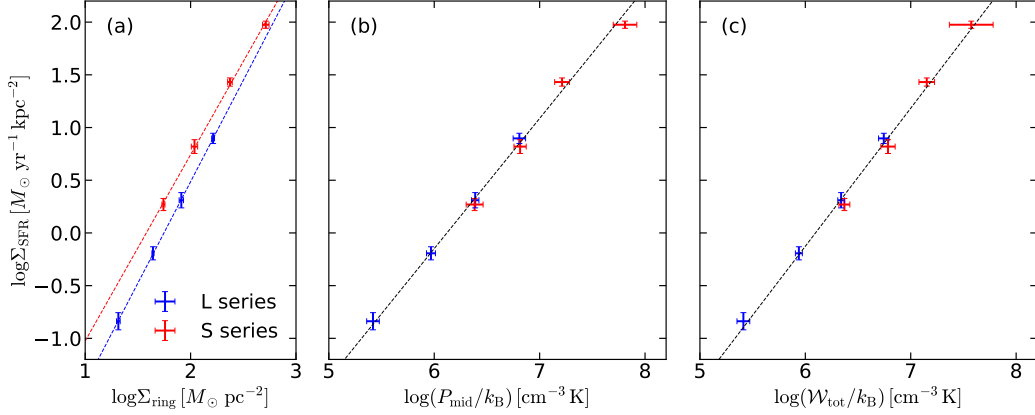


Figure 2.20. Dependence of the SFR surface density Σ_{SFR} on (a) the ring surface density Σ_{ring} , (b) the midplane pressure P_{mid} , and (c) the total gas weight \mathcal{W}_{tot} . The L and S series lie on different lines, Equation (2.34), in the $\Sigma_{\text{SFR}}-\Sigma_{\text{ring}}$ plane. In contrast, the two series follow the same relation, Equation (2.35), over nearly three orders of magnitude in the $\Sigma_{\text{SFR}}-P_{\text{mid}}$ or $\Sigma_{\text{SFR}}-\mathcal{W}_{\text{tot}}$ plane. The pressure (or weight) provides a better predictor for star formation than gas surface density alone because it allows for (varying) compression of the ISM by the stellar potential.

2.5 Summary and Discussion

2.5.1 Summary

Nuclear rings are the sites of compact and extremely vigorous star formation, powered by bar-driven inflows from the larger-scale ISM. Despite many observational and theoretical studies of nuclear rings, it has remained unclear what determines the gas ring’s properties and SFR, and how star formation in nuclear rings proceeds with time. To address these issues, we construct a semi-global model of a nuclear ring where the bar-driven mass inflows are treated by the boundary conditions. An advantage of our framework over fully global simulations is that it enables us to directly control the mass inflow rate and ring radius.

We have modified the TIGRESS framework (Kim & Ostriker 2017) for self-consistently simulating the star-forming ISM to make it suitable for galactic center regions with nonperiodic boundary conditions. As before, gravitational collapse leading to star formation and feedback utilizes sink particles that model star clus-

ters, which produce FUV heating and SN explosions. To account for the shielding of FUV radiation in high-density environments expected in nuclear rings, we make the FUV intensity decrease exponentially with local density (Equation 2.10). To balance cooling in these heavily shielded region, we include a simplified treatment of CR heating by ionization (Equation 2.11).

We have run two series of models that differ in the specific angular momentum of the inflow and therefore the resulting ring size R_{ring} : models in the **S** series have small rings with $R_{\text{ring}} = 150 \text{ pc}$ and models in the **L** series have large rings with $R_{\text{ring}} = 600 \text{ pc}$. While the gravitational potential profile is the same for the two series, the ring gas in the **S** series experiences stronger vertical compression than the **L** series because the vertical gravity is stronger closer to the galactic center. The initial gas distribution is near vacuum and the subsequent evolution is governed by the gas inflows through two nozzles located at the y -boundaries (Figure 2.3). In each series, we consider four models that differ in the mass inflow rate \dot{M}_{in} (Table 2.1). We run all models beyond $t = 300 \text{ Myr}$, long enough for the system to reach a quasi-steady state.

The main results of this chapter can be summarized as follows:

1. *Overall evolution:* Inflowing gas streams collide with each other after half an orbit, forming strong shocks at the contact points between the streams. As the orbital kinetic energy is lost, the gas streams gradually circularize to make a nuclear ring. Star formation soon becomes widely distributed along the whole length of the ring, and SN feedback produces hot gas that fills most of the volume. Within $\sim 100 \text{ Myr}$, the system reaches a quasi-steady state in which the gas properties and the SFR do not vary much with time.
2. *Star formation and feedback:* In the quasi-steady state, star formation occurs throughout the ring and the SFR exhibits only modest (within a factor of ~ 2) temporal fluctuations. For both the **L** and **S** series, the SFR is solely determined by the inflow rate as $\dot{M}_{\text{SF}} \approx 0.8 \dot{M}_{\text{in}}$. The ring gas mass $M_{\text{ring}} \propto \dot{M}_{\text{in}}^{0.6}$, with the rings in the **S** series about four times less massive than in the

L series. SN from clusters create many holes along the ring as superbubbles break out, but the feedback never destroys the entire ring. As the star particles diffuse out of the ring, SN from relatively old clusters can occur outside of the ring, dumping most of their energy in the ambient hot medium rather than the ring gas. Because SN feedback is *wasted* outside of the ring gas, a higher SFR is required to maintain equilibrium than would be needed if the gas and SNe were cospatial in a more uniform disk.

3. *Winds:* Our models naturally develop biconical, helically outflowing winds due to SN feedback (Figure 2.8). The opening up of the gas streamlines allows the winds accelerate from subsonic to supersonic velocities, readily reaching $\sim 600\text{--}900 \text{ km s}^{-1}$ at $z = 1 \text{ kpc}$, with the largest velocity occurring near the symmetry axis ($R = 0$).
4. *Ring properties:* Most of the mass is in cold-warm gas, with pressure and density close to the thermal equilibrium curve in which radiative cooling is balanced by FUV and CR heating. Dissipation of kinetic energy is also a significant heating source for the cold-unstable phase with $T < 5050 \text{ K}$. The mean sound speed of the cold-warm gas is only $\sim 3\text{--}4 \text{ km s}^{-1}$ (Table 2.2), much lower than the turbulent velocity dispersion $\sigma_z \sim (10\text{--}25) \text{ km s}^{-1}$, which mildly increases with Σ_{SFR} (Figure 2.15). The scale height increases monotonically with Σ_{SFR} due to an increase in σ_z in the L series, while it is roughly constant or decreases for high Σ_{SFR} due to the increased gravity of star particles in the S series. Rings are more eccentric for models with larger \dot{M}_{in} and/or smaller R_{ring} . Gas in these models tends to have shorter t_{dep} , and is thus rapidly depleted by star formation before the orbits can be fully circularized. In eccentric gas rings, the orbits of young star particles also inherit large eccentricities. Due to the precession of orbits, however, the distribution of old star particles is more or less circular, regardless of the ring shape.

5. *Vertical dynamical equilibrium:* The ISM in the nuclear rings satisfies vertical dynamical equilibrium, in which the total pressure (turbulent exceeding thermal) balances the weight of the gas. The pressure at the z -boundaries is non-negligible in models with strong outflows and small vertical extent (Figure 2.17). For the parameters of our models, the weight is dominated mostly by the external gravity term, with the gravity of the newly created sink particles making a secondary contribution. Because the gas is consumed rapidly, the self-gravity term does not become large. Scalings of \mathcal{W}_{ext} , \mathcal{W}_{sp} , and \mathcal{W}_{gas} with the gas surface density in the ring, Σ_{ring} , are consistent with expectations.
6. *Scaling relations for pressure and star formation:* Consistent with expectations for driving by momentum injection from SNe, the turbulent pressure varies nearly linearly with the SFR surface density (Equation 2.29). The corresponding turbulent yield Υ_{turb} (Equation 2.33) is a factor of $\sim 2\text{--}3$ smaller than the values in local-box simulations; this reduced efficiency may be due to feedback that is *lost* when SNe go off outside of the ring. The combination of vertical dynamical equilibrium with the $P_{\text{turb}}\text{--}\Sigma_{\text{SFR}}$ relation leads to a nearly linear dependence of Σ_{SFR} on P_{mid} (or the total weight \mathcal{W}_{tot}), given by Equation (2.35) (or (2.36)). Both the **S** and **L** series lie along a single relation. The power is the same as found by Kim et al. (2013), while the coefficient is a factor of $\sim 1.5\text{--}2.3$ higher due to the reduced feedback efficiency. For the individual **S** and **L** series, there are power-law relationships between Σ_{SFR} and Σ_{ring} with slopes between 1 and 2, consistent with expectations for scalings intermediate between $\Sigma_{\text{SFR}} \propto \mathcal{W}_{\text{ext}} \propto \Sigma_{\text{ring}}$ and $\Sigma_{\text{SFR}} \propto \mathcal{W}_{\text{sp}} + \mathcal{W}_{\text{gas}} \propto \Sigma_{\text{ring}}^2$. However, the **S** series is offset to higher Σ_{SFR} than the **L** series due to the stronger vertical gravity of the bulge at the locations of the smaller rings. Importantly, we conclude that the $\Sigma_{\text{SFR}}\text{--}P_{\text{mid}}$ (or \mathcal{W}_{tot}) relation is more general (as well as more physically fundamental) than the $\Sigma_{\text{SFR}}\text{--}\Sigma_{\text{ring}}$ relation. The pressure relation provides a better predictor for star formation because

it explicitly allows for variations in the vertical compression of the ISM by stellar gravity, which differ with environment even within a given galactic center region.

2.5.2 Discussion

Inflows and star formation: Our results show that the ring SFR, \dot{M}_{SF} , is controlled primarily by the mass inflow rate \dot{M}_{in} rather than the ring mass. This is overall consistent with the numerical results that the ring SFR is, when averaged over a few 100 Myr, roughly equal to the mass inflow rate to the ring in global simulations of barred galaxies (Seo & Kim 2013, 2014; Seo et al. 2019), suggesting that observed star formation histories in nuclear rings (e.g., Allard et al. 2006; Sarzi et al. 2007; Gadotti et al. 2019) may primarily reflect the time variations in the mass inflow rates. The strong correlation between \dot{M}_{SF} and \dot{M}_{in} is a direct (and causal) consequence of the mass conservation: in our models, 80% of the inflowing gas is consumed by star formation, while the remaining 20% is ejected as galactic winds. While \dot{M}_{SF} and M_{ring} , or Σ_{SFR} and Σ_{ring} , are also correlated, this relationship is more indirect, depending on environmental parameters such as the external gravity and on the feedback strength (see Section 2.4.2). In fact, given that \dot{M}_{SF} appears to be causally determined by \dot{M}_{in} , M_{ring} may be considered as *responding* to the inflow rate. That is, $M_{\text{ring}} \sim t_{\text{dep}} \dot{M}_{\text{in}}$, where in some circumstances the depletion time is relatively insensitive to the ring properties and depends primarily on the bulge potential (see below).

In our semi-global simulations, \dot{M}_{in} is fixed to a constant value and the resulting \dot{M}_{SF} and t_{dep} do not change appreciably with time (see discussion of t_{dep} below). Our simulations do not have the boom/bust behavior of other models (e.g., Kruijssen et al. 2014; Krumholz et al. 2017; Torrey et al. 2017; Armillotta et al. 2019) because star formation is distributed throughout the ring and the associated feedback is never strong enough to disperse the ring or make it quiescent as a whole. The recent global simulations of Sormani et al. (2020b) also found that

the depletion time in the CMZ is roughly constant, with the SFR varying linearly with the CMZ mass, which is most likely affected by the mass inflow rate.

Our models employ a steady and symmetric injection of gas streams from two nozzles. The simple, symmetric inflow we impose is intentionally idealized, since this is our first study of nuclear star formation with a new numerical framework. The inflow results in the formation of nuclear rings over which gas and star particles are roughly uniformly distributed. A visual inspection of the nuclear rings in 78 barred galaxies presented by Comerón et al. (2010) shows that rings with symmetric star formation are more common than those with lopsided star formation.^{††} Nevertheless, there are notable examples of lopsided nuclear rings, including our own CMZ (e.g., Henshaw et al. 2016; Barnes et al. 2017) and the ring in M83 (e.g., Harris et al. 2001). Asymmetric star formation in such rings may be caused by the mass inflow rates that are highly asymmetric and nonsteady (e.g., Harada et al. 2019). Large-scale simulations (e.g. Armillotta et al. 2019; Seo et al. 2019; Tress et al. 2020) with time-varying, asymmetric inflows, as well as observations (e.g., Sormani & Barnes 2019) motivate further study of lopsided ring formation at high resolution. We will address this issue in Chapter 3.

Feedback yield: The turbulent yield (Equation 2.33) in our simulations is smaller than the value in the previous simulations with SN feedback of Shetty & Ostriker (2012) and Kim et al. (2013). Considering the balance between the turbulent driving and dissipation, Ostriker & Shetty (2011) showed that the turbulent yield is given by $\Upsilon_{\text{turb}} = f_p p_*/(4m_*)$, where p_* is the asymptotic radial momentum injected per SN and m_* is the total mass in stars per SN ($m_* \approx 100 M_\odot$ for a Kroupa IMF). The parameter f_p encapsulates details of the driving and dissipation and is expected to be $f_p \sim 0.5\text{--}2$, with tests showing $f_p \approx 1$ for a range of parameters, and a slight decreasing trend toward higher SFR (Kim et al. 2011a, 2013; Ostriker & Shetty 2011; Shetty & Ostriker 2012). Kim et al. (2013) and Kim & Ostriker (2015a) (including magnetic fields) adopted $p_* = 3 \times 10^5 M_\odot \text{ km s}^{-1}$ as a fiducial

^{††}Color composite images of 16 symmetric rings among the sample are available in Ma et al. (2018).

value (based on isolated SNe in uniform gas), and found $\Upsilon_{\text{turb}} \sim 700\text{--}900 \text{ km s}^{-1}$ for solar neighborhood conditions (irrespective of magnetic field strengths; see Kim & Ostriker 2015a), decreasing to $\Upsilon_{\text{turb}} \sim 500 \text{ km s}^{-1}$ for a factor of ~ 20 higher SFR. In a local-disk TIGRESS suite (Kim et al. 2020a; Ostriker & Kim 2022), exploring more extreme conditions up to $\Sigma_{\text{SFR}} \sim 1 M_{\odot} \text{ yr}^{-1} \text{ kpc}^{-2}$, Υ_{turb} further decreases to $\sim 270 \text{ km s}^{-1}$, which is about $\sim 36\%$ lower than an extrapolation from Kim et al. (2013) and 70% larger than what we found in this chapter (Equation 2.33).

It should be noted that $\sim 80\text{--}90\%$ of all SNe in our simulations are resolved so that, as in the local-disk TIGRESS suite, p_* is determined self-consistently via nonlinear gas interactions. Assuming $f_p = 1$, Equation (2.33) translates to $p_* \sim 0.4\text{--}0.8 \times 10^5 M_{\odot} \text{ km s}^{-1}$. This is a factor of ~ 5 lower than what was found for isolated SNe at densities comparable to solar neighborhood ISM, but closer to the momentum injection in high-density environments (e.g. Kim & Ostriker 2015b; Martizzi et al. 2015), and also quite comparable to results from experiments in which multiple SNe explode at short ($\sim 0.01 \text{ Myr}$) intervals for a range of ambient density (Kim et al. 2017a). This could explain the generally smaller turbulent feedback yield in simulations using the full TIGRESS framework (Kim et al. 2020a,c, and this chapter) than the idealized simulations with a fixed p_* (Shetty & Ostriker 2012; Kim et al. 2013; Kim & Ostriker 2015a).

In the present simulations, an additional effect comes into play to reduce p_* : many SNe explode slightly exterior to the ring or close to the ring boundary, dumping their energy into the ambient hot gas and bulk motions of the ring instead of driving internal turbulence within the ring. This could be the primary reason for the smaller turbulent yield in our simulations compared to TIGRESS simulations where the momentum is more fully captured by the surrounding cold–warm gas. Additionally, when SNe are very crowded, partial cancellation of the vertical momenta due to interactions of neighboring shells could also contribute to reducing Υ_{turb} . All of these considerations explain why SN feedback is somewhat less efficient in driving turbulence within star-forming nuclear ring regions compared to

outer disk environments.

Depletion time: The depletion time measured in our simulations, $t_{\text{dep,ring}} \sim 10\text{--}100 \text{ Myr}$, is very short compared to the solar neighborhood TIGRESS model ($\sim 2 \text{ Gyr}$; Kim & Ostriker 2017), although analogous TIGRESS simulations modeling regions with higher gas and stellar density – closer to those of the present models – have $t_{\text{dep}} \sim 70\text{--}400 \text{ Myr}$ (Kim et al. 2020a). If star formation is locally regulated by stellar feedback (including SNe), the depletion time is determined by balancing the ISM weight $\mathcal{W} = (\Sigma/2) \langle g_z \rangle$ and the midplane pressure $P_{\text{mid}} \equiv \Upsilon_{\text{tot}} \Sigma_{\text{SFR}} \equiv \Upsilon_{\text{tot}} \Sigma / t_{\text{dep}}$, such that $t_{\text{dep}} = 2\Upsilon_{\text{tot}} / \langle g_z \rangle$. Here, Σ is the local gas surface density (equivalent to Σ_{ring} for the present case), $\langle g_z \rangle$ denotes the mass-weighted vertical gravity, and Υ_{tot} is the total feedback yield. The analysis given in Section 2.4.2 suggests that the short t_{dep} of the present simulations results from the combined effect of reduced Υ_{tot} (see above) and strong $\langle g_z \rangle$, with the latter being more important. Similar to our results, Sormani et al. (2020b) found from analysis of their simulations that the decrease in the CMZ $t_{\text{dep}} \sim 100 \text{ Myr}$ compared to the outer region $t_{\text{dep}} \sim (1\text{--}2) \text{ Gyr}$ was consistent with expectations from self-regulation, with $\langle g_z \rangle$ dominated by the stellar potential. The small depletion time in our galactic center simulations together with the result that the gravitational field is dominated by the stellar component (including newly formed stars) appears qualitatively consistent with Utomo et al. (2017). They found that $\sim 30\%$ of the Extragalactic Database for Galaxy Evolution (EDGE) galaxy sample have a central drop in t_{dep} , and that the drop in t_{dep} is correlated with a central increase in stellar surface density.

Our depletion time is still much shorter than observational values of $10^2\text{--}10^3 \text{ Myr}$ for most galactic centers and starburst galaxies, although observed values can be as short as $3\text{--}10 \text{ Myr}$ in regions of extremely high surface density (Kennicutt 1998; Bigiel et al. 2008; Genzel et al. 2010; Narayanan et al. 2012; Utomo et al. 2017; Wilson et al. 2019). Also, observations using the DYnamics of Newly-Assembled Massive Objects (DYNAMO) sample – local analogs of clumpy, high

redshift ($z \sim 1\text{--}2$) galaxies – have suggested there may be superlinear pressure enhancement in regions with high Σ_{SFR} (Fisher et al. 2019), although these regions are not well resolved spatially, and the trend is moderated when molecular gas (instead of ionized gas) velocity dispersions are used to estimate the ISM weight (Girard et al. 2021). Molina et al. (2020) find an upper limit on pressure slightly above the prediction of Equation (2.33). While higher-resolution observations are essential (and improved estimates of the stellar gravity are needed), current empirical work indicates that our models for star formation and feedback cannot fully explain real galaxies at high SFRs.

Several physical elements not yet included in the present models may explain the lower t_{dep} than in real galaxies. First, our current models only include FUV and CR heating and Type II SNe, while neglecting magnetic fields, CR pressure, and forms of early feedback (see below). All of these contribute to support and/or dispersal of the large-scale ISM and/or individual clouds, and thus may help to lengthen the depletion time (e.g., Hennebelle & Iffrig 2014; Kim & Ostriker 2015a; Girichidis et al. 2016; Kim et al. 2020a, 2021a, 2020c). For instance, typical magnetic fields in nuclear rings are of order $\sim 60 \mu\text{G}$ (see Beck 2015, and references therein). The corresponding magnetic pressure is $P_{\text{mag}}/k_{\text{B}} \sim 1 \times 10^6 \text{ K cm}^{-3}$, which can be dynamically significant. We will investigate effects of magnetic fields in Chapter 4.

Second, since we do not model the destruction of star clusters, the old, massive sink particles remain concentrated at the midplane, increasing \mathcal{W}_{sp} and $\langle g_z \rangle$ and thus reducing t_{dep} . In reality, however, they are expected to be disrupted and dispersed both radially and vertically by cluster-cluster collisions and/or the tidal gravity (e.g., Portegies Zwart et al. 2002; de Grijs & Anders 2012; Väisänen et al. 2014), reducing Σ_{sp} and increasing t_{dep} .

Third, in this chapter we do not model early feedback such as stellar winds, photoionization, and radiation pressure from young stars, which can disperse natal clouds even before the onset of the first SNe, limiting their lifetime star formation efficiency (e.g., Rogers & Pittard 2013; Rahner et al. 2017; Kim et al. 2018b,

2021a). Rather than our simple model of 100% star formation efficiency when sink particles form, a more realistic treatment would include significant mass return over several Myr. Since the total momentum injection from early feedback is low compared to the injection from SNe (Kim et al. 2018b; Lancaster et al. 2021a,b), these processes are not likely to alter large-scale SFRs in outer-galaxy environments where dynamical times within clouds are several Myr. However, early feedback is potentially quite important in denser galactic center environments.

Finally, we remark that inclusion of these physical elements may lead to stronger and/or more localized star formation and ensuing feedback. In this case, the rings may become more prone to local destruction, and the SFR and the depletion time may exhibit large temporal fluctuations, even if the mass inflow rate is kept constant. Assessing the relation between the ring SFR and the mass inflow rate would thus require more realistic treatments of star formation and feedback.

Chapter 3

Effects of Varying Mass Inflows on Star Formation in Nuclear Rings*

3.1 Overview

Nuclear rings at the centers of barred spiral galaxies are conspicuous in ultraviolet or H α , indicative of on-going massive star formation activity (Maoz et al. 1996; Benedict et al. 2002). The ring star formation rate (SFR) inferred from H α luminosity is in the range of 0.1–10 M_{\odot} yr $^{-1}$ (Mazzuca et al. 2008; Ma et al. 2018), which is high enough to produce pseudobulges with masses of 10 8 –10 10 M_{\odot} within 1 Gyr, provided that the ring is continuously supplied with fresh gas (Kormendy & Kennicutt 2004). Both observations and simulations indicate that in barred galaxies, gas falls into the nuclear ring through a pair of dust lanes located on the leading side of a bar (e.g., Athanassoula 1992; Benedict et al. 1996; Regan et al. 1997, 1999; Laine et al. 1999; Schinnerer et al. 2002; Kim et al. 2012b; Sormani et al. 2015a; Sormani & Barnes 2019; Shimizu et al. 2019). The mass inflow rates through the dust lanes

*A version of this chapter has been published as "Effects of Varying Mass Inflows on Star Formation in Nuclear Rings of Barred Galaxies", Moon, S., Kim, W.-T., Kim, C.-G., & Ostriker, E. C. 2022, *The Astrophysical Journal*, 925, 99

inferred by kinematic observations are $1\text{--}7 M_{\odot} \text{ yr}^{-1}$ (Benedict et al. 1996; Regan et al. 1997; Laine et al. 1999; Sormani & Barnes 2019; Shimizu et al. 2019), similar to the observed range of the ring SFR.[†]

Despite numerous studies mentioned above, it is still uncertain what controls star formation in nuclear rings. On the one hand, Kruijssen et al. (2014) (see also, Loose et al. 1982; Krugel & Tutukov 1993; Elmegreen 1994; Krumholz et al. 2017; Torrey et al. 2017) proposed that star formation in nuclear rings is strongly episodic. In this scenario, inflowing gas gradually piles up in a ring. When the ring becomes massive enough, it undergoes gravitational instability and this leads to an intense burst of star formation. The related strong stellar feedback quenches further star formation, rendering the ring quiescent until it once again becomes massive enough to become unstable. This cycle repeats, and the resulting ring SFR is episodic with periods of 20–40 Myr (Krumholz et al. 2017). On the other hand, global simulations of Seo & Kim (2013, 2014) and Seo et al. (2019) found that the SFR history in the nuclear ring is very similar to the history of the mass inflow rates through the bar, suggesting that the ring SFR is primarily determined by the inflow rate.

In global simulations of nuclear rings (e.g., Seo et al. 2019; Armillotta et al. 2019; Sormani et al. 2020b; Tress et al. 2020), the inflow rate is naturally time variable and feedback is always active following star formation, so that it is difficult to discern what dominates in shaping the star formation history of nuclear rings. To separate the effects of feedback from those of the mass inflow, in Chapter 2 we designed semi-global models that focus on nuclear rings and nearby regions, handling the bar-driven mass inflows along dust lanes by gas streams through two nozzles located at the domain boundaries. A key advantage of this semi-global framework is the ability to adjust the mass inflow rate as a free parameter. Based on simulations with the inflow rates kept constant in time, we found that the ring SFR is tightly correlated with the inflow rate and that the midplane pressure

[†]Hatchfield et al. (2021) showed that only $\sim 30\%$ of the inflowing gas along the dust lanes directly land on the ring, while the rest overshoots and accrete at later passages (see also, Regan et al. 1997), making the true accretion rate smaller by a factor of about 3 than the inferred rate.

powered by supernova (SN) feedback balances the weight of the overlying gas. In these simulations, SN feedback never destroys the rings completely and induces only modest (within a factor of ~ 2) temporal fluctuations of the SFR.

While the models considered in Chapter 2 are informative in understanding ring star formation for a constant inflow rate, the mass inflows in real barred galaxies result from dynamical interactions of gas with a stellar bar and are thus likely time variable. For example, Sormani & Barnes (2019) measured the density and velocity of the gas associated with the dust lanes of the Galactic bar and predicted that the mass inflow rate to the central molecular zone (CMZ), the nuclear ring in the Milky Way, should display a factor of few variations in the future ~ 12 Myr. Global numerical simulations (e.g., Seo et al. 2019; Armillotta et al. 2019; Tress et al. 2020) also found that the mass inflow rate varies by more than an order of magnitude over timescales of a few tens to hundreds of Myr, potentially responsible for the observed episodic star formation in nuclear rings (Allard et al. 2006; Sarzi et al. 2007; Gadotti et al. 2019; Prieto et al. 2019). To understand the history of the ring SFR, it is therefore desirable to run models with time-dependent mass inflow rates.

Another important issue regards lopsided star formation in nuclear rings. Although a majority of nuclear rings appear more or less symmetric in the distributions of star-forming regions, some rings show clear asymmetric star formation around their circumference (Comerón et al. 2010; Ma et al. 2018). Notable examples of asymmetric star formation include the CMZ (Bally et al. 1988; Henshaw et al. 2016) and the nuclear ring of M83 (Harris et al. 2001; Callanan et al. 2021), in which star formation is not uniformly distributed but concentrated roughly in a quarter-to-half portion of the ring. Possible causes for such asymmetry include a recent minor merger potentially responsible for an offset between the photometric and kinematic nucleus (e.g., Sakamoto et al. 2004; Knapen et al. 2010) and asymmetric mass inflow along the two dust lanes, the latter of which can readily be checked by direct numerical simulations using the framework presented in Chapter 2.

In this chapter, we extend Chapter 2 to investigate how time-varying and/or asymmetric inflow rates affect temporal and spatial variations of the ring SFR. We consider two series of models. In the first series, the inflow rate from two nozzles is symmetric but oscillates in time with period $\Delta\tau_{\text{in}}$. By running models with the same time-averaged rate but differing $\Delta\tau_{\text{in}}$, we study the relationship between $\Delta\tau_{\text{in}}$ and the time variations of the SFR. In the second series, the inflow rate of the two nozzles is forced to be asymmetric, either from the beginning or suddenly at a specified time. By comparing three representative cases of asymmetric inflows, we find conditions for lopsided star formation in nuclear rings.

The remainder of this chapter is organized as follows. In Section 3.2, we briefly describe our semi-global models and numerical methods to evolve the models subject to radiative heating and cooling, star formation, and SN feedback. In Section 3.3, we present the numerical results for the temporal and spatial distributions of star formation in nuclear rings. We summarize and discuss our results in Section 3.4.

3.2 Methods

In Chapter 2, the mass inflow rates through two nozzles were kept symmetric and constant with time. Here we study ring star formation when the mass inflow rate varies with time or becomes asymmetric. In this section, we briefly summarize the equations we solve and the treatment of star formation and feedback: we refer the reader to Chapter 2 for a complete description of our semi-global models of nuclear rings.

3.2.1 Equations

Our computational domain is a Cartesian cube with side $L = 2048$ pc surrounding a nuclear ring. We discretize the domain uniformly with 512^3 cells with grid spacing of $\Delta x = 4$ pc. The domain rotates at an angular frequency $\Omega_p = 36 \text{ km s}^{-1} \text{ kpc}^{-1} \hat{\mathbf{z}}$, representing the pattern speed of a bar. We use the **Athena** code (Stone et al. 2008)

to integrate the equations of hydrodynamics in the rotating frame, coupled with self-gravity, heating and cooling, star formation, and SN feedback. The governing equations we solve read

$$\frac{\partial \rho}{\partial t} + \nabla \cdot (\rho \mathbf{v}) = 0, \quad (3.1)$$

$$\frac{\partial(\rho \mathbf{v})}{\partial t} + \nabla \cdot (\rho \mathbf{v} \mathbf{v} + P \mathbb{I}) = -2\rho \boldsymbol{\Omega}_p \times \mathbf{v} - \rho \nabla \Phi_{\text{tot}}, \quad (3.2)$$

$$\begin{aligned} \frac{\partial}{\partial t} \left(\frac{1}{2} \rho v^2 + \frac{P}{\gamma - 1} \right) + \nabla \cdot \left[\left(\frac{1}{2} \rho v^2 + \frac{\gamma P}{\gamma - 1} \right) \mathbf{v} \right] \\ = -\rho \mathbf{v} \cdot \nabla \Phi_{\text{tot}} - n_{\text{H}}^2 \Lambda + n_{\text{H}} \Gamma_{\text{PE}} + n_{\text{H}} \Gamma_{\text{CR}}, \end{aligned} \quad (3.3)$$

where ρ is the gas density, \mathbf{v} is the gas velocity in the rotating frame, P is the gas pressure, \mathbb{I} is the identity matrix, $n_{\text{H}} = \rho/(1.4271 m_{\text{H}})$ is the hydrogen number density assuming the solar abundances, $n_{\text{H}}^2 \Lambda$ is the volumetric cooling rate, $n_{\text{H}} \Gamma_{\text{PE}}$ is the photoelectric heating rate, and $n_{\text{H}} \Gamma_{\text{CR}}$ is the heating rate by CR ionization. We assume that the cooling function Λ depends only on the gas temperature T , and adopt the forms suggested by Koyama & Inutsuka (2002) for $T < 10^{4.2}$ K and Sutherland & Dopita (1993) for $T > 10^{4.2}$ K.

The total gravitational potential $\Phi_{\text{tot}} = \Phi_{\text{cen}} + \Phi_{\text{ext}} + \Phi_{\text{self}}$ consists of the centrifugal potential $\Phi_{\text{cen}} = -\frac{1}{2}\Omega_p^2(x^2+y^2)$, the external gravitational potential Φ_{ext} giving rise to the background rotation curve, and the self-gravitational potential Φ_{self} that is related to ρ and the newly-formed star particle density ρ_{sp} via

$$\nabla^2 \Phi_{\text{self}} = 4\pi G(\rho + \rho_{\text{sp}}). \quad (3.4)$$

The background potential Φ_{ext} arises from the central supermassive black hole modeled by the Plummer sphere

$$\rho_{\text{BH}} = \frac{3M_{\text{BH}}}{4\pi r_{\text{BH}}^3} \left(1 + \frac{r^2}{r_{\text{BH}}^2} \right)^{-5/2} \quad (3.5)$$

with mass $M_{\text{BH}} = 1.4 \times 10^8 M_{\odot}$ and the softening radius $r_{\text{BH}} = 20$ pc, and a

spherical stellar bulge modeled by the modified Hubble profile

$$\rho_b(r) = \frac{\rho_{b0}}{(1 + r^2/r_b^2)^{3/2}} \quad (3.6)$$

with the central density $\rho_{b0} = 50 M_\odot \text{ pc}^{-3}$ and the scale radius $r_b = 250 \text{ pc}$. The total stellar mass enclosed within the nuclear ring is $M_b \equiv \int_0^{R_{\text{ring}}} 4\pi r^2 \rho_b(r) dr = 6.7 \times 10^9 M_\odot$, where $R_{\text{ring}} = 600 \text{ pc}$ is the ring radius[‡]. The rotation curve resulting from Φ_{ext} is similar to the observations of a prototypical nuclear-ring galaxy NGC 1097 (Onishi et al. 2015; see also Figure 2.1). With these parameters, the orbital period (in rotating frame) at R_{ring} is $t_{\text{orb}} = 18.4 \text{ Myr}$.

At each timestep, we check for all cells whether (1) $\rho > \rho_{\text{LP}}$, where we take the threshold $\rho_{\text{LP}} \equiv 8.86 c_s^2 / (G \Delta x^2)$ (for c_s the sound speed) as indicative of runaway gravitational collapse, based on evaluation of the Larson-Penston asymptotic profile at radius half of the grid spacing Δx , (2) Φ_{self} has a local minimum, and (3) the velocity is converging in all directions. If the above three conditions are met simultaneously in a given cell, we spawn a sink particle representing a star cluster and convert a portion of the gas mass in the surrounding 27 cells to the mass of the sink particle. The sink particles are allowed to accrete gas from their neighborhood until the onset of first SN explosion, which occurs at $t \sim 4 \text{ Myr}$ after creation. We track the trajectories of the sink particles using the Boris integrator (Boris 1970, see also Appendix A) which conserves the Jacobi integral very well.

Assuming that the sink particles fully sample the Kroupa (2001) initial mass function, we assign the FUV luminosities based on their mass and age using STARBURST99 (Leitherer et al. 1999). Treating the individual sink particles as sources of FUV radiation, we set the mean FUV intensity J_{FUV} based on radiation transfer in plane-parallel geometry, with an additional local attenuation in dense regions. We then scale the photoelectric heating rate Γ_{PE} in proportion to J_{FUV} , while allowing for the metagalactic FUV background (a small contribution). The

[‡]In our semi-global models, the ring radius is set by the velocity (or, more precisely, the specific angular momentum) of the inflows, as indicated by Equation 2.12.

heating rate Γ_{CR} by CR ionization is taken to be proportional to the SFR averaged over a 40 Myr timescale, assuming that CRs are accelerated in SN remnants.

Sink particles with age $\sim 4\text{--}40$ Myr produce feedback representing type II SNe, with rates based on the tabulation in **STARBURST99**. The amount of the feedback energy or momentum depends on the gas density. If the gas density surrounding an SN is so low that the Sedov-Taylor stage is expected to be resolved, we inject the total energy $E_{\text{SN}} = 10^{51}$ erg, with 72% and 28% in thermal and kinetic forms, respectively. If the gas density is instead too high for the shell formation radius to be resolved, we inject the radial momentum of $p_* = 2.8 \times 10^5 M_{\odot} \text{ km s}^{-1} (n_{\text{H}}/\text{cm}^{-3})^{-0.17}$, corresponding to the terminal momentum injected by a single SN (Kim & Ostriker 2015b). Each SN also returns the ejecta mass of $M_{\text{ej}} = 10 M_{\odot}$ from a sink particle back to the gas. The reader is referred to Kim & Ostriker (2017) for the full description of the sink formation and SN feedback.

3.2.2 Models

In our semi-global models, the simulation domain is initially filled with rarefied gas with number density $n_{\text{H}} = 10^{-5} \exp[-|z|/(50 \text{ pc})] \text{ cm}^{-3}$ and temperature $T = 2 \times 10^4 \text{ K}$. Gas flows in to the domain through two nozzles located at the y -boundaries, mimicking bar-driven gas inflows along dust lanes. The mass inflow rate \dot{M}_{in} is controlled by varying the gas density inside the nozzles. Chapter 2 focused on the cases with constant \dot{M}_{in} over time. In this chapter we report on two additional suites of models to explore the effects of time variations and asymmetry in the mass inflow rates. Table 3.1 lists the models we consider.

In the first suite, we let the mass inflow rate vary sinusoidally with time in logarithmic scale as

$$\ln \left(\frac{\dot{M}_{\text{in}}}{M_{\odot} \text{ yr}^{-1}} \right) = A - B \cos \left(\frac{2\pi t}{\Delta\tau_{\text{in}}} \right), \quad (3.7)$$

where $\Delta\tau_{\text{in}}$ is the oscillation period. The dimensionless constants A and B param-

Table 3.1. Summary of all models

Model (1)	$\dot{M}_{\text{in},0}$ ($M_{\odot} \text{ yr}^{-1}$) (2)	$\mathcal{R}(\dot{M}_{\text{in}})$ (3)	$\Delta\tau_{\text{in}}$ (Myr) (4)	Remarks (5)
constant	0.5	1	∞	constant inflow rate; identical to model L1 of Chapter 2
P15	0.5	20	15	\dot{M}_{in} varying sinusoidally in time
P50	0.5	20	50	\dot{M}_{in} varying sinusoidally in time
P100	0.5	20	100	\dot{M}_{in} varying sinusoidally in time
asym	0.5	1	-	9 times higher inflow rate in the upper nozzle than the lower nozzle
off	$1.0 \rightarrow 0.5^{\text{a}}$	1^{c}	-	lower nozzle shut off after 150 Myr
boost	$0.1 \rightarrow 0.5^{\text{b}}$	1^{c}	-	inflow rate from the upper nozzle boosted after 150 Myr

Note. (1) Model name. (2) Time-averaged mass inflow rate. (3) and (4) Amplitude and period of the inflow rate variation, respectively. (5) Comments

^a $\dot{M}_{\text{in}} = 1 M_{\odot} \text{ yr}^{-1}$ and $0.5 M_{\odot} \text{ yr}^{-1}$ before and after $t = 150 \text{ Myr}$, respectively.

^b $\dot{M}_{\text{in}} = 0.1 M_{\odot} \text{ yr}^{-1}$ and $0.5 M_{\odot} \text{ yr}^{-1}$ before and after $t = 150 \text{ Myr}$, respectively.

^c The inflow rate of models off and boost is constant except for a discontinuous jump at $t = 150 \text{ Myr}$.

eterize the time-averaged inflow rate $\dot{M}_{\text{in},0} \equiv \int_0^{\Delta\tau_{\text{in}}} \dot{M}_{\text{in}} dt / \int_0^{\Delta\tau_{\text{in}}} dt$ and the oscillation amplitude $\mathcal{R}(\dot{M}_{\text{in}}) \equiv \max(\dot{M}_{\text{in}})/\min(\dot{M}_{\text{in}})$, such that $\dot{M}_{\text{in},0}/(M_\odot \text{ yr}^{-1}) = I_0(B)e^A$ and $\mathcal{R}(\dot{M}_{\text{in}}) = e^{2B}$, where I_0 is the zeroth-order modified Bessel function of the first kind. In the first suite, we fix $\dot{M}_{\text{in},0} = 0.5 M_\odot \text{ yr}^{-1}$ and $\mathcal{R}(\dot{M}_{\text{in}}) = 20$, corresponding to $A = -1.19$ and $B = 1.50$, and consider three models P15, P50, and P100 with $\Delta\tau_{\text{in}} = 15, 50$, and 100 Myr, respectively. We also include model **constant** with $\mathcal{R}(\dot{M}_{\text{in}}) = 1$ and $\Delta\tau_{\text{in}} = \infty$, which is identical to model L1 in Chapter 2. Note that $\dot{M}_{\text{in}}(t)$ denotes the total inflow rate through the two nozzles: the mass inflow rate from one nozzle is $\dot{M}_{\text{in}}(t)/2$ in the first suite.

In the second suite, we consider three models termed **asym**, **off**, and **boost** to investigate the effect of asymmetric inflows. In model **asym**, the mass inflow rates from the upper (at the positive y -boundary) and the lower (at the negative y -boundary) nozzles are $0.45 M_\odot \text{ yr}^{-1}$ and $0.05 M_\odot \text{ yr}^{-1}$, respectively, and do not vary in time throughout the simulation. The mass inflow rate in model **off** is initially $0.5 M_\odot \text{ yr}^{-1}$ from each nozzle, but the lower nozzle is abruptly turned off at $t = 150$ Myr, while the upper nozzle keeps supplying the gas with the same rate all the time. In model **boost**, the mass inflow rate from each nozzle is set to $0.05 M_\odot \text{ yr}^{-1}$ at early time, but the upper nozzle suddenly boosts the inflow rate to $0.45 M_\odot \text{ yr}^{-1}$ at $t = 150$ Myr, while the inflow rate from the lower nozzle is kept unchanged. Note that the total mass inflow rate for all three models in the second suite is $0.5 M_\odot \text{ yr}^{-1}$ after $t = 150$ Myr.

3.3 Results

In this section, we present the temporal histories of the SFR, gas mass, and depletion time, and examine the relation between the SFR and the inflow rate. We also present the results of the second suite of models with asymmetric inflows in terms of the spatial distributions of young clusters.

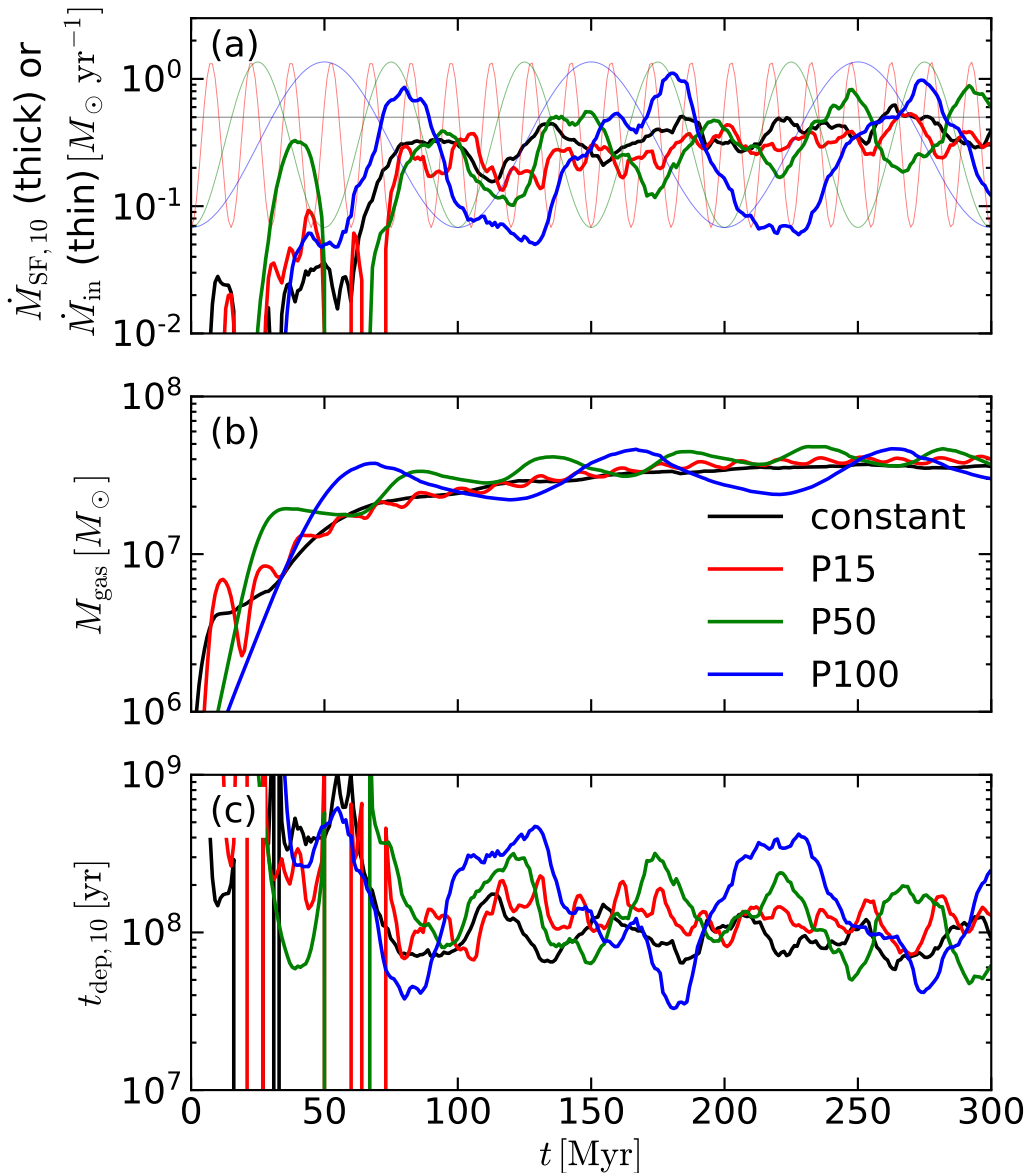


Figure 3.1. Temporal histories of (a) the SFR (thick) and the inflow rate (thin), (b) the total gas mass inside the computational domain, and (c) the gas depletion time for models **constant** (black), **P15** (red), **P50** (green), and **P100** (blue).

3.3.1 Time Variation of the SFR

We calculate the SFR using the sink particles that formed in the past 10 Myr as

$$\dot{M}_{\text{SF},10}(t) = \frac{M_{\text{sp}}(t) - M_{\text{sp}}(t - 10 \text{ Myr})}{10 \text{ Myr}}, \quad (3.8)$$

where $M_{\text{sp}}(t)$ is the total mass in the sink particles at time t . Figure 3.1 plots for models **constant**, P15, P50, and P100 the temporal histories of the SFR, the total gas mass M_{gas} in the computational domain, and the depletion time averaged over the past 10 Myr,

$$t_{\text{dep},10} \equiv M_{\text{gas}} / \dot{M}_{\text{SF},10}. \quad (3.9)$$

We note that a depletion time $t_{\text{dep},40}$ over 40 Myr (or other time) can be analogously defined. At early time, the gas streams from the nozzles collide with each other multiple times, increasing the SFR temporarily. A nuclear ring forms at $t \sim 100$ Myr, after which the evolution depends strongly on $\Delta\tau_{\text{in}}$. While models **constant** and P15 show weak fluctuations, the SFR in models P50 and P100 varies quasi-periodically with large amplitudes, even though the gas mass is almost the same. In all models with $\dot{M}_{\text{in},0} = 0.5 M_{\odot} \text{ yr}^{-1}$, the ring mass is $M_{\text{gas}} \sim 4 \times 10^7 M_{\odot}$, weakly varying with time, with peaks in the mass phase-delayed relative to the peak in \dot{M}_{in} . For quantitative comparison, we define the fluctuation amplitude \mathcal{R} by taking the ratio of the maximum to minimum values of $\dot{M}_{\text{SF},10}$, M_{gas} , and $t_{\text{dep},10}$ during $t = 200\text{--}300$ Myr. Table 3.2 gives $\mathcal{R}(\dot{M}_{\text{SF},10})$, $\mathcal{R}(M_{\text{gas}})$, and $\mathcal{R}(t_{\text{dep},10})$ for all the models.

Although the mass inflow rate for model **constant** is constant in time, its SFR shows random fluctuations with amplitude $\mathcal{R}(\dot{M}_{\text{SF},10}) = 2.4$, due to the turbulence driven by SN feedback, consistent with the results of Chapter 2. When the mass inflow rate oscillates with time, the fluctuation amplitudes increase with increasing $\Delta\tau_{\text{in}}$. In model P100, for instance, the SFR varies by a factor of 17 while the gas mass varies by a factor of 2, resulting in a factor of 10 variations of the depletion time. The fluctuations become smaller in model P50, with a factor of 5 variations

Table 3.2. Fluctuation amplitudes of $\dot{M}_{\text{SF},10}$, M_{gas} , and $t_{\text{dep},10}$

Model	$\mathcal{R}(\dot{M}_{\text{SF},10})$	$\mathcal{R}(M_{\text{gas}})$	$\mathcal{R}(t_{\text{dep},10})$
constant	2.4	1.1	2.3
P15	2.3	1.2	2.4
P50	5.4	1.3	5.2
P100	17	2.0	10
asym	2.3	1.1	2.4
off	2.5	1.1	2.8
boost	2.4	1.4	2.6

in the SFR and the depletion time. When the inflow rate oscillates very rapidly as in model P15, the fluctuation amplitudes are almost the same as those in model **constant**, as well as in the second suites of models **asym**, **off**, and **boost** in which the mass inflow rate is constant after $t = 150$ Myr.

3.3.2 Relation between the SFR and the Inflow Rate

Figure 3.1(a) shows that for models P100 and P50, the SFR varies coherently with the inflow rate with some time delay. To quantify the delay, we define the characteristic delay time t_{delay} as the time lag at which the cross-correlation between the SFR and the inflow rate is maximized, that is, $t_{\text{delay}} \equiv \text{argmax}_\tau (\dot{M}_{\text{SF},10} \star \dot{M}_{\text{in}})(\tau)$. Our numerical results correspond to $t_{\text{delay}} = 25$ Myr and $t_{\text{delay}} = 19$ Myr for models P100 and P50, respectively. Multiple effects contribute to the time delay. First, it takes approximately 3 Myr for the inflowing gas to travel from the nozzle to the ring located at R_{ring} . Second, our SFR measurement introduces some delay, approximately 4 Myr, because it counts all star formation events in the past 10 Myr. Subtracting the above two effects, the delay time for models P100 and P50 reduces to 18 Myr and 12 Myr, respectively. The resulting delay time can be interpreted as the timescale for the newly accreted gas first to enhance the overall mass in the ring, and then to produce local enhancements in the density above the (numerical)

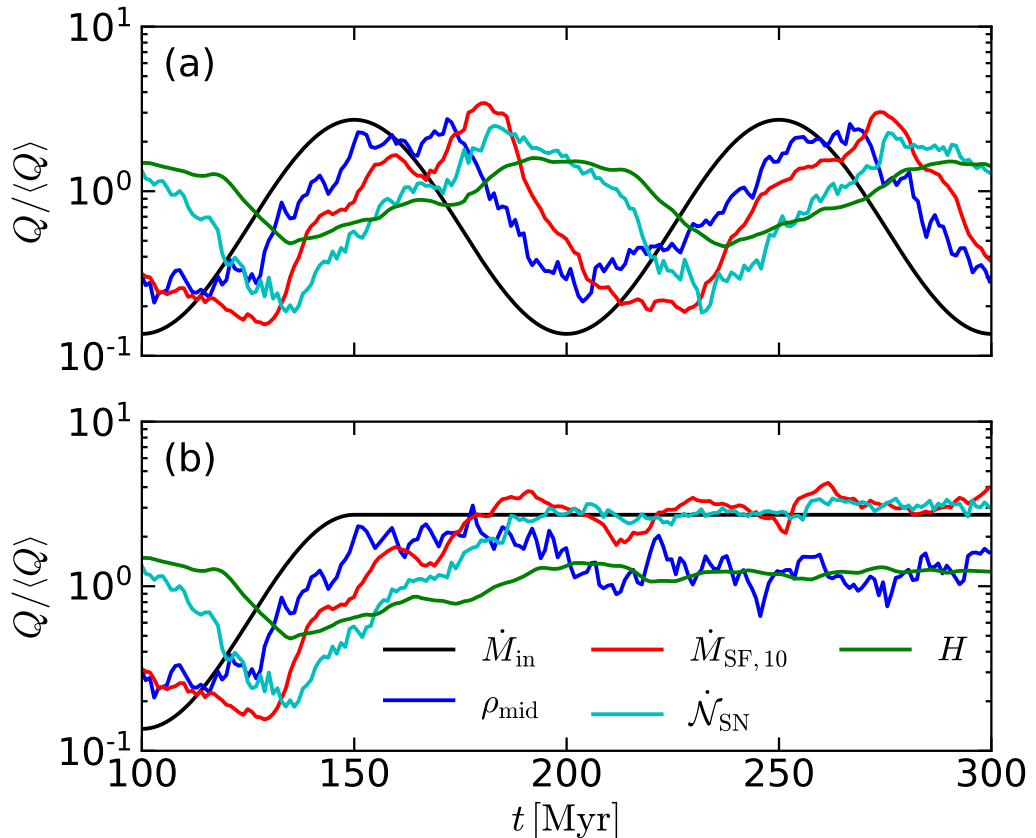


Figure 3.2. Time histories of the inflow rate (black), the mean midplane density of cold-warm gas with temperature $< 2 \times 10^4$ K (blue), the SFR (red), the rate of SN explosions (cyan), and the gas scale height (green) for model P100. Because the SN feedback is active for 4–40 Myr after the star formation, the SN rate lags behind the SFR. Panels (a) and (b) correspond, respectively, to model P100 and its restart experiment from $t = 150$ Myr, with \dot{M}_{in} fixed to the maximum rate (see text). All quantities are normalized by the time-averaged values between $t = 100$ – 300 Myr of model P100 for comparison.

threshold for star formation. We note, from Figure 3.1(*b*), that there are localized peaks in the ring gas mass that are earlier in phase by ~ 10 Myr relative to the peak in SFR for both models P100 and P50. This phase offset of the peak in M_{gas} is comparable to ~ 0.7 vertical oscillation periods associated with Φ_{ext} . This appears to be the minimum time required for an enhancement in the SFR to develop via stochastic processes such as turbulent compression and gravitational contraction.

Unlike in models P100 and P50, there is no apparent correlation between the SFR and the inflow rate in model P15. This is because the SFR fluctuations due to the time variations of \dot{M}_{in} are too weak to stand out against the feedback-driven fluctuations (see below).

To better understand what drives temporal variations of the SFR, Figure 3.2(*a*) plots for model P100 the temporal histories of the mass inflow rate, the mean mid-plane density ρ_{mid} of cold-warm gas with $T < 2 \times 10^4$ K, the SFR, the number of SN explosions per unit time $\dot{\mathcal{N}}_{\text{SN}}$, and the gas scale height $H \equiv (\int \rho z^2 dV / \int \rho dV)^{1/2}$. All the quantities are normalized by their respective time average over $t = 100$ –300 Myr. Overall, the time variations of \dot{M}_{in} lead to the changes in, sequentially, ρ_{mid} , SFR, $\dot{\mathcal{N}}_{\text{SN}}$, and H , with approximate delay times of 12, 25, 36, and 47 Myr, respectively. This makes sense since the mass inflows first enhance the ring density to promote star formation. The associated enhancement in SN feedback then inflates the ring vertically, increasing H . Both the mass inflows and feedback can affect the SFR by changing ρ_{mid} , with the latter being through H . All the quantities vary quasi-periodically with the dominant period of 100 Myr.

To examine whether the quasi-periodic cycles of the SFR are really driven by $\dot{M}_{\text{in}}(t)$ rather than the SN feedback, we restart model P100 from $t = 150$ Myr by fixing the inflow rate to $\max(\dot{M}_{\text{in}}) = 1.36 M_{\odot} \text{ yr}^{-1}$ thereafter, which we term model P100_*restart*. Figure 3.2(*b*) plots the resulting time histories of \dot{M}_{in} , ρ_{mid} , SFR, $\dot{\mathcal{N}}_{\text{SN}}$, and H of model P100_*restart*, normalized by the time-averaged values of model P100 for direct comparison. With fixed \dot{M}_{in} , the system reaches a quasi-steady state at $t \sim 200$ Myr in which the SFR and the other quantities do not

vary much with time. The short-term ($\lesssim 40$ Myr) fluctuations in the averaged quantities are due purely to turbulence driven by the SN feedback, which is active for 4–40 Myr after the star formation. The corresponding fluctuation amplitude in the SFR is $\mathcal{R}(\dot{M}_{\text{SF},10}) = 2.4$ in model `P100_restart`, which is 7 times smaller than that in model `P100`, but comparable to the fluctuation amplitude in model `constant`. This demonstrates that the large-amplitude, quasi-periodic variations of the SFR in model `P100` are caused by $\dot{M}_{\text{in}}(t)$, while the stochastic SN feedback is responsible for small-amplitude (a factor of ~ 2), short-term fluctuations of the SFR with timescale $\lesssim 40$ Myr. Of course, longer-term variations in the SN feedback rate *induced* by variations in the inflow rate and SFR are also dynamically important, as noted above (see also Section 3.3.3)

Figure 3.3 plots the histories of the various quantities for models `P50`, `P15`, `off`, and `boost`. Model `P50` behaves qualitatively similarly to model `P100`, in that the oscillating inflows drive long-term (~ 50 Myr), large-amplitude variations of the SFR, while short-term, small-amplitude fluctuations are due to the SN feedback. Note however that the oscillation amplitudes of the SFR decreases with decreasing $\Delta\tau_{\text{in}}$. This is because in our simulations about 80% of the inflowing gas turns to stars (see Chapter 2), so that neglecting the effect of the SN feedback changing the scale height, the SFR is roughly given by

$$\dot{M}_{\text{SF},10}(t) \approx \frac{0.8}{10 \text{ Myr}} \int_{t-t_{\text{delay}}-10 \text{ Myr}}^{t-t_{\text{delay}}} \dot{M}_{\text{in}}(t) dt, \quad (3.10)$$

where t_{delay} is the delay time between the mass inflow and star formation mentioned above. Since our SFR is proportional to the gas mass accreted over a 10 Myr interval, its amplitude should be an increasing function of $\Delta\tau_{\text{in}}$ even though the oscillation amplitude of \dot{M}_{in} is the same. Note that the averaging interval of 10 Myr is likely a lower limit, considering that the time taken for an inflowing gas parcel to turn into stars is not unique but distributed around t_{delay} . When $\Delta\tau_{\text{in}} \lesssim 10$ Myr, the effect of the temporal variations of \dot{M}_{in} on the SFR would be smoothed out almost completely. In addition, small-amplitude fluctuations of the SN feedback are

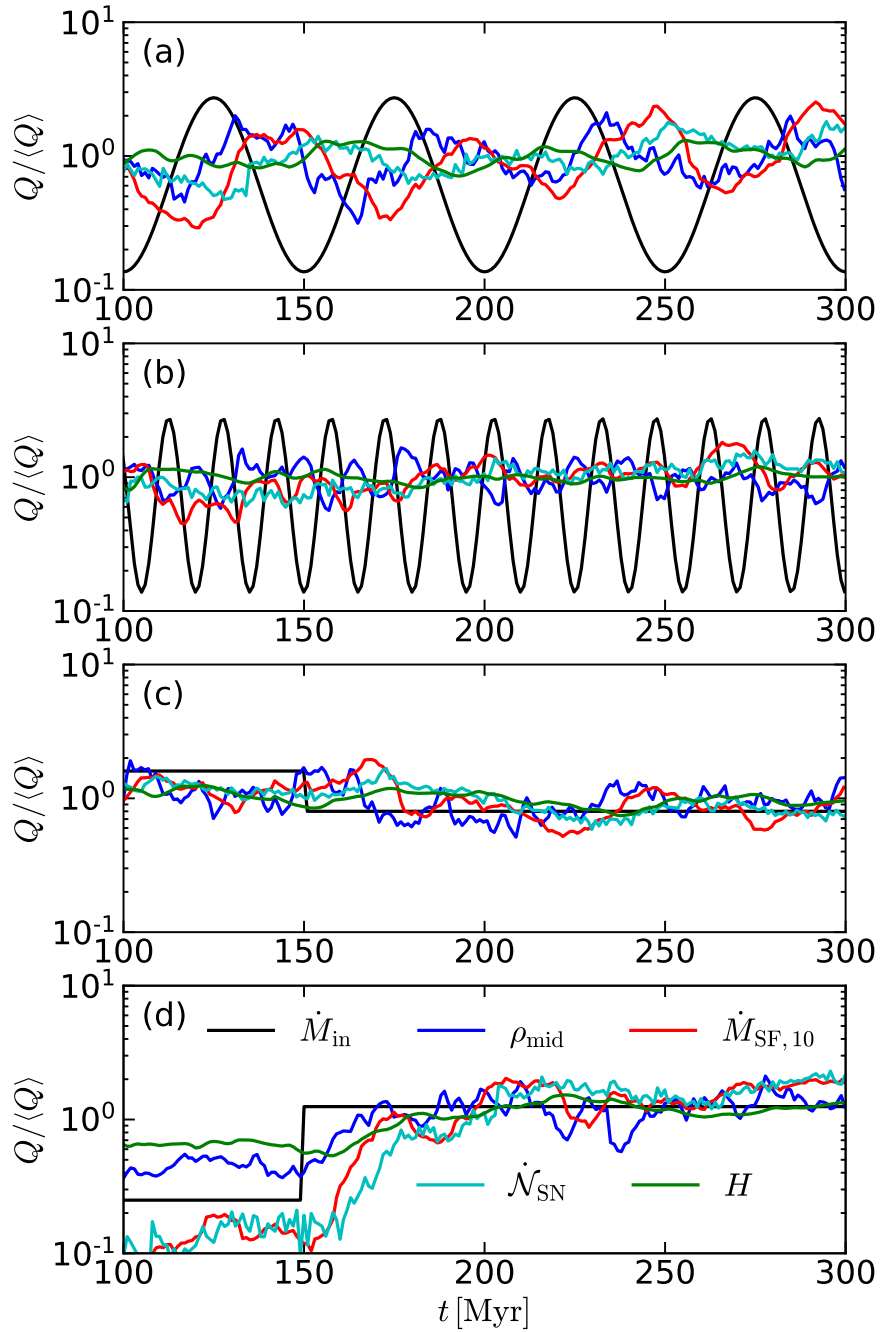


Figure 3.3. Similar to Figure 3.2, for models (a) P50, (b) P15, (c) off, and (d) boost.

present in all models, tending to reduce the effect of the time-varying inflow rate for small $\Delta\tau_{\text{in}}$. Considering the SN timescale of ~ 40 Myr (combined with the short vertical dynamical time in galactic center regions) it is very likely that the star formation can follow the variations imposed by the inflow when $\Delta\tau_{\text{in}} \gtrsim 40$ Myr, as is indeed seen in models P50 and P100. In model **off** or **boost**, where the inflow rate drops by a factor of 2 or increases by a factor of 5, respectively, at $t = 150$ Myr, the SFR decreases or increases by a similar factor and undergoes feedback-induced, small-amplitude fluctuations with $\mathcal{R}(\dot{M}_{\text{SF},10}) = 2.5$, similarly to that in model **constant**.

3.3.3 Self-regulation Theory

As Figure 3.1 shows, the gas depletion time in model P100 varies by about an order of magnitude, while the ring gas mass is almost constant. In this subsection, we shall show that this is consistent with the results of the self-regulated star formation theory (Ostriker et al. 2010; Ostriker & Shetty 2011) provided that the time delay between star formation and the ensuing SN feedback is properly considered (see Figure 3.2a).

According to the self-regulation theory, an (unmagnetized) disk in vertical dynamical equilibrium should obey

$$\begin{aligned} P_{\text{mid}} &\equiv \frac{1}{A_{\text{ring}}} \iint (P + \rho v_z^2) |_{z=0} dx dy \\ &= \mathcal{W} \equiv \frac{1}{2} \Sigma_{\text{gas}} \langle g_z \rangle, \end{aligned} \quad (3.11)$$

where P_{mid} is the total (thermal plus turbulent) midplane pressure averaged over the ring area A_{ring} (see below), \mathcal{W} is the weight of the overlying gas above or below the midplane, Σ_{gas} is the mean gas surface density within the ring area, and $\langle g_z \rangle$ is the density-weighted mean vertical gravity defined as

$$\langle g_z \rangle \equiv \frac{\iiint \rho g_z dx dy dz}{\iiint \rho dx dy dz}. \quad (3.12)$$

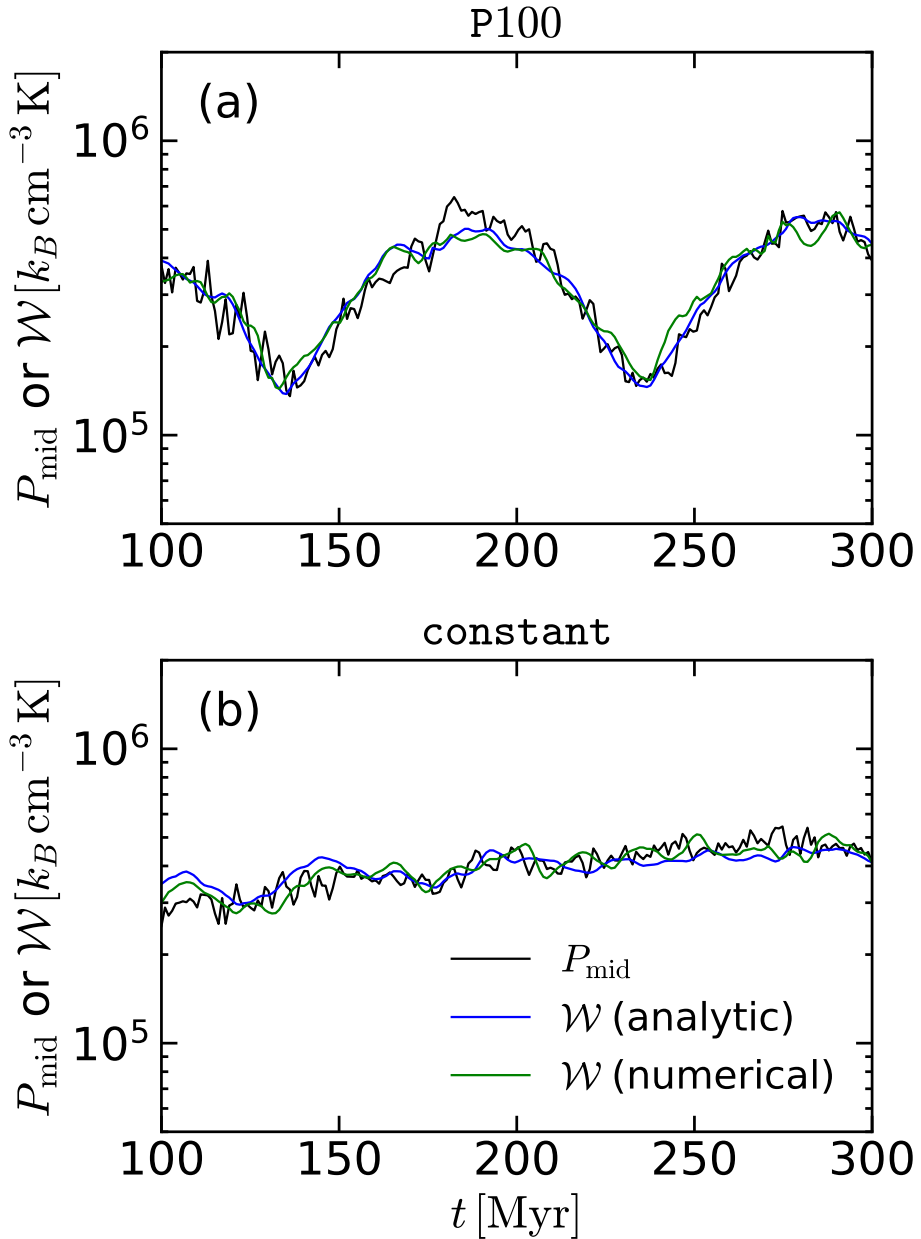


Figure 3.4. Temporal evolution of midplane pressure P_{mid} and gas weight \mathcal{W} for models (a) P100 and (b) constant. The blue and green lines correspond to the weights calculated by using the analytic and numerical $\langle g_z \rangle$, respectively (see text). In all epochs, $\mathcal{W} \approx P_{\text{mid}}$, indicating that the system is approximately in instantaneous vertical equilibrium.

Here, the integration is performed over the annular region between $R_{\min} = 400$ pc and $R_{\max} = 800$ pc, where $A_{\text{ring}} = \pi(R_{\max}^2 - R_{\min}^2)$, and over the upper (or lower) half of the computational domain in the vertical direction. Equation (3.11) assumes that the pressure above the gas layer is small compared to P_{mid} , i.e. $\Delta(P + \rho v_z^2) \approx P_{\text{mid}}$. When the gravitational potential is dominated by the stellar bulge (Equation 3.6), it can be shown that

$$\langle g_z \rangle = f \left(\frac{2}{\pi} \right)^{1/2} \frac{GM_b H}{R_{\text{ring}}^3}, \quad (3.13)$$

where f is a dimensionless parameter of order unity that depends on the spatial gas distribution: e.g., $f = 1$ for a thin ring with a Gaussian density distribution in the vertical direction. We find $f = 0.64$ and 0.72 for model P100 and **constant**. Figure 3.4 plots the relationship between P_{mid} and \mathcal{W} for models P100 and **constant**, showing that the two quantities agree with each other within $\sim 12\%$ and $\sim 8\%$, respectively: other models also show a good agreement between P_{mid} and \mathcal{W} . This demonstrates that the system maintains an instantaneous vertical equilibrium, while undergoing (quasi-periodic) long-term oscillations in response to changes in the inflow rate. We also note that the weights from the analytic (Equation 3.13) and numerically measured $\langle g_z \rangle$ (Equation 3.12) are practically the same, indicating that Equation (3.13) is a good approximation for the vertical gravitational field in our simulations.

The self-regulation theory further asserts that the midplane pressure is sustained by feedback. In the present case, SN feedback supplies both thermal (through hot bubbles) and turbulent pressures, although other forms of feedback or other pressure contributions (e.g., magnetic pressure) may be important more generally (Ostriker et al. 2010; Ostriker & Shetty 2011; Kim & Ostriker 2015a). Assuming that the midplane pressure is proportional to the SFR surface density $\Sigma_{\text{SFR}} \equiv \dot{M}_{\text{SF}}/A_{\text{ring}}$, one can write $P_{\text{mid}} = \Upsilon_{\text{tot}} \Sigma_{\text{SFR}}$, where Υ_{tot} is the total feedback yield (see Chapter 2; see also Kim et al. 2011a, 2013; Kim & Ostriker 2015a). We find $\Upsilon_{\text{tot}} = 340 \text{ km s}^{-1}$ from the time averaged P_{mid} and Σ_{SFR} for model P100

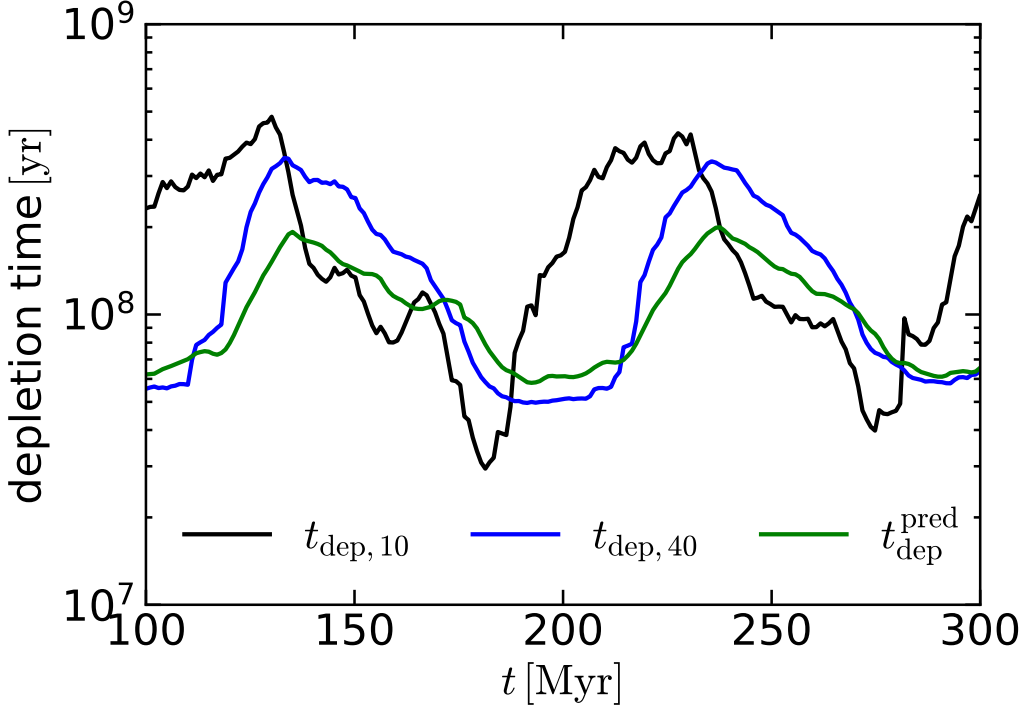


Figure 3.5. Comparison for model P100 of the measured depletion times averaged over 10 Myr ($t_{\text{dep},10}$, black) and 40 Myr ($t_{\text{dep},40}$, blue), together with the predicted depletion time (Equation 3.14, green). Note that $t_{\text{dep}}^{\text{pred}}$ follows $t_{\text{dep},40}$ quite well.

(with $\sim 2\%$ differences for other models). Identifying the pressure predicted from dynamical equilibrium (Equation 3.11) with the pressure predicted from star formation feedback then gives the prediction for the gas depletion time (Equation 3.9) as

$$t_{\text{dep}}^{\text{pred}} = \frac{2\Upsilon_{\text{tot}}}{\langle g_z \rangle} = \frac{(2\pi)^{1/2} R_{\text{ring}}^3 \Upsilon_{\text{tot}}}{f G M_b H}. \quad (3.14)$$

Figure 3.5 compares the measured $t_{\text{dep},10}$ and the predicted $t_{\text{dep}}^{\text{pred}}$ for model P100. Although $t_{\text{dep}}^{\text{pred}}$ oscillates in time in a similar fashion to the directly-measured $t_{\text{dep},10}$ as the ring repeatedly shrinks and expands vertically to change H , the amplitude and phase are not well matched.

The temporal offset between $t_{\text{dep},10}$ and $t_{\text{dep}}^{\text{pred}}$ implies that one has to consider the time delay between star formation and SN feedback: while $\dot{M}_{\text{SF},10}$ and $t_{\text{dep},10}$ only accounts for the stars formed in the past 10 Myr, the SN feedback that sustains

the midplane pressure also depends on previous star formation, occurring in star particles with age up to 40 Myr (Leitherer et al. 1999; Kim & Ostriker 2017). Since the scale height H (and P_{mid} , implicitly) in Equation (3.14) is responsive to SNe (Figure 3.2a), the corresponding predicted depletion time is sensitive to a longer-term average of the SFR. This motivates us to compare $t_{\text{dep}}^{\text{pred}}$ with the depletion time $t_{\text{dep},40}$ averaged over 40 Myr instead of $t_{\text{dep},10}$. Figure 3.5 shows $t_{\text{dep},40}$ agrees with $t_{\text{dep}}^{\text{pred}}$ much better than $t_{\text{dep},10}$, indicating that the self-regulation theory predicts the *time-varying* depletion time averaged over the timescale associated with the dominant feedback process, which is ~ 40 Myr for SNe in our current models. The slight mismatch in the amplitude is due to the secondary effect of time-varying Υ_{tot} , which we do not consider in this work. The phase offset and larger fluctuation of $t_{\text{dep},10}$ compared to $t_{\text{dep},40}$ is because the SN feedback is delayed behind $\dot{M}_{\text{SF},10}$. We note that Equation (3.11) implies $M_{\text{gas}} = \Sigma_{\text{gas}} A_{\text{ring}} \propto P_{\text{mid}} / \langle g_z \rangle \propto \dot{N}_{\text{SN}} / H$, which is roughly constant since H is correlated with \dot{N}_{SN} (see Figure 3.2a), in agreement with Figure 3.1(b)[§]. The above analyses suggest that the self-regulation theory is applicable even when the ring star formation is time-varying, as long as feedback time delays and appropriate temporal averaging windows are taken into account.

3.3.4 Spatial Distributions of Star Clusters

We now explore how asymmetry in the mass inflows affects the spatial distributions of star particles in the rings. Figure 3.6 plots the projected distributions in the x - y plane of gas and young star clusters with age younger than 10 Myr, for models **P100**, **asym**, **off**, and **boost** from left to right at four selected epochs from $t = 151$ Myr to 210 Myr. Note that the inflow rate in models **off** and **boost** changes abruptly at $t = 150$ Myr. In model **P100**, the fading gas streams over time manifest the continuous decrease of the inflow rate during this time span. The time-varying kinetic energy of the streams makes the ring more eccentric and promotes its precession. With the symmetric mass inflow rate in this model, young star clusters are distributed

[§]Since most of the gas in our simulations is contained in the ring region, M_{gas} agrees with $\Sigma_{\text{gas}} A_{\text{ring}}$ within $\sim 8\%$.

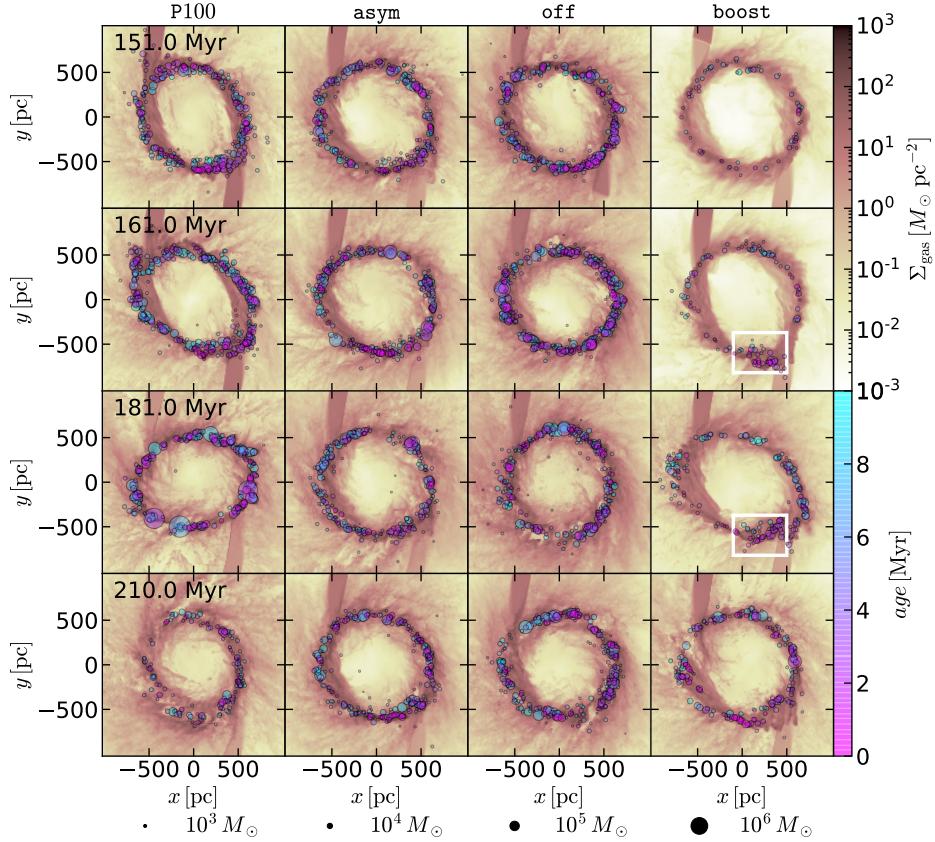


Figure 3.6. Spatial distributions of the gas surface density and star clusters younger than 10 Myr, with the color and size coded by their age and mass, respectively, projected on the x - y plane for various models. From left to right, each column corresponds to models P100, asym, off, and boost. From top to bottom, each row corresponds to the snapshots at $t = 151, 163, 183$, and 203 Myr. The white boxes in the two middle panels of model boost indicate the star forming regions triggered by the enhanced inflows from the top nozzle at $t = 150$ Myr.

more-or-less uniformly across the whole length of the ring.

The ring of model `asym` is more circular since the inflowing gas has constant kinetic energy. While the inflow rate from the upper nozzle is 9 times higher than that from the lower one in this model, star clusters with age $\lesssim 10$ Myr are still distributed almost uniformly throughout the ring, as in model P100. This is because the depletion time (~ 100 Myr) is longer than the ring orbital time (~ 20 Myr), allowing the gas from the upper and lower streams to be well mixed before turning into stars. The inflow rate in model `off` becomes asymmetric after $t = 150$ Myr, due to the cessation of the lower stream. Nevertheless, the continued inflow from the upper nozzle smoothly lands on the ring without causing large deformation of the ring. The distribution of star particles in model `off` is relatively symmetric despite the asymmetric inflow rate, similarly to model `asym`.

Unlike the other models, however, model `boost` shows lopsided distributions of star particles for a few tens of Myr after the boosted inflow, due mainly to the enhanced SFR in the lower part of the ring marked by the white boxes in the second and third rows of the last column in Figure 3.6. In this model, the boosted inflow from the upper nozzle has such large inertia that it is almost unhindered when it hits the ring at $(x, y) \sim (-500, 400)$ pc on a nearly ballistic orbit. The inflowing streams converge and collide with the ring at the opposite side, triggering star formation at $(x, y) \sim (0, -600)$ pc. This star formation, induced directly by the boosted inflow, makes the overall distribution of star particles lopsided. However, this phase of asymmetric star formation persists only for a few orbital periods as the ring gradually adjusts its shape and size corresponding to the boosted inflow. Gas from the boosted inflow then smoothly joins the ring at the near side and spreads along the ring over the depletion time, returning to distributed star formation again.

To quantify the degree of the lopsided star formation, we divide the ring into two parts by a straight line $y = \tan(\phi)x$, where ϕ is the position angle of the dividing line measured counterclockwise from the positive x -axis. We calculate the

Table 3.3. SFR asymmetry

Model	\mathcal{A}_{\max}	ϕ_0 (deg)
constant	1.2	112
P15	1.3	21
P50	1.5	175
P100	1.2	162
asym	1.8	167
off	1.6	142
boost	4.9	80

SFR separately in each part using the star particles with age younger than 10 Myr, and then average it over 21 snapshots taken from 161 to 181 Myr at 1 Myr interval. We define the asymmetry parameter $\mathcal{A}(\phi) (\geq 1)$ as the (higher-to-lower) ratio of the averaged SFRs from the two parts for a given ϕ . We then repeat the calculations by varying ϕ to find the maximum value $\mathcal{A}_{\max} = \max_{\phi} \mathcal{A}(\phi)$. Note that the position angle ϕ_0 corresponding to \mathcal{A}_{\max} differs for all models.

Table 3.3 lists the maximum asymmetry parameter \mathcal{A}_{\max} and the corresponding position angle ϕ_0 . Model **constant** has $\mathcal{A}_{\max} = 1.2$ due to the randomness of star-forming positions under the symmetric inflows. Models P15, P50, and P100 have similar or slightly higher \mathcal{A}_{\max} than model **constant** due probably to perturbations introduced by time variability of the inflow rate. Models **asym** and **off** have $\mathcal{A}_{\max} = 1.8$ and 1.6, respectively, which are higher than the asymmetry parameter of model **constant** but still quite small considering a large asymmetry in the inflow rate. In contrast, model **boost** has $\mathcal{A}_{\max} = 4.9$, that is, the boosted mass inflow from the upper nozzle makes the SFR in the lower right side of the dividing line with $\phi_0 = 80^\circ$ higher by a factor of about 5 than in the opposite side, which is caused by the new star clusters in the boxed regions in Figure 3.6. The similar asymmetry parameter for gas mass is almost unity for all models, because the newly accreted gas mass during one orbit $\dot{M}_{\text{in}} t_{\text{orb}}$ is smaller than the existing ring gas mass $\dot{M}_{\text{SF}} t_{\text{dep}} \approx$

$\dot{M}_{\text{in}} t_{\text{dep}}$, quickly spreading along the whole length of the ring within t_{orb} . Our results suggest that asymmetric inflows alone are unable to create lopsided star formation in the rings. Rather, asymmetry in the ring star formation in our models requires a large (and sudden) boost in the inflow rate from one nozzle.

3.4 Summary and Discussion

We perform semi-global numerical simulations of nuclear rings in which bar-driven mass inflows are represented by gas streams from two nozzles located at the domain boundaries. To focus on what drives temporal and spatial variations of the ring SFR, we consider two series of models: one with time-varying inflow rate and the other in which the mass inflow rates from the two nozzles are differentially set. Our simulations show both the mass inflow rate and SN feedback affect the ring SFR. The oscillating inflow rate with period $\Delta\tau_{\text{in}}$ induces large-amplitude, quasi-periodic (with period equal to $\Delta\tau_{\text{in}}$) variations of the SFR, with the delay time of $\sim 10\text{--}20$ Myr, when $\Delta\tau_{\text{in}} \gtrsim 50$ Myr. During the delay time, gas accreted to the ring undergoes turbulent compression and/or gravitational contraction to increase its density above the threshold for star formation.

Unlike the mass inflow rate, the SN feedback is stochastic and responsible only for small-amplitude, short-term fluctuations of the SFR, with timescale $\lesssim 40$ Myr (although the SN rate also varies in response to a convolution of the SFR and stellar evolution delay time). Since our standard definition of the SFR is proportional to the mass inflow rate averaged over a 10 Myr span, the effect of the inflow rate to the time variability of the SFR decreases with decreasing $\Delta\tau_{\text{in}}$. Together with the stochastic effect of SN feedback, this makes the SFR almost independent of \dot{M}_{in} for $\Delta\tau_{\text{in}} \lesssim 15$ Myr. Asymmetry in the inflow rates from the two ends of a bar does not necessarily lead to asymmetric star formation in nuclear rings. We find that ring star formation is lopsided only a few Myr after the inflow rate from one nozzle is suddenly boosted by a large factor. In what follows, we discuss our findings in comparison with observations.

Temporal variation of ring SFR: The stellar age distributions in nuclear rings inferred from optical absorption spectra indicate that the ring star formation is likely episodic, with approximately 100 Myr timescales, rather than continuous (Allard et al. 2006; Sarzi et al. 2007; Gadotti et al. 2019). It is uncertain what causes the observed variability of the ring star formation, yet existing theories and numerical simulations suggest that it is perhaps due to either SN feedback combined with fluid instabilities (Loose et al. 1982; Krugel & Tutukov 1993; Elmegreen 1994; Kruijssen et al. 2014; Krumholz et al. 2017; Torrey et al. 2017) or the mass inflow rate (Seo & Kim 2013, 2014; Seo et al. 2019) which is known to vary with time (Seo et al. 2019; Sormani & Barnes 2019; Armillotta et al. 2019; Tress et al. 2020). Our numerical experiments in the present chapter show that while both the SN feedback and the inflow rate can affect the ring SFR, only the latter can induce significant variations of the recent SFR with amplitude $\gtrsim 5$ over timescale $\gtrsim 50$ Myr. Since star formation is almost random and widely distributed along a ring in our simulations, the resulting feedback is local and stochastic, driving only modest (within a factor ~ 2) variations of the SFR (see also Chapter 2) on short timescales. Only if the local star formation events were temporally correlated throughout the ring would the resulting feedback simultaneously quench star formation and make the ring quiescent as a whole. Our results therefore suggest that the intermittent episodes of star formation separated by ~ 100 Myr observed in nuclear rings are likely driven by variations in the mass inflow rather than SN feedback.

In our models, variations in the SFR lead to variations in the SN rate, and this is reflected in time-varying total midplane pressure, gas scale height, and ISM weight since SN feedback is the main source of thermal and turbulent energy. We show that the predictions of the self-regulated equilibrium theory are satisfied in our simulations, even allowing for slow temporal variations (i.e. on a timescale longer than the local vertical dynamical time). We also show that the time-varying depletion time agrees with the quasi-equilibrium prediction provided that an appropriate averaging window is used that accounts for the delay between feedback

and star formation.

Lopsided star formation in nuclear rings: It has long been known that the star formation in the CMZ is asymmetric, such that most star formation occurs in positive longitudes, notably at Sgr B1 and B2 complexes (Bally et al. 2010). Similar asymmetry has also been noted for the nuclear ring in M83 (Harris et al. 2001; Callanan et al. 2021). Our second series (models `asym`, `off`, and `boost`) offers a possible explanation for lopsided star formation. The results of these models show that asymmetric inflows alone do not lead to lopsided star formation, because the gas from the upper and lower nozzles tend to be mixed up within a few orbital times, making the distribution of star particles in model `asym` indistinguishable from that in model `constant`. A sudden decrease of the inflow rate from one of the nozzles in model `off` does not create notable asymmetry, either. However, when the inflow rate from one of the nozzles suddenly increases by a large factor, as in model `boost`, the boosted inflow follows ballistic orbits and triggers enhanced star formation at the far side of the ring where the orbits converge, making the distribution of young clusters lopsided for a few Myr.

In real galaxies, boosted inflows may originate from fluid instabilities. For example, a global simulation of Sormani et al. (2018) for the CMZ asymmetry found that the combination of wiggle and thermal instabilities creates dense clumps randomly distributed in the dust lanes. Whenever the clumps infall along the dust lanes to the CMZ, the inflow rate becomes suddenly asymmetric and boosted by a large factor, making the gas distribution and hence star formation lopsided in the CMZ. Dale et al. (2019) performed hydrodynamic simulations of an isolated, turbulent molecular cloud plunging into the CMZ, which may also represent a dense clump produced by the wiggle and thermal instabilities of the dust lanes. Dale et al. (2019) showed that the compressive Galactic tidal force, as manifested by the orbit convergence near the pericenter passage, enhances the SFR at the downstream, qualitatively similar to what happens in model `boost`.

We note that while our models can explain lopsided star formation, they do not

show any noticeable asymmetry in the gas distribution which is observed in the CMZ and nuclear ring of M83. In the case of M83, the asymmetric gas distribution might be caused by a recent minor merger, as indicated by an offset between the photometric and kinematic nucleus (Sakamoto et al. 2004; Knapen et al. 2010). Another possibility is that the mass inflow occurs in the form of massive clumps rather than smooth streams, which may be caused by fluid instabilities (Sormani et al. 2018) as mentioned above. To study the effects of such clumpy inflows on the ring SFR and gas distribution, it is necessary to run simulations that resolve density inhomogeneity, shear, and turbulent velocities in the dust-lane inflows.

The CMZ is known to harbor several prominent molecular clouds which are likely progenitors of massive star clusters (e.g., Hatchfield et al. 2020). It has been proposed that such clouds are parts of two spiral arms (Sofue 1995; Sawada et al. 2004; Ridley et al. 2017), on either a closed elliptical orbit (Molinari et al. 2011) or an open ballistic stream (Kruijssen et al. 2015). Although different orbital models place the clouds at different distances along the line of sight, they generally agree that all the CMZ clouds including Sgr A–C, the *brick*, and the *dust ridge* clouds are situated at the near side of the CMZ.[¶] If these clouds are the results of recently boosted inflows from the far-side dust lane, the inflow rate might have been much lower in the past than the current value estimated by Sormani & Barnes (2019), leading to the low SFR observed today. If this is really the case, the CMZ might be on the verge of starburst in the near future (see, e.g., Longmore 2014; Lu et al. 2019).

Comparison to other simulations: In our models the SN feedback alone induces a factor of ~ 2 fluctuations of the SFR with timescale $\lesssim 40$ Myr (see also Chapter 2). This appears consistent with the results of the global simulations of Sormani et al. (2020b) who found that the star formation in their simulated CMZ varies within a factor of ~ 2 . In contrast, the global simulations of Torrey et al. (2017) for

[¶]Although the two spiral arm model seems to place the Sgr B2 complex and brick at the far side, the absorption and proper motion data strongly suggest that they are at the near side. Ridley et al. (2017) reconciled this inconsistency by suggesting that those clouds are kinematically detached, jutting out of the near-side arm.

late-type, non-barred galaxies found that the star formation in the central 100 pc region goes through burst/quench cycles with the SFR varying more than an order of magnitude (fluctuations are lower on \sim kpc scales). Also, the global simulations of Armillotta et al. (2019) for a Milky Way-like galaxy found that the ring SFR varies more than an order of magnitude, although the most dominant cycle with period of ~ 50 Myr, driven by SN feedback, has an amplitude of ~ 5 .

It is uncertain what makes the SFR fluctuations in Torrey et al. (2017) and Armillotta et al. (2019) larger than those in our models and Sormani et al. (2020b). But, we conjecture that the *effective* feedback strength in the former might have been stronger than that in the latter due to low resolution. In Torrey et al. (2017) and Armillotta et al. (2019), the mass resolution ($\sim 10^3 M_\odot$) is probably not high enough to resolve the Sedov-Taylor stage for most SNe exploding inside dense gas. In this case, the feedback is in the form of momentum, amounting to an imposed value $p_* \sim 3-5 \times 10^5 M_\odot \text{ km s}^{-1}$ per SN (Hopkins et al. 2018, in these simulations an approximate treatment of early feedback is also applied, which may increase the momentum budget).

When SNe are instead resolved, the feedback is in the form of energy and p_* is self-consistently determined by the interactions of SN remnants with their surroundings. When SNe occur in rapid succession, simulations with a cloudy interstellar medium show that p_* per SN may be reduced relative to the single-SN value (see Kim et al. 2017a). Also, Chapter 2 found that a significant fraction of the total SN energy is *wasted* in the ambient hot medium outside the ring, yielding $p_* \sim 0.4-0.8 \times 10^5 M_\odot \text{ km s}^{-1}$. In test simulations (not presented in this thesis) similar to model **constant** that implement feedback by injecting momentum instead of energy, we found that when p_* is large, the SFR fluctuates with larger amplitudes. Also, at lower mass resolution (for a given ring mass), the feedback energy from a given collapsed region will be a larger fraction of the total gravitational binding energy of the ring, and can therefore more easily disperse the ring. Thus, the amplitude of SFR fluctuations in simulations may be sensitive to both the specific

parameter choices adopted for implementing feedback, and the resolution of the simulation.

Limitation of models: Our prescription of star formation and feedback lacks several physical elements that might affect the star formation history. First, our models do not include early feedback mechanisms such as stellar winds and radiation, which can halt accretion and growth of sink particles before first SN explosions at $t \sim 4$ Myr. Over the lifetime of a cluster, the momentum injection from SNe far exceeds that from winds and radiation, but this early feedback limits the star formation efficiency in individual molecular clouds (Rogers & Pittard 2013; Rahner et al. 2017; Kim et al. 2018b, 2021b).

Second, our spatial resolution is insufficient to resolve internal substructure within self-gravitating regions. With collapse of internal overdensities and the resulting early feedback, the lifetime star formation efficiency in self-gravitating structures might be lower, which could increase the overall gas density in the ring. A higher density ring could be more prone to large-scale instability and star formation bursts. Thus, the combination of higher resolution and additional feedback could potentially produce larger feedback-driven fluctuations.

Chapter 4

Effects of Magnetic Fields on Gas Dynamics and Star Formation in Nuclear Rings*

4.1 Overview

One characteristic result of nonlinear dynamical interactions between a bar and gas in disk galaxies is the formation of a pair of large-scale shocks running along the leading sides of the bar inside the corotation. Gas entering a shock front loses angular momentum and is deflected inward. A fraction of shocked gas is swept up by the infalling gas from larger radii, while the remainder goes around and hits the shock at the opposite side (Athanassoula 1992; Regan et al. 1999; Kim et al. 2012b; Hatchfield et al. 2021). In optical images, the compressed gas is seen as narrow dust lanes along which gas is funnelled toward the central regions. The observed mass inflow rate is of the order of $\dot{M}_{\text{in}} \sim 0.1\text{--}10 M_{\odot} \text{ yr}^{-1}$ and is known to be time-variable (Benedict et al. 1996; Regan et al. 1997; Meier et al. 2008; Elmegreen et al. 2009; Shimizu et al. 2019; Sormani et al. 2019).

The inflowing gas has a residual angular momentum and thus readily forms a

*A version of this chapter will be submitted to an academic journal

circumnuclear ring which is active in star formation. Star-forming nuclear rings are found in about $\sim 20\%$ of disk galaxies in the local universe (Comerón et al. 2010) and have SFRs of $\sim 0.1\text{--}10 M_{\odot} \text{ yr}^{-1}$ (Mazzuca et al. 2008; Ma et al. 2018). While nuclear rings are sometimes found in unbarred galaxies, a majority of such galaxies have oval distortions, strong spiral arms, or close companions that are thought to provide non-asymmetric gravitational torques similar to bars (Comerón et al. 2010). Spectroscopic observations have revealed that nuclear rings live long, composed of not only young star clusters formed recently but also old stellar populations with ages ranging from ~ 100 Myr to a few Gyrs. The reconstructed star formation histories are characterized by a large time variability, involving multiple timescales ranging from a few tens of Myrs to a few Gyrs (e.g., Allard et al. 2006; Sarzi et al. 2007; Gadotti et al. 2019; Prieto et al. 2019; Nogueras-Lara et al. 2020).

Recently, a number of authors studied gas dynamics and star formation in and around nuclear rings by using numerical simulations with realistic treatment of star formation and feedback. For example, Armillotta et al. (2019) conducted hydrodynamic simulations of the ISM to study gas flows and star formation in the Central Molecular Zone (CMZ), a nuclear ring of the Milky Way. They found that the SFR of the CMZ goes through several burst-quench cycles of with a mixture of a short period ~ 50 Myr and long period (~ 200 Myr), although the gas mass remains relatively constant over time. Tress et al. (2020) and Sormani et al. (2020b) used a moving-mesh technique to attain high spatial and mass resolutions in the CMZ, resolving Sedov-Taylor blastwaves for most supernova (SN) explosions in their simulations. Contrary to Armillotta et al. (2019), they found that the SFR in the ring steadily increases in time in proportion to the gas mass, with the depletion time almost constant within a factor of ~ 2 . Seo et al. (2019) ran hydrodynamic simulations coupled with N -body stellar dynamics to study how a nuclear ring forms and evolves in a situation where a bar forms and grows self-consistently. They found that star formation in a nuclear ring is sustained for a long (> 1 Gyr) period of time, and that the ring SFR is found to correlate well with the mass

inflow rate to the ring.

The time variations of the ring SFR can in principle be affected by both the bar-driven inflow and SN feedback. To isolate the effects of time-varying mass inflow rate from those of SN feedback on the ring star formation, in Chapter 2 we have developed a semiglobal numerical framework that allows to explicitly control the mass inflow rate to the ring via boundary conditions. We found that, when the mass inflow rate is fixed in time, the SFR and depletion time are almost constant within a factor of ~ 2 for a wide range of \dot{M}_{in} ($0.125\text{--}8 M_{\odot} \text{ yr}^{-1}$). By allowing the mass inflow rate to vary with time in a prescribed way, in Chapter 3 we found that time-varying mass inflows with a sufficient oscillation amplitude cause episodic star formation, provided that the timescale of the inflow rate variations is sufficiently long ($\gtrsim 50 \text{ Myr}$). We also found that while the SFR is solely determined by the inflow rate, gas mass or depletion time depends additionally on the external gravitational field and feedback yields through the requirement of vertical dynamical equilibrium, consistent with the prediction of the pressure-regulated, feedback-modulated star formation theory (Ostriker & Kim 2022, see also, Ostriker et al. 2010; Ostriker & Shetty 2011).

While the studies mentioned above have improved our understanding on physical processes for star formation in nuclear rings, they were all limited to unmagnetized models. Observations show that nuclear rings in real galaxies are magnetized, potentially affecting star formation there. Assuming an energy equipartition between magnetic fields and CRs, the average magnetic field strengths in nuclear rings are estimated to be $\sim 55 \mu\text{G}$ for NGC 1097 (Beck et al. 2005), $\sim 63 \mu\text{G}$ for NGC 1365 (Beck et al. 2005), and $\sim 84 \mu\text{G}$ for NGC 5792 (Yang et al. 2022), much stronger than in spiral arms of normal disk galaxies (Beck 2015). Beck et al. (1999, 2005) mapped radio continuum emissions in barred galaxies and found that the magnetic fields are predominantly parallel to the dust lanes, while penetrating the nuclear rings with a large pitch angle ($\sim 40^\circ$). Strong magnetic fields would provide an additional pressure support for gas against gravity, suppressing star

formation (Pillai et al. 2015; Tabatabaei et al. 2018). Indeed, Tabatabaei et al. (2018) found a strong positive correlations between the gas depletion time and the magnetic field strength for individual giant clumps distributed along the nuclear ring of NGC 1097. No such correlation between the depletion time and a turbulent velocity dispersion suggests that it may be magnetic fields that suppress the ring star formation rather than SN feedback.

In this chapter, we run magnetohydrodynamic (MHD) simulations of star formation in magnetized nuclear rings by considering magnetized gas inflows at the domain boundaries. To focus on the effects of magnetic fields on ring star formation, we fix the mass inflow rate and ring size, while varying the magnetic field strength of the inflowing gas. By comparing the results from models with different field strengths, we will quantify how magnetic fields affect evolution of nuclear rings and star formation therein.

In addition to star formation in magnetized nuclear rings, our models are also useful to explore magnetized gas accretion inward of a nuclear ring, potentially forming a circumnuclear disk (CND) near a galaxy center. Based on the measured magnetic field strength and pitch angle in the nuclear ring of NGC 1097, Beck et al. (2005) suggested that magnetic stress can drive gas accretion from a ring to fuel an AGN. Other proposed mechanisms for gas inflows near a galaxy center include bars-within-bars (Shlosman et al. 1989), nuclear spirals (Maciejewski 2004; Kim & Elmegreen 2017), and SN feedback (Wada 2004; Tress et al. 2020). We in this work use direct numerical simulations to study gas accretion and its outcomes in the presence magnetic fields and star formation feedback.

The remainder of this chapter is organized as follows. In Section 4.2, we outline the equations that we solve, summarize the TIGRESS[†] framework for dealing with the ISM and star formation physics, and describe our treatment of the boundary conditions for magnetized gas inflows. In Section 4.3, we present overall time evolution of our models with a focus on star formation histories, and examine gas

[†]TIGRESS is the acronym of Three-phase Interstellar medium in Galaxies Resolving Evolution with Star formation and Supernova feedback

Table 4.1. Model parameters

Model	R_{ring}	\dot{M}_{in}	β_{in}	$B_{\text{in},c}$	$B_{\text{in,avg}}$
(1)	(2)	(3)	(4)	(5)	(6)
	(pc)	($M_{\odot} \text{ yr}^{-1}$)		(μG)	(μG)
Binf	500	1.0	∞	0	0
B100	500	1.0	100	1.6	0.76
B30	500	1.0	30	3.0	1.4
B10	500	1.0	10	5.2	2.4

accretion toward the center driven by magnetic stresses. In Section 4.4, we present the temporal evolution of the magnetic field strength in the ring and explore their effects on the ring star formation. Finally, we summarize and discuss our results in Section 4.5.

4.2 Numerical Methods

To resolve a central kiloparsec region of a barred galaxy with high resolution, we adopt the semiglobal numerical models introduced in Chapter 2. In this approach, our computational domain covers only a nuclear ring and its immediate vicinity, and bar-driven mass inflows are realized as boundary conditions. Nonlinear interactions between the bar and gas leading to dust-lane shocks occur outside of the computational domain, and therefore are not explicitly modeled. Instead, we control the mass inflow rate and angular momentum of the inflows using free parameters. In this section, we present the basic equations we solve (Section 4.2.1), summarize the TIGRESS framework for star formation and feedback (Section 4.2.2), and describe the inflow boundary conditions for magnetized gas (Section 4.2.3).

4.2.1 Governing Equations

Our computational domain is a Cartesian cube with side $L = 2048$ pc located at the galaxy center. The domain rotates at an angular speed $\Omega_p = 36 \text{ km s}^{-1} \text{ kpc}^{-1} \hat{\mathbf{z}}$, corresponding to a bar pattern speed. We include the radiative heating and cooling of the ISM, gaseous self-gravity, and fixed external gravity responsible for the background rotation curve. The governing equations we solve are

$$\frac{\partial \rho}{\partial t} + \nabla \cdot (\rho \mathbf{v}) = 0, \quad (4.1)$$

$$\begin{aligned} \frac{\partial(\rho \mathbf{v})}{\partial t} + \nabla \cdot (\rho \mathbf{v} \mathbf{v} + P \mathbb{I} + \mathbf{T}) \\ = -2\rho \Omega_p \times \mathbf{v} - \rho \nabla \Phi_{\text{tot}}, \end{aligned} \quad (4.2)$$

$$\begin{aligned} \frac{\partial E}{\partial t} + \nabla \cdot [E \mathbf{v} + (P \mathbb{I} + \mathbf{T}) \cdot \mathbf{v}] \\ = -\rho \mathbf{v} \cdot \nabla \Phi_{\text{tot}} - \rho \mathcal{L}, \end{aligned} \quad (4.3)$$

$$\frac{\partial \mathbf{B}}{\partial t} = \nabla \times (\mathbf{v} \times \mathbf{B}), \quad (4.4)$$

$$\nabla^2 \Phi_{\text{self}} = 4\pi G(\rho + \rho_{\text{sp}}). \quad (4.5)$$

Here, ρ and ρ_{sp} is the volume density of gas and young star particles, respectively, \mathbf{v} is the gas velocity in the rotating frame, P is the gas pressure, \mathbb{I} is the identity matrix, $\mathbf{T} = B^2/(8\pi)\mathbb{I} - \mathbf{B}\mathbf{B}/(4\pi)$ is the Maxwell stress tensor, $E = \rho v^2/2 + P/(\gamma - 1) + B^2/(8\pi)$ is the total energy density for the adiabatic index $\gamma = 5/3$, $\Phi_{\text{tot}} = \Phi_{\text{self}} + \Phi_{\text{ext}} + \Phi_{\text{cen}}$ is the total gravitational potential, consisting of the self-gravitational potential Φ_{self} , the external gravitational potential Φ_{ext} , and the centrifugal potential $\Phi_{\text{cen}} = -\frac{1}{2}\Omega_p^2(x^2 + y^2)$, and $\rho \mathcal{L}$ is the net cooling rate per unit volume.

In our models, the external gravity $\Phi_{\text{ext}} = \Phi_{\text{BH}} + \Phi_b$ is due to a central supermassive black hole and a stellar bulge. The black hole is modeled by a Plummer

potential

$$\Phi_{\text{BH}} = -\frac{GM_{\text{BH}}}{\sqrt{r^2 + r_{\text{BH}}^2}} \quad (4.6)$$

with mass $M_{\text{BH}} = 1.4 \times 10^8 M_{\odot}$ and the softening length $r_{\text{BH}} = 20$ pc. For the stellar bulge, we take

$$\Phi_b = -\frac{4\pi G \rho_{b0} r_b^3}{r} \ln \left(\frac{r}{r_b} + \sqrt{1 + \frac{r^2}{r_b^2}} \right). \quad (4.7)$$

with the central density $\rho_{b0} = 50 M_{\odot} \text{ pc}^{-3}$ and the scale radius $r_b = 250$ pc. The resulting rotation curve and the circular velocity at the ring position are similar to the cases of NGC 1097 in Onishi et al. (2015).

The net cooling rate of gas per unit volume in Equation (4.3) is given by

$$\rho \mathcal{L} = n_{\text{H}}(n_{\text{H}}\Lambda - \Gamma_{\text{PE}} - \Gamma_{\text{CR}}), \quad (4.8)$$

where $n_{\text{H}} = \rho/(\mu_{\text{H}} m_{\text{H}})$ is the hydrogen number density with the mean molecular weight per hydrogen $\mu_{\text{H}} = 1.4271$ assuming the solar abundances. For the cooling function $\Lambda(T)$, we take the fitting formula of Koyama & Inutsuka (2002) (see, Kim et al. 2008b, for typo-corrected version) for $T < 10^{4.2}$ K and the collisional ionization equilibrium cooling curve at solar metalicity of Sutherland & Dopita (1993) for $T > 10^{4.2}$ K. The gas temperature T is related to density and pressure via an ideal equation of state $P = \rho k_{\text{B}} T / (\mu m_{\text{H}})$, with the mean molecular weight $\mu(T)$ varying with T from $\mu_{\text{ato}} = 1.295$ for neutral gas to $\mu_{\text{ion}} = 0.618$ for fully ionized gas (Kim & Ostriker 2017).

In Equation (4.8), Γ_{PE} represents the photoelectric heating rate by far-ultraviolet (FUV) radiation impinging on dust grains, and is given by

$$\Gamma_{\text{PE}} = \Gamma_{\text{PE},0} \left(\frac{\mu(T) - \mu_{\text{ion}}}{\mu_{\text{ato}} - \mu_{\text{ion}}} \right) \left(\frac{J_{\text{FUV}}}{J_{\text{FUV},0}} + 0.0024 \right), \quad (4.9)$$

where $\Gamma_{\text{PE},0} = 2 \times 10^{26} \text{ erg s}^{-1}$ (Koyama & Inutsuka 2002) and $J_{\text{FUV},0} = 2.1 \times$

$10^4 \text{ erg s}^{-1} \text{cm}^{-2} \text{sr}^{-1}$ (Draine 1978) are normalization factors based on the solar neighborhood conditions. The term in the first parentheses in Equation (4.9) makes the photoelectric heating reduced at high T at which dust grains sublime, shutting it off completely in the fully ionized gas. The small factor in the last parentheses is responsible for a small contribution of the metagalactic FUV background.

We use the same approximate method as in Chapter 2 to calculate the mean FUV intensity J_{FUV} from young star particles in the simulations. For this, we first calculate the luminosity surface density Σ_{FUV} of all star particles in the simulation domain, and then allow for local dust attenuation to set

$$J_{\text{FUV}} = \frac{\Sigma_{\text{FUV}}}{4\pi} \left(\frac{1 - E_2(\tau_{\perp}/2)}{\tau_{\perp}} \right) e^{-n_{\text{H}}/n_0}, \quad (4.10)$$

where E_2 is the second exponential integral, $\tau_{\perp} = \kappa_d \Sigma$ with $\kappa_d = 10^3 \text{ cm}^{-2} \text{g}^{-1}$ is the vertical optical depth for the mean gas surface density Σ averaged over the entire domain, and n_0 is a turnover density above which the local shielding becomes significant. For the models presented in this chapter, we take $n_0 = 50 \text{ cm}^{-3}$ which yields J_{FUV} comparable to the values obtained by applying the adaptive ray-tracing method of Kim et al. (2017b).

Inside dense regions where FUV radiation is heavily shielded, the heating is dominated by the CR ionization. The associated heating rate Γ_{CR} in Equation (4.8) is given by

$$\Gamma_{\text{CR}} = q_{\text{CR}} \xi_{\text{CR}} \left(\frac{\mu(T) - \mu_{\text{ion}}}{\mu_{\text{ato}} - \mu_{\text{ion}}} \right), \quad (4.11)$$

where $q_{\text{CR}} = 10 \text{ eV}$ is the energy yield per ionization (Glassgold et al. 2012, see also Gong et al. 2017) and ξ_{CR} denotes the the CR ionization rate. The term inside the parentheses is again to shut off CR heating in fully ionized gas. Assuming that ξ_{CR} is proportional to the SFR surface density Σ_{SFR} and is attenuated by a factor of Σ_0/Σ above a critical gas surface density $\Sigma_0 = 10.7 M_{\odot} \text{ pc}^{-2}$ (Neufeld & Wolfire 2017), we set

$$\xi_{\text{CR}} = \xi_{\text{CR},0} \frac{\Sigma_{\text{SFR}}}{\Sigma_{\text{SFR},0}} \min \left\{ 1, \frac{\Sigma_0}{\Sigma} \right\}, \quad (4.12)$$

where $\xi_{\text{CR},0} = 2 \times 10^{-16} \text{s}^{-1}$ is the CR ionization rate in the solar neighborhood (Indriolo et al. 2007; Neufeld & Wolfire 2017).

Equations (4.1)–(4.4) are discretized on a uniform mesh with 512^3 cells: the corresponding grid spacing is $\Delta x = 4 \text{ pc}$. We update the physical quantities using a modified version of the `Athena` code (Stone et al. 2008), which employs the MUSCL-Hancock scheme with the constrained transport algorithm to preserve $\nabla \cdot \mathbf{B} = 0$ within machine precision (Stone & Gardiner 2009), and applies the first-order flux correction when needed (Lemaster & Stone 2009). We apply the Green’s function convolution method aided by fast Fourier transform (FFT) (e.g., Skinner & Ostriker 2015) to solve the Poisson equation (Equation 4.5) with the vacuum boundary condition, i.e., $\Phi_{\text{self}} \rightarrow 0$ at infinity.

4.2.2 Star Formation and Feedback

We handle star formation and feedback using a modified TIGRESS framework (Kim & Ostriker 2017, see also Chapter 2). Here, we briefly summarize the TIGRESS model: we refer the reader to Kim & Ostriker (2017) and Chapter 2 for a more complete description.

We create a sink particle whenever the following three conditions are met simultaneously: (1) $\rho > \rho_{\text{LP}} = 8.86c_s^2/(G\Delta x^2)$ with a local sound speed c_s , the threshold density based on the Larson-Penston collapse solution, (2) Φ_{self} is a local minimum, and (3) the velocity is converging in all directions. A portion of the gas mass in the surrounding 27 cells is converted to the initial mass of a newly created sink particle. Sink particles are allowed to accrete mass and momentum from their surroundings and merge with nearby particles within $3\Delta x$ until the onset of the first SN explosion ($\sim 4 \text{ Myr}$). For orbits of sink particles, we solve their equations of motion $\ddot{\mathbf{x}} = -\nabla\Phi_{\text{tot}} - 2\boldsymbol{\Omega}_p \times \dot{\mathbf{x}}$ using the Boris algorithm that preserves the Jacobi integral very accurately (Boris 1970, see also Appendix A).

Sink particles with age less than 40 Myr exert feedback in the form of the photoelectric heating (Equation 4.9), CR heating (Equation 4.11), and the type II SN

explosion. The amount of energy and momentum injected by SN feedback depends on the density of the ambient medium. If the ambient density is low enough that the shell-formation radius is expected to be at least partially resolved, we regard the SN remnants as being in the Sedov-Taylor phase and inject 72% of the SN energy $E_{\text{SN}} = 10^{51}$ erg in the form of thermal energy and the remaining 28% in the form of kinetic energy. If the ambient density is too high for the shell-formation radius to be resolved, we assume the SN remnants have already cooled down below our resolution limit and inject the radial momentum $p_* = 2.8 \times 10^5 M_{\odot} \text{ km s}^{-1} (n_{\text{H}}/\text{cm}^{-3})^{-0.17}$ (Kim & Ostriker 2015b), expected at the snowplow phase. In both cases, an SN returns the ejecta mass $M_{\text{ej}} = 10 M_{\odot}$ back to the surrounding 27 cells.

4.2.3 Magnetized Inflow Streams

In Chapter 2, we introduced the semiglobal framework that treats the bar-driven mass inflows as the boundary conditions for hydrodynamic simulations. Here, we modify the boundary conditions slightly to handle magnetized inflows.

We inject gas streams into the computational domain through two circular nozzles with radius $\zeta_{\text{in}} = 112 \text{ pc}$ placed at y -boundaries: the coordinates of the nozzle centers are $(x, y, z) = (\mp b_{\text{in}}, \pm L/2, 0)$, where $b_{\text{in}} = 512 \text{ pc}$ is the impact parameter of the inflows (see Figure 2.3 for schematic diagram). Here and hereafter, the upper and lower signs correspond to the upper and lower nozzles, respectively. We set the streaming velocity at the nozzles to

$$\mathbf{v}_{\text{in}} = \mp v_{\text{in}} (\sin \theta_{\text{in}} \hat{\mathbf{x}} + \cos \theta_{\text{in}} \hat{\mathbf{y}}), \quad (4.13)$$

where $\theta_{\text{in}} = 10^\circ$ is the inclination angle of the streams relative to the y -axis. The condition of the angular momentum conservation implies that the inflow speed v_{in} determines the location where the nuclear ring forms. By setting the specific angular momentum (in the inertial frame) of the inflows equal to $R_{\text{ring}} v_{\text{rot}}(R_{\text{ring}})$,

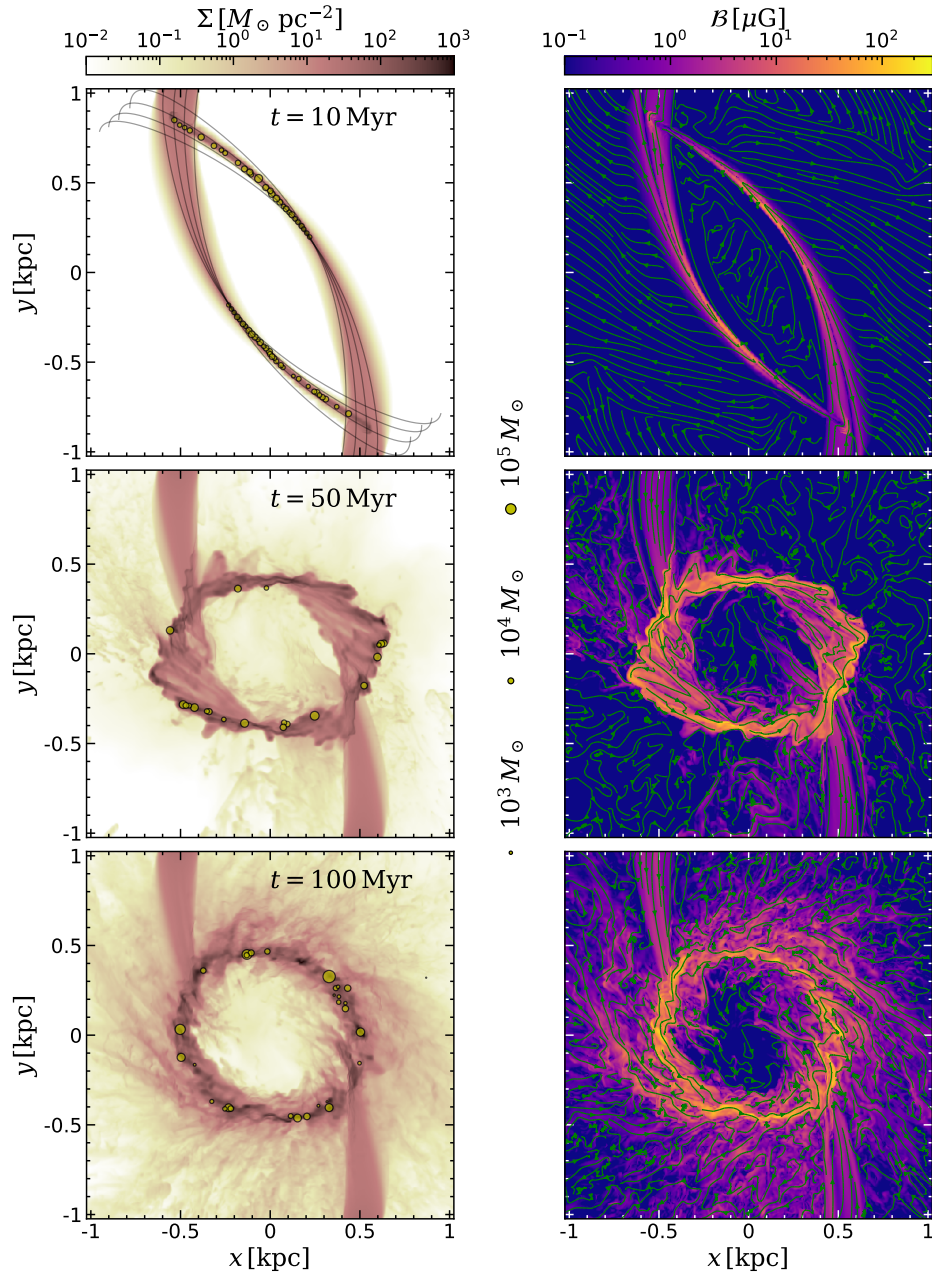
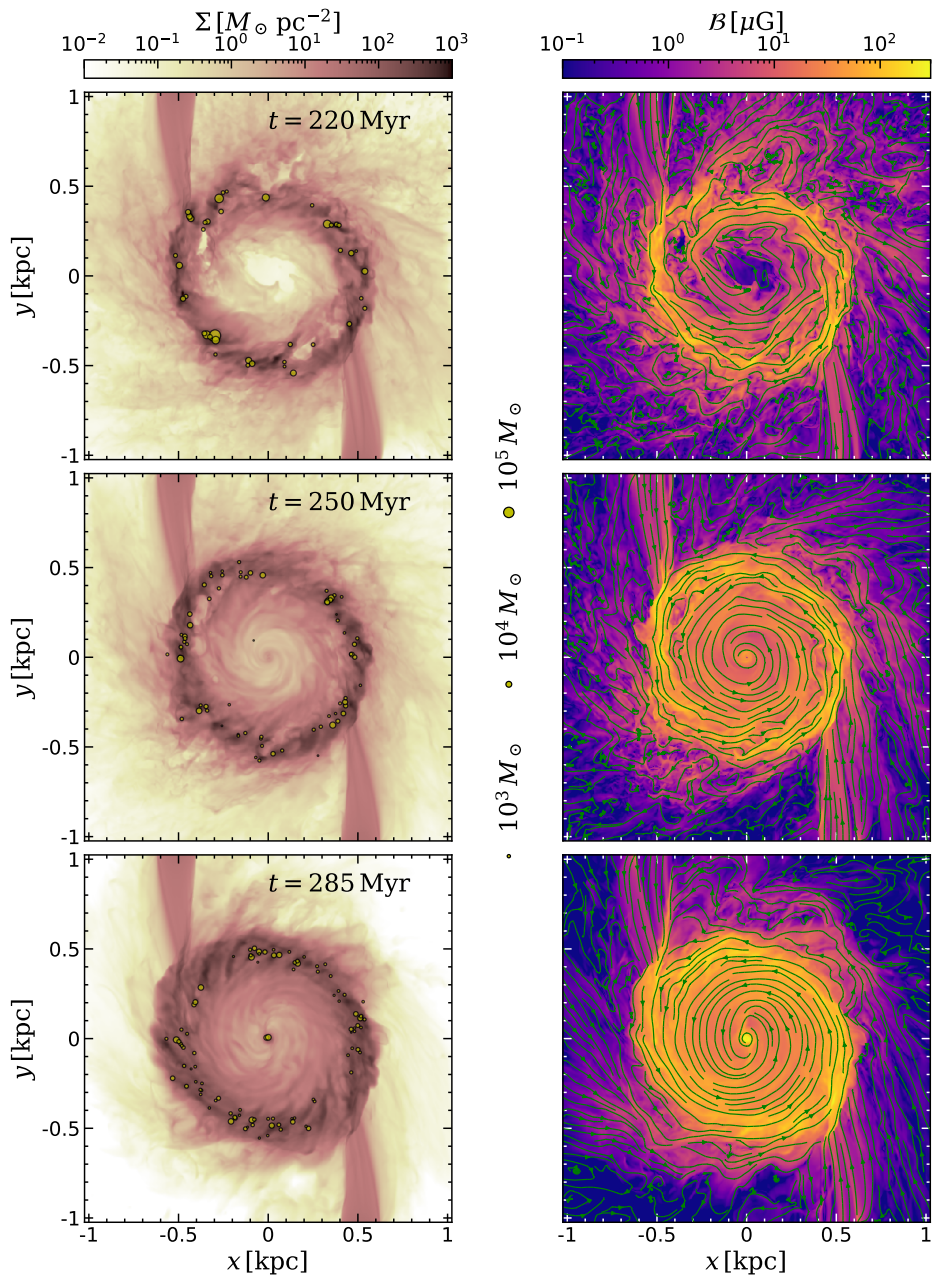


Figure 4.1. Face-on views of model B100 at $t = 10, 50, 100, 220, 250$, and 285 Myr (the figure continues to the next page). The left column displays the gas surface density and newly formed star particles with age < 1 Myr, while the right column plots the streamlines of the projected magnetic fields $\mathcal{B}_x = (\int \rho B_x dz) / (\int \rho dz)$ and $\mathcal{B}_y = (\int \rho B_y dz) / (\int \rho dz)$, overlaid over the map of $\mathcal{B} = (\mathcal{B}_x^2 + \mathcal{B}_y^2)^{1/2}$. The black solid lines in the top left panel are the ballistic trajectories that a test particle injected with \mathbf{v}_{in} would follow.

**Figure 4.1.** (continued)

with the circular velocity $v_{\text{rot}} \equiv (Rd\Phi_{\text{ext}}/dR)^{1/2}$, we obtain

$$v_{\text{in}}(x, \pm L/2) = \frac{R_{\text{ring}} v_{\text{rot}}(R_{\text{ring}}) - R^2 \Omega_p}{|x \cos \theta_{\text{in}} \mp (L/2) \sin \theta_{\text{in}}|}, \quad (4.14)$$

We fix the ring radius to $R_{\text{ring}} = 500$ pc and use Equations (4.13)–(4.14) to find the corresponding inflow velocity inside the nozzles.

The density of the inflowing gas ρ_{in} sets the mass inflow rate through

$$\dot{M}_{\text{in}} = \iint \rho_{\text{in}} v_{\text{in}} \cos \theta_{\text{in}} dx dz, \quad (4.15)$$

where the integrations are performed over the two nozzles, i.e., $y = \pm L/2$ and $[(x \pm b_{\text{in}})^2 + z^2]^{1/2} < \zeta_{\text{in}}$. We fix the mass inflow rate to $1 M_{\odot} \text{ yr}^{-1}$ by taking $\rho_{\text{in}} = 0.138 M_{\odot} \text{ pc}^{-3}$.

Radio polarization observations (Beck et al. 2005; Lopez-Rodriguez et al. 2021) indicate that the magnetic fields are parallel to dust lanes. Motivated by this, we take the magnetic fields inside the nozzles parallel to the inflow velocity as

$$\mathbf{B}_{\text{in}} = \frac{B_{\text{in}}}{v_{\text{in}}} \mathbf{v}_{\text{in}}, \quad (4.16)$$

with the amplitude given by

$$B_{\text{in}} = \left(\frac{8\pi P_{\text{in}}}{\beta_{\text{in}}} \right)^{1/2} \cos \left(\frac{\pi \zeta}{2\zeta_{\text{in}}} \right). \quad (4.17)$$

Here, $P_{\text{in}} = \rho_{\text{in}} k_{\text{B}} T_{\text{in}} / (\mu_{\text{H}} m_{\text{H}})$ is the thermal pressure of the inflowing gas with temperature $T_{\text{in}} = 2 \times 10^4$ K, β_{in} is a plasma parameter measuring the ratio of thermal to magnetic pressure, and $\zeta = [(x \pm b_{\text{in}})^2 + z^2]^{1/2}$ is the distance from the nozzle center. The cosine term ensures that the fields vanish at the nozzle boundaries, preventing the gas just outside the nozzles from accidentally acquiring too large Alfvén speeds. In **Athena**, the velocity and magnetic fields are cell-centered and face-centered, respectively. Despite Equation (4.16), the mismatch in the evaluation points of \mathbf{B}_{in} and \mathbf{v}_{in} yields non-vanishing $\mathbf{v}_{\text{in}} \times \mathbf{B}_{\text{in}}$ at the innermost ghost

zones at early time, as explained in Appendix B. This allows seed magnetic fields to leak into our computational domain through Equation (4.4), which are subsequently stretched by the inflows to become parallel to the streams, smoothly matching the boundary conditions (see Section 4.3.1).

We allow gas to freely escape from the simulation domain, but forbid inflows except through the nozzles. We accomplish this by setting the hydrodynamic variables in the ghost zones by extrapolating from two adjacent active zones, while keeping the normal velocity to zero if the velocity is directed inward. The magnetic fields in the ghost zones are simply copied from the innermost active zones.

4.2.4 Models

We consider four models with $\beta_{\text{in}} = \infty, 100, 30$, and 10 . Table 4.1 summarizes the model parameters for all models. Column (1) lists the model names. Columns (2) and (3) give the ring radius and the mass inflow rate, respectively, which are the same for all models. Column (4) gives β_{in} . Column (5) and (6) give the magnetic field strength at the nozzle centers $B_{\text{in},c} = B_{\text{in}}(r = 0)$ and the mean field strength inside the nozzles $B_{\text{in,avg}}$, respectively. Our fiducial model B100 has $\beta_{\text{in}} = 100$, $B_{\text{in},c} = 1.6 \mu\text{G}$, and $B_{\text{in,avg}} = 0.76 \mu\text{G}$. The simulation domain is initially filled with rarefied gas with density $n_{\text{H}} = 10^{-5} \exp[-|z|/(50 \text{ pc})] \text{ cm}^{-3}$ and temperature $T = 2 \times 10^4 \text{ K}$, and subsequent evolution is entirely governed by the inflows.

4.3 Evolution

In this section, we describe overall evolution of our fiducial model B100 in terms of the gas and magnetic field distribution and star formation. We also measure the accretion rates inside the ring and compare them with theoretical predictions.

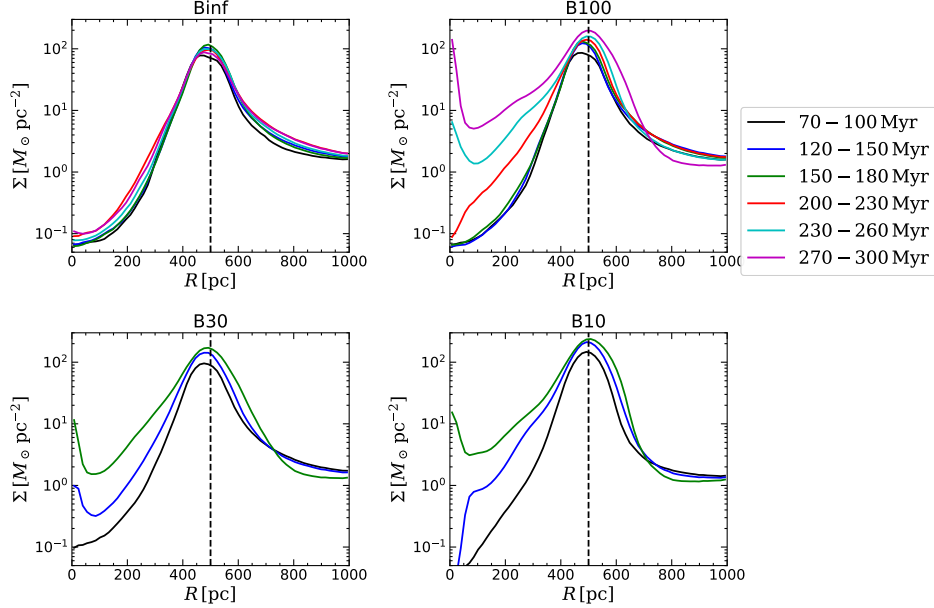


Figure 4.2. Evolution of the radial distribution of the azimuthally-averaged gas surface density for all models. Colors indicates the time interval for a temporal average. The vertical dashed lines mark the ring location R_{ring} .

4.3.1 Overall Evolution

Figure 4.1 plots snapshots of gas surface density together with young star particles as well as the projected magnetic fields overlaid over the total strength map in our fiducial model B100 at a few selected epochs. Figure 4.2 plots the evolution of the radial profiles of the azimuthally-averaged surface density for all models.

The early evolution of model B100 is qualitatively similar to the unmagnetized models presented in Chapter 2. Initially, the gas streams injected from the nozzles rapidly cool below ~ 100 K as they follow almost ballistic orbits depicted in the top left panel of Figure 4.1. Due to orbit crowding, the gas becomes compressed and produces strings of star particles downstream. The ensuing FUV feedback heats up the gas in the dust lanes to $T \sim 10^4$ K. After a half orbital time (~ 8 Myr), the streams from the opposite boundaries collide with each other, which drives strong shocks with Mach number ~ 16 . The streams lose their orbital kinetic energy as they pass through the shocks multiple times, and form a nuclear ring with radius

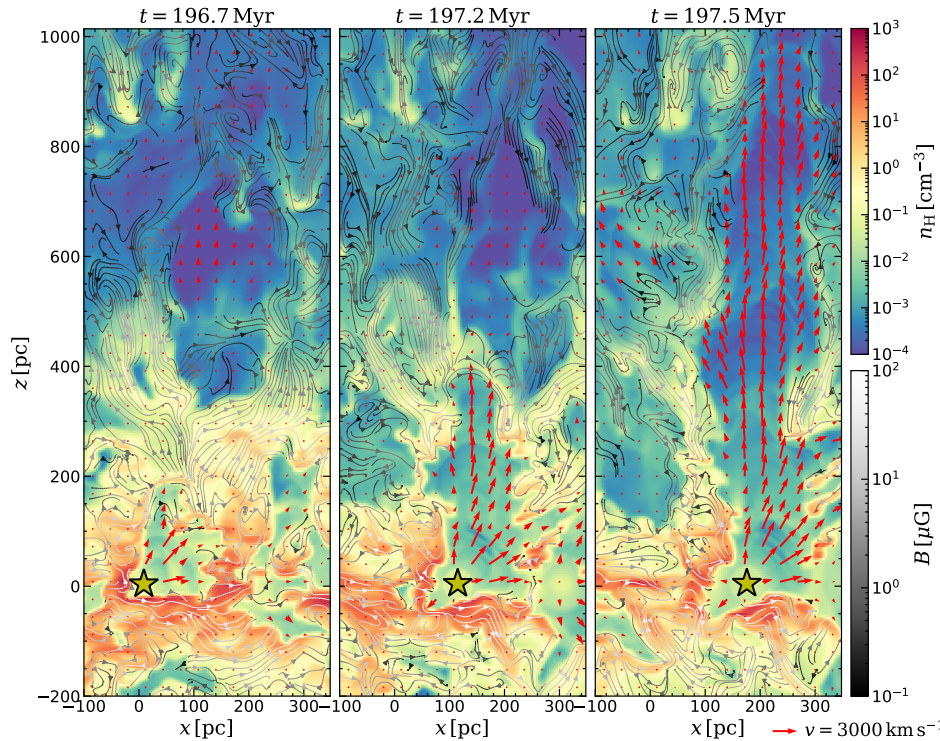


Figure 4.3. Superbubble breakout in the vertical direction. Each panel from left to right shows the density slice of model B100 at $y = -438, -433$, and -419 pc, the y -position of a sink particle with mass $2 \times 10^6 M_\odot$ (denoted by the yellow star) at $t = 196.7, 197.2$, and 197.5 Myr, respectively. The streamlines in grey represent the magnetic fields lines with the strength $B = (B_x^2 + B_y^2 + B_z^2)^{1/2} > 0.1 \mu\text{G}$. The red arrows are in-plane velocity vectors, (v_x, v_z) , with their lengths proportional to the speed $(v_x^2 + v_z^2)^{1/2}$. The expanding superbubble surrounding the star particle lifts the toroidal magnetic fields near the midplane to high-altitude regions to produce poloidal fields.

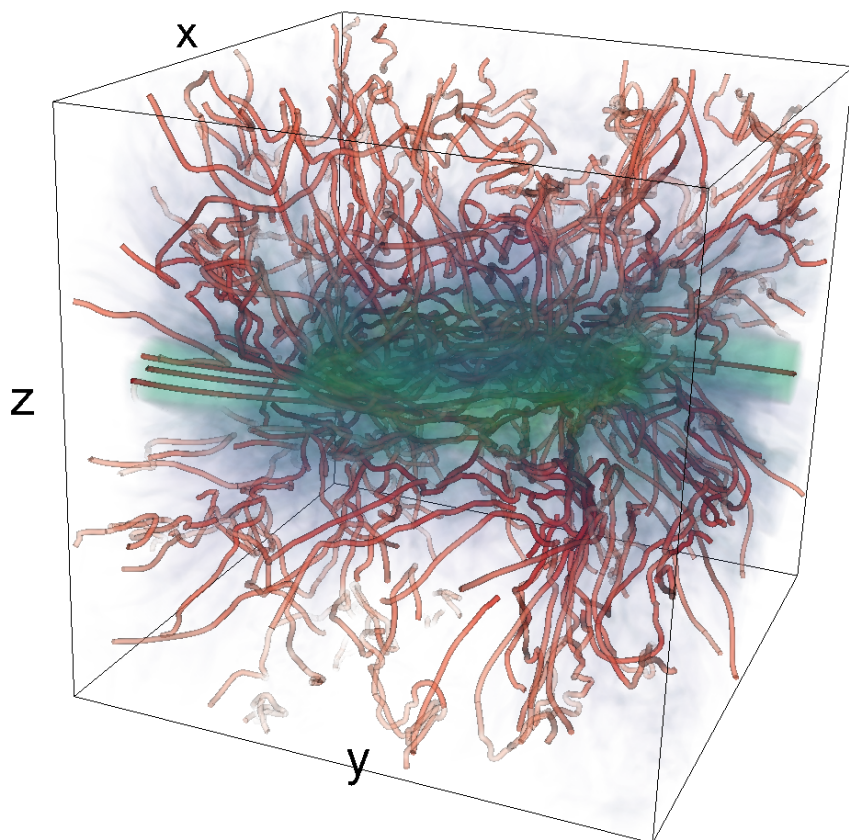


Figure 4.4. Perspective visualization of the three-dimensional magnetic field structure in model B100 at $t = 250$ Myr. The magnetic field lines are represented by red tubes, while the gas density is volume rendered in blue-green. Note that the magnetic fields are predominantly toroidal inside the nuclear ring because of the differential rotation, and poloidal in high- z regions by SN-driven outflows.

$R \sim R_{\text{ring}}$ at $t \sim 50 \text{ Myr}$ (corresponding to ~ 3 orbital times).

Still, the ring is elongated with the major axis precessing under the external gravitational potential. It takes another $\sim 50 \text{ Myr}$ for the ring to fully circularize (the third row of Figure 4.1). The ring soon reaches a quasi-steady equilibrium where the FUV and CR heating balances the radiative cooling, the SN feedback balances the turbulent dissipation, and the thermal and turbulent pressures remain approximately constant. The ring gas mass also stays roughly constant as the net mass inflow rate balances the star formation rate. Star formation proceeds randomly throughout the whole length of the ring. Although the resulting SN feedback disperses the gas and drives turbulence locally and temporarily, it never destroys the ring entirely nor quench star formation completely (Section 4.3.2; see also Chapter 2).

As mentioned in Section 4.2.3 (and Appendix B), our boundary conditions introduce weak seed magnetic fields in the active domain, which are stretched along the dust lanes by the inflowing gas. Except for initial $\sim 10 \text{ Myr}$, magnetic fields remain well aligned with the inflow velocity and do not systematically grow in time, although turbulent perturbations induced by SN feedback from the ring induce temporal fluctuations. As the streams form a ring, magnetic fields becomes predominantly toroidal in the ring, with large fluctuations due to SN feedback. The magnetic fields in the ring becomes stronger and more regular with time (see Section 4.4.1), presumably due to both the small- and large-scale dynamo driven by SN feedback and rotational shear inside the ring, the discussion of which we defer to Section 4.5.2.

Strong magnetic fields make evolution of model B100 deviates significantly from that of model B_{inf} after $t \sim 200 \text{ Myr}$ in two ways. First, while the surface density profile does not change much with time in model B_{inf} (Figure 4.2), an accretion flow develops from the ring in model B100 toward the center in the form of trailing spirals, gradually filling the regions inside the ring. The accreting gas piles up at the center, forming a CND with radius of $\sim 50 \text{ pc}$. Second, strong magnetic fields and

associated pressure make the SFR decreased with time in model B100 (see Section 4.4.2). Although star formation occurs also in the CND, its rate is, on average, a factor 30 times smaller than that in the ring.

Figure 4.3 plots the spatial distribution of gas and magnetic fields in the x - z slices through the three consecutive positions of a moving star cluster with mass $2 \times 10^6 M_\odot$. Repeated SN explosions creates a superbubble around the cluster. The overpressurized bubble easily expands along the vertical direction where the gas density decreases, eventually breaking out and rapidly rising up with velocities exceeding 10^3 km s^{-1} . Magnetic field lines are lifted to high- $|z|$ regions and stretched by flows of hot gas to generate a poloidal component. Figure 4.4 plots volumetric rendering of three-dimensional magnetic field geometry and gas density, showing that the magnetic fields are predominantly toroidal in the ring and poloidal in the regions away from the midplane.

The last-left panel of Figure 4.1 shows that the ring abounds with dense spiral segments in trailing shape with a pitch angle of $\lesssim 45^\circ$ and an almost regular azimuthal spacing of $\sim 100\text{--}150 \text{ pc}$. These spiral segments start to appear roughly at $t \sim 260\text{--}270 \text{ Myr}$ and keep being destroyed and regenerated thereafter. The quasi-regular spacing of these spiral segments suggests that they result from the magneto-Jeans instability (MJI) in which magnetic tension forces from bent field lines suppress the stabilizing effect of epicyclic motions (Elmegreen 1987; Kim & Ostriker 2001; Kim et al. 2002). Indeed, the corresponding dispersion relation (Equation 21 of Kim et al. 2002) for the parameters adopted from model B100 at $t \sim 270\text{--}300 \text{ Myr}$ yields the most-unstable wavelength of $\sim 120 \text{ pc}$, entirely consistent with the numerical results. Due to the azimuthal compression by the MJI, some spiral segments attain sufficient density and form stars.

Evolution of models B10 and B30 is qualitatively similar to that of B100 in the sense that the inflow streams collide to form a star-forming nuclear ring, and accretion flows from the ring toward the center develop when the magnetic stress becomes strong enough (see Section 4.3.3). Figure 4.2 shows that unlike in model

B_{inf}, the rings in models B100, B30, and B10 become denser and thicker with time. The surface density inside the magnetized rings increases with time due to the radial accretion flows, forming a CND characterized by the central upturn of the radial surface density profile for $R \lesssim 50$ pc. We note that we are unable to evolve the magnetized models for arbitrarily long time, because the Alfvén speed becomes too large in the low-density region above and below the magnetized CND, severely limiting the Courant-Friedrichs-Lowy timestep.

4.3.2 Star Formation History

We define the SFR, \dot{M}_{SF} , as the total mass of sink particles with age less than 10 Myr, divided by 10 Myr. Figure 4.5 plots the temporal histories of \dot{M}_{SF} , the total gas mass M_{gas} , the gas depletion time $t_{\text{dep}} = M_{\text{gas}}/\dot{M}_{\text{SF}}$, and the ratio of the total magnetic energy E_{mag} to thermal energy E_{thm} inside the computational domain. In model **B_{inf}**, the SFR initially increases until $t \sim 17$ Myr because of the unhindered star formation at the orbit crowding regions. The FUV heating from the initial star formation and the turbulence injected by the SN feedback, however, soon suppress the star formation in the orbit-crowding regions, decreasing the ring SFR for $t \sim 20$ –30 Myr, during which star formation occurs mostly at the contact points where gas is compressed by the stream collisions. As the ring forms, the star forming regions become more and more evenly distributed along the whole length of the ring and the SFR increases again. After $t \sim 50$ Myr, the SFR becomes almost constant, reaching a steady-state value $\dot{M}_{\text{SF}} \sim 0.8$ –0.9 $M_{\odot} \text{ yr}^{-1}$, with a factor of ~ 2 stochastic fluctuations due to turbulence driven by SN feedback, similar to the models presented in Chapter 2.

The early star formation history of model B100 is very similar to that of model **B_{inf}** until $t \sim 200$ Myr, except for a brief period around $t \sim 25$ Myr when the magnetic fields compressed by the colliding streams lower the SFR near the contact points. After $t \sim 200$ Myr, however, strong magnetic fields in model B100 make the SFR reduced over time. The evolution of the SFR in models B30 and B10 is

qualitatively similar: it reaches a quasi-steady value at $t \sim 50\text{--}100\,\text{Myr}$ and starts to decline at $t \sim 120\,\text{Myr}$. An secularly increasing trend of M_{gas} shown in Figure 4.5(b) indicates that the decline of the SFR in magnetized models is not caused by the reduction of gas mass. It is rather because a larger fraction of the ring gas becomes inert for star formation, as reflected in the increasing t_{dep} at late time (Figure 4.5(c)). As the SFR drops below \dot{M}_{in} , the excess gas piles up in the ring and moves toward the center to form a CND, increasing M_{gas} .

Figure 4.5(d) shows that for the early ring-forming stage ($t < 100\,\text{Myr}$), the total magnetic energy is always smaller than the thermal energy, except for model B10 where $E_{\text{mag}}/E_{\text{thm}}$ becomes larger than unity for $t \sim 25\text{--}50\,\text{Myr}$. The magnetic energy in the computational domain gradually increases with time and eventually exceeds the thermal energy at $t = 77, 125$, and $228\,\text{Myr}$ for models B10, B30, and B100, respectively. We note that the magnetic energy advected with the inflow streams is very small because $\mathbf{v} \parallel \mathbf{B}$ near the nozzles for most of the time, and therefore cannot account for the increase of E_{mag} (see Appendix C). We also note that the time when E_{mag} exceeds E_{thm} roughly corresponds to the time when the SFR of the magnetized models starts to deviate from that of model B_{inf}. We will present more detailed analysis on the relation between magnetic fields and star formation in Section 4.4.2.

4.3.3 Magnetically Driven Accretion Flow

Figures 4.1 and 4.2 show that all magnetized models develop an accretion flow from the ring toward the center. For rotating magnetized disks, Appendix D shows the total mass accretion rate in a quasi-steady state can be written as

$$\dot{M}_{\text{acc}} \approx \dot{M}_{\text{Max}} + \dot{M}_{\text{Rey}}, \quad (4.18)$$

where \dot{M}_{Max} and \dot{M}_{Rey} are the mass accretion rates due to the Maxwell and Reynolds stresses, respectively (see Equations D.5). Figure 4.6 plots the temporal histories of \dot{M}_{acc} measured at $R = 100\,\text{pc}$ for all models, in comparison

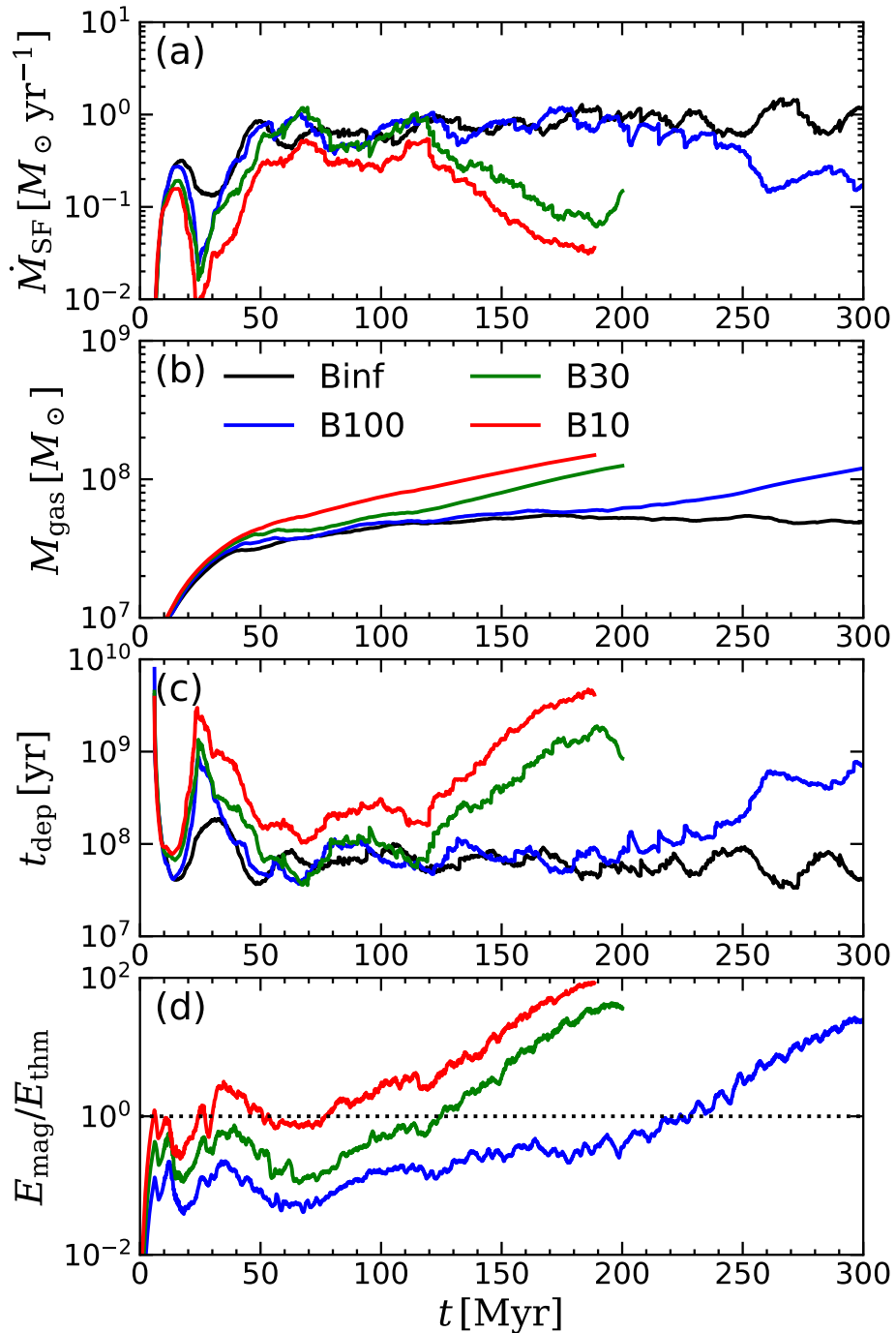


Figure 4.5. Temporal histories of (a) the SFR \dot{M}_{SF} , (b) the total gas mass M_{gas} , (c) the gas depletion time t_{dep} , and (d) the ratio $E_{\text{mag}}/E_{\text{thm}}$ of the total magnetic to kinetic energy inside the computational domain. The black, blue, green, and red lines correspond to models Binf, B100, B30, and B10, respectively.

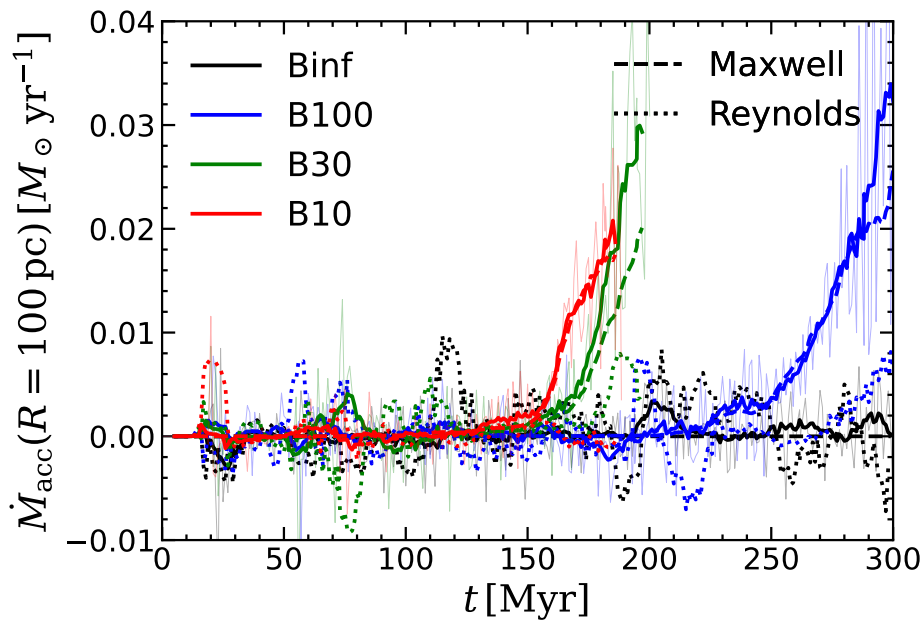


Figure 4.6. Temporal histories of the accretion rate at $R = 100 \text{ pc}$ for models Binf (black), B100 (blue), B30 (green), and B10 (red). Thin and thick solid lines correspond to the instantaneous and time-averaged (using a 10 Myr window) \dot{M}_{acc} , respectively, directly measured from the simulations. Dashed and dotted lines are the predicted accretion rates due to the Maxwell and Reynolds stress, using Equation (D.5) (averaged with a 10 Myr window), respectively. The increasing trend of \dot{M}_{acc} in magnetized models is well explained by the Maxwell stress.

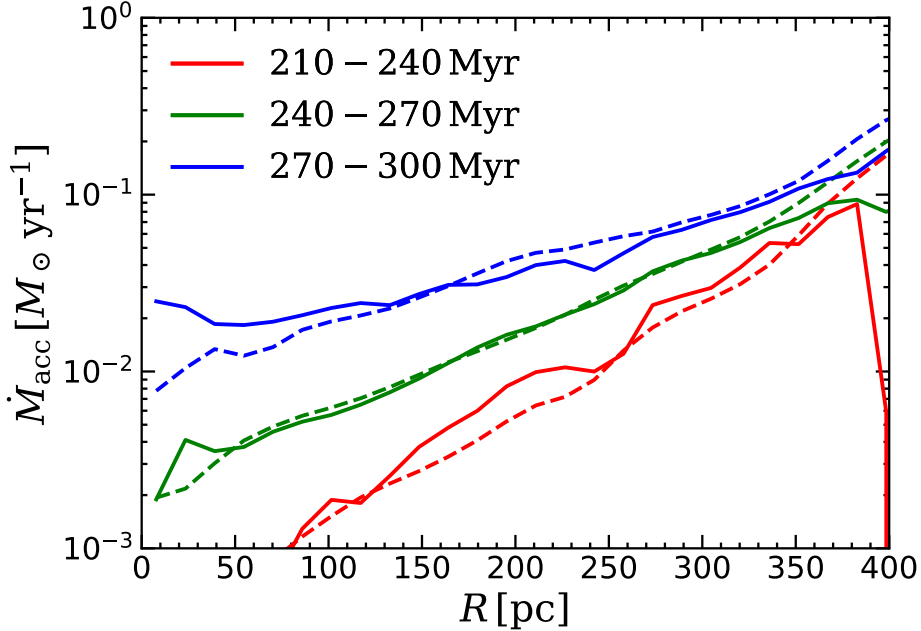


Figure 4.7. Radial profiles of the mass accretion rate at different epochs for model B100. Solid and dashed lines correspond to the measured and predicted accretion rate due to the Maxwell stress.

with the predictions due to the Reynolds and Maxwell stresses. In model B_{inf}, $\dot{M}_{\text{acc}} \sim 4 \times 10^{-4} M_{\odot} \text{ yr}^{-1}$ on average. While \dot{M}_{acc} in the magnetized models also remain small at early time, it starts to increase rapidly when $E_{\text{mag}}/E_{\text{thm}} \simeq 1$ and reaches $\dot{M}_{\text{acc}} \sim 0.02\text{--}0.03 M_{\odot} \text{ yr}^{-1}$ at the end of the runs. The temporal changes of \dot{M}_{acc} are in good agreement with \dot{M}_{Max} , indicating the mass accretion in our models is mainly driven by magnetic tension. The Reynolds stress makes some secondary contributions (up to $\sim 10\%$ of the Maxwell stress) at late times.

Figure 4.7 plots the radial profiles of \dot{M}_{acc} averaged for a few selected time interval for model B100, together with \dot{M}_{Max} . The accretion rate is not constant in radius but decreases toward the center, implying that mass is being deposited at all radii $< R_{\text{ring}}$, consistent with Figure 4.2. For $t = 270\text{--}300 \text{ Myr}$, the accretion rate near the ring is $\sim 0.1 M_{\odot} \text{ yr}^{-1}$, i.e., one tenth of the bar-driven inflow rate, while it decreases to $0.02\text{--}0.03 M_{\odot} \text{ yr}^{-1}$ near the center. The radial dependence of the measured accretion rates is overall in good agreement with \dot{M}_{Max} , indicating

the accretion flows are mediated by the magnetic tension forces.

4.4 Magnetic Fields in the Ring

In this section, we present evolution of the regular and turbulent magnetic fields in nuclear rings and explore their effects on the ring star formation. We also discuss vertical dynamical equilibrium in the presence of magnetic fields.

4.4.1 Growth of Magnetic Fields

The magnetic fields inside the ring and its interior are approximately axisymmetric (Figure 4.1), which motivates us to decompose the fields into a regular component $\bar{\mathbf{B}}$ and a irregular, turbulent component $\delta\mathbf{B}$ as

$$\mathbf{B}(R, \phi, z) = \bar{\mathbf{B}}(R, z) + \delta\mathbf{B}(R, \phi, z), \quad (4.19)$$

where the overbar denotes an azimuthal average

$$\bar{A}(R, z) \equiv \frac{1}{2\pi} \int_0^{2\pi} A d\phi, \quad (4.20)$$

for any physical quantity A .

Figure 4.8 plots the spatial distributions of the azimuthally-averaged \bar{n}_H , $|\bar{\mathbf{B}}| \equiv (\bar{B}_R^2 + \bar{B}_\phi^2 + \bar{B}_z^2)^{1/2}$, and $|\delta\bar{\mathbf{B}}|^2 \equiv (\delta\bar{B}_R^2 + \delta\bar{B}_\phi^2 + \delta\bar{B}_z^2)^{1/2}$ in the R - z plane, for model B100 at $t = 200$ and 300 Myr. At $t = 200$ Myr, gas and magnetic fields are concentrated mostly in the nuclear ring delineated by the black circle centered at $(R, z) = (500, 0)$ pc with radius 100 pc, while the regions outside of the ring is filled with diffuse, magnetized gas. Magnetic fields are dominated by the turbulent component over the regular component, especially outside the rings: the density-weighted average regular and turbulent magnetic field strengths are 8 and $22 \mu\text{G}$, respectively. As mentioned before, the magnetically-driven accretion from the ring forms a CND near the center at $t \sim 250$ Myr, marked by the rectangles in the

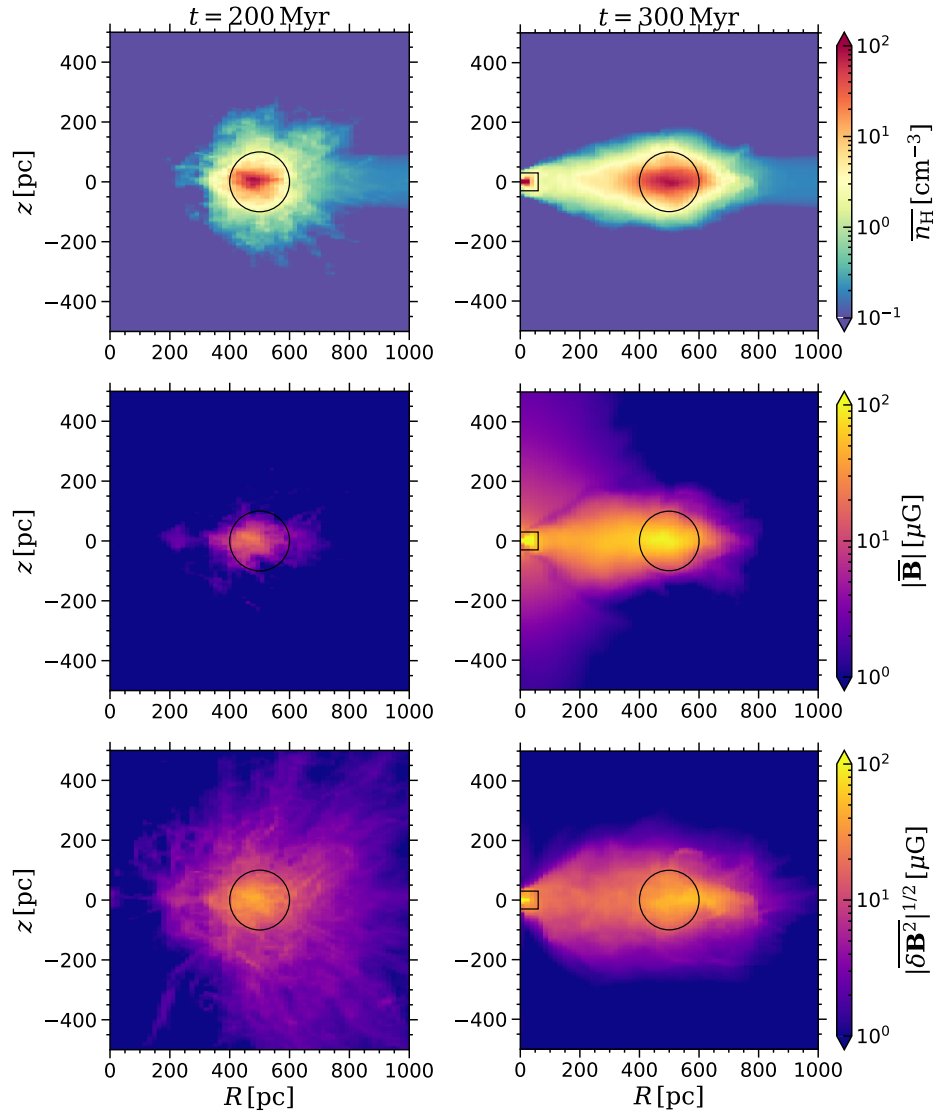


Figure 4.8. Spatial distributions of the azimuthally-averaged hydrogen number density (top) and the regular (middle) and turbulent (bottom) components of the magnetic fields at $t = 200$ (left column) and 300 Myr (right column). The black circles centered at $(R, z) = (500, 0)$ pc with radius 100 pc outline the ring, while the rectangles near $R = 0$ in the right column mark the CND.

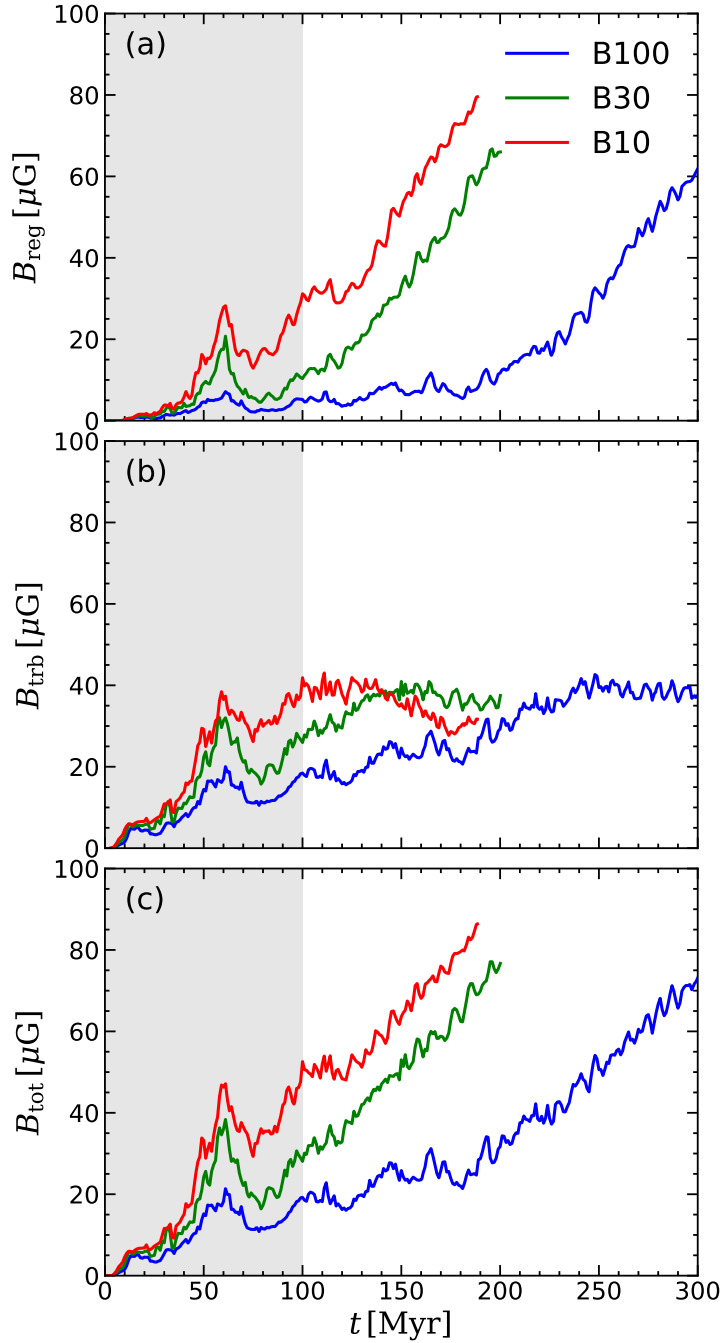


Figure 4.9. Temporal histories of the (a) regular, (b) turbulent, and (c) total magnetic field strength in the ring for models B100 (blue), B30 (green), and B10 (red). Magnetic fields are dominated by the turbulent component at early time, but become predominantly regular at late time.

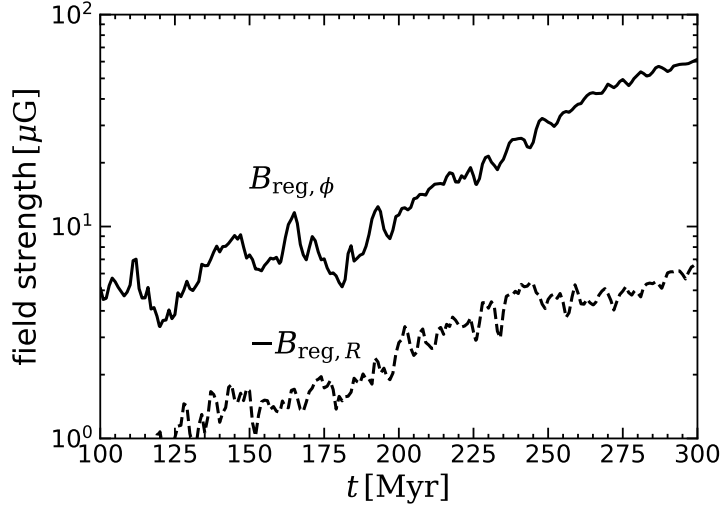


Figure 4.10. Temporal changes of the azimuthal (solid) and radial (dashed) components of \mathbf{B}_{reg} . Note that $B_{\text{reg},R}^r < 0$, i.e., it points toward the center. The pitch angle $\theta_p \equiv -\tan^{-1}(B_{\text{reg},R}/B_{\text{reg},\phi})$ is roughly constant at $\theta_p \sim 12^\circ$ for $t = 100$ – 240 Myr and $\sim 6^\circ$ for $t = 270$ – 300 Myr.

right column of Figure 4.8. The CND in our models is denser and more strongly magnetized than the ring.

To quantify the magnetic fields in the ring, we define the density-weighted average of the regular, turbulent, and total magnetic fields in the ring as

$$B_{\text{reg},j} \equiv \frac{\iint \bar{\rho} \bar{B}_j dR dz}{\int \bar{\rho} dR dz}, \quad (4.21)$$

$$B_{\text{trb},j} \equiv \frac{\iint \bar{\rho} \delta \bar{B}_j^{2^{1/2}} dR dz}{\int \bar{\rho} dR dz}, \quad (4.22)$$

$$B_{\text{tot},j} \equiv \frac{\iint \bar{\rho} \bar{B}_j^{2^{1/2}} dR dz}{\int \bar{\rho} dR dz}, \quad (4.23)$$

where the integration is performed over the circular regions shown in Figure 4.8. Note that $\bar{B}_j^2 = \bar{B}_j^2 + \delta \bar{B}_j^2$ by definition. Figure 4.9 plots the time evolution of $B_{\text{reg}} = |\mathbf{B}_{\text{reg}}|$, $B_{\text{trb}} = |\mathbf{B}_{\text{trb}}|$, and $B_{\text{tot}} = |\mathbf{B}_{\text{tot}}|$ for all models. We note that the ring is quite eccentric and undergoes damped oscillations of eccentricity before it enters

a quasi-steady state at $t \sim 100$ Myr, in which case $\bar{\mathbf{B}}$ and $\delta\mathbf{B}$ do not represent the regular and turbulent components.[‡]

The regular magnetic fields grow superlinearly in time (neglecting temporal fluctuations), reaching $B_{\text{reg}} \sim 60\text{--}80 \mu\text{G}$ at the end of the simulations. In contrast, the turbulent fields grow initially but soon saturate at $B_{\text{trb}} \sim 40 \mu\text{G}$. The total magnetic fields are initially dominated by the turbulent component, but are taken over by the regular component at later times. The growth rate of the magnetic fields is largely insensitive to β_{in} , suggesting that the field amplification is not related to the inflow boundary conditions. The magnetic fields grow earlier in models with smaller β_{in} because of the stronger seed fields. The growth of magnetic fields is likely driven by SN feedback and rotational shear, of which we will discuss in Section 4.5.2.

Figure 4.10 plots the temporal changes of the radial and azimuthal components of \mathbf{B}_{reg} for model B100 (the vertical regular fields are negligible), showing that both components grow in time. The sign of the radial component is negative, consistent with observed large-scale magnetic fields in the nuclear ring of NGC 1097 (Beck et al. 1999, 2005; Lopez-Rodriguez et al. 2021). However, the pitch angle of the regular fields, $\theta_p \equiv -\tan^{-1}(B_{\text{reg},R}/B_{\text{reg},\phi})$ is $\sim 6^\circ\text{--}12^\circ$, much smaller than $\theta_p \sim 40^\circ$ inferred from the observations, suggesting that there is large room for improvement in the theoretical modeling of magnetic fields especially with star formation and SN feedback.

4.4.2 Effects of Magnetic Fields on Star Formation

It is well known that magnetic fields inhibit star formation by providing additional pressure to resist gravitational collapse (McKee & Zweibel 1995; Hennebelle & Inutsuka 2019; Kim et al. 2021b). To assess the dynamical importance of magnetic fields relative to thermal and turbulent pressures, we measure the sound speed, vertical velocity dispersion, and Alfvén speed of the cold–warm medium with $T <$

[‡]During its eccentricity oscillations, the ring become almost circular at $t \sim 60$ Myr temporarily, producing the peak of B_{reg} , B_{trb} , and B_{tot} at that time.

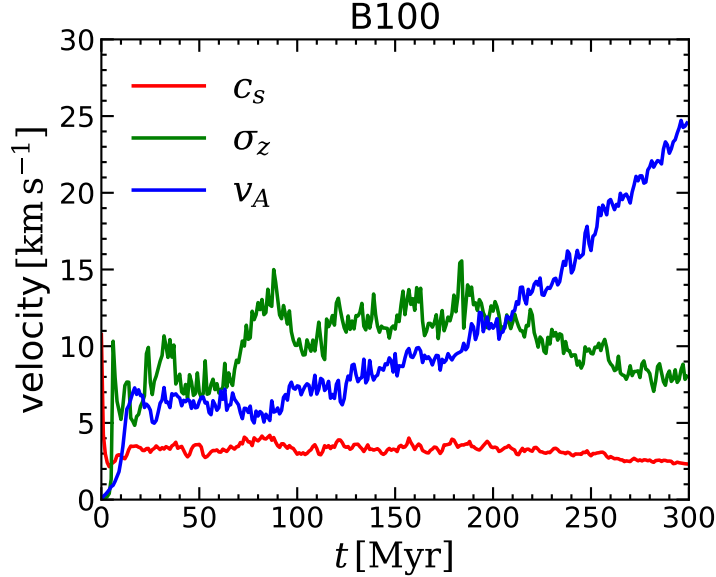


Figure 4.11. Temporal histories of the sound speed c_s (red), the vertical velocity dispersion σ_z (green), and the Alfvén speed v_A (blue) in model B100. While $c_s \sim 3 \text{ km s}^{-1}$ and $\sigma_z \sim 10 \text{ km s}^{-1}$ are relatively constant, v_A grows secularly with time to make turbulence become sub-Alfvénic at $t \sim 200 \text{ Myr}$.

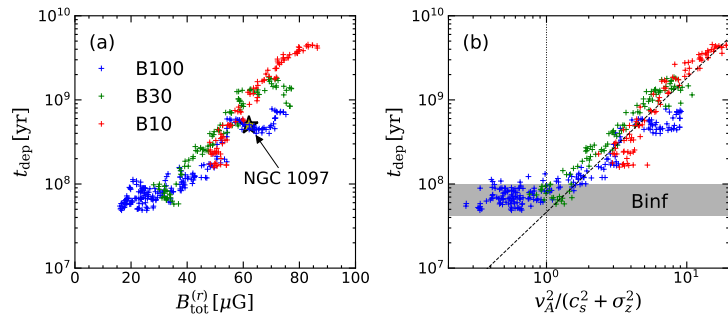


Figure 4.12. (a) Gas depletion time *vs.* the total magnetic field strength in the ring. Blue, green, and red symbols correspond to models B100, B30, and B10. The yellow star draws the observed values for the nuclear ring of NGC 1097 (Tabatabaei et al. 2018; Prieto et al. 2019). (b) Depletion time as a function of $\mathcal{E}_M \equiv v_A^2 / (\sigma_z^2 + c_s^2)$ in the cold–warm medium. The magnetic fields that become dynamically important for $\mathcal{E}_M > 1$ raise the depletion time. The vertical dotted line indicates $\mathcal{E}_M = 1$, while the dashed line draws $t_{\text{dep}} \propto \mathcal{E}_M^{1.6}$. The shaded region represents the range of the depletion time in model Binf for $t = 100\text{--}200 \text{ Myr}$.

2×10^4 K as

$$c_s = \left(\frac{\iiint_{z=-\Delta z}^{z=\Delta z} P \Theta dx dy dz}{\iiint_{z=-\Delta z}^{z=\Delta z} \rho \Theta dx dy dz} \right)^{1/2}, \quad (4.24)$$

$$\sigma_z = \left(\frac{\iiint_{z=-\Delta z}^{z=\Delta z} \rho v_z^2 \Theta dx dy dz}{\iiint_{z=-\Delta z}^{z=\Delta z} \rho \Theta dx dy dz} \right)^{1/2}, \quad (4.25)$$

$$v_A = \left(\frac{\iiint_{z=-\Delta z}^{z=\Delta z} B^2 / (4\pi) \Theta dx dy dz}{\iiint_{z=-\Delta z}^{z=\Delta z} \rho \Theta dx dy dz} \right)^{1/2}, \quad (4.26)$$

where $\Theta = 1$ for $T < 2 \times 10^4$ K and 0 otherwise. Figure 4.11 plots temporal changes of c_s , σ_z , and v_A of model B100, showing that $c_s \sim 3 \text{ km s}^{-1}$ and $\sigma_z \sim 10 \text{ km s}^{-1}$ exhibit modest variations with time. In contrast, the Alfvén speed secularly increases by nearly a factor of four from $v_A \sim 6 \text{ km s}^{-1}$ to $v_A \sim 24 \text{ km s}^{-1}$. After $t \sim 200$ Myr, the magnetic energy dominates the thermal and turbulent kinetic energies and the turbulence becomes sub-Alfvénic in the cold–warm medium. We note that this epoch roughly coincides with the time when the SFR starts to decline from its steady state value (Fig. 4.5a) and the gas accretion is initiated from the ring (Figure 4.6).

Figure 4.12 plots the gas depletion time as a function of B_{tot} or $\mathcal{E}_M \equiv v_A^2 / (\sigma_z^2 + c_s^2)$ for all magnetized models. Overall t_{dep} has a positive correlation with B_{tot} , suggesting that the magnetic fields inhibit star formation. For $\mathcal{E}_M \lesssim 1$, the measured depletion time is almost independent of \mathcal{E}_M and indistinguishable from that of model Binf shown as the shade. In contrast, when $\mathcal{E}_M \gtrsim 1$, the depletion time increases with \mathcal{E}_M as $t_{\text{dep}} \propto \mathcal{E}_M^{1.6}$, evidencing that star formation is suppressed by magnetic fields when the magnetic pressure becomes comparable or larger than the hydrodynamic (thermal plus turbulent) pressures. This is because the magnetic pressure within the cold–warm medium resists turbulent compression, lowering the mass fraction of dense ($n_H \gtrsim 500 \text{ cm}^{-3}$) star-forming gas. We note that not only radial collapse is opposed by the background toroidal magnetic fields but also azimuthal collapse is hindered by the transverse Alfvénic disturbances traveling along the ring (McKee & Zweibel 1995; Gammie & Ostriker 1996).

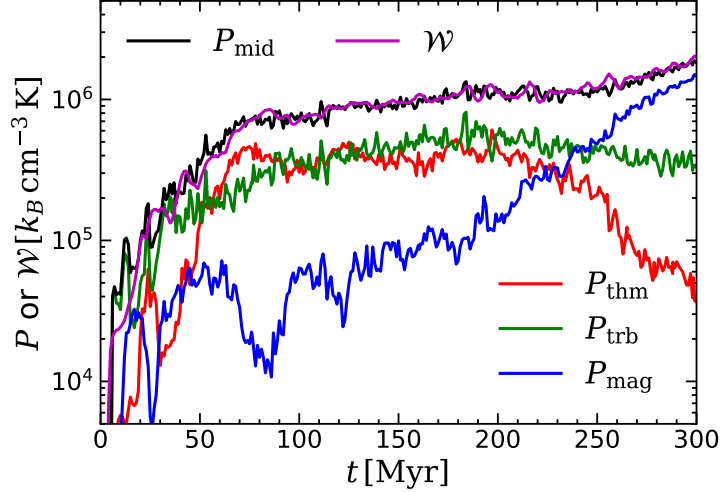


Figure 4.13. Temporal histories of the total midplane pressure (black) and gas weight (magenta), as well as the thermal (red), turbulent (green), and magnetic (blue) components of the midplane pressure. For all time, $P_{\text{mid}} \approx \mathcal{W}$, indicating that the vertical dynamical equilibrium holds very well. While the midplane pressure comes mostly from the thermal and turbulent components at early time, the magnetic pressure dominates after $t \sim 240$ Myr.

While the magnetic pressure locally stabilizes the cold–warm medium to reduce star formation, the ring is subject to the MJI that may promote star formation, as mentioned in Section 4.3.1. An efficient operation of the MJI needs strong magnetic fields and weak shear: the MJI becomes transient under strong shear. The ring in model B100 has relatively strong shear with the shear parameter of $q \equiv -d \ln \Omega / d \ln R = 0.87$. The associated shearing time is $t_{\text{shear}} = (q\Omega)^{-1} = 2.6$ Myr, which is about factor 2 shorter than the growth time $|\omega_{\max}|^{-1} \sim 5$ Myr of the fastest growing mode of the MJI at $t \sim 270$ –300 Myr. The resulting amplification factor of the MJI is $\exp(2\Gamma t_{\text{shear}}) \sim 3$, which is too small to trigger burst of star formation. Nevertheless, the MJI produce trailing spirals undergoing star formation, and is responsible for a modest increase of the SFR or decrease of t_{dep} for models B100 and B30 near the end of the simulations, seen in Figure 4.5(a),(c).

4.4.3 Vertical Dynamical Equilibrium

An insightful framework to understand galactic SFR is the pressure-regulated, feedback-modulated (PRFM) star formation theory (Ostriker & Kim 2022; see also Ostriker et al. 2010; Ostriker & Shetty 2011). This theory assumes that the ISM in disk galaxies should satisfy the vertical dynamical equilibrium between the total midplane pressure and the weight of the overlying gas, and that it is the star formation feedback that heats the gas and drives turbulence to maintain the required amount of midplane pressure. In this picture, the SFR is determined by the *demand* for the feedback to yield the pressure required for vertical dynamical equilibrium, which not only depends on the gas surface density but also on the local stellar density and the velocity dispersion (or gas scale height). Here we check if the vertical dynamical equilibrium holds in the magnetized nuclear ring, and assess the relative importance of the magnetic pressure to the other pressures.

We measure the thermal, turbulent, and magnetic pressures at the midplane as

$$P_{\text{thm}} = \frac{1}{2\Delta z A_{\text{ring}}} \iiint_{z=-\Delta z}^{z=\Delta z} P dz dx dy, \quad (4.27)$$

$$P_{\text{trb}} = \frac{1}{2\Delta z A_{\text{ring}}} \iiint_{z=-\Delta z}^{z=\Delta z} \rho v_z^2 dz dx dy, \quad (4.28)$$

$$P_{\text{mag}} = \frac{1}{2\Delta z A_{\text{ring}}} \iiint_{z=-\Delta z}^{z=\Delta z} -T_{zz} dz dx dy, \quad (4.29)$$

where the integration in the horizontal directions is performed over the annular region between $R_{\min} = 300$ pc and $R_{\max} = 700$ pc encompassing the nuclear ring, and $A_{\text{ring}} \equiv \pi(R_{\max}^2 - R_{\min}^2)$. Note that P_{mag} represents the effective magnetic pressure including the vertical magnetic tension (Boulares & Cox 1990). The weight of the ISM is given by

$$\mathcal{W} = \frac{1}{A_{\text{ring}}} \iiint_{z=0}^{z=L/2} \rho \frac{\partial \Phi_{\text{tot}}}{\partial z} dz dx dy. \quad (4.30)$$

It follows from Equation (4.2) that under quasi-steady equilibrium, $P_{\text{mid}} \equiv P_{\text{thm}} +$

$P_{\text{trb}} + P_{\text{mag}} \approx \mathcal{W}$ if the pressures at the horizontal and the upper boundaries of the cylindrical annulus is small compared to the midplane value.

Figure 4.13 plots P_{mid} and \mathcal{W} as well as the contributions of each pressure components for model B100, showing $P_{\text{mid}} \approx \mathcal{W}$ indeed holds well for all time. The magnetic pressure that is quite weak for $t \lesssim 150$ Myr keeps increasing and eventually exceeds the thermal and turbulent pressures after $t \sim 240$ Myr. As the ring becomes magnetically supported against the vertical gravity, the demand for the stellar feedback to replenish the thermal and turbulent pressures diminishes, causing the SFR to decline in Figure 4.5(a), qualitatively consistent with the PRFM theory.

4.5 Summary and Discussion

4.5.1 Summary

Nuclear rings at the centers of barred galaxies are active in star formation and threaded by magnetic fields with a mean strength of $\sim (50\text{--}100) \mu\text{G}$ (Beck et al. 2005; Yang et al. 2022). To study how magnetic fields affect star formation in nuclear rings, we consider magnetized gas streams to the rings and apply the semiglobal models of Chapter 2 to run MHD simulations. We adopt the modified TIGRESS framework (Kim & Ostriker 2017) to model the star formation and related FUV and SN feedback, as well as the shielding of FUV radiation and CR heating in dense environments. We fix the mass inflow rate to $\dot{M}_{\text{in}} = 1 M_{\odot} \text{ yr}^{-1}$ and the ring size to $R_{\text{ring}} = 500 \text{ pc}$, and vary the magnetic field strength of the streams via the plasma parameter $\beta_{\text{in}} = 10, 30, 100$. We also run a hydrodynamic model with $\beta_{\text{in}} = \infty$ for comparison. The magnetic fields in the streams are set parallel to the inflow velocity, consistent with observations (Beck et al. 2005; Lopez-Rodriguez et al. 2021). The main results of this work can be summarized as follows:

1. *Overall Evolution:* The two gas streams injected from the domain boundaries at the opposite sides collide with each other after about half an orbital time,

dissipating their orbital kinetic energy via shocks. As the gas orbits gradually circularize, a well-defined nuclear ring forms at the radius where the specific angular momentum of the inflowing gas matches that of the circular orbit. At about $t \sim 100$ Myr, the nuclear ring reaches a quasi-steady state in which the shape, SFR and gas mass remain approximately constant with time. Stars form randomly across the whole circumference of the ring, where the resulting feedback renders the ring turbulent. When the magnetic fields in the rings become strong enough (with Alfvén speed larger than the turbulent velocity dispersion), the associated magnetic stress develops radial accretion flows from the ring (Figs. 4.1 and 4.2) and decreases SFR. Due to actions of MJI with strong shear, the ring forms transient trailing spiral segments, some of which undergo star formation.

2. *Magnetic Fields and Their Growth:* Magnetic fields in the ring consists of the regular component and the irregular turbulent component. The turbulent magnetic fields grow in strength over time and saturates at $\sim 40 \mu\text{G}$ independent of β_{in} , likely due to the SN driven turbulent dynamo. In contrast, the regular magnetic fields do not saturate but keep growing with time, reaching $60\text{--}80 \mu\text{G}$ at the end of the runs. While the turbulent magnetic fields are approximately isotropic, the regular magnetic fields are dominated by the azimuthal component with a pitch angle of $\theta_p \sim 6^\circ\text{--}12^\circ$. While the overall field direction is mostly toroidal near the midplane, expansions of superbubbles created by clustered SN drag the toroidal fields to produce poloidal fields in high- $|z|$ regions.
3. *Magnetically Driven Accretion:* All our magnetized models develop accretion flows that slowly fill the regions inside the ring and eventually form a CND with radius $\lesssim 50$ pc at the center. This is in stark contrast to the unmagnetized model where the interior region is always filled with hot, rarefied gas. The gas accretion rates measured in the simulations are consistent with the theoretical quasi-steady rates due to the Maxwell stress, indicating that the

radial accretion is driven by magnetic tension. Consequently, the accretion rate that is proportional to the magnetic stress depends on the galactocentric radius and reaches $\sim (0.02\text{--}0.1) M_{\odot} \text{ yr}^{-1}$ at late time (Figs. 4.6 and 4.7).

4. *Effects of Magnetic Fields on Star Formation:* Since magnetic fields suppress star formation, the gas depletion time t_{dep} in the rings increases with the total magnetic field strength as $t_{\text{dep}} \propto \mathcal{E}_M^{1.6}$ for $\mathcal{E}_M = v_A^2 / (\sigma_z^2 + c_s^2) \lesssim 1$, although t_{dep} is almost independent of $\mathcal{E}_M < 1$ (Fig. 4.12). The ring well maintains the vertical dynamical equilibrium instantaneously, in which the weight of the ISM is balanced by the midplane total pressure. While the magnetic pressure is negligible in the vertical force balance at early time, it becomes dominant to lower the SFR at late time ($t \gtrsim 240$ Myr in model B100), as the magnetic support reduces the demand for SN feedback to replenish the thermal and turbulent pressures in the PRFM theory of Ostriker & Kim (2022).

4.5.2 Discussion

In our simulations, both regular and turbulent fields grow in strength with time, although the latter saturates at $\sim 40 \mu\text{G}$. We attribute the rapid growth and saturation of the turbulent fields to small-scale turbulent dynamo in which turbulent eddies resulting from SN feedback randomly stretch, twist, and fold the field lines to amplify them (Brandenburg & Subramanian 2005). Similar turbulent dynamo appears to operate in a number of simulations where turbulent magnetic fields rapidly grow out of very small seed fields due to SN-driven turbulence (e.g., Rieder & Teyssier 2016, 2017; Butsky et al. 2017; Pakmor et al. 2017; Gent et al. 2021). These studies have found that the growth rate of the turbulent dynamo is sensitive to the numerical resolution because the fastest growth occurs at the smallest resolvable scale, although the saturation amplitude is mostly independent of the numerical resolution.

Compared to the small-scale dynamo, large-scale dynamo responsible for or-

dered magnetic fields is still poorly understood. One possible explanation for the growth of B_{reg} in our simulations is that the strong differential rotation in the ring stretches the radial magnetic fields into the azimuthal direction to amplify the toroidal fields, while the expanding superbubbles due to clustered SN feedback produce poloidal magnetic fields by bending the toroidal magnetic fields.

For a shearing velocity field $\mathbf{v} = R\Omega(R)\mathbf{e}_\phi$, Equation (4.4) gives $\partial B_\phi / \partial t = -q\Omega B_R$, where q is the rate of shear. In our simulations, $q = 0.87$ and $\Omega = 0.45 \text{ Myr}^{-1}$ at $R = R_{\text{ring}}$. Taking $B_R = -1 \mu\text{G}$, it is possible for B_ϕ to grow to $40 \mu\text{G}$ in 100 Myr, enough to explain the growth of the regular azimuthal fields shown in Figure 4.10.

Since differential rotation alone cannot amplify the radial fields, the growth of $B_{\text{reg},R}$ requires additional explanation. Kulsrud (2000, see also Section 13.4.2 of Kulsrud 2005) proposed a qualitative model of dynamo driven by superbubbles, where the toroidal field lines lifted by the bubbles twist due to the Coriolis force and then escape from a galaxy, leaving net radial magnetic fields in the midplane. Such mechanism would require high SFR or shallow galactic potential, because the field lines would otherwise fall back to the midplane rather than genuinely escape a galaxy (Rafikov & Kulsrud 2000). In our simulations, clustered SN feedback often creates large superbubbles breaking out of the ring and carrying the ring magnetic fields to the domain boundary (Fig. 4.3), which potentially excite the aforementioned mechanism to amplify $B_{\text{reg},R}$. Comparison of Figures 4.5 and 4.9 indicates that the growth of $B_{\text{reg},R}$ slows down significantly as soon as the SFR decreases, which appears consistent with the above scenario.

One characteristic result of our simulations is that superbubbles breaking out of the cold–warm gas layer near the midplane drag the toroidal magnetic fields to produce poloidal magnetic fields in high-altitude regions (Figures 4.3 and 4.4). This provides one possible explanation of the origin of the observed toroidal-to-poloidal magnetic field transition in the CMZ, a nuclear ring of the Milky Way (Nishiyama et al. 2010). The poloidal magnetic walls of venting superbubbles (e.g., Figure

4.3) would likely be illuminated by the relativistic particles accelerated in-situ at SN shocks, potentially creating some nonthermal radio filaments found near radio bubbles (e.g., Radio Arc and Sgr C filament Heywood et al. 2022). We note that, for those filaments without any evident sources, Barkov & Lyutikov (2019) proposed that transiting pulsar wind nebulae may inject the relativistic particles to locally cast the background poloidal magnetic fields into view. The volume-filling poloidal magnetic fields generated by SN feedback (Figure 4.4) could naturally serve as a screen for such scenario.

The results of our simulations show that the magnetic torque produces significant inflows of gas from a nuclear ring toward the center, forming a CND. The mass accretion rate depends on R such that it is $0.02\text{--}0.03 M_{\odot} \text{ yr}^{-1}$ near the CND and as large as $\sim 0.1 M_{\odot} \text{ yr}^{-1}$ near the ring, although it becomes flatter over time. Assuming that the mass accretion occurs at a rate of $\sim 0.1 M_{\odot} \text{ yr}^{-1}$ in a steady fashion, the total mass of a CND produced by the magnetically driven accretion in 100 Myr would be $\sim 10^7 M_{\odot}$ which is in rough agreement with the observed CND masses (e.g., Combes et al. 2019). The magnetically driven mass accretion rate is proportional to $-B_R B_{\phi} = (B_R^2 + B_{\phi}^2)^{1/2} \sin(2\theta_P)/2$, so that the accretion rate would be higher if the magnetic fields are more loosely wrapped.

In Section 4.4.2, we compared the growth timescale of the MJI appropriate to our model conditions to the shearing timescale to conclude that the MJI is not strong enough to substantially enhance the SFR, because our models have strong shear ($q = 0.87$). The rate of shear in real nuclear rings may vary a lot from galaxy to galaxy depending on the mass distribution in central $\lesssim 1 \text{ kpc}$. For example, the rotation curve is almost flat ($q \sim 1$) in the ring of NGC 1097 (Onishi et al. 2015), while it is rising ($q \gtrsim 0.6$) in the CMZ (Sormani et al. 2020a). It would be interesting to examine whether the MJI in low-shear nuclear rings can counterbalance the stabilizing effect of magnetic pressure and even enhance the SFR.

Tabatabaei et al. (2018) measured the magnetic field strength in 11 giant clumps

in the nuclear ring of NGC 1097 and found a negative correlation between the star formation efficiency and magnetic field strength, suggesting that magnetic fields are inhibiting star formation in the nuclear ring of NGC 1097. The observed average magnetic field strength $62 \mu\text{G}$ (Tabatabaei et al. 2018) and depletion time $5 \times 10^8 \text{ yr}$ (Prieto et al. 2019) are consistent with the results of our simulations, as shown in Figure 4.12(a). Our numerical results suggest that the nuclear ring in NGC 1097 is indeed in the regime where magnetic fields are dynamically important to suppress star formation.

While our simulations demonstrate an interesting possibility of star formation quenching in nuclear rings and mass accretion to the center caused by magnetic fields, it is still uncertain what governs the growth of large-scale magnetic fields in nuclear rings and how their strength and pitch angles depend both on underlying rotation curve and feedback physics. These issues may be resolved by running more realistic simulations with improved physics. First of all, our present work assumes that magnetic fields in the gas streams are parallel to the velocity, this may not be the case in real galaxies and a small offset between the directions of \mathbf{B}_{in} and \mathbf{v}_{in} may result in significant changes in the strength and structure of magnetic fields in nuclear rings. To address this issue, it is necessary to run global simulations of barred galaxies in which gas streams along the dust lanes are modeled self-consistently. Second, since the free-fall time of star-forming clumps in the ring is shorter than the SN delay time of $\sim 4 \text{ Myr}$, early feedback in the form of radiation and stellar winds may affect gas dynamics in extreme environments such as nuclear rings. Lastly, ambipolar diffusion would reduce the magnetic field strength in the densest star-forming gas, making the negative effects of magnetic fields on star formation less pronounced.

Chapter 5

Conclusions and Future Work

5.1 Conclusions

This thesis aimed to understand what physical processes control the SFR in nuclear rings. To address this question, we designed numerical experiments of star-forming nuclear rings fed by bar-driven mass inflows. Although our semi-global framework (Figure 2.3) is limited by idealized treatment of mass inflows, it provides a unique opportunity to explicitly control the mass inflow rate and achieve high numerical resolution at the region of interest. Based on the results of three-dimensional (magneto)hydrodynamic simulations including the effects of star formation and feedback, we argue that the ring SFR and its time evolution are causally controlled by the mass inflow rate mediated by gas density, although the presence of strong magnetic fields can complicate this picture. Our main conclusions that led to the above statement are summarized as follows:

1. When the mass inflow rate is kept constant in time, the system remains very close to a steady equilibrium where star formation proceeds almost randomly throughout the whole length of the ring at an approximately constant rate. While feedback-driven turbulence induce a factor of ~ 2 stochastic fluctuations in the SFR, the SN feedback alone does not create large-amplitude burst-quench cycles, contrary to the predictions from one-dimensional ax-

isymmetric models. We conclude that the SN feedback is unlikely to cause episodic starbursts in three dimensions, unless the star formation and resulting feedback are spatially synchronized across the ring as if the ring is azimuthally symmetric.

2. When the mass inflow rate varies in time, the internal density structure of a ring adjusts itself while maintaining the vertical dynamical equilibrium, eventually causes SFR to vary in response. Because it takes a certain amount of time for this process to occur, too rapid variations in the inflow rate have limited effects on SFR. Mass inflow rates in real barred galaxies would have both slowly-varying and rapidly fluctuating components, where the star formation history in nuclear rings likely reflects the former. The critical timescale which divides “rapid” and “slow” is around an order of a few tens of megayears. When the inflow rate is abruptly increased for only one of the two dust lanes due to, e.g., infall of massive clumps, a brief period of lopsided star formation can ensue, which may explain observed asymmetry in some nuclear rings including our own CMZ.
3. The turbulent and thermal pressures at the ring midplane balance the weight of the overlying ISM, establishing vertical dynamical equilibrium. Short dynamical times resulting from galactic center environments keep the system close to equilibrium even when the mass inflow rate varies with time. Because of the mismatch between the gas streamlines and the trajectory of newborn clusters, some SN explosions occur outside of a nuclear ring, dumping their energy and momentum into hot ambient medium instead of replenishing the turbulent pressure in the ring. Combined with the strong external gravity due to high stellar density, the dynamical equilibrium requires relatively high SFR at a given amount of gas. Because of this, we expect nuclear rings to have shorter depletion time compared to outer disk region, although strongly magnetized rings may have longer depletion time (see below).

4. Magnetic fields in star-forming nuclear rings are efficiently amplified by SN-driven turbulence, while differential rotation generates large-scale toroidal magnetic fields out of radial components. When magnetic pressure of the ISM exceeds turbulent and thermal pressure, it smooths out the density contrast and prevents local gravitational collapse, lowering the SFR. For strongly magnetized nuclear rings, the SFR can significantly fall below the mass inflow rate, complicating the relation between the mass inflow rate and the ring SFR. Gas depletion time is positively correlated with the ratio of magnetic to hydrodynamic (turbulent plus thermal) pressure. When magnetic fields become sufficiently strong, the ring becomes susceptible to the MJI, although its growth is limited by strong shear. We suggest that some nuclear rings that have relatively long depletion time might possess strong magnetic fields. However, the rapid growth of the MJI in weak shear environment might potentially lead to bursts of star formation in some nuclear rings (see the next section).
5. Maxwell stress associated with the self-consistently generated large-scale toroidal magnetic fields causes mass accretion from a nuclear ring to central few tens of parsecs. The mass accretion rate increases with growing magnetic field strength and is consistent with the prediction from the angular momentum transport due to the magnetic tension. While the accretion rate is found to be less than 10% of the bar-driven inflow rate in our simulations, in general it will depend on the background rotation curve as well as the strength and pitch angle of magnetic fields. In contrast, gas launched toward the center by SN feedback tend to be destroyed by a central hot bubble rather than forming quasi-steady accretion flows. We suggest that magnetically driven accretion may help to produce the CNDs observed in the centers of external galaxies as well as of the Milky Way.

5.2 Future Work

This work mainly focused on the process of star formation in nuclear rings, using idealized, semi-global numerical simulations including the most important but limited set of ISM physics. There are many future directions that can be taken to extend this work by, e.g., adding other important physics, releasing restrictions imposed by artificial (although intentional) boundary conditions, or focusing on other aspects of circumnuclear star formation phenomena. Here, we list some examples to motivate further studies.

1. *Effects of early feedback:* Stellar winds and radiations from young massive stars can rapidly destroy the natal cloud, limiting the lifetime star formation efficiency well before the onset of the first SNe at ~ 4 Myr after the cluster formation (Kim et al. 2018b; Kruijssen et al. 2019). Such *early* feedback processes would play important roles especially in the high density galactic center regime where the cluster formation proceeds more rapidly compared to outer disk environments. An immediate next step would be to investigate effects of the early feedback on the ring star formation, with the special attention paid to whether it can change our conclusion regarding the steadiness of ring star formation.
2. *Effects of shear:* Toroidal magnetic fields are known to have *destabilizing* effects in galactic gaseous disks by damping the epicyclic motion, producing a new type of instability called the MJI (Lynden-Bell 1966; Elmegreen 1987; Kim & Ostriker 2001; Kim et al. 2002). Although the MJI grows to only a modest amplitude and does not induce strong starburst in our simulations, this is probably because our models have rather strong shear that limits the growth of non-axisymmetric disturbances. It needs to be examined whether our conclusion that magnetic fields suppress star formation in nuclear rings should be modified for the rings with low shear.
3. *Galactic wind launched by starburst nuclear ring:* The hot bubbles produced

by multiple SNe in the ring can break out of a warm gas layer and thereby launch galactic winds. Existing simulations of galactic winds employed local shearing-box to achieve high resolution at the expense of lack of realistic geometry (Kim et al. 2020b; Rathjen et al. 2021), suffered from limited resolution above and below the disk midplane due to the inherent nature of the (semi-)Lagrangian schemes (Hu 2019; Pandya et al. 2021), or used a prescribed feedback injection rather than self-consistent modeling of the star formation and feedback (Fielding et al. 2017; Fielding et al. 2018; Schneider et al. 2018, 2020). The semi-global numerical model we have developed in this work provides a unique opportunity to bridge this gap by simultaneously achieving uniformly high resolution of local models and realistic geometry of global models, as well as self-consistent treatment of star formation and feedback. Controlled numerical simulations including SN feedback, magnetic fields, and radiation in a step-by-step manner will not only clarify effects of each individual physical agents on wind properties but also reveal multiphase structure of galactic winds.

4. *Magnetically assisted mass inflow in hundred parsec scales:* Growing consensus is that bar-driven inflow does not extend all the way down to the central hundreds of parsecs, where different mechanisms are required to further transport gas inward (see Storchi-Bergmann & Schnorr-Müller 2019, and references therein). While a number of mechanisms have been proposed such as nuclear spiral shocks (Maciejewski 2004; Kim & Elmegreen 2017), magnetic fields (Beck et al. 2005), and SN feedback (Wada & Norman 2002; Emsellem et al. 2015), effects of magnetic fields have received relatively little attention. Moreover, comprehensive understanding of how these processes would work together in realistic multiphase ISM remains largely elusive. Our findings that magnetic stress alone can cause mass accretion with rates on the order of $0.01\text{--}0.1 M_{\odot} \text{ yr}^{-1}$ motivate more focused study of mass transport processes occurring at central 100 pc scales, including non-axisymmetric gravitational

potential and magnetic fields as well as star formation and feedback.

Bibliography

- Allard, E. L., Knapen, J. H., Peletier, R. F., & Sarzi, M. 2006, MNRAS, 371, 1087
- Alloin, D., & Kunth, D. 1979, A&A, 71, 335
- Ann, H. B., & Thakur, P. 2005, ApJ, 620, 197
- Armillotta, L., Krumholz, M. R., Di Teodoro, E. M., & McClure-Griffiths, N. M. 2019, MNRAS, 490, 4401
- Arsenault, R. 1989, A&A, 217, 66
- Athanassoula, E. 1992, MNRAS, 259, 345
- Athanassoula, E. 1994, in Proc. Int. Astrophysics Conf., Mass-Transfer Induced Activity in Galaxies, ed. I. Shlosman (Cambridge: Cambridge Univ. Press), 143
- . 2005, MNRAS, 358, 1477
- Athanassoula, E., Bosma, A., Creze, M., & Schwarz, M. P. 1982, A&A, 107, 101
- Athanassoula, E., Lambert, J. C., & Dehnen, W. 2005, MNRAS, 363, 496
- Bally, J., Stark, A. A., Wilson, R. W., & Henkel, C. 1988, ApJ, 324, 223
- Bally, J., Aguirre, J., Battersby, C., et al. 2010, ApJ, 721, 137
- Barkov, M. V., & Lyutikov, M. 2019, MNRAS, 489, L28
- Barnes, A. T., Longmore, S. N., Battersby, C., et al. 2017, MNRAS, 469, 2263

- Beck, R. 2015, A&A Rev., 24, 4
- Beck, R., Ehle, M., Shoutenkov, V., Shukurov, A., & Sokoloff, D. 1999, Nature, 397, 324
- Beck, R., Fletcher, A., Shukurov, A., et al. 2005, A&A, 444, 739
- Beck, R., & Krause, M. 2005, Astronomische Nachrichten, 326, 414
- Benedict, F. G., Smith, B. J., & Kenney, J. D. P. 1996, AJ, 111, 1861
- Benedict, G. F., Howell, D. A., Jørgensen, I., Kenney, J. D. P., & Smith, B. J. 2002, AJ, 123, 1411
- Bigiel, F., Leroy, A., Walter, F., et al. 2008, AJ, 136, 2846
- Binney, J., Gerhard, O. E., Stark, A. A., Bally, J., & Uchida, K. I. 1991, MNRAS, 252, 210
- Binney, J., & Tremaine, S. 2008, Galactic Dynamics: Second Edition (Princeton University Press)
- Bittner, A., Sánchez-Blázquez, P., Gadotti, D. A., et al. 2020, A&A, 643, A65
- Boris, J. P. 1970, in Proc. Fourth Conf. Numerical Simulation of Plasmas, ed. J. P. Boris & R. A. Shanny (Washington, DC: Naval Research Laboratory), 3–67
- Boulares, A., & Cox, D. P. 1990, ApJ, 365, 544
- Brandenburg, A., & Subramanian, K. 2005, Phys. Rep., 417, 1
- Buta, R. 1986, ApJS, 61, 609
- . 1995, ApJS, 96, 39
- Buta, R., & Combes, F. 1996, Fund. Cosmic Phys., 17, 95
- Butsky, I., Zrake, J., Kim, J.-h., Yang, H.-I., & Abel, T. 2017, ApJ, 843, 113

- Byrd, G., Rautiainen, P., Salo, H., Buta, R., & Crocher, D. A. 1994, AJ, 108, 476
- Callanan, D., Longmore, S. N., Kruijssen, J. M. D., et al. 2021, MNRAS, 505, 4310
- Combes, F. 1996, in Astronomical Society of the Pacific Conference Series, Vol. 91, IAU Colloq. 157: Barred Galaxies, ed. R. Buta, D. A. Crocker, & B. G. Elmegreen, 286
- Combes, F. 2001, in Advanced Lectures on the Starburst-AGN, ed. I. Arétxaga, D. Kunth, & R. Mújica (Singapore: World Scientific), 223
- Combes, F., & Gerin, M. 1985, A&A, 150, 327
- Combes, F., García-Burillo, S., Boone, F., et al. 2004, A&A, 414, 857
- Combes, F., García-Burillo, S., Audibert, A., et al. 2019, A&A, 623, A79
- Comerón, S., Knapen, J. H., Beckman, J. E., et al. 2010, MNRAS, 402, 2462
- Comerón, S., Martínez-Valpuesta, I., Knapen, J. H., & Beckman, J. E. 2009, ApJ, 706, L256
- Comerón, S., Salo, H., Laurikainen, E., et al. 2014, A&A, 562, A121
- Contopoulos, G., & Grosbol, P. 1989, A&A Rev., 1, 261
- Contopoulos, G., & Papayannopoulos, T. 1980, A&A, 92, 33
- Dale, J. E., Kruijssen, J. M. D., & Longmore, S. N. 2019, MNRAS, 486, 3307
- de Grijs, R., & Anders, P. 2012, ApJ, 758, L22
- Devereux, N. 1987, ApJ, 323, 91
- Draine, B. T. 1978, ApJS, 36, 595
- . 2011, Physics of the Interstellar and Intergalactic Medium (Princeton University Press)

- Ellison, S. L., Nair, P., Patton, D. R., et al. 2011, MNRAS, 416, 2182
- Elmegreen, B. G. 1987, ApJ, 312, 626
- . 1994, ApJ, 425, L73
- Elmegreen, B. G., Galliano, E., & Alloin, D. 2009, ApJ, 703, 1297
- Elmegreen, B. G., & Parravano, A. 1994, ApJ, 435, L121
- Emsellem, E., Renaud, F., Bournaud, F., et al. 2015, MNRAS, 446, 2468
- Englmaier, P., & Gerhard, O. 1997, MNRAS, 287, 57
- Fazeli, N., Busch, G., Eckart, A., et al. 2020, A&A, 638, A53
- Fielding, D., Quataert, E., & Martizzi, D. 2018, MNRAS, 481, 3325
- Fielding, D., Quataert, E., Martizzi, D., & Faucher-Giguère, C.-A. 2017, MNRAS, 470, L39
- Fisher, D. B., Bolatto, A. D., White, H., et al. 2019, ApJ, 870, 46
- Fisher, D. B., & Drory, N. 2011, ApJ, 733, L47
- Gadotti, D. A., Sánchez-Blázquez, P., Falcón-Barroso, J., et al. 2019, MNRAS, 482, 506
- Gadotti, D. A., Bittner, A., Falcón-Barroso, J., et al. 2020, A&A, 643, A14
- Gajda, G., Lokas, E. L., & Athanassoula, E. 2016, ApJ, 830, 108
- Gammie, C. F., & Ostriker, E. C. 1996, ApJ, 466, 814
- Garcia-Barreto, J. A., Downes, D., Combes, F., et al. 1991, A&A, 244, 257
- García-Burillo, S., Combes, F., Schinnerer, E., Boone, F., & Hunt, L. K. 2005, A&A, 441, 1011
- Gent, F. A., Mac Low, M.-M., Käpylä, M. J., & Singh, N. K. 2021, ApJ, 910, L15

- Genzel, R., Tacconi, L. J., Gracia-Carpio, J., et al. 2010, MNRAS, 407, 2091
- Ginsburg, A., Henkel, C., Ao, Y., et al. 2016, A&A, 586, A50
- Girard, M., Fisher, D. B., Bolatto, A. D., et al. 2021, ApJ, 909, 12
- Girichidis, P., Naab, T., Walch, S., et al. 2016, ApJ, 816, L19
- Glassgold, A. E., Galli, D., & Padovani, M. 2012, ApJ, 756, 157
- Gong, M., Ostriker, E. C., & Wolfire, M. G. 2017, ApJ, 843, 38
- Harada, N., Sakamoto, K., Martín, S., et al. 2019, ApJ, 884, 100
- Harris, J., Calzetti, D., Gallagher, John S., I., Conselice, C. J., & Smith, D. A. 2001, AJ, 122, 3046
- Hatchfield, H. P., Sormani, M. C., Tress, R. G., et al. 2021, ApJ, 922, 79
- Hatchfield, H. P., Battersby, C., Keto, E., et al. 2020, ApJS, 251, 14
- Heckman, T. M. 1980, A&A, 88, 365
- Hennebelle, P., & Ifrig, O. 2014, A&A, 570, A81
- Hennebelle, P., & Inutsuka, S.-i. 2019, Frontiers in Astronomy and Space Sciences, 6, 5
- Henshaw, J. D., Longmore, S. N., Kruijssen, J. M. D., et al. 2016, MNRAS, 457, 2675
- Heywood, I., Rammala, I., Camilo, F., et al. 2022, ApJ, 925, 165
- Ho, L. C., Filippenko, A. V., & Sargent, W. L. W. 1997, ApJ, 487, 591
- Hopkins, P. F. 2015, MNRAS, 450, 53
- Hopkins, P. F., Wetzel, A., Kereš, D., et al. 2018, MNRAS, 480, 800
- Hsieh, P.-Y., Matsushita, S., Liu, G., et al. 2011, ApJ, 736, 129

- Hu, C.-Y. 2019, MNRAS, 483, 3363
- Huntley, J. M., Sanders, R. H., & Roberts, W. W., J. 1978, ApJ, 221, 521
- Immer, K., Schuller, F., Omont, A., & Menten, K. M. 2012, A&A, 537, A121
- Indriolo, N., Geballe, T. R., Oka, T., & McCall, B. J. 2007, ApJ, 671, 1736
- Kalnajs, A. J. 1973, PASA, 2, 174
- Kataria, S. K., & Das, M. 2018, MNRAS, 475, 1653
- Kennicutt, Robert C., J. 1994, in Proc. Int. Astrophysics Conf., Mass-Transfer Induced Activity in Galaxies, ed. I. Shlosman (Cambridge: Cambridge Univ. Press), 131
- Kennicutt, Robert C., J. 1998, ApJ, 498, 541
- Kennicutt, R. C., & Evans, N. J. 2012, ARA&A, 50, 531
- Kim, C.-G., Kim, W.-T., & Ostriker, E. C. 2008a, ApJ, 681, 1148
- . 2008b, ApJ, 681, 1148
- . 2011a, ApJ, 743, 25
- Kim, C.-G., & Ostriker, E. C. 2015a, ApJ, 815, 67
- . 2015b, ApJ, 802, 99
- . 2017, ApJ, 846, 133
- . 2018, ApJ, 853, 173
- Kim, C.-G., Ostriker, E. C., & Kim, W.-T. 2013, ApJ, 776, 1
- Kim, C.-G., Ostriker, E. C., & Raileanu, R. 2017a, ApJ, 834, 25
- Kim, C.-G., Ostriker, E. C., Somerville, R. S., et al. 2020a, ApJ, 900, 61

- . 2020b, ApJ, 900, 61
- Kim, E., Kim, S. S., Choi, Y.-Y., et al. 2018a, MNRAS, 479, 562
- Kim, J.-G., Kim, W.-T., & Ostriker, E. C. 2018b, ApJ, 859, 68
- Kim, J.-G., Kim, W.-T., Ostriker, E. C., & Skinner, M. A. 2017b, ApJ, 851, 93
- Kim, J.-G., Ostriker, E. C., & Filippova, N. 2021a, ApJ, 911, 128
- . 2021b, ApJ, 911, 128
- Kim, S. S., Saitoh, T. R., Jeon, M., et al. 2011b, ApJ, 735, L11
- Kim, W.-T., & Elmegreen, B. G. 2017, ApJ, 841, L4
- Kim, W.-T., Kim, C.-G., & Ostriker, E. C. 2020c, ApJ, 898, 35
- Kim, W.-T., & Moon, S. 2016, ApJ, 829, 45
- Kim, W.-T., & Ostriker, E. C. 2001, ApJ, 559, 70
- Kim, W.-T., Ostriker, E. C., & Stone, J. M. 2002, ApJ, 581, 1080
- Kim, W.-T., Seo, W.-Y., & Kim, Y. 2012a, ApJ, 758, 14
- Kim, W.-T., Seo, W.-Y., Stone, J. M., Yoon, D., & Teuben, P. J. 2012b, ApJ, 747, 60
- Kim, W.-T., & Stone, J. M. 2012, ApJ, 751, 124
- Kim, Y., & Kim, W.-T. 2014, MNRAS, 440, 208
- Knapen, J. H., Sharp, R. G., Ryder, S. D., et al. 2010, MNRAS, 408, 797
- Koepferl, C. M., Robitaille, T. P., Morales, E. F. E., & Johnston, K. G. 2015, ApJ, 799, 53
- Kormendy, J., & Kennicutt, Robert C., J. 2004, ARA&A, 42, 603

- Koyama, H., & Inutsuka, S.-i. 2002, *ApJ*, 564, L97
- Kroupa, P. 2001, *MNRAS*, 322, 231
- Kruegel, E., & Tutukov, A. V. 1993, *A&A*, 275, 416
- Kruijssen, J. M. D., Dale, J. E., & Longmore, S. N. 2015, *MNRAS*, 447, 1059
- Kruijssen, J. M. D., Longmore, S. N., Elmegreen, B. G., et al. 2014, *MNRAS*, 440, 3370
- Kruijssen, J. M. D., Schruba, A., Chevance, M., et al. 2019, *Nature*, 569, 519
- Krumholz, M. R., & Kruijssen, J. M. D. 2015, *MNRAS*, 453, 739
- Krumholz, M. R., Kruijssen, J. M. D., & Crocker, R. M. 2017, *MNRAS*, 466, 1213
- Kulsrud, R. M. 2000, in *Plasmas in the Universe: Proceedings of the International School of Physics “Enrico Fermi”*, Course CXLII, ed. B. Coppi, A. Ferrari, & E. Sindoni (Amsterdam: IOS Press), 107–125
- Kulsrud, R. M. 2005, *Plasma physics for astrophysics* (Princeton, NJ: Princeton University Press)
- Laine, S., Kenney, J. D. P., Yun, M. S., & Gottesman, S. T. 1999, *ApJ*, 511, 709
- Lancaster, L., Ostriker, E. C., Kim, J.-G., & Kim, C.-G. 2021a, *ApJ*, 914, 89
- . 2021b, *ApJ*, 914, 90
- Leitherer, C., Schaerer, D., Goldader, J. D., et al. 1999, *ApJS*, 123, 3
- Lemaster, M. N., & Stone, J. M. 2009, *ApJ*, 691, 1092
- Li, Z., Shen, J., & Kim, W.-T. 2015, *ApJ*, 806, 150
- Lin, L., Li, C., Du, C., et al. 2020, *MNRAS*, 499, 1406

- Longmore, S. N. 2014, in *The Labyrinth of Star Formation*, ed. D. Stamatellos, S. Goodwin, & D. Ward-Thompson, Vol. 36 (Cham: Springer International Publishing), 373
- Longmore, S. N., Bally, J., Testi, L., et al. 2013, *MNRAS*, 429, 987
- Loose, H. H., Kruegel, E., & Tutukov, A. 1982, *A&A*, 105, 342
- Lopez-Rodriguez, E., Beck, R., Clark, S. E., et al. 2021, *ApJ*, 923, 150
- Lu, X., Zhang, Q., Kauffmann, J., et al. 2019, *ApJ*, 872, 171
- Lynden-Bell, D. 1966, *The Observatory*, 86, 57
- Ma, C., de Grijs, R., & Ho, L. C. 2017, *ApJS*, 230, 14
- . 2018, *ApJ*, 857, 116
- Maciejewski, W. 2004, *MNRAS*, 354, 892
- Maoz, D., Barth, A. J., Sternberg, A., et al. 1996, *AJ*, 111, 2248
- Martizzi, D., Faucher-Giguère, C.-A., & Quataert, E. 2015, *MNRAS*, 450, 504
- Martizzi, D., Fielding, D., Faucher-Giguère, C.-A., & Quataert, E. 2016, *MNRAS*, 459, 2311
- Mazzuca, L. M., Knapen, J. H., Veilleux, S., & Regan, M. W. 2008, *ApJS*, 174, 337
- McKee, C. F., & Zweibel, E. G. 1995, *ApJ*, 440, 686
- Meier, D. S., Turner, J. L., & Hurt, R. L. 2008, *ApJ*, 675, 281
- Mihos, J. C., & Hernquist, L. 1994, *ApJ*, 425, L13
- Molina, J., Ibar, E., Godoy, N., et al. 2020, *A&A*, 643, A78
- Molinari, S., Bally, J., Noriega-Crespo, A., et al. 2011, *ApJ*, 735, L33
- Morgan, W. W. 1958, *PASP*, 70, 364

- Nair, P. B., & Abraham, R. G. 2010, ApJS, 186, 427
- Narayanan, D., Krumholz, M. R., Ostriker, E. C., & Hernquist, L. 2012, MNRAS, 421, 3127
- Neufeld, D. A., & Wolfire, M. G. 2017, ApJ, 845, 163
- Nishiyama, S., Hatano, H., Tamura, M., et al. 2010, ApJ, 722, L23
- Nogueras-Lara, F., Schödel, R., Gallego-Calvente, A. T., et al. 2020, Nature Astronomy, 4, 377
- Oh, S., Oh, K., & Yi, S. K. 2012, ApJS, 198, 4
- Onishi, K., Iguchi, S., Sheth, K., & Kohno, K. 2015, ApJ, 806, 39
- Orr, M. E., Hayward, C. C., Medling, A. M., et al. 2020, MNRAS, 496, 1620
- Osmer, P. S., Smith, M. G., & Weedman, D. W. 1974, ApJ, 192, 279
- Ostriker, E. C., & Kim, C.-G. 2022, arXiv e-prints, arXiv:2206.00681
- Ostriker, E. C., McKee, C. F., & Leroy, A. K. 2010, ApJ, 721, 975
- Ostriker, E. C., & Shetty, R. 2011, ApJ, 731, 41
- Pakmor, R., Gómez, F. A., Grand, R. J. J., et al. 2017, MNRAS, 469, 3185
- Pandya, V., Fielding, D. B., Anglés-Alcázar, D., et al. 2021, MNRAS, 508, 2979
- Pastoriza, M. G. 1975, Ap&SS, 33, 173
- Patsis, P. A., & Athanassoula, E. 2000, A&A, 358, 45
- Piñol-Ferrer, N., Fathi, K., Carignan, C., et al. 2014, MNRAS, 438, 971
- Pierce-Price, D., Richer, J. S., Greaves, J. S., et al. 2000, ApJ, 545, L121
- Pillai, T., Kauffmann, J., Tan, J. C., et al. 2015, ApJ, 799, 74

- Piner, B. G., Stone, J. M., & Teuben, P. J. 1995, ApJ, 449, 508
- Portegies Zwart, S. F., Makino, J., McMillan, S. L. W., & Hut, P. 2002, ApJ, 565, 265
- Prendergast, K. H. 1962, in The Distribution and Motion of Interstellar Matter in Galaxies, ed. L. Woltjer, 217
- Prendergast, K. H. 1967, in Radio Astronomy and the Galactic System, ed. H. van Woerden, Vol. 31, 303
- Prieto, M. A., Fernandez-Ontiveros, J. A., Bruzual, G., et al. 2019, MNRAS, 485, 3264
- Rafikov, R. R., & Kulsrud, R. M. 2000, MNRAS, 314, 839
- Rahner, D., Pellegrini, E. W., Glover, S. C. O., & Klessen, R. S. 2017, MNRAS, 470, 4453
- Ramón-Fox, F. G., & Aceves, H. 2020, MNRAS, 491, 3908
- Rathjen, T.-E., Naab, T., Girichidis, P., et al. 2021, MNRAS, 504, 1039
- Rautiainen, P., & Salo, H. 2000, A&A, 362, 465
- Regan, M. W., Sheth, K., & Vogel, S. N. 1999, ApJ, 526, 97
- Regan, M. W., & Teuben, P. 2003, ApJ, 582, 723
- Regan, M. W., Vogel, S. N., & Teuben, P. J. 1997, ApJ, 482, L143
- Ridley, M. G. L., Sormani, M. C., Treß, R. G., Magorrian, J., & Klessen, R. S. 2017, MNRAS, 469, 2251
- Rieder, M., & Teyssier, R. 2016, MNRAS, 457, 1722
- . 2017, MNRAS, 471, 2674
- Roberts, W. W., J., Huntley, J. M., & van Albada, G. D. 1979, ApJ, 233, 67

- Rogers, H., & Pittard, J. M. 2013, MNRAS, 431, 1337
- Sakamoto, K., Matsushita, S., Peck, A. B., Wiedner, M. C., & Iono, D. 2004, ApJ, 616, L59
- Salak, D., Nakai, N., Hatakeyama, T., & Miyamoto, Y. 2016, ApJ, 823, 68
- Sanders, R., Morano, E., & Druguet, M.-C. 1998, Journal of Computational Physics, 145, 511
- Sanders, R. H., & Huntley, J. M. 1976, ApJ, 209, 53
- Sanders, R. H., & Tubbs, A. D. 1980, ApJ, 235, 803
- Sarzi, M., Allard, E. L., Knapen, J. H., & Mazzuca, L. M. 2007, MNRAS, 380, 949
- Sawada, T., Hasegawa, T., Handa, T., & Cohen, R. J. 2004, MNRAS, 349, 1167
- Schinnerer, E., Maciejewski, W., Scoville, N., & Moustakas, L. A. 2002, ApJ, 575, 826
- Schmidt, E. O., Mast, D., Díaz, R. J., et al. 2019, AJ, 158, 60
- Schmidt, M. 1959, ApJ, 129, 243
- Schneider, E. E., Ostriker, E. C., Robertson, B. E., & Thompson, T. A. 2020, ApJ, 895, 43
- Schneider, E. E., Robertson, B. E., & Thompson, T. A. 2018, ApJ, 862, 56
- Schwarz, M. P. 1981, ApJ, 247, 77
- . 1984, MNRAS, 209, 93
- Seo, W.-Y., & Kim, W.-T. 2013, ApJ, 769, 100
- . 2014, ApJ, 792, 47
- Seo, W.-Y., Kim, W.-T., Kwak, S., et al. 2019, ApJ, 872, 5

- Sérsic, J. L., & Pastoriza, M. 1965, PASP, 77, 287
- . 1967, PASP, 79, 152
- Shen, J., & Sellwood, J. A. 2004, ApJ, 604, 614
- Sheth, K., Vogel, S. N., Regan, M. W., Thornley, M. D., & Teuben, P. J. 2005, ApJ, 632, 217
- Shetty, R., & Ostriker, E. C. 2012, ApJ, 754, 2
- Shimizu, T. T., Davies, R. I., Lutz, D., et al. 2019, MNRAS, 490, 5860
- Shin, J., Kim, S. S., Baba, J., et al. 2017, ApJ, 841, 74
- Shlosman, I., Begelman, M. C., & Frank, J. 1990, Nature, 345, 679
- Shlosman, I., Frank, J., & Begelman, M. C. 1989, Nature, 338, 45
- Skinner, M. A., & Ostriker, E. C. 2015, ApJ, 809, 187
- Sofue, Y. 1995, PASJ, 47, 527
- Song, Y., Linden, S. T., Evans, A. S., et al. 2021, ApJ, 916, 73
- Sorensen, S. A., Matsuda, T., & Fujimoto, M. 1976, Ap&SS, 43, 491
- Sormani, M. C., & Barnes, A. T. 2019, MNRAS, 484, 1213
- Sormani, M. C., Binney, J., & Magorrian, J. 2015a, MNRAS, 449, 2421
- . 2015b, MNRAS, 451, 3437
- . 2015c, MNRAS, 454, 1818
- Sormani, M. C., Magorrian, J., Nogueras-Lara, F., et al. 2020a, MNRAS, 499, 7
- Sormani, M. C., Sobacchi, E., Fragkoudi, F., et al. 2018, MNRAS, 481, 2
- Sormani, M. C., Tress, R. G., Glover, S. C. O., et al. 2020b, MNRAS, 497, 5024

- Sormani, M. C., Treß, R. G., Glover, S. C. O., et al. 2019, MNRAS, 488, 4663
- Springel, V. 2010, MNRAS, 401, 791
- Sternberg, A., McKee, C. F., & Wolfire, M. G. 2002, ApJS, 143, 419
- Stone, J. M., & Gardiner, T. 2009, NewA, 14, 139
- Stone, J. M., Gardiner, T. A., Teuben, P., Hawley, J. F., & Simon, J. B. 2008, ApJS, 178, 137
- Storchi-Bergmann, T., & Schnorr-Müller, A. 2019, Nature Astronomy, 3, 48
- Strickland, D. K., Heckman, T. M., Colbert, E. J. M., Hoopes, C. G., & Weaver, K. A. 2004, ApJS, 151, 193
- Sutherland, R. S., & Dopita, M. A. 1993, ApJS, 88, 253
- Tabatabaei, F. S., Minguez, P., Prieto, M. A., & Fernández-Ontiveros, J. A. 2018, Nature Astronomy, 2, 83
- Telesco, C. M., & Gatley, I. 1981, ApJ, 247, L11
- Tokuyama, S., Oka, T., Takekawa, S., et al. 2019, PASJ, 71, S19
- Torrey, P., Hopkins, P. F., Faucher-Giguère, C.-A., et al. 2017, MNRAS, 467, 2301
- Tress, R. G., Sormani, M. C., Glover, S. C. O., et al. 2020, MNRAS, 499, 4455
- Utomo, D., Bolatto, A. D., Wong, T., et al. 2017, ApJ, 849, 26
- Väisänen, P., Barway, S., & Randriamanakoto, Z. 2014, ApJ, 797, L16
- van Albada, T. S., & Sanders, R. H. 1982, MNRAS, 201, 303
- Veilleux, S., Cecil, G., & Bland-Hawthorn, J. 2005, ARA&A, 43, 769
- Wada, K. 2004, in Coevolution of Black Holes and Galaxies, ed. L. C. Ho (Cambridge: Cambridge University Press), 186

- Wada, K., & Norman, C. A. 2002, ApJ, 566, L21
- Wada, K., Papadopoulos, P. P., & Spaans, M. 2009, ApJ, 702, 63
- Wang, J., Kauffmann, G., Overzier, R., et al. 2012, MNRAS, 423, 3486
- Weinberger, R., Springel, V., & Pakmor, R. 2020, ApJS, 248, 32
- Wilson, C. D., Elmegreen, B. G., Bemis, A., & Brunetti, N. 2019, ApJ, 882, 5
- Wolfire, M. G., McKee, C. F., Hollenbach, D., & Tielens, A. G. G. M. 2003, ApJ, 587, 278
- Wyse, R. F. G., Gilmore, G., & Franx, M. 1997, ARA&A, 35, 637
- Yang, Y., Irwin, J., Li, J., et al. 2022, ApJ, 927, 4
- Yoast-Hull, T. M., Gallagher, J. S., & Zweibel, E. G. 2016, MNRAS, 457, L29
- Yukita, M., Swartz, D. A., Tennant, A. F., Soria, R., & Irwin, J. A. 2012, ApJ, 758, 105
- Yusef-Zadeh, F., Hewitt, J. W., Arendt, R. G., et al. 2009, ApJ, 702, 178
- Zhang, D. 2018, Galaxies, 6, 114

Appendix A

Orbit Integration of Sink Particles with the Coriolis Force

Here, we describe how we apply the Boris algorithm, which is widely used in plasma simulations, to integrate the equations of motion for sink particles in a rotating frame; we also present a test result. Note that Equation (2.14) is formally equivalent to the equations of motion for charged particles under the Lorentz force if we substitute $-\nabla\Phi_{\text{tot}} \rightarrow q\mathbf{E}/m$ and $2\Omega_p \rightarrow q\mathbf{B}/m$.

As in the original TIGRESS implementation, we adopt a *Kick-Drift-Kick* (KDK) leap-frog integrator, for which a semi-implicit discretization of Equation (2.14) leads to

$$\frac{\mathbf{v}^{n+1/2} - \mathbf{v}^{n-1/2}}{\Delta t} = \mathbf{g}^n - 2\Omega_p \times \left(\frac{\mathbf{v}^{n+1/2} + \mathbf{v}^{n-1/2}}{2} \right), \quad (\text{A.1})$$

where $\mathbf{g} = -\nabla\Phi_{\text{tot}}$ is the gravitational acceleration. Boris (1970) noted that the *electric* and *magnetic* forces in Equation (A.1) can be separated by changing the variables to

$$\mathbf{v}^- \equiv \mathbf{v}^{n-1/2} + \frac{\Delta t}{2}\mathbf{g}^n, \quad (\text{A.2})$$

$$\mathbf{v}^+ \equiv \mathbf{v}^{n+1/2} - \frac{\Delta t}{2}\mathbf{g}^n, \quad (\text{A.3})$$

yielding

$$\frac{\mathbf{v}^+ - \mathbf{v}^-}{\Delta t} = (\mathbf{v}^+ + \mathbf{v}^-) \times \boldsymbol{\Omega}_p. \quad (\text{A.4})$$

Taking the inner product of Equation (A.4) with $(\mathbf{v}^+ + \mathbf{v}^-)$ reveals $|\mathbf{v}^+| = |\mathbf{v}^-|$, i.e., Equation (A.4) describes a pure rotation of the vector \mathbf{v}^- into \mathbf{v}^+ , with $\boldsymbol{\Omega}_p$ being the axis of the rotation, as depicted in Figure A.1. It can be shown that the rotation angle θ in Figure A.1 satisfies $\tan(\theta/2) = \Omega_p \Delta t$. Assuming $\boldsymbol{\Omega}_p$ is parallel to the z -axis, Equation (A.4) can be decomposed to

$$v_x^+ = \frac{1 - (\Omega_p \Delta t)^2}{1 + (\Omega_p \Delta t)^2} v_x^- + \frac{2\Omega_p \Delta t}{1 + (\Omega_p \Delta t)^2} v_y^-, \quad (\text{A.5})$$

$$v_y^+ = -\frac{2\Omega_p \Delta t}{1 + (\Omega_p \Delta t)^2} v_x^- + \frac{1 - (\Omega_p \Delta t)^2}{1 + (\Omega_p \Delta t)^2} v_y^-, \quad (\text{A.6})$$

$$v_z^+ = v_z^-. \quad (\text{A.7})$$

In the Boris algorithm, therefore, it takes three steps to update $\mathbf{v}^{n-1/2}$ to $\mathbf{v}^{n+1/2}$. (1)

Apply the gravitational force for a half time step as in Equation (A.2), (2) solve for the epicyclic rotation using Equation (A.5)–(A.7), and (3) apply the gravitational force for the remaining half time step according to Equation (A.3).

As a test calculation, we consider a particle orbiting solely under a rotating, rigid-body potential $\Phi_{\text{ext}} = \frac{1}{2}R^2\Omega_0^2$ with $\Omega_0 = 1$, $\Omega_p = 0.5$ and $\Phi_{\text{self}} = 0$. The orbit is limited to the $z = 0$ plane. The equations of motion for such a particle are given by

$$\ddot{x} = -(\Omega_0^2 - \Omega_p^2)x + 2\Omega_p \dot{y}, \quad (\text{A.8a})$$

$$\ddot{y} = -(\Omega_0^2 - \Omega_p^2)y - 2\Omega_p \dot{x}. \quad (\text{A.8b})$$

Equations (A.8a) and (A.8b) are linear, coupled ordinary differential equations

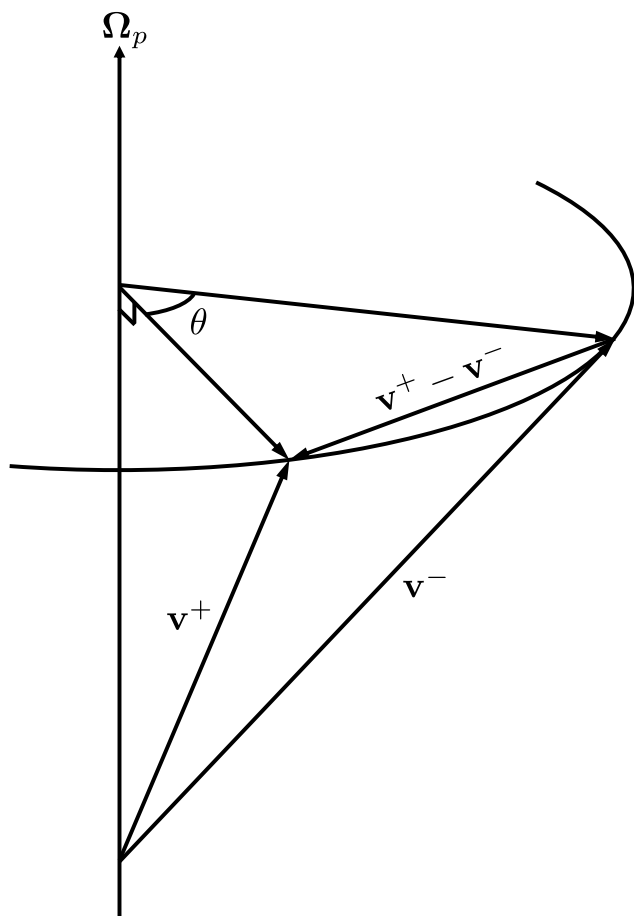


Figure A.1. Illustration of the velocity vector rotation described by Equation (A.4). The rotation angle θ is defined in the plane perpendicular to Ω_p .

with analytic solutions

$$x(t) = A_1 \cos(\Omega_- t) + A_2 \sin(\Omega_- t) + A_3 \cos(\Omega_+ t) + A_4 \sin(\Omega_+ t), \quad (\text{A.9a})$$

$$y(t) = -A_2 \cos(\Omega_- t) + A_1 \sin(\Omega_- t) + A_4 \cos(\Omega_+ t) - A_3 \sin(\Omega_+ t), \quad (\text{A.9b})$$

where $\Omega_{\pm} \equiv \Omega_0 \pm \Omega_p$ and

$$A_1 = (\Omega_+ x(0) + \dot{y}(0))/(2\Omega_0), \quad (\text{A.10})$$

$$A_2 = (\dot{x}(0) - \Omega_+ y(0))/(2\Omega_0), \quad (\text{A.11})$$

$$A_3 = (\Omega_- x(0) - \dot{y}(0))/(2\Omega_0), \quad (\text{A.12})$$

$$A_4 = (\dot{x}(0) + \Omega_- y(0))/(2\Omega_0), \quad (\text{A.13})$$

with initial position $[x(0), y(0)]$ and velocity $[\dot{x}(0), \dot{y}(0)]$.

As the initial conditions, we take $(x, y) = (1, 0)$ and $(\dot{x}, \dot{y}) = (0, 2)$ at $t = 0$ and integrate Equation (A.8) using the Boris algorithm with a fixed time step of $\Delta t = 0.1/\Omega_0$. For comparison, we also integrate Equation (A.8) using the standard KDK leap-frog integrator. Figure A.2 compares the resulting orbits in the x - y plane, the position offsets relative to the analytic predictions (Equation A.9), and the errors in the Jacobi integral $E_J \equiv \frac{1}{2}(\dot{x}^2 + \dot{y}^2) + \Phi_{\text{tot}}$. The position offsets oscillate and secularly grow with time in both methods, but the growth rate is much lower in the Boris algorithm. The relative errors in the Jacobi integral are bounded below 0.2% in the Boris algorithm.

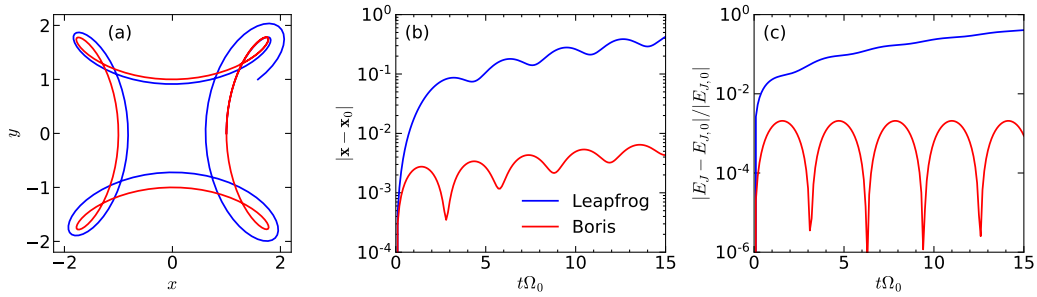


Figure A.2. Comparison between the Boris algorithm (red) and the standard leapfrog integrator (blue) for (a) the particle orbits in the x - y plane, (b) the position offsets between the numerical and analytic solutions, and (c) the relative errors in the Jacobi integral E_J under the rotating, rigid-body potential $\Phi_{\text{ext}} = \frac{1}{2}R^2\Omega_0^2$ with $\Omega_0 = 1$ and $\Omega_p = 0.5$. The initial conditions are $(x, y) = (1, 0)$ and $(\dot{x}, \dot{y}) = (0, 2)$ and $\Delta t = 0.1/\Omega_0$ is taken for the timestep.

Appendix B

Seed Magnetic Fields

Because \mathbf{B}_{in} is set parallel to \mathbf{v}_{in} for gas streams at the boundaries, no magnetic fields can be introduced into the computational domain if \mathbf{B}_{in} and \mathbf{v}_{in} are evaluated at the same location. However, `Athena` defines the magnetic fields and velocity at the cell centers and face centers, respectively, and this slight mismatch in the evaluation positions leads to $\mathbf{v}_{\text{in}} \times \mathbf{B}_{\text{in}} \neq 0$, inducing seed magnetic fields in the active zones adjacent to the nozzle boundaries for a brief period of time.

To illustrate this, Figure B.1 diagrams a part of the computational domain near the positive- y boundary. The thick lines denote the ghost zones belonging to the upper nozzle, while the thin lines mark the adjacent active zones. The blue arrows at the cell centers represent (v_x, v_y) of the stream at $t = 0$, which are non-zero only in the ghost zones and zero in the active zones. The red dashed arrows at the cell faces indicate (B_x, B_y) of the stream at $t = 0$, which are also non-zero only in the ghost faces and zero in the active faces: the red solid arrows at the cell centers are computed by averaging the neighboring face-centered fields. Because $B_y = 0$ initially at the outermost cell faces of the active domain (where B_y is updated via Equations 4.1–4.5), the y -component of the cell-centered magnetic fields at the first ghost zones (adjacent to the active domain) is reduced by half, resulting in \mathbf{B} inclined to \mathbf{v} which is fixed by the boundary conditions. As a result, non-vanishing electromotive forces are assigned to the edges of the outermost active cells which

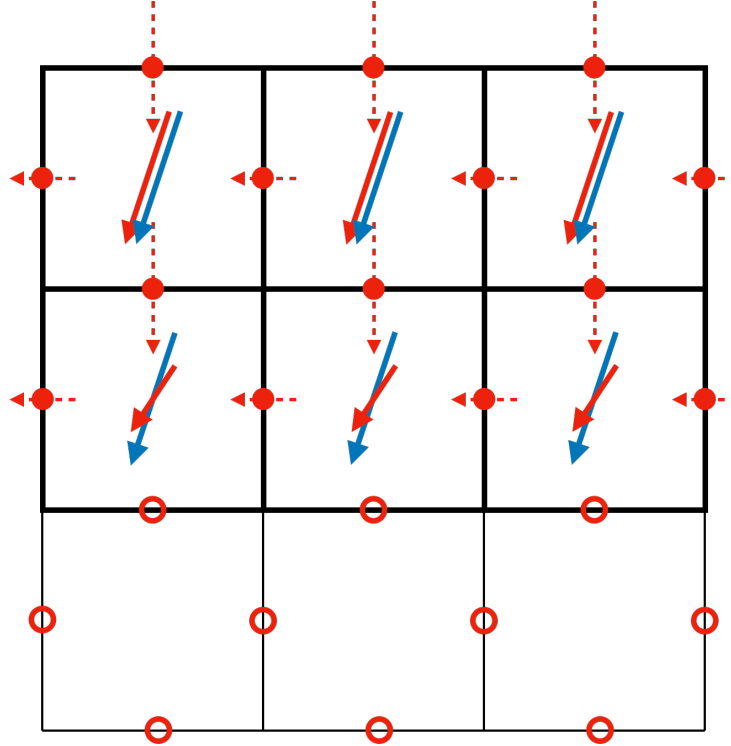


Figure B.1. Illustration of the magnetic fields and velocity vectors in the ghost zones (thick lines) belonging to the nozzle at the positive y -boundary. The thin lines indicate the adjacent active zones. The blue arrows represent the velocity vectors, defined at the cell centers. The dashed and solid arrows in red indicate the face- and cell-centered magnetic field vectors, respectively, with the latter computed from the former. Filled and open circles mark the ghost and active cell faces, respectively.

subsequently induce magnetic fields into the computational domain. We stress that this process occurs only for a few Myr in the very beginning: B_y at the outermost cell faces soon attains the same values as in the ghost zones to satisfy Equation (4.16). We also note that our initial conditions for the gas streams obey $\nabla \cdot \mathbf{B} = 0$ in the active domain, which is preserved by the constrained transport algorithm in **Athena**.

Appendix C

Magnetic Energy Conservation

Here, we show that the inflow boundary conditions for gas streams has little effect on the growth of the magnetic energy in our simulations. We start with the rate of change of the total magnetic energy in the computational domain, which is given by

$$\frac{dE_{\text{mag}}}{dt} = \int \frac{\partial}{\partial t} \left(\frac{B^2}{8\pi} \right) dV = \frac{1}{4\pi} \int \mathbf{B} \cdot [\nabla \times (\mathbf{v} \times \mathbf{B})] dV, \quad (\text{C.1})$$

where Equation (4.4) is used. Integrating Equation (C.1) by parts and applying the divergence theorem, one obtains

$$\frac{dE_{\text{mag}}}{dt} = \frac{1}{4\pi} \oint [(\mathbf{v} \times \mathbf{B}) \times \mathbf{B}] \cdot d\mathbf{A} - \frac{1}{4\pi} \int \mathbf{v} \cdot [(\nabla \times \mathbf{B}) \times \mathbf{B}] dV, \quad (\text{C.2})$$

where $d\mathbf{A}$ denotes the area element. The first term in the right hand side of Equation (C.2) represents the Poynting flux integrated over the domain boundaries, while the second term is the amount of work done by the fluid against the Lorentz force per unit time. It is evident that there is no magnetic energy flux through the boundaries when $\mathbf{v} \parallel \mathbf{B}$. One can further expand the cross products in the first term to write

$$\frac{dE_{\text{mag}}}{dt} = - \oint \mathbf{v} \cdot \mathbf{T} \cdot d\mathbf{A} - \oint \frac{B^2}{8\pi} \mathbf{v} \cdot d\mathbf{A} - \frac{1}{4\pi} \int \mathbf{v} \cdot [(\nabla \times \mathbf{B}) \times \mathbf{B}] dV. \quad (\text{C.3})$$

In this form, the first and second term correspond to the work done by the Maxwell stress at the boundaries and the advection of magnetic energy by the inflowing gas, respectively. Again, the two terms exactly cancel each other when $\mathbf{v} \parallel \mathbf{B}$.

As explained in Appendix B, \mathbf{v} is not parallel to \mathbf{B} at the domain boundaries for initial ~ 10 Myr, in which case the boundary work term does not exactly cancel the advection term, resulting the growth of E_{mag} . However, as the domain is subsequently filled with gas, the growth of magnetic energy is soon dominated by the volumetric work term (the last term in Equation (C.3)), while the stress term and the advection term cancel each other as \mathbf{v} aligns with \mathbf{B} . To see this, we estimate the rate of the magnetic energy growth due to the advection term alone by

$$\begin{aligned} \frac{dE_{\text{mag,adv}}}{dt} &= - \oint_{\text{nozzles}} \frac{B_{\text{in}}^2}{8\pi} \mathbf{v}_{\text{in}} \cdot d\mathbf{A} = - \frac{2k_B T_{\text{in}}}{\beta_{\text{in}} \mu_H m_H} \int_0^{\zeta_{\text{in}}} \rho_{\text{in}} \mathbf{v}_{\text{in}} \cdot \hat{\mathbf{y}} \cos^2 \left(\frac{\pi\zeta}{2\zeta_{\text{in}}} \right) 2\pi\zeta d\zeta \\ &\approx 0.6 \frac{k_B T_{\text{in}} \dot{M}_{\text{in}}}{\beta_{\text{in}} \mu_H m_H}, \end{aligned} \quad (\text{C.4})$$

where Equation (4.17) is used. For the parameters of model B100, $dE_{\text{mag,adv}}/dt \sim 1.4 \times 10^{49} \text{ erg Myr}^{-1}$, such that the total magnetic energy that would be advected into the computational domain during 10 Myr is $1.4 \times 10^{50} \text{ erg}$, which is on the similar order with $E_{\text{mag}} = 4.3 \times 10^{50} \text{ erg}$ of model B100 measured at $t = 10$ Myr. On the other hand, the total magnetic energy advected into the computational domain at the end of the run ($t = 300$ Myr) is $4.2 \times 10^{51} \text{ erg}$, which is about two orders of magnitude smaller than the measured $E_{\text{mag}} = 7.2 \times 10^{53} \text{ erg}$ at the same time. Since the Maxwell stress term tends to cancel the advection term when \mathbf{v} is parallel to \mathbf{B} , this indicates that the actual magnetic energy that is flowing through the nozzles should be negligible compared to what is generated by an MHD dynamo through the last term in Equation (C.3). We thus conclude that our boundary conditions have little effect on the magnetic energy growth and that the magnetic field amplification in our simulations is driven by an MHD dynamo.

Appendix D

Mass Accretion Rates due to Maxwell and Reynolds Stresses

For gas to move radially inward slowly while moving on an approximately circular orbit, it must lose angular momentum. Here we derive the theoretical accretion rates due to the Maxwell and Reynolds stresses.

Multiplying R to the azimuthal component of Equation (4.2) yields

$$\frac{\partial(\rho R v_\phi)}{\partial t} + \nabla \cdot (\rho R v_\phi \mathbf{v} + R P \mathbf{e}_\phi) = -R \mathbf{e}_\phi \cdot (\nabla \cdot \mathbf{T}) - 2R \Omega_p \rho v_R - \rho \frac{\partial \Phi_{\text{tot}}}{\partial \phi}, \quad (\text{D.1})$$

where \mathbf{e}_ϕ is the unit vector in the azimuthal direction. The second and third terms in the left hand side of Equation (D.2) are the angular momentum flux due to macroscopic bulk fluid motion and the microscopic thermal motion of its constituent particles, respectively. The three source terms in the right hand side are the torque density due to the Lorentz force, the Coriolis force, and gravity, respectively. To focus on the radial mass inflow, we azimuthally average Equation (D.1).

Integrating the resulting equation in the vertical direction, one obtains

$$\frac{\partial \langle \rho R v_\phi \rangle}{\partial t} + \frac{1}{R} \frac{\partial R^2 \langle \rho v_R v_\phi \rangle}{\partial R} = -\frac{1}{R} \frac{\partial R^2 \langle T_{R\phi} \rangle}{\partial R} - 2R \Omega_p \langle \rho v_R \rangle, \quad (\text{D.2})$$

where $\langle A \rangle \equiv (2\pi)^{-1} \iint Ad\phi dz$ for any physical quantity A , and $T_{R\phi} = -B_R B_\phi / (4\pi)$ is the R - ϕ component of the Maxwell stress tensor. Note that $\langle \rho \partial \Phi_{\text{tot}} / \partial \phi \rangle = \langle \rho \partial \Phi_{\text{self}} / \partial \phi \rangle \approx 0$ unless there is a systematic azimuthal offset between the density and self-gravitational potential. The magnetic torque term is due to the magnetic tension alone.

We decompose the velocity field into ordered and random components: $\mathbf{v} = v_{\text{circ}} \mathbf{e}_\phi + \mathbf{u}$, where $v_{\text{circ}} \equiv v_{\text{rot}} - R\Omega_p$ is the circular velocity in the rotating reference frame and \mathbf{u} is the random velocity. Substituting \mathbf{u} for \mathbf{v} , Equation (D.2) becomes

$$\frac{\partial \langle \rho R u_\phi \rangle}{\partial t} - \frac{\dot{M}_{\text{acc}}}{2\pi R} \frac{\partial R v_{\text{circ}}}{\partial R} + \frac{1}{R} \frac{\partial R^2 \langle \rho u_R u_\phi \rangle}{\partial R} = -\frac{1}{R} \frac{\partial R^2 \langle T_{R\phi} \rangle}{\partial R} - 2R\Omega_p \langle \rho u_R \rangle, \quad (\text{D.3})$$

where $\dot{M}_{\text{acc}} \equiv -2\pi R \langle \rho u_R \rangle$ is the mass inflow rate at radius R . Assuming a quasi-steady state (which turns out to be the case in our simulations) and neglecting the Coriolis term which is unimportant for small R , Equation (D.3) is simplified to

$$\dot{M}_{\text{acc}} \approx \dot{M}_{\text{Max}} + \dot{M}_{\text{Rey}}, \quad (\text{D.4})$$

where \dot{M}_{Max} and \dot{M}_{Rey} are the mass accretion rates due to the Maxwell and Reynolds stress, defined as

$$\dot{M}_{\text{Max}} = 2\pi \left(\frac{\partial R v_{\text{circ}}}{\partial R} \right)^{-1} \frac{\partial R^2 \langle T_{R\phi} \rangle}{\partial R} \quad (\text{D.5a})$$

$$\dot{M}_{\text{Rey}} = 2\pi \left(\frac{\partial R v_{\text{circ}}}{\partial R} \right)^{-1} \frac{\partial R^2 \langle \rho u_R u_\phi \rangle}{\partial R}, \quad (\text{D.5b})$$

respectively. Figures 4.6 and 4.7 show that the mass accretion in our simulations is dominated by \dot{M}_{Max} , that is, magnetic tension.

요 약

핵고리는 막대은하 중심에서 흔히 발견되는 고리 형태의 구조물이다. 핵고리는 대체로 별탄생이 활발히 일어나는 지역이며, 작은 크기 ($\sim 1 \text{ kpc}$) 에도 불구하고 은하 전체에 맞먹는 별형성률을 보여주기도 한다. 은하 중심에서 집중적으로 일어나는 이러한 별형성은 유사팽대부를 비롯한 중심부 고밀도 항성 구조물들의 기원과 관련이 있다고 여겨진다. 또한 핵고리의 활발한 별탄생으로부터 비롯된 복사, 항성풍, 초신성 폭발 등과 같은 되먹임 작용은 은하풍의 형성이나 은하핵의 활동성에도 영향을 미칠 것으로 생각된다. 관측적으로 핵고리의 별형성률은 다양한 시간척도와 진폭을 가지고 변화해 온 것으로 보이는데, 무엇이 핵고리의 별형성률을 결정하며 그것의 시간적 변화를 야기하는지에 대한 이론적 이해는 미진하다. 이에 본 학위논문에서는 3차원 자기유체역학적 수치모의실험을 통하여 핵고리의 별형성률에 중요한 영향을 줄 것으로 생각되는 질량 유입률과 초신성 되먹임 및 자기장의 효과를 단계적으로 살펴보고 이를 통해 핵고리의 별형성률을 조절하는 물리적 기작을 밝히고자 하였다.

제 2장에서는 본 학위논문에서 사용한 준광역 모형을 소개하고 이를 이용하여 질량 유입률을 일정하게 통제했을 경우에 핵고리의 별형성이 어떤 양상으로 일어나는지 알아보았다. 다양한 크기와 질량 유입률을 갖는 모형들에 대하여 3차원 유체역학적 수치모의실험을 수행한 결과 핵고리의 별형성률은 고리의 크기와는 무관하며 질량 유입률과 강한 상관관계를 보인다는 것을 발견하였다. 핵고리의 별형성률은 약 2배 내외의 무작위적 요동을 제외하면 모든 경우 시간에 따라 일정하게 유지되었는데 이는 관측되는 핵고리 별형성률의 시간에 따른 변화를 초신성 되먹임의 효과만으로 설명할 수 없음을 시사한다. 핵고리의 별형성률이 질량 유입률에 의해 결정되는 반면, 핵고리의 기체 질량은 되먹임에 의한 중심면 압력이 중심면 위쪽에 놓인 기체의 무게와 정역학적 평형을 이루는 과정에서 결정되었다.

제 3장에서는 질량 유입률이 시간에 따라 변화하거나 비대칭적일 경우 핵고리의 별형성이 어떠한 양상으로 일어날 것인지 알아보았다. 질량 유입률의 변화 주기가 너무 짧은 ($< 50 \text{ Myr}$) 경우를 제외하면 핵고리의 별형성률은 약간의 시차를 두고 질량 유입률을 따라 변화하였다. 별형성률의 변화에 따라 중심면 압력과 기체 무게 역시 시간에 따라 변화하였지만 질량 유입률이 일정한 경우와 마찬가지로 수직 방향 정역학적

평형은 항상 잘 유지되었다. 별형성률과 기체 질량의 관계는 PRFM*이론이 예측하는 바와 잘 부합하였다. 비대칭적인 질량 유입이 항상 비대칭적인 별형성을 일으키지는 않으나, 두 면지띠 (dust lane) 중 한 쪽의 질량 유입률이 갑자기 증가하는 경우에는 일시적으로 비대칭적 별형성이 일어날 수 있음을 보였다.

제 4장에서는 자기장이 핵고리의 역학적 진화와 별형성에 미치는 역할을 알아보기 위하여 앞서 사용한 준광역 모형을 발전시켜 자기장을 포함한 질량 유입을 다룰 수 있게 하였다. 다양한 초기 자기장을 갖는 모형에 대해 3차원 자기유체역학적 수치모의 실험을 수행한 결과 자기장이 핵고리 영역에서 빠르게 증폭됨을 발견하였는데, 이는 초신성 되먹임과 차등회전이 함께 작용한 결과라고 생각된다. 연이은 초신성 폭발에 의해 만들어진 초거품(superbubble)은 중심면 기체층을 뚫고 높은 고도로 팽창하는 과정에서 고리 영역의 원환(toroidal) 자기장을 끌고 나가 자오면(poloidal) 자기장을 생성하였다. 자기압력은 열적 압력과 난류에 의한 운동학적 압력을 능가하여 종국에는 핵고리의 별형성률을 떨어트렸다. 자기장력(magnetic tension)에 의한 돌림힘은 기체의 각운동량을 빼앗아 핵고리로부터 중심방향으로의 강착 흐름을 야기하여 핵주변원반(circumnuclear disk)을 형성하였다.

이러한 결과들을 종합해 볼 때 핵고리의 별형성률이 긴 시간 간격 동안 변화하는 것은 주로 질량 유입률의 변화에 기인하는 것이며, 초신성 되먹임은 비교적 작은 진폭과 시간척도를 갖는 무작위적 요동을 일으키는 한편 수직 방향 정역학적 평형을 유지함으로서 고갈시간을 결정하는 역할을 한다고 결론지을 수 있었다. 단, 자기장이 아주 강한 핵고리의 경우 별형성률이 질량 유입률보다 매우 작아질 수 있어서 별형성률과 질량 유입률의 관계를 다소 복잡하게 만들 수 있으므로 추후 이에 대한 더 많은 연구가 이루어져야 할 것이다.

주요어: 나선은하, 은하진화, 별탄생, 은하중심, 성간물질, 항성되먹임, 자기유체역학적 수치모의실험

학 번: 2016-26780

*Pressure-regulated, feedback-modulated theory

감사의 글

오랜 시간동안 제게 천문학을 가르쳐 주시고 더 나아갈 수 있도록 격려해 주신 김웅태 교수님께 깊이 감사드립니다. 지도학생이 즐겁게 연구하고 학자로서 성장할 수 있도록 모든 지원을 아끼지 않는 지도교수님을 만난 것은 제 인생에 더없이 큰 행운입니다. 그동안 교수님께 직접 보고 배운 학문하는 자세를 바탕으로 좋은 열매를 맺어 보답하겠습니다. I am deeply indebted to my mentor, Eve Ostriker, for providing continuous support and encouragement during my PhD study. I was more than fortunate to have been able to work with you. 김창구 박사님께서 개발하신 TIGRESS 코드가 없었다면 제 학위논문은 가능하지 않았을 것입니다. 때로는 논문의 공동 지도자로서, 때로는 연구실 선배로서 다방면으로 많은 도움을 주셔서 진심으로 감사드립니다.

부족한 논문을 꼼꼼히 읽어주시고 고견을 주신 심사위원 윤성철 교수님, 김지훈 교수님, 김태선 교수님, 김종수 박사님께도 감사드립니다. 특히 지도학생이 아닌데도 불구하고 지속적인 관심과 격려를 보내 주시고 졸업 후의 삶에 대해 조언해주신 김태선 교수님께 감사드립니다. I thank Kengo Tomida for all the encouragement and advice that he gave me. 구본철 교수님, 퇴임하시기 전 교수님께 성간물질에 대해 배우는 행운을 누렸습니다. 최고의 강의로 연구에 꼭 필요한 지식과 지혜를 가르쳐 주셔서 감사드립니다. 휴게실에서 항상 밝게 인사해 주시고 은하에 대한 여러 궁금증을 해소해 주신 이명균 교수님, 교수님의 “행복한 천문학자”를 물려받고 싶습니다. 세상 속의 천문학자에 대해 생각해 보게 해 주신 윤성철 교수님, 목표로 삼아야 할 좋은 과학자의 본을 보여 주셔서 감사드립니다. 아무것도 모르는 학부시절 연구가 무엇인지 미약하게나마 체험할 기회를 주신 임명진 교수님께도 이 자리를 빌어 감사의 말씀을 드립니다. 마지막으로 마음속에 천문학이라는 씨앗을 심어주신 은사님이신 박성은 선생님께 감사드립니다.

천문학과 행정실 선생님들 덕분에 박사과정 동안 학업에 온전히 집중할 수 있었습니다. 졸업하는 순간까지도 출퇴근 인증을 잊어 증빙자료를 제출해도 싫은 소리 한번 안 하신 이효주 선생님, 감사합니다. 지금은 다른 곳에 계시는 노현주 선생님, 민아라 선생님, 선생님들께서 보여주신 따뜻한 책임감을 본받고 싶습니다. 살기좋은 19

동을 만들어주신 원선희 선생님, 김경숙 선생님, 유영선 선생님, 박현지 선생님께도 감사드립니다.

CnTAG를 거쳐간 그룹원들께도 감사의 말을 전하고 싶습니다. 먼저 학부 연구생 시절 친절하게 대해주신 용휘 형, 형묵이 형, 성원이 형과는 이야기 나눌 기회가 많지 않았던 것이 못내 아쉽습니다. 오랜 시간을 함께 보낸 우영이 형이 졸업할 때에는 허전함을 감출 수 없었습니다. 형 덕분에 인간적으로나 학문적으로나 의지할 곳이 있었습니다. 가장 가까이에서 연구에 꼭 필요한 많은 기술을 전수해 주시고 낯선 미국 땅에서 어려움 없이 머물다 갈 수 있게 많은 도움을 주신 정규 형, 감사합니다. 먼저 졸업하고 새로운 길을 걷고 있는 승원이, 동녁이, 가인이에게는 진심을 담아 응원의 말을 전합니다. 한결이, 다정이, 영우에게는 많은 도움을 주지 못해 미안한 마음이 앞섭니다. 남은 대학원 생활도 행복하기를 바라며 멋지게 해내리라 믿어 의심치 않습니다. My special thanks go to Alwin Mao, who cared me a lot whenever I visited Princeton.

동고동락했던 천문가족들에게도 감사드립니다. 종호 형, 비가 오나 눈이 오나 호텔 캘리포니아를 들으며 술 마시던 날들이 종종 그립습니다. 대학원 입학 전부터 고락을 함께 했다는 표현이 가장 잘 어울리는 민철이 형, 남은 날들은 즐거움만 펼쳐지기를 진심으로 기원합니다. 학부 시절부터 동기로서 함께했던 주형이, 성용이와 동료 천문학자로 다시 만난다면 더없이 기쁠 것 같습니다. 동갑내기 친구들인 속깊은 겨레, 따뜻한 호진이, 성실 그 자체인 정환이, 어른스러운 지수·하늘이 덕분에 즐거운 대학원 생활을 보낼 수 있었습니다. 보이지 않는 곳에서 천문학과의 발전을 위해 고심하고 노력한 윤수에게 고맙고 그 노력이 꼭 보답받기를 바랍니다. 기쁜 마음으로 결혼식 반주를 맡아주었던 오르가ニ스트 소피아에게도 정말 고맙습니다. 동아리를 비롯해 많은 추억을 공유한 한길이형, 물리, 음악, 술을 비롯해 인생을 풍요롭게 만들어 주는 많은 것을 나누어 주어 고맙습니다. 기혼자의 삶을 나눌 수 있어서 너무 재미있었던 수현 이계계도 고맙다는 말을 꼭 하고 싶습니다. 나이많은 형이랑 놀아주고 건강도 챙겨준 선호, 창석이와 재홍이에게도 고맙습니다. 특히 학문적으로나 신앙적으로나 본받을 것이 많았던 선호에게 고맙고 좋은 천문학자가 되리라 믿습니다. 지금은 먼 곳에서 공부하고 있는 다은이와 재연이에게는 응원의 말을 전합니다. 인생을 즐길 줄 아는 자전거왕 다인이와 심미안을 가진 주연이, 무엇이든 잘 해낼 성아, 미소천사 무건이,

자유로운 영혼의 소유자 브라이언에게도 함께 보냈던 모든 시간이 즐거웠고 고마웠다는 말을 전합니다. Khwammai, I learned a positive attitude toward life thanks to you.

낙성대동 성당 엘리에젤 성가대는 자칫 멋밋할 수 있었던 대학원 생활에 활력을 불어넣어 주었습니다. 성당 안팎을 나들며 함께 노래하던 날들은 제게 무엇과도 바꿀 수 없는 큰 행복이었고 앞으로도 평생 마음속에 남아 있을 것입니다. 특히 인생에서 중요한 것이 무엇인지 생각해 보게 해준 이영선 마멜다와 천기현 라파엘에게 감사의 마음을 전하며 그 선한 영향력을 계속 간직하기를 바랍니다.

사랑하는 아버지, 어머니. 긴 시간 동안 묵묵히 저를 믿고 지지해 주셔서 감사드립니다. 살갑지 못한 아들이지만 앞으로 제가 받은 사랑을 조금이라도 돌려드릴 수 있기를 바라며 이 작은 결실을 두 분께 바칩니다. 자기 인생을 스스로 만들어 나갈 줄 아는 멋진 동생 상훈아, 항상 우리 가족을 행복하게 해 주어서 고맙고 많이 사랑한다. 박사과정 막바지에 물심양면으로 지원을 아끼지 않아 주신 새로운 가족 장인, 장모님과 큰형님, 큰처형, 작은형님, 작은처형, 감사하고 사랑합니다.

마지막으로 긴 학위과정 동안 누구보다 저를 배려해주고 버팀목이 되어 준 사랑하는 아내 정선이에게 마음을 담아 고맙다는 말을 전합니다.